PONTIFÍCIA UNIVERSIDADE CATÓLICA
DO RIO DE JANEIRO

Geovane de Almeida Santos da Silva

Monitoring of the Hygrothermal Degradation of Composite Repairs for Offshore Metallic Pipelines

Tese de Doutorado

Thesis presented to the Programa de Pós-graduação em Engenharia de Materiais e de Processos Químicos e Metalúrgicos of PUC-Rio in partial fulfillment of the requirements for the degree of Doutor em Engenharia de Materiais e de Processos Químicos e Metalúrgicos.

Advisor: Prof. José Roberto Moraes d’Almeida

Co-Advisor: Prof. Daniel Carlos Taissum Cardoso

Rio de Janeiro
Abril de 2023

Pontifícia Universidade Católica
do Rio de Janeiro

Geovane de Almeida Santos da Silva

Monitoring of the Hygrothermal Degradation of Composite Repairs for Offshore Metallic Pipelines

Thesis presented to the Programa de Pós-graduação em Engenharia de Materiais e de Processos Químicos e Metalúrgicos of PUC-Rio in partial fulfillment of the requirements for the degree of Doutor em Engenharia de Materiais e de Processos Químicos e Metalúrgicos. Approved by the Examination Committee.

Prof. José Roberto Moraes d'Almeida
Orientador
Departamento de Engenharia Química e de Materiais – PUC-Rio

Prof. Daniel Carlos Taissum Cardoso
Co-Orientador
Departamento de Engenharia Civil e Ambiental – PUC-Rio

Prof. Flávio de Andrade Silva
Departamento de Engenharia Civil e Ambiental – PUC-Rio

Profa. Marília Garcia Diniz
Departamento de Engenharia Mecânica – UERJ

Profa. Janine Domingos Vieira
Departamento de Engenharia Civil – UFF

Dr. Lucio Rossi de Souza
Departamento de Ciência e Engenharia Macromolecular – Case Western
Reserve University (CWRU)

Rio de Janeiro, 11 de abril de 2023

Geovane de Almeida Santos da Silva

Graduou-se em Engenharia Mecânica na UERJ em 2015. Terminou o Mestrado em Engenharia de Materiais na PUC-Rio em 2018. Já participou de bancas examinadoras de defesas de TCC de alunos de Engenharia Mecânica na UERJ e de co-orientação de trabalhos finais. Participa do grupo de pesquisa do Laboratório de Compósitos no subsolo do Tecgraf na PUC-Rio, tendo colaborado com o projeto TCBR 495 da Petrobras sobre reparos compósitos realizado neste laboratório. Já publicou artigos científicos em revistas conceituadas, sendo um deles um artigo de Review sobre degradação em juntas de compósito causada pela absorção de umidade em névoa salina. Participou também de congressos da área de polímeros e compósitos.

Ficha Catalográfica

Silva, Geovane de Almeida Santos da

Monitoring of the hygrothermal degradation of composite repairs for offshore metallic pipelines / Geovane de Almeida Santos da Silva ; orientador: José Roberto Moraes d’Almeida ; co-orientador: Daniel Carlos Taissum Cardoso. – 2023.
270 f. : il. color. ; 30 cm

Tese (doutorado)–Pontifícia Universidade Católica do Rio de Janeiro, Departamento de Engenharia Química e de Materiais, 2023.
Inclui bibliografia

1. Engenharia Química e de Materiais – Teses. 2. Epóxi e fibras de vidro. 3. Absorção de umidade. 4. Inchamento. 5. Degradação mecânica. 6. Arrhenius. I. Almeida, José Roberto Moraes d'. II. Cardoso, Daniel Carlos Taissum. III. Pontifícia Universidade Católica do Rio de Janeiro. Departamento de Engenharia Química e de Materiais. IV. Título.

CDD: 620.11

Acknowledgements

Firstly, I thank God for having blessed my track to finishing my PhD.

I would like to thank my mom for always being there for me, supporting me and giving me the best advices, even when I was feeling discouraged.

I would like to thank my father (*in memorian*), who always supported my engineering career. I am sure he is proud of my achievements as well as I am proud of being his son.

I thank my advisor Prof. José Roberto Moraes d'Almeida for his time and effort for the text revisions, experimental support, discussions, online meetings and the best research advices, especially for opening up the opportunity for me to acquire experience in my internship in Switzerland. Also, special thanks for Prof. Daniel Carlos Taissum Cardoso, my co-advisor, for including me in the research project responsible for the results obtained for my work. Also, for the advices and revisions on my work.

Special thanks to the research group in Laboratório de Compósitos from PUC-Rio for the enriching discussions and exchange of ideas concerning the project. Also, for the moments of distraction within the daily laboratory activities. Also, thanks to Priscilla, Marcello and Bruno who also helped in the operation of the heating chambers, withdrawal of specimens and some tests.

I am more than thankful to the research project from Petrobras carried out in PUC-Rio that allowed me to gather experimental data for my thesis.

Thanks to PUC facilities for the space and machinery provided for the tests. Also, I am grateful for EPFL facilities in the city of Lausanne, Switzerland, and their research group for the knowledge acquired and contribution to my work. Also, for the availability of the burn-off and DMTA tests.

This work would not be possible without the support that the technicians from PUC-Rio provided for me. Lucas, who carried out the DSC tests, the LEM group for providing the destructive test machines, Marques for helping cutting the specimens and producing the silicon mould for the epoxy samples fabrication, Druval who performed the FTIR tests, Thamires who helped me with the SEM imaging tests and others that I might have forgotten to mention.

Thanks to CENPES for the DMA tests.

Thanks to the offshore repair manufacturer for providing the neat epoxy resin and the fiber-reinforced composites, essential to my work.

This study was financed in part by the Coordenação de Aperfeiçoamento de Pessoal de Nível Superior - Brasil (CAPES) – Finance Code 001.

Abstract

Da Silva, Geovane de Almeida Santos; d'Almeida, José Roberto Moraes (Advisor); Cardoso, Daniel Carlos Taissum (Co-Advisor). **Monitoring of the Hygrothermal Degradation of Composite Repairs for Offshore Metallic Pipelines**. Rio de Janeiro, 2023. 270p. Tese de Doutorado – Departamento de Engenharia Química e de Materiais, Pontifícia Universidade Católica do Rio de Janeiro.

Generally, the marine environment is the most aggressive natural environment for metallic pipelines, promoting corrosion, leading to catastrophic failures. The traditional welded metallic repairs are high-cost and inconvenient repair methods for the industry. Polymeric composites (FRP) are a potential repair material due to their high resistance/weight ratio and high resistance to corrosion and environmental degradation. However, polymeric composites are also susceptible to severe degradation when exposed to harsh environment conditions, including water absorption, temperature, UV and pressure. To better understand the degradation mechanism, glass-fiber reinforced polymer matrix composite (GFRP) and neat epoxy samples were fabricated and analyzed as a function of aging time and temperature in a saline atmosphere. In addition, a group of composites had their exposed edges coated with epoxy resin to simulate common real-life practices in the field, namely coated FRP. A two-component DGEBA epoxy resin and a bidirectional glass-fiber woven fabric were used as matrix and reinforcement, respectively. The fiberglass fabric had a longitudinal to transverse fiber ratio of 2:1. The materials were subjected to salt spray aging in three chambers at 35, 55 and 70°C for approximately 15171 hours. The salt concentration in the solution used was 5.0 % by weight. Samples were periodically removed from the chambers to have their mass gain measured by the gravitational method. Their dimensional changes were also measured to evaluate the swelling behavior of the materials. Thermal analyses with DSC and DMTA were performed to evaluate the curing degree of the polymeric materials tested and the effects of temperature on the material's post-curing. Chemical analyses with FTIR tests were performed to investigate the occurrence of post-curing, hydrolysis and thermo-oxidation processes during aging. Composite samples for bending and interlaminar shear strength (ILSS) destructive tests were periodically tested to have their degradation monitored over time. Impulse Excitation Technique and colorimetry tests were also performed as complementary non-destructive tests (NDT). The first part of this work focuses on the assessment of the moisture absorption behavior of both composite and neat epoxy resin. The relationship between the moisture gain capacity of the materials, considering the fiber volume fraction, was investigated. Besides, non-Fickian absorption models were also applied to the experimental data of FRP and neat epoxy resin to account for deviations from the standard Fickian model. Then, polymeric relaxations and polymer-water interactions, as well as network changes induced by moisture and temperature, were investigated. A modification to the Berens-Hopfenberg (BH) non-Fickian model was proposed to account for post-curing effects on the moisture absorption; such modification applied for post-curing was not found in literature. In the second part of this work, the swelling behavior of neat epoxy resin, uncoated and coated composites was evaluated and correlated with moisture absorption. The orthotropy of the composite was evident, since this material showed greater swelling capacity in the thickness direction. A Fickian-like model was implemented to the thickness swelling to investigate swelling strain saturation and swelling front. The third part of this work focuses on the destructive tests and evaluation of the hygrothermal effects on the material degradation. Temperature proved to be an accelerating factor for property degradation. In addition, a methodology to estimate the service-life curve of the repair systems and extrapolate it to lower temperatures was elaborated. The methodology of property extrapolation for long-term hygrothermal exposure in salt spray environments could not be found in literature. Parameters like property retention plateau and degradation rate were estimated for room temperature (25°C). Arrhenius curves were also plotted to evaluate the time required to reach the properties' retention levels for each temperature. Finally, two non-destructive techniques were performed on the uncoated FRP and on neat epoxy resin as complementary tests in order to validate the results found in other techniques. The Impulse Excitation Technique (IET) was performed to evaluate the Young modulus and good correlation was found between IET and destructive bending tests. From the colorimetry tests, the effects of moisture and temperature were visible, as the resin's color change was stronger at longer aging time and higher temperatures.

Keywords

Epoxy/glass fibers composites; moisture absorption; swelling; mechanical degradation; Arrhenius.

Resumo

Da Silva, Geovane de Almeida Santos; d'Almeida, José Roberto Moraes (Orientador); Cardoso, Daniel Carlos Taissum (Co-Orientador). **Monitoramento da Degradação Hidrotérmica de Reparos de Compósito de Tubulações Metálicas Offshore**. Rio de Janeiro, 2023. 270p. Tese de Doutorado – Departamento de Engenharia Química e de Materiais, Pontifícia Universidade Católica do Rio de Janeiro.

Geralmente, o ambiente marinho é o ambiente natural mais agressivo para tubulações metálicas, promovendo corrosão, levando a falhas catastróficas. O método de reparo tradicional metálico soldado é um método de reparo inconveniente e custoso para a indústria. Compósitos poliméricos (FRP) são um material com potencial para reparo devido a sua alta razão resistência/peso e alta resistência à corrosão e degradação ambiental. Porém, os compósitos poliméricos também são suscetíveis a degradação severa quando expostos a condições ambientais agressivas, incluindo absorção de água, temperatura, UV e pressão. Para um melhor entendimento do mecanismo de degradação, amostras de compósito de matriz polimérica reforçado por fibras de vidro e resina epóxi pura foram fabricados e analisados em função do tempo e temperatura de envelhecimento em uma atmosfera salina. Além disso, um grupo de compósitos tiveram suas bordas cobertas com resina epóxi para similar práticas reais comuns no campo, denominado *coated FRP*. Uma resina epóxi DGEBA bicomponente e um tecido bidirecional de fibras de vidro foram usados como matriz e reforço, respectivamente. O tecido de fibra de vidro detém de uma razão de fibras longitudinais por transversais de 2:1. Os materiais foram sujeitos a envelhecimento de névoa salina em três câmaras à 35, 55 e 70°C por aproximadamente 15171 horas. A concentração de sal na solução usada foi 5.0% por massa. As amostras foram periodicamente retiradas das câmaras de envelhecimento para terem seus ganhos de massa mensurados pelo método gravitacional. Suas mudanças dimensionais também foram capturadas para avaliação do comportamento de inchamento dos materiais. Análises térmicas com DSC e DMTA foram feitas para avaliar o grau de cura dos materiais poliméricos e os efeitos da temperatura na pós-cura do material. Análises químicas com testes FTIR foram feitas para investigar a ocorrência de processos de pós-cura, hidrólise e termo-oxidação durante o envelhecimento. Amostras de compósito para testes destrutivos de flexão e resistência ao cisalhamento (ILSS) foram testados

periodicamente para terem suas degradações monitoradas com o tempo. Testes de Excitação por Impulso (IET) e Colorímetro foram realizados como testes não-destrutivos (NDT) complementares. A primeira parte deste trabalho foca na avaliação do comportamento de absorção de umidade nos compósitos e resina epóxi pura. A relação entre a capacidade de absorção de umidade dos materiais, considerando a fração volumétrica de fibras, foi investigada. Além disso, modelos de absorção não-Fickianos também foram aplicados aos dados experimentais do FRP e resina epóxi para considerar desvios do modelo Fickiano padrão. Com isso, relaxações poliméricas e interações polímero-água, assim como mudanças na rede polimérica induzidas por umidade e temperatura, foram investigados. Uma modificação ao modelo não-Fickiano de Berens-Hopfenberg (BH) foi proposta para incluir os efeitos de pós-cura na absorção de umidade; tal modificação aplicada a pós-cura não foi encontrada na literatura. Na segunda parte deste trabalho, o comportamento de inchamento da resina epóxi pura e compósitos revestidos e não-revestidos foi avaliado e correlacionado com a absorção de umidade. A ortotropia do compósito ficou evidente, visto que o material apresentou maior capacidade de inchamento na direção da espessura. Um modelo do tipo Fickiano foi implementado ao inchamento na espessura com o intuito de investigar deformação de inchamento de saturação e a frente de inchamento. A terceira parte deste trabalho foca nos testes destrutivos e na avaliação dos efeitos hidrotérmicos na degradação do material. A temperatura se mostrou um fator acelerador para degradação de propriedade. Além disso, uma metodologia para estimar a curva de serviço de sistemas de reparo e extrapolá-la para temperaturas mais baixas foi elaborada. Metodologias de extrapolação de propriedades para exposição hidrotérmica de longa duração não foram encontradas na literature. Parâmetros como platô de retenção de propriedade e taxa de degradação foram estimados para temperatura ambiente. Curvas de Arrhenius também foram plotadas para avaliar o tempo requerido para alcançar os níveis de retenção em cada temperatura testada. Por fim, duas técnicas não-destrutivas foram utilizadas no FRP e resina epóxi pura como testes complementares como forma de validar os resultados encontrados em outras técnicas. A Técnica de Excitação por Impulso (IET) foi realizada para obter o módulo de Young e boa correlação foi obtida entre o teste IET e o ensaio destrutivo de flexão. Através dos testes colorimétricos, os efeitos de umidade e temperatura

foram visíveis, já que a mudança de cor da resina foi mais forte para tempos longos e temperaturas mais altas.

Palavras-chave

Compósitos de epóxi/fibras de vidro; absorção de umidade; inchamento; degradação mecânica; Arrhenius.

Table of Contents

List of Figures

List of Tables

GLOSSARY

ASME	American Society of Mechanical Engineers
ASTM	American Society for Testing and Materials
BH	Berens-Hopfenberg
BMI	Bismaleimide
c	Moisture concentration
CB	Carbon Black
CFRP	Carbon Fiber Reinforced Polymer
CNT	Carbon Nanotubes
D	Diffusivity
DGEBA	Diglycidyl ether of bisphenol-A
D_d	Diffusivity of the densely crosslinked phase
D_l	Diffusivity of the less densely crosslinked phase
DLJ	Double-lap Joint
DLS	Double-lap Shear
DMTA	Dynamic Mechanical Thermal Analysis
DSC	Differential Scanning Calorimeter
DW	Distilled Water
EG	Expanded Graphite
EP	Epoxy
FFRC	Flax Fiber Reinforced Composite
FRP	Fiber Reinforced Polymer
FTIR	Fourier Transform Infrared Spectroscopy
GFRP	Glass Fiber Reinforced Polymer
GHz	Gigahertz
GnP	Graphene nanoplatelets
Hz	Hertz
IET	Impulse Excitation Technique
ILSS	Interlaminar Shear Strength
ISO	International Organization for Standardization
M	Moisture Content
M_F	Fickian moisture saturation

MHz	Megahertz
M_m	Saturation water content
M_R	Relaxation-induced saturation content
MWCNT	Multiwall carbon nanotubes
Na	Sodium
NaCl	Sodium Chloride
NDT	Non-Destructive Technique
O	Oxygen
PEI	Polieterimide
PPS	Polyphenylene sulfide
PR	Property Retention
Q	Activation Energy
R	Universal Gas Constant
RH	Relative Humidity
RT	Room Temperature
S_∞	Mechanical property retention plateau
SEM	Scanning Electron Microscope
Si	Silicon
SR	Strength Retention
SS	Salt Spray
SW	Seawater
T	Temperature
T_g	Glass Transition Temperature
THz	Terahertz
TSF	Time Shift Factor
UV	Ultraviolet
V_f	Fiber Volume Fraction
V_m	Matrix Volume Fraction
V_v	Void Volume Fraction
wt%	Weight fraction

1. Introduction

Natural resources, such as oil and gas, correspond to the largest global portion of fossil fuels, representing the main source of energy of the world. Metallic pipelines are the safest long-distance means of transport for these resources. Currently, most of the pipeline systems consists of metal pipes due to its higher resistance, relative joints simplicity and low cost [1,2].

However, these pipelines are likely to deteriorate due to several factors, including construction defects and natural forces, especially the underground and underwater pipes, which may suffer severe degradation, like cracks, dents, abrasion and erosion, which may lead to leaking, causing material loss [1,2].

Generally, marine environment is the most aggressive natural media for metallic pipelines, promoting corrosion, which may result in catastrophic failure [3,4]. Though, suspended structures, i.e., non-immersed pipes, located at coastal neighborhoods are also vulnerable to corrosion due to the accumulation of salt, pollutants and humidity at the metallic surface – carried by the wind – , as well as the pH level and biological effects [3,5].

The most reliable repair solution for a corroded steel pipe is the removal of the entire pipe or only the damaged section and the replacement with a new section or the wrapping of the damaged region with either a welded metallic repair or a steel repair clamp (Figure 1) [1,2]. The former solution involves a considerable cost and the inconvenience caused to the industry [2], and the latter is a complex process, especially with underwater or underground pipes mainly due to the difficulty of the welding and installation processes in these conditions [1].

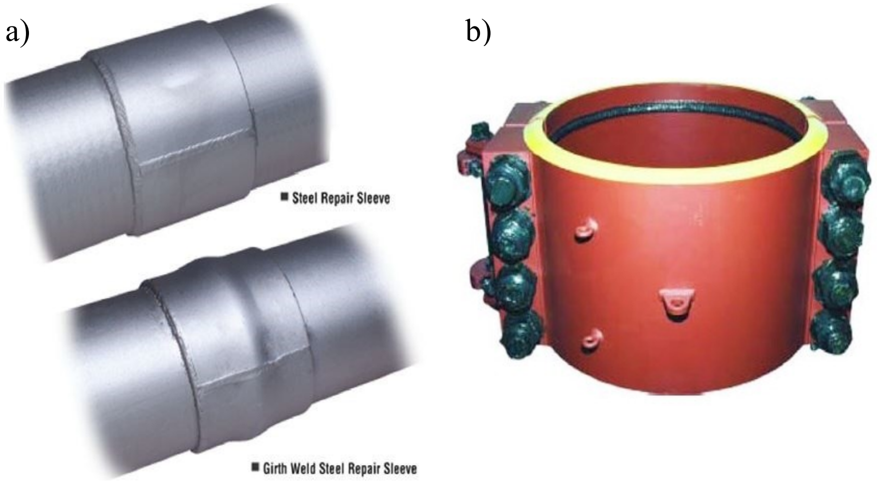

Figure 1. Conventional welded repair. (a) Steel repair sleeve, (b) Steel repair clamp [1].

According to Abbas and Shafiee [3], the maintenance costs of the installations operating under marine conditions, such as naval structures, renewable energy offshore platforms and oil and gas subsea installations represent from 20 to 40% of the total operational costs. About 80% of this cost is related to the maintenance of corrosion-related problems, according to Lim *et al.* [2]. According to the United States Department of Transport, the annual average cost related to corrosion is estimated to be US$7 billion to monitor, replace and maintain fluid transmission lines [2].

Therefore, global researchers have been searching for alternative lightweight, resistant and durable materials that would form an effective and easily installable repair [1].

Polymeric composites are widely acceptable in aerospace industry and in naval structures [6] and are also a potential repair for metallic components and pipelines [1] due to its high resistance/weight ratio and high resistance to corrosion and environmental degradation, which may lead to even greater advantages in comparison with conventional construction materials, like steel [7–9]. Besides, fiber reinforced polymer composites (FRP) are more easily processed for repairs in comparison with techniques using metals [10]. FRP is also used in many areas of civil engineering, as in bridges and buildings repairs. Adhesion and filament winding techniques are employed to improve the resistance and stiffness of reinforced concrete beams, increasing its durability and decreasing its cost [11].

However, polymeric materials are also susceptible to moisture-induced degradation; therefore, the understanding of the degradation mechanism is of uttermost importance to assess the service-life of the composite repair. Moreover, the mechanisms involved in hygrothermal degradation, such as post-cure, void content, temperature, matrix swelling and chemical interaction, must be better understood.

1.1. Objective

The objective of this work was to monitor the progress of hygrothermal degradation suffered by polymeric composites when exposed to moist environment and temperature. An epoxy-matrix glass-fiber reinforced composite applied in the real-life offshore industry was used and aged in salt spray. This environment aimed to simulate the environment that composite repairs installed in suspended pipes close to a marine environment are exposed to. The temperatures used were higher than room temperature to simulate conditions more severe than those the repairs are exposed to.

To achieve this objective, the following partial objectives were developed:

1) Assessment of the moisture absorption behavior of both composite and neat epoxy resin, relating experimental data with Fickian and non-Fickian absorption models. The BH Model was modified to include post-curing effects on the absorption behavior of the material.
2) Evaluation of volumetric and linear swelling behavior of the neat epoxy resin and composites, and its correlation with moisture absorption. The swelling front penetrating the material was speculated from a proposed Fickian-like model for the thickness swelling.
3) Characterization of the flexural and interlaminar shear mechanical behaviors of the composites as a function of the aging time and estimation of the service-life curves of the repair systems.
4) Development of a methodology for extrapolation of the service-life curve of repairs exposed to salt spray at temperatures different from the experimental temperature range, allowing the evaluation of the lifetime at different temperatures. Such methodology was not found in the literature. The service-life of the repair at room temperature was obtained.
5) Assessment through two non-destructive techniques of the effects of aging on the Young's modulus and damping characteristic, and also on the color variation of the composite repair.

2. Literature Review

2.1. Composite Repairs

Composite repair systems have been designed for both in-air and underwater applications for a wide range of temperatures [12]. However, while polymeric composites are suitable to replace traditional repair systems, these materials can suffer serious degradations due to its exposure to severe environment conditions, including distilled water and saltwater absorption, temperature, UV and pressure [6,7,13–18]. Therefore, an investigation of the degradation process of these materials is necessary.

Polymeric composite repairs generally consist in the composite adhesively bonded to a metallic surface by means of a polymeric adhesive. The combination of the unique properties of the FRPs with the advantages of the adhesion has turned this type of repair into an attractive method for structures reinforcement and repair. However, water molecules can still penetrate the joints' interfaces. When this happens, degradation occurs faster than the diffusion through the bulk material. Thus, the efficiency of the FRP/steel joint highly depends on the quality, integrity and durability of the adhesive bond between the adherents [9]. Thus, it is essential to understand the degradation mechanism in each component: composite and composite/adhesive/steel joint. However, this work focuses on the study of the degradation mechanism and prediction of the lifespan of the polymer composite itself.

2.2. Materials

The elements of a repair are selected based on the required performance of the composite under certain service conditions. In this section, the main types of fibers and resins employed in repairs will be briefly discussed, focusing on the material to be studied: woven glass-fiber reinforced epoxy composite system, as well as its cure process.

2.2.1. Matrix

The main goal of the matrix is to bundle the fibers in a cohesive structure and protect them from the harsh environment. In addition, the matrix transfers the applied load to the fibers, which rule the mechanical performance of the laminate given its higher strength compared to that of the resins. Moreover, the matrix rules some matrix-dependent properties, such as the interlaminar shear resistance, resistance to crack growth, toughness and resistance to impact and abrasion of the composites [1,19].

Given the better properties of the thermoset resins over the thermoplastic ones, epoxy, vinylester, polyester and phenol formaldehyde are the most commonly used resins in structural applications [1].

2.2.1.1. Epoxy

Due to the combination of good mechanical resistance, processing versatility, thermal stability, high resistance to moisture, excellent adhesive properties and low shrinkage in curing, the epoxy resin has been widely applied in high-performance fiber reinforced composites. Considering the importance of pipeline repairs, the epoxy resins are the most adequate for both underwater and underground applications [1,19].

There are two main types of epoxies used in the industry: i) diglycidyl ether of bisphenol A (DGEBA), which is widely applied in filament winding, pultrusion and some adhesives; and ii) tetraglycidyl methylenedianiline (TGMDA). Generally, the epoxy resins are bicomponent, which means that they need a curing agent, which is a process that basically consists in the opening of the oxirane ring and the crosslinking in the polymer's network. The cured epoxy's properties are strongly dependent on the curing agent used [19].

2.2.2. Fibers

The purpose of the fibers is mainly to carry the applied load, especially when it is applied in the direction parallel to the fiber. Then, the fiber-dominated properties are basically the mechanical properties, such as the tensile and flexural strengths. The most commonly used fibers for composite reinforcements are the glass, carbon and aramid. Due to its low cost, high mechanical and impact resistances, easy availability and better compatibility with resins, glass fibers are widely employed in commercial composites [1,19].

The three most common glass fibers are the E-glass, S-2 and quartz, with the former being the most common one and the cheapest, presenting a satisfactory combination of mechanical resistance (~3.45 GPa) and Young modulus (~75.8 GPa) [20].

2.2.3. Curing process

The cure of a thermoset polymer is a process where low-molecular weight resins become highly crosslinked. In this process, the thermal, electrical and mechanical properties are established. A classic curing process for epoxy resins is depicted in Figure 2, which consists in two thermal ramps and two isothermal plateaus. The first ramp and plateau are used to allow the resin to flow and the volatile components to escape. The dashed viscosity line in Figure 2 shows that during this stage, the resin melts when heated and its viscosity decreases dramatically. The second ramp and plateau correspond to the polymerization stage of the curing cycle. In the second ramp, the viscosity slightly decreases due to the additional heat, and then it considerably increases as the crosslinks are formed, reaching the gel stage, indicated by a red ellipse in Figure 2. The resin then is maintained at this cure temperature for 4-6 hours until the crosslinking is completed [19].

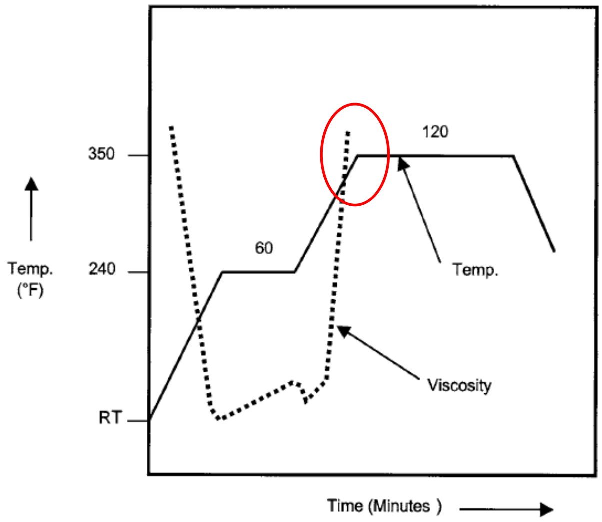

Figure 2. Typical thermal cure profile of a composite [19].

After the curing process, the chemical structure of the resin may not have been completely formed due to its high viscosity at the gel point, making it difficult for the monomers to be transported through the bulk material. In view of this, the industry adopts a procedure, called post-cure, which consists in an additional heating after the matrix curing, usually at a temperature lower than that used in the cure process, aiming to promote the reaction with the remaining unreacted monomers, increasing the crosslink density. Santana *et al.* [21] reported that two mechanisms are involved in this phenomenon: the residual monomers are covalently bonded to the polymeric structure and unreacted monomers are volatilized during the heating process. Bagis and Rueggeberg [22] found out that the higher the temperature used in the post-cure, the lower the content of unreacted monomers remaining in the bulk material.

Then, after undergoing post-cure, either during the fabrication process or in high-temperature service life, the composite presents a relief of internal stresses [19,21], besides generally experiencing an improvement in the mechanical properties, such as the increase in glass transition temperature [23], flexural resistance [21], shear resistance [24] and stiffness [25]. These topics will be further discussed.

2.3. Composite's Hygrothermal degradation

2.3.1. Ways of water penetration in composites

The water penetration in the composites is mainly governed by the diffusion mechanism. There are three major ways of moisture penetration in polymer composites. One of them is the diffusion of water into the bulk matrix through micropores in the polymers, called free volumes [26,27]. The other common mechanisms are capillarity and transport through microcracks, voids and porosities at interfaces [28]. The capillarity mechanism involves the flux of water molecules through the fiber/matrix interface, followed by the diffusion into the bulk resin. Transport of moisture through microcracks and voids involves not only the flux but also the storage of water into the microcracks and other microdefects [26,29]. In addition, if the processing of the composite is not properly done, in other words, if the manufacturing process and/or cure of the composite generates voids and flaws on the interface, the water will favorably penetrate by capillarity and accelerate the composite's degradation. This is the case of the epoxy/glass fiber composite system analyzed by Pomiès *et al.* [6], which presented higher saturation content than the pure resin, which is unexpected, since the addition of a hydrophobic fiber to the polymer is supposed to decrease the absorption capacity of the composite. Therefore, it can be deduced that there may have been some flaws at the interface region on the exposed edges of the composite.

Zafar *et al.* [30] investigated the moisture absorption behavior of the neat epoxy resin and the epoxy-based composite reinforced by one single carbon fiber, labeled as *Model Composite*, with both edges of the fiber exposed to water in demineralized water and seawater at room temperature for 300 days. The sorption curve as a function of the square root of time in seconds is shown in Figure 3. It can be noticed that the composites presented greater saturation levels than the neat resin, being attributed to imperfections at the fiber/matrix interface, which may have created secondary transport paths by capillarity. Additionally, a reduction in the saturation level with the addition of salt is also visible. The diffusivity value of the epoxy resin in seawater was slightly lower than in demineralized water (7.89 x 10^{-14} m^2/s and 8.40 x 10^{-14} m^2/s respectively).

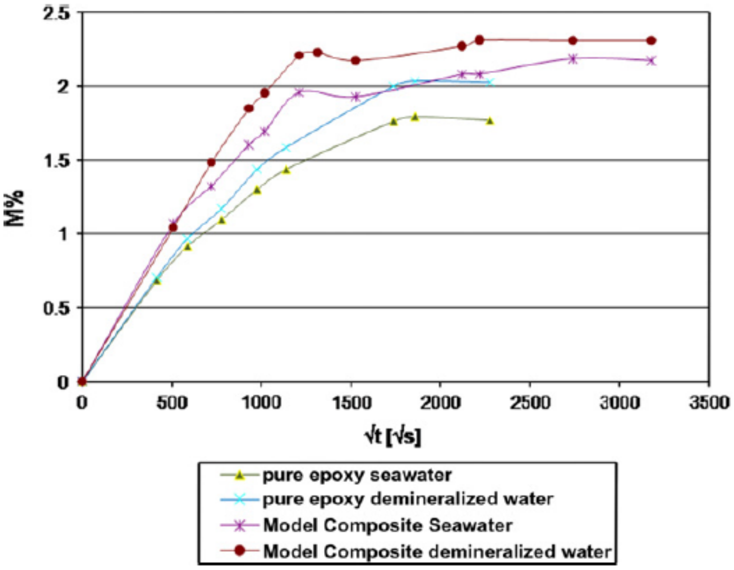

Figure 3. Diffusion curves of pure epoxy and model composites samples in seawater and demineralized water [30].

Provided that the fiber/matrix interface is a crucial and vulnerable constituent of the composite, an eventual moisture attack at this region leads to loss of resistance, stiffness and integrity, besides the occurrence of hydrolysis reaction, depending on the nature of the composite's components [13]. These degradation processes will be more thoroughly discussed in this work.

2.3.2. Types of fibers

Part 4 of ASME PCC-2-2006 [31] recommends the composite materials for repair systems to include, but not limited to, continuous glass, aramid, or carbon fiber reinforcement in a thermoset polymer (e.g., polyester, polyurethane, phenolic, vinyl ester, or epoxy) matrix.

While some synthetic fibers, such as glass and carbon may absorb negligible moisture content, other synthetic fibers, like aramid, and also natural fibers may absorb considerable moisture content due to its lower hydrophobicity or even hydrophilicity [1,32]. Therefore, it can be claimed that the absorption behavior of composite materials not only depends on the fiber nature, but also on the fiber volume fraction, as seen in Figure 4a, where Choi *et al.* [33] observed that the higher the epoxy matrix volume fraction (V_m) of the CFRP, i.e., the lower the carbon fiber content, the greater the water absorption rate. The diffusivity coefficients exhibited a linear increase with the increase in the matrix fraction (Figure 4b).

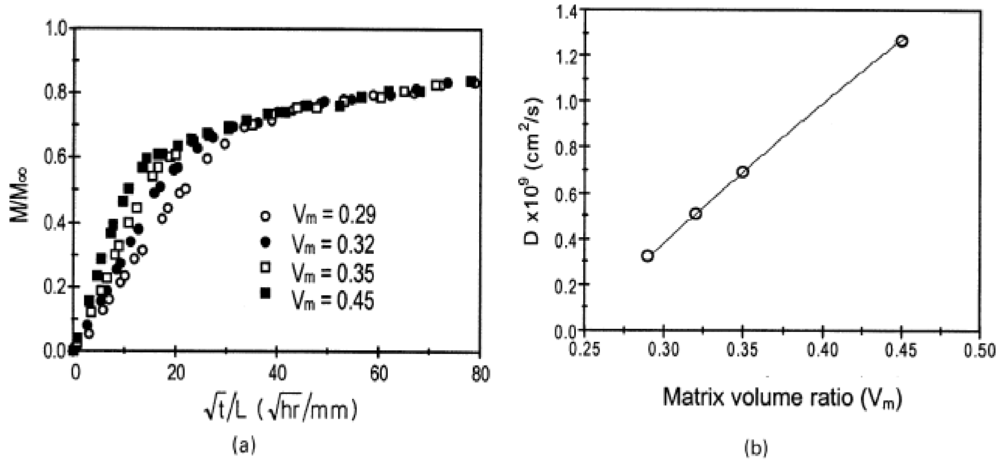

Figure 4. a) Moisture absorption curves and b) diffusion coefficients of laminates with varying epoxy matrix volume fractions [33].

Even though glass and carbon fibers do not absorb water, they can change the water diffusion path, changing then the effective length of water diffusion, which is the actual path the water molecules need to travel, represented by the solid lines in Figure 5. Additionally, the increment in the fiber volume fraction implies in a more anisotropic fiber arrangement, increasing the length of water diffusion, decreasing the diffusivity rate. Another factor that influences the water path is the fiber orientation, as illustrated by Figure 5. Choi *et al.* [33] reported that the diffusivity of the CFRP specimens with 45° fiber orientation presented intermediary values to those with 0° and 90° orientation, with the former presenting the highest diffusivity value and the latter the lowest one, owing to the less obstacles for the water to overcome (see Figure 5).

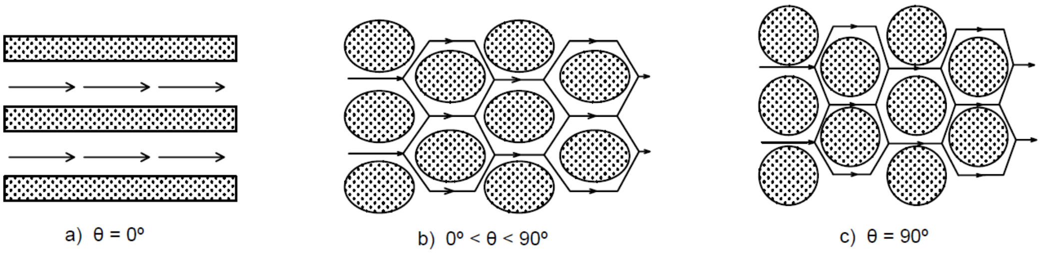

Figure 5. Diffusion path of moisture in the laminate through-thickness direction [33].

Aiming to compare the sorption behavior of composites reinforced with carbon and glass fibers, some authors have found out that the GFRPs tend to present greater absorption capacity than the CFRPs [34–37]. Guermazi *et al.* [34] and Jesthi and Nayak [35] state that this behavior is related to the glass fiber's higher susceptibility to moisture absorption due to the presence of some hygroscopic elements on the fiber surface. From another perspective, Heshmati *et al.* [37] associated the lower permeability of CFRP compared with GFRP to both higher fiber content and quality of fabrication. On the other hand, Barjasteh and Nutt [38] reported a stronger absorption in CFRP than in GFRP, both with ~67% fiber volume fraction, attributing it to the smaller carbon fiber diameters, which may have resulted in a larger interfacial area. Thus, with the goal to combine the properties of glass and carbon fibers, these authors also studied the behavior of hybrid carbon/glass composites. While Barjasteh and Nutt [38] and Guermazi *et al.* [34] found diffusivity and saturation values of hybrid composites intermediary to those of GFRP and CFRP, Jesthi and Nayak [35] reported lower diffusivity in comparison with the plain carbon and glass reinforced composites.

Additionally, researchers have been studying the effects of the addition of nanoparticles on the moisture uptake of polymers [39–41]. The addition of nanofillers to the polymeric matrix, such as nanoclay, induces physical and chemical interactions between the constituents, and as a result, the moisture capacity is reduced and the composite's degradation is hampered [40,41]. Nanoclay creates a tortuous path for the water penetration, similar to Figures 5b and 5c. The same behavior was observed by Prolongo *et al.* [39] with the addition of carbon nanotubes and carbon nanofillers to the epoxy matrix. Besides creating a tortuous path for water diffusion, the carbon nanotubes (CNTs) promoted strong chemical interfaces with the epoxy matrix [39].

2.3.3. Macromolecular structure of polymers

In addition to the factors that influence the sorption mechanisms previously discussed, the water uptake also depends on the structure and morphology of polymers. There are some theories put forward by researchers that relate the polymer’s moisture absorption capacity to its fraction of free volumes, which corroborates with the fact that the crystalline phase of a semi-crystalline polymer does not absorb water [42,43]. This means that the more amorphous the polymer is, the greater its moisture absorption [44]. This behavior was observed by Pomiès *et al.* [6], who found a higher moisture content in the epoxy/glass fiber composite than in the PPS/glass fiber one (semi-crystalline matrix), both with the same fiber content, since the epoxy’s higher amorphicity leads to a more considerable misorientation of the polymer chains, creating more diffusion paths for the water molecules than in the thermoplastic matrix, where the crystalline domains tend to inhibit diffusion.

However, there are several free-volume rich polymers that absorb low water content. Thus, it can be stated that the free volume is necessary for water diffusion, but is not the major factor [42].

In view of this, a second group of theories was put forward involving the formation of hydrogen bonds between polar groups of polymers and water molecules. In other words, a polymer which has chemical functional groups with high affinity with water will result in a greater absorption level [42]. For instance, the relatively high water absorption capacity of epoxy resins is due to the presence of hydroxyl groups (-OH-), attracting the polar water molecules [44]. Therefore, the water absorbed level can be directly related to the polar groups concentration, as reported in the works of Cabral-Fonseca *et al.* [24] and Visco *et al.* [45], where unsaturated polyester absorbed more water than vinylester owing to the different polarity and crosslink density. Nodehi *et al.* [46] and Ramirez *et al.* [47] found that polyester resin absorbed far more moisture than epoxy resin, which in turn absorbed more than vinylester.

With respect to the polymer-water interactions, two types of water molecules may coexist in the polymer at a moist environment: the free water molecules, or mobile, which diffuse within the polymer and do not directly interact with the polymer’s chain, getting trapped in the voids and flaws of the material, and the bound molecules, or immobile, which directly interact with the polymeric chain and create hydrogen bonds with the polymer's hydroxyl groups [42,48]. Regarding the epoxy matrix, some studies have been reported confirming the presence of strong hydrogen bonds between epoxy and water molecules (immobile) [49,50]. Some authors have reported the moisture absorption capacity of the epoxy matrices, showing that it can be comparable to those of other thermoset polymers [44,45,47,51].

2.3.4. Moisture diffusion

The hygrothermal aging of polymeric matrices involves the absorption of water molecules in the material and the best experimental method to measure the absorbed moisture content is the gravimetric method, in which the specimens are either immersed in water at a controllable temperature or exposed to moist atmosphere, and periodically withdrawn from the aging chamber to have their weight measured [16,52]. The water content M is determined following the equation 1 [52]:

$$\mathrm{M}(\%) = \frac{M_t - M_0}{M_0} \times 100 \qquad (1)$$

where M_t is the sample's mass at time t and M_0 is the initial mass, corresponding to the time $t = 0$ hours.

The moisture absorption is ruled by the diffusion process, whose kinetic is described by the Second Fick's Law [53]:

$$\frac{\partial c}{\partial \mathrm{t}} = \frac{\partial}{\partial \mathrm{x}}\left(D_x \frac{\partial c}{\partial \mathrm{x}}\right) \qquad (2)$$

where c is the moisture concentration, x is the depth of penetration inwards the material and D_x is the diffusivity coefficient of moisture at the through-thickness direction. By keeping the temperature, moisture concentration in the composite's surroundings and diffusivity value constants, equation 2 can be written as [53]:

$$\frac{\partial c}{\partial \mathrm{t}} = D_x \frac{\partial^2 \mathrm{c}}{\partial \mathrm{x}^2} \qquad (3)$$

where the boundary conditions are:

$c = c_i \qquad 0 < x < h \qquad t = 0$

$c = c_m \qquad x = 0;\ x = h \qquad t > 0$

where h is the thickness of a thin and semi-infinite plate-shaped composite, c_i is the initial water content in the composite immediately when the material is exposed to moisture and c_m is the water content at both edges of the composite.

Then, from equation 3, the unidimensional moisture concentration distribution across the laminate thickness is written as:

$$\frac{c-c_i}{c_m-c_i} = 1 - \frac{4}{\pi}\sum_{n=0}^{\infty}\frac{1}{(2n+1)} sin\frac{(2n+1)\pi x}{h} exp\left[-\frac{(2n+1)^2\pi^2 D_x t}{h^2}\right] \quad (4)$$

For a thin plate (*w/h* >> 1, *l/h* >> 1), where *h*, *w* and *l* are thickness, width and length of the plate, respectively, and considering that the diffusion occurs in the through-thickness direction, the solution of equation 4 is given by [54]:

$$\frac{M_t}{M_m} = 1 - \frac{8}{\pi^2}\sum_{n=0}^{\infty}\frac{exp\left[-(2n+1)^2\pi\left(\frac{Dt}{h^2}\right)\right]}{(2n+1)^2} \quad (5)$$

where M_t is the absorbed moisture content at time t and M_m is the maximum moisture content, in which the material is saturated (saturation stage) and the driving force for diffusion is negligible. This equation rapidly converges with time, so a good approximation can be obtained with the first term of this series [55].

Equation 4 is graphically demonstrated by Figure 6, where each curve represents a value of the non-dimensional relation $\frac{Dt}{h^2}$, where M_i is the initial mass, M_m the saturation content, h the thickness and x the position in the sample. It can be noted that after a certain amount of time, the saturation moisture content is reached through the thickness of the laminate [56].

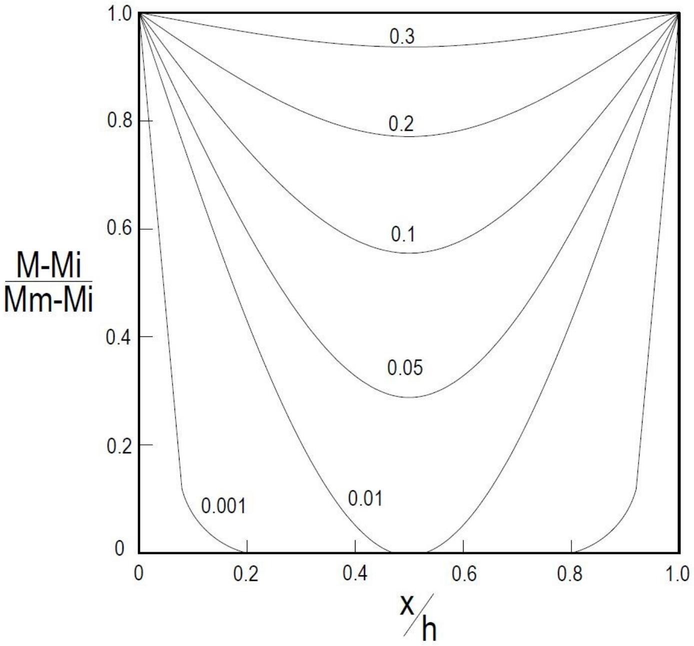

Figure 6. Moisture profile as a function of time. The numbers on the curves are the dimensionless value of Dt/h^2 (Adapted from Ref. [56]).

An analytical simplification of equation 5 for $M_t/M_\infty > 0.5$ is given by [53]:

$$\frac{M_t}{M_m} = 1 - exp\left[-7.3\left(\frac{Dt}{s^2}\right)^{0.75}\right] \tag{6}$$

where $s = h$ if both faces of the specimen are exposed to the environment and $s = 2h$ if only one face is exposed [53].

From equation 6, when under constant temperature and moisture, the necessary time to reach a specific moisture content can be expressed by [57]:

$$t = \frac{h^2}{D}\left[\frac{-1}{7.3} ln\left(1 - \frac{M_t - M_0}{M_m - M_0}\right)\right]^{4/3} \tag{7}$$

In the absence of initial moisture ($M_0 = 0$), the required time to reach 99.9% of the saturation content is approximately [53]:

$$t_{99.9} = \frac{0.67h^2}{D} \tag{8}$$

For short-term exposure ($t \leq 0.005h^2/D$), the moisture content M initially varies linearly with the square root of time t, following the equation 9 [6]:

$$M_t = \left(\frac{4M_m\sqrt{D}}{h\sqrt{\pi}}\right)\sqrt{t} \tag{9}$$

Equation 9 allows the determination of D from the initial slope of the curve M_t *vs*. $\sqrt{t}$, considering that M_m is a known value and experimentally measured.

These equations and considerations aforementioned lead to typical Fickian sorption curves similar to the graph depicted in Figure 7, where *M* (%) is obtained from equation 1 [53].

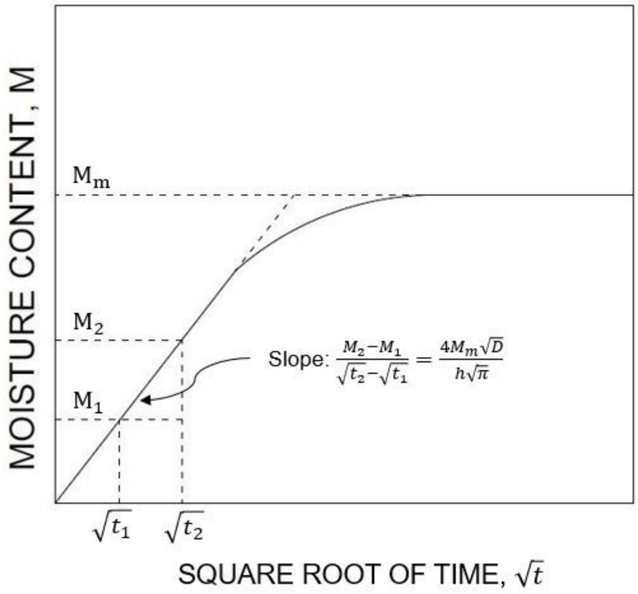

Figure 7. Typical Fickian absorption behavior, which illustrates the weight gain (*M*) with the square root of time [53].

Apolinario *et al.* [52] carried out water sorption tests in flax fiber reinforced polyester composite (FFRC) and glass fiber reinforced composite (GFRP) and the water uptake as a function of the square root of time is illustrated in Figure 8. In addition, the authors treated a group of flax fibers with silane to improve the adhesion to the matrix. The Fickian behavior could be observed with an initial linear weight gain until the saturation level was reached in all materials tested. It can also be noted that the hydrophilic flax fibers tend to accelerate the diffusion process, while the glass fiber acts as a barrier to water sorption in comparison with the neat polyester resin due to the higher hydrophobicity of glass fibers. This hypothesis was also put forward by Gellert and Turley [58] and Bian *et al.* [59].

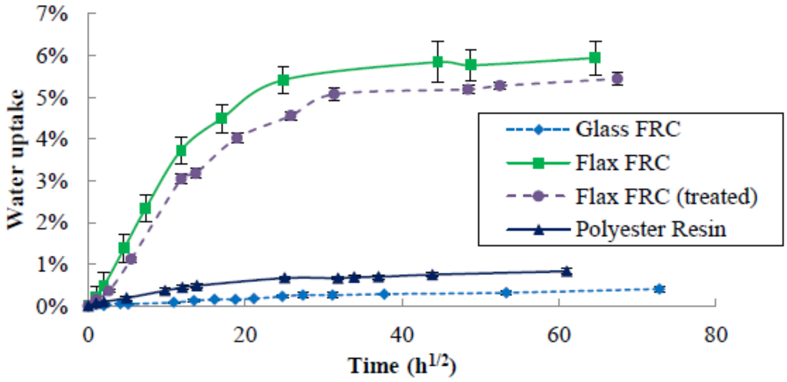

Figure 8. Water uptake as a function of aging time of polyester resin, GFRC and FFRC (pure and silane-treated). The composites were immersed in water at 30°C [52].

The equations 6 and 9 are strictly valid for composites with width and length much larger than thickness and represent the through-thickness diffusion process (Figure 9). For anisotropic, transversely isotropic and finite composite panels, the water diffusion through all six surfaces, i.e., including the edges, needs to be considered. Then, in order to compensate for the water penetrating the edges, the so-called "edge effect", the transverse diffusivities (D_y and D_z) need to be acknowledged, as follows [6,53,60]:

$$D = D_x\left(1 + \frac{h}{l}\sqrt{\frac{D_y}{D_x}} + \frac{h}{w}\sqrt{\frac{D_z}{D_x}}\right)^2 \qquad (10)$$

where the dimensions h, l and w are displayed in Figure 9. In this case, the diffusion is called anisotropic.

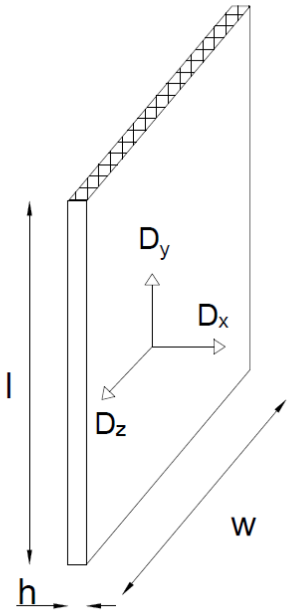

Figure 9. Specimen's dimensions and the diffusivity directions.

When the material is isotropic, the diffusivity values are equal ($D_x = D_y = D_z$), which implies that [60]:

$$D = D_x\left(1 + \frac{h}{l} + \frac{h}{w}\right)^2 \qquad (11).$$

Pomiès *et al.* [6] reported that the PPS/glass fiber composite with dimensions 25.4 x 229 mm presented a faster absorption than the one with dimensions 50 x 50 mm. The values of the through-thickness (D_x) and transversal diffusivities (D_y and D_z) for the former geometry were 0.09 x 10^{-4} e 2.89 x 10^{-4} mm^2/h, respectively. The faster absorption of the first geometry is mainly due to its larger superficial area, besides the possibility of a moisture penetration through the exposed edges by wicking. However, the saturation levels were the same for both geometries. Chateauminiois *et al.* [60] concluded that the diffusivity values in the fibers direction of epoxy-matrix GFRP samples were higher than those transverse to the fibers at both 50 and 90°C. Furthermore, they found out that the greater the specimens' length, the slower the absorption, without presenting significant changes in the saturation level. This was attributed to the larger volume of the larger specimens. Heshmati *et al.* [61] studied the absorption of GFRP for bridge repairs using two prismatic specimens: one with length/thickness ratio equal to 100 and other one with length/thickness ratio equal to 50. The width of all specimens was the same. The authors concluded that the maximum sorption level in both specimens were similar, however, the diffusion rate of the latter specimen was greater than the former ones.

Aiming to incorporate essential factors to the diffusional process, Shen and Springer [53] developed adaptations to this law, including the diffusivities in directions parallel and normal to the fibers, as well as the volume fraction and diffusivity values of matrix and fiber. This model is shown in the simplified equations 12 and 13, where D_{11} and D_{22} are the diffusivity constants in directions parallel and normal to the fibers respectively, V_f is the fiber volume fraction and D_m the matrix diffusivity value. In these equations, the diffusivity value of the fiber was ignored because of its negligible value in comparison with that of the matrix.

$$D_{11} = (1 - V_f)D_m \qquad (12)$$

$$D_{22} = \left(1 - 2\sqrt{V_f/\pi}\right)D_m \qquad (13)$$

Fan *et al.* [62] compared the results from the Fickian model (Equation 5) and the Shen and Springer model (Equations 12 and 13) on the absorption of GFRP immersed in deionized water and observed that at room temperature the Fickian model over-predicted the moisture absorption, while the Springer model better fitted the experimental response. Conversely, at a temperature closer to the T_g (50°C), the Fickian law better predicted the material's absorption behavior.

One of the factors that most influence the moisture penetration is temperature. Diffusion is well-known for being a thermally activated process, where the diffusivity *D*, previously described, is related to temperature following the Arrhenius equation [20]:

$$D = D_0 exp\left(\frac{-Q}{RT}\right) \qquad (14)$$

where D_0 is a material constant, *Q* is the activation energy of the diffusional process (J/mol), *R* is the universal gas constant and *T* is the absolute temperature in Kelvin. Consequently, the diffusivity *D* is exponentially proportional to temperature due to the greater atomic mobility with the increased temperature [63]. Equation 14 can be simplified using natural logarithm (Equation 15), becoming a linear relationship. Figure 10a depicts the typical graph of this equation, while Figure 10b shows the results found by Guermazi *et al.* [34] for glass-fiber, carbon-fiber and carbon-glass hybrid composites. From this analysis, the diffusional activation energy of a system can be measured, which indicates how easy the moisture penetrates the material. Additionally, this graph plotted using experimental data of more than two temperatures allows the calculation of the diffusivity at any desired temperature, which means that the conduction of accelerated sorption tests makes it possible to estimate the diffusional behavior of the material at any desired temperature.

$$lnD = lnD_0 - \frac{Q}{R} \cdot \frac{1}{T} \qquad (15)$$

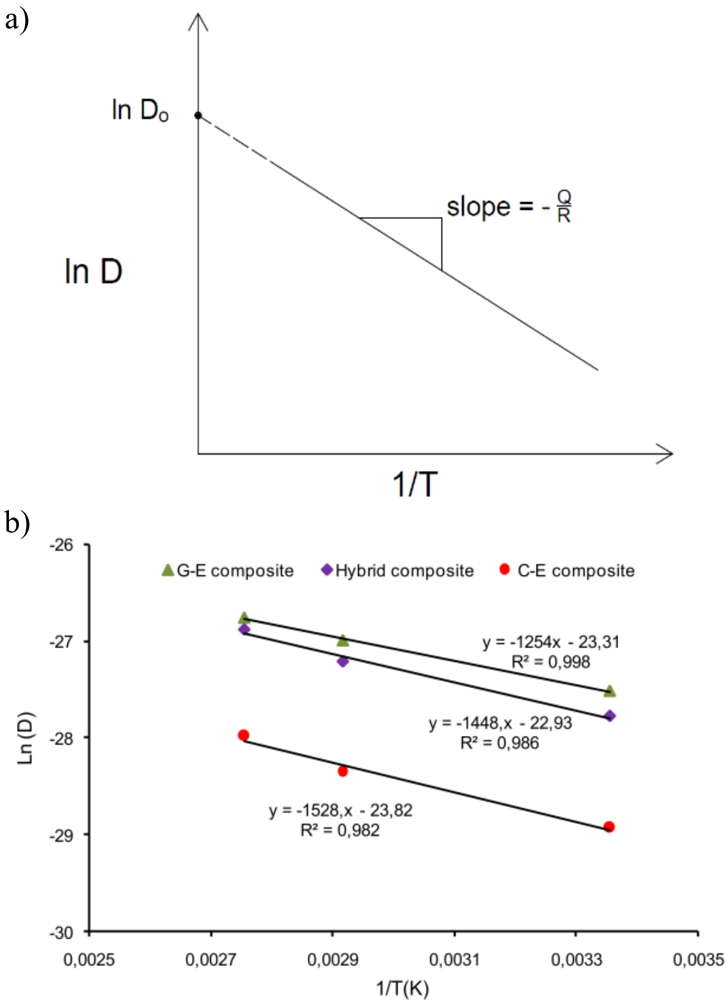

Figure 10. a) Characteristic ln D *vs*. 1/T graph, where it is possible to measure the diffusional activation energy of the material and b) results from the study of Guermazi *et al.* [34] for three different composite materials, where G-E stands for plain glass-fiber composite, C-E for plain carbon-fiber composite and hybrid for carbon/glass hybrid composites.

Indeed, Pomiès *et al.* [6] observed that the samples immersed at a higher temperature presented a faster absorption (Figure 11). However, the saturation levels of the samples immersed at room temperature (RT) and higher temperature were nearly the same. Similarly, Heshmati *et al.* [17] also observed that the increase in temperature from 20 to 45°C enhanced the diffusivity values and that at both temperatures the saturation content remained the same, even though it took longer to be reached at lower temperatures. Then, it can be estimated that temperature may not affect the saturation level, only makes it faster to be reached. Therefore, it is assumed that the immersion tests at high temperature can be adopted as accelerated aging tests [6,18,64].

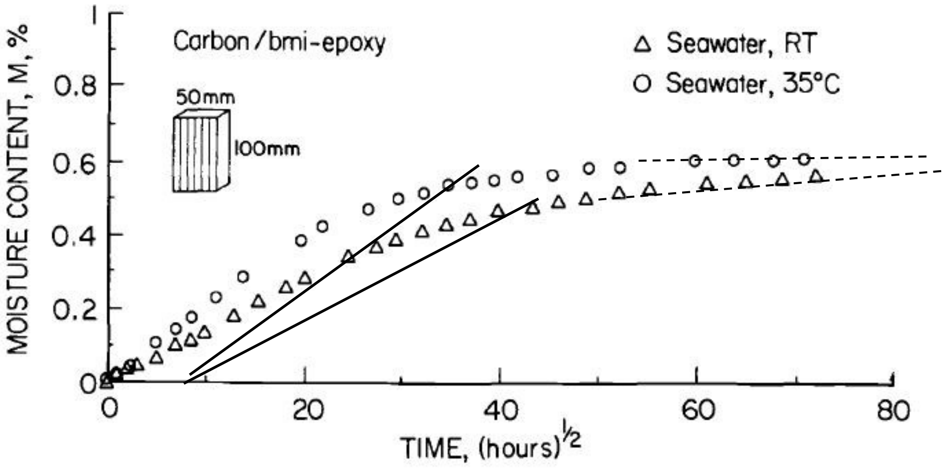

Figure 11. Weight gain *vs.* square root of exposure time in hours of BMI-epoxy/carbon fiber composite [6].

Panaitescu *et al.* [65], on the other hand, obtained results controversial to the aforementioned ones. The exposure of a polyurethane-based GFRP to 85% relative humidity (RH) at room temperature, 40°C and 70°C resulted in saturation values equal to 0.19%, 0.26% and 0.28%, respectively. In the immersion tests in distilled water at 40°C and 70°C, the samples presented saturation contents equal to 0.36% and 2.21%, respectively. The same trend was observed by Chu *et al.* [66]. The study carried out by Choi *et al.* [33] disputed that the saturation level of the epoxy-based carbon fiber composites immersed in water at 95°C is virtually the same as at 85°C. On the other hand, the samples immersed at 70°C and 35°C presented significantly lower saturation levels, yet similar to each other. Some authors have reported possible explanations for this phenomenon. Du Plessix *et al.* [67] and Robert *et al.* [68] claim that when the temperature is high enough (~70°C), i.e., closer to the T_g, the thermal expansion coefficient increases, making the matrix swelling more prominent, leading to a higher free volume density, increasing the composite's absorption capacity.

Regarding the effect of the relative humidity environment on the absorption behavior, some authors argue that the specimens exposed to this environment absorb less moisture than those immersed in distilled water due to the lower moisture content in the surroundings [65,66]. Conversely, Choi *et al.* [33] reported that the samples exposed to 95% RH presented a higher moisture content than the ones immersed in water at the same temperature (70°C), but no explanation for the phenomenon is presented by the authors. The increase in temperature promoted stronger moisture sorption in all these studies.

The moisture uptake results obtained by Li *et al.* [69] for immersion of epoxy-based carbon composite (CFRP) samples in artificial seawater with 3.5% NaCl at 30, 50 and 70°C presented in Figure 12 confirms that both diffusivity and saturation content increased with temperature. Moreover, a non-Fickian behavior can be observed for aging time longer than 90 days, where the equilibrium trend was interrupted, followed by an increase in moisture content at a slower pace. Unlike the initial Fickian diffusion stage, this stage is less affected by temperature. This non-Fickian behavior was attributed to the swelling-induced relaxation process of the polymer. At the end of the absorption (7 months), the water absorbed reached a second equilibrium level at 50 e 70°C, while at 30°C an increasing trend can still be found. After 210-days aging, the specimens were removed from the solution and left for drying at room environment and a fast initial decrease in the moisture content could be observed, followed by a stabilization, indicating an irreversible water uptake in the composites. An in-depth analysis of the non-Fickian behaviors will be further discussed in section 2.4.

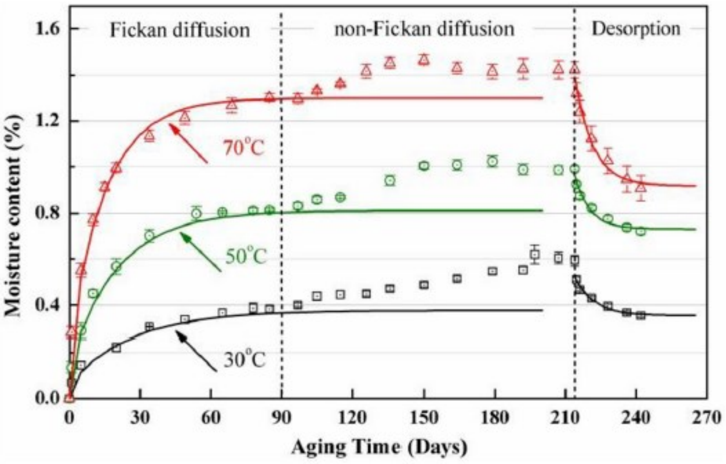

Figure 12. Moisture absorption behavior of CFRP in water solution with 3.5% NaCl at different temperatures [69].

2.3.5. Salinity effect

When polymeric composites are employed in marine applications such as offshore structures, ship hulls, fuel storage tanks and steel piping repairs, they are also exposed to seawater salinity in their service lifetime [6,70]. Moisture penetration kinetics of saline water in the composite is the same as that of distilled water, although the presence of salt reduces the saturation level. Considering the polymer as a semipermeable membrane, the salt is not as readily absorbed by the resin as the water, due to its larger size, resulting in the creation of an osmotic pressure due to the difference in concentrations in the specimen versus the surroundings. There is an accumulation of salt on the surface of the specimen, which inhibits the water absorption, creating a lower salt concentration in the water inside the composite compared to the surrounding water. Therefore, it is assumed that the driving force for moisture absorption is reduced, decreasing the saturation level [30,70].

However, the diffusivity value is generally not affected by salinity, as shown in the graph in Figure 13, where Pomiès *et al.* [6] performed immersion tests with PPS/glass fiber (Figure 13a) and epoxy/glass fiber (Figure 13b) composites in distilled water and artificial seawater, both at 35°C. In this graph it can be noted that for the PPS/glass fiber composite, the saturation stage was reached, with the equilibrium content in saltwater being lower than in distilled water. On the other hand, for the epoxy/glass fiber composite, the saturation stage was not reached within the aging time. In both cases, the initial slope of both conditions was similar, indicating similar diffusivity values.

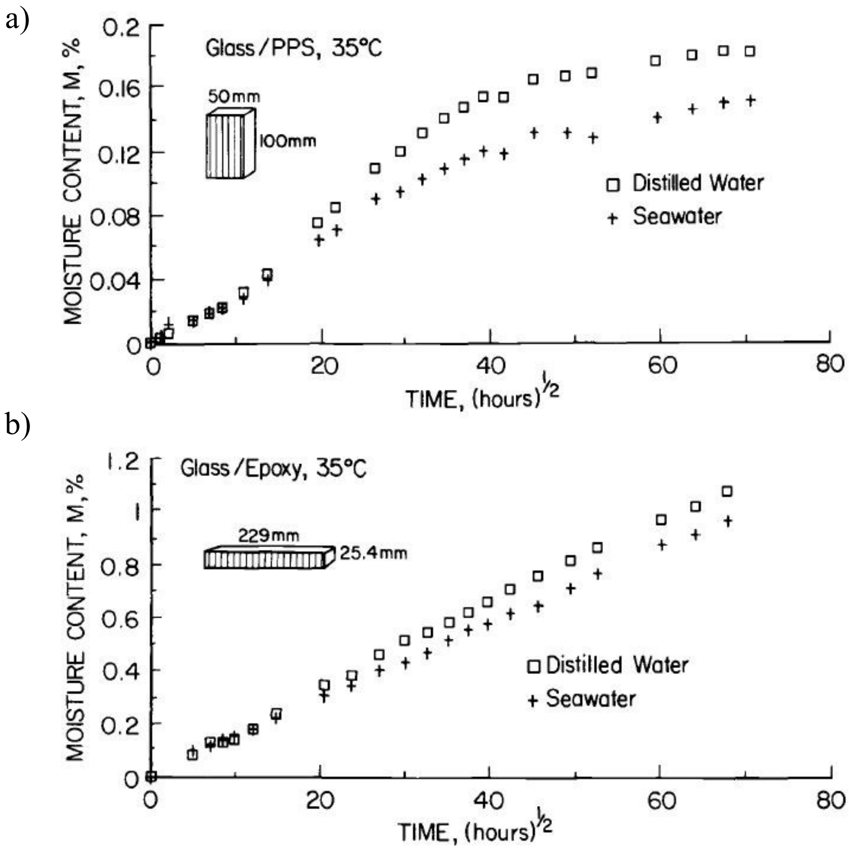

Figure 13. Weight gain vs. square root of time in hours of (a) PPS/glass fiber and (b) epoxy/glass fiber composites, both at 35°C [6].

In a molecular level, the explanation for this phenomenon is described by Heshmati *et al.* [17], who state that the decrease in the saturation level can be associated with the relatively large size of the salt molecules, which obstruct some diffusion routes of the material during the immersion, mitigating the water uptake.

In the study of Heshmati *et al.* [17], the authors investigated the water uptake behavior of an epoxy-based adhesive in distilled water (DW), seawater (SW) and relative humidity (RH) and the sorption graph obtained as a function of the square root of days is shown in Figure 14. In this graph, it can be noted that the immersion in seawater results in a lower saturation level if compared to the distilled water. Also, it is visible that the exposure of composites to relative humidity results in the lowest water uptake among the conditions tested, reinforcing that the results found by Choi *et al.* [33] mentioned in section 2.3.4 for the RH environment were a particular case different from the general trend.

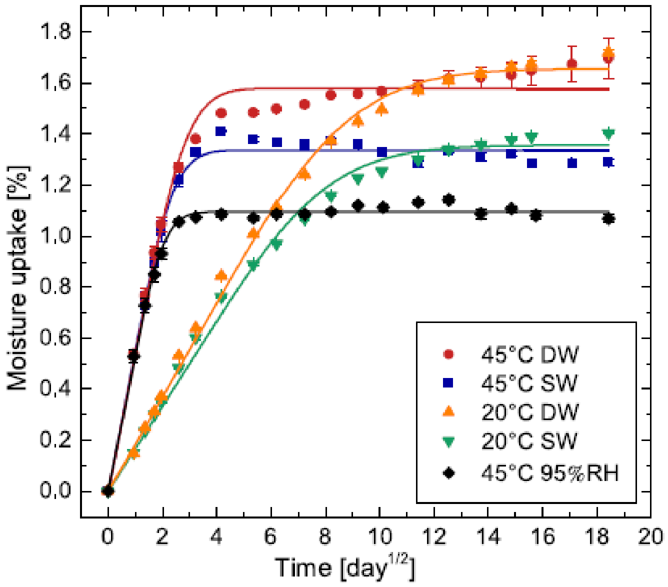

Figure 14. Moisture uptake curves of epoxy specimens as a function of temperature and exposure conditions [17].

Fang *et al.* [71] reported that after 180 days of aging, the total moisture uptake of the specimens immersed in distilled water and seawater were 1.21 e 0.57, respectively. Grant and Bradley [70] observed the same behavior in graphite/epoxy systems with fiber volume fraction of approximately 0.61-0.65 immersed in distilled water and seawater for three months.

Silva *et al.* [72] observed that the epoxy-based GFRP samples immersed in deionized water at 23°C presented greater diffusivity values than those ones immersed in seawater even at high temperatures (7.53 x 10^4 mm^2/s in deionized water at 23°C and 0.138, 0.305 e 0.444 x 10^4 mm^2/s in 5.0% NaCl solution at 35, 50 and 65°C, respectively). The same trend was found for the saturation values, which can be explained by the formation of osmotic pressure, as previously explained.

ASTM D1141 standard [73] recommends the preparation of substitute ocean water by adding about 35 gL^{-1} of NaCl to pure water (~3.5%). The influence of salt concentration on moisture uptake in CFRP was evaluated by Li *et al.* [69], who performed sorption tests in artificial seawater containing 0, 3.5 and 5 wt% of NaCl at 30°C for 7 months. It is visible in Figure 15 that the difference in the absorption among the different concentrations was marginal, although with a slightly greater saturation content observed for samples immersed in distilled water and lower for those immersed in 5 wt% NaCl solution. The difference in absorption with the salt concentration could not be well distinguished, indicating that probably the salt concentration has a negligible influence on the absorption capacity. The non-Fickian and desorption processes of the work of Li *et al.* [69] were previously discussed (Figure 12).

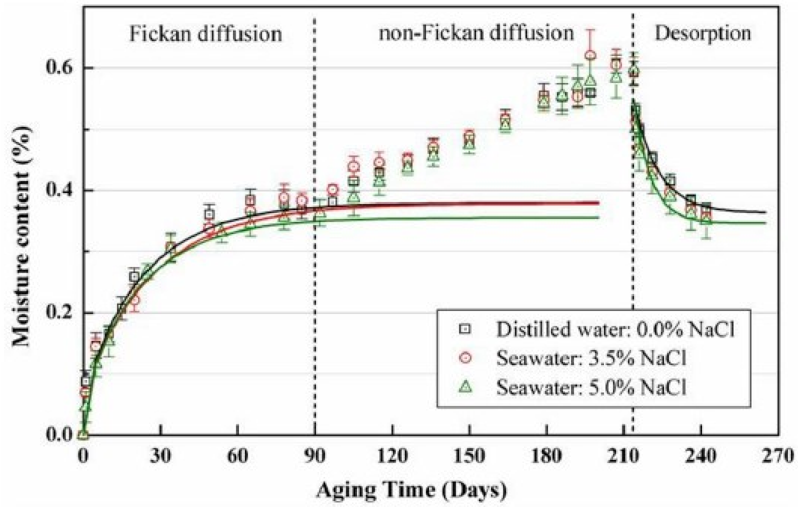

Figure 15. Moisture absorption behavior of CFRP in different saline concentrations at 30°C [69].

2.3.6. Hydrostatic pressure effect

Grant and Bradley [70] studied the absorption behavior of two graphite/epoxy systems (T2C145/F263 and IM7/977-2) and a graphite/fluorene-based-epoxy system (IM7/SP500-2) immersed in seawater at room temperature and at 20.7 MPa hydrostatic pressure and found out that the hydrostatic pressure induced a slight increase in the total seawater absorbed in comparison with the ones at room temperature (Figure 16). These results are in agreement with those reported by Humeau *et al.* [74], who observed an increase in the water uptake and diffusivity values of GFRP under high pressure when compared with those under atmospheric pressure. This phenomenon is because the water uptake in the composite is significantly dependent on its porosity level. Thus, as pressure rises, the absorption increases proportionally to the porosity level [74]. According to Tucker *et al.* [75], the moisture sorption of CFRP under a pressure of 610 meters of seawater was higher than that of specimens under atmospheric pressure, although the diffusivities remained the same, proving that the higher pressure did not accelerate the absorption, but induced capillary flow through the material's pores. However, there is a concurring mechanism when the material is submitted to high pressure, which is the closing of voids. Avena and Bunsell [76] argue that there is a compressibility of the polymers at pressures less than 104 atmospheres due to the closing of the free volume and microdefects. Thus, the authors reported that the GFRP specimens under 20 MPa presented saturation level and diffusivity close to those under atmospheric pressure.

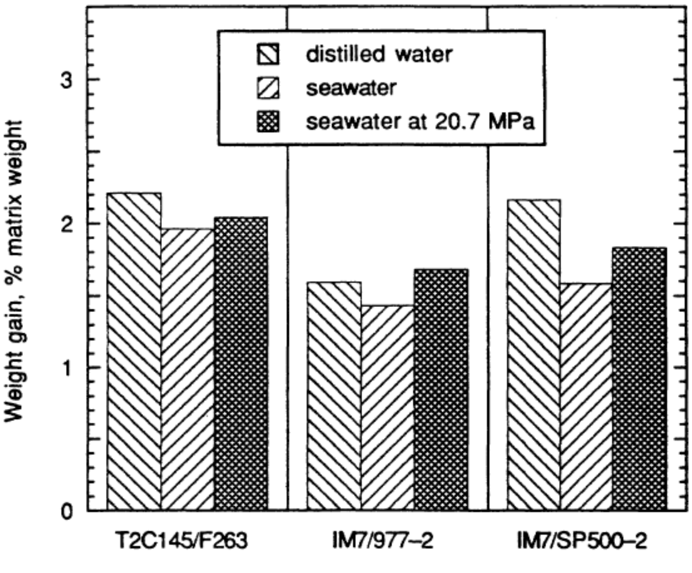

Figure 16. Moisture saturation levels of graphite-fiber composites in distilled water and seawater at room pressure and in seawater at 20.7 MPa for three months. In all conditions, the room temperature was used [70].

2.3.7. Structural degradation of composites

The study of the degradation mechanisms of FRPs involves both physical and chemical aspects of aging. While physical degradation refers to an alteration of the mechanical properties that can be reversible after short-term exposure after drying of the composite, the chemical degradation occurs with longer exposure duration and mainly involves irreversible degradation of resin and fiber, as well as the fiber/matrix interface, changing the material's molecular structure [77].

2.3.7.1. Physical degradation

The moisture absorption of the glass-fiber and carbon-fiber reinforced polymeric composites causes, more importantly, the degradation of the matrix-dominated properties, such as interlaminar and in-plane shear resistances, as well as transverse strength [6]. The loss of these mechanical properties are mainly attributed to plasticization [6,16,26,29] and matrix swelling and its induced internal stresses [6,60,64,78], leading to fiber/matrix debonding and delamination [6,13,29].

The polymers and polymeric matrices of fiber reinforced composites own an intrinsic property called glass transition temperature (T_g), above which the polymer's mechanical properties are substantially reduced. Therefore, the structural polymers' in-service temperature should be below T_g aiming to ensure satisfactory stiffness, mechanical resistance and integrity [23], otherwise, its mechanical properties will be drastically reduced, which could lead to a critical decrease of the material's in-service application [26]. The ISO24817:2017 [79] and ASME PCC-2-2006 [31] standards recommend the maximum in-service temperature of a repair component, either for non-leaking (Type A) or leaking (Type B) pipelines, destined to low-duty applications to be 20°C lower than the material's T_g. Additionally, ISO 24817:2017 [79] standard considers the repair's lifespan, whose expectancy is defined by the project and can be limited to the type of defect and in-service conditions, like internal corrosion. The minimum lifespan recommended for a composite repair is two years [80].

Karbhari *et al.* [81] and Bai *et al.* [8] stated that the polymeric resins suffer stiffness loss when applied at a temperature range close to T_g, not only worsening the mechanical performance, but also promoting an increase in the moisture absorption capacity. The authors demonstrated that the thermal gradient between the materials' components may lead to an increase in viscosity, porosity and defects.

When the polymeric matrix suffers the moisture-induced plasticization effect, there is a decrease in T_g, viscosity and/or elastic modulus, enhancing the viscous contribution to the mechanical behavior of the polymer, since it is a viscoelastic material [26,82]. Theoretically, plasticization leads to larger intermolecular spaces or free volumes, and may involve either the weakening or the scission of interpolymer bonds [82], promoting a greater mobility of the polymeric chains, decreasing its stiffness and increasing its deformability, resulting in a loss of mechanical integrity [36]. Fang *et al.* [71] carried out DSC analysis and found out that the GFRP samples immersed in water and saltwater suffered plasticization with a decrease in T_g. After 6-months aging, the T_g of the composites immersed in water and saltwater experienced a decrease from 78.5°C to 76.2°C and 76.5°C, respectively, as shown in Figure 17.

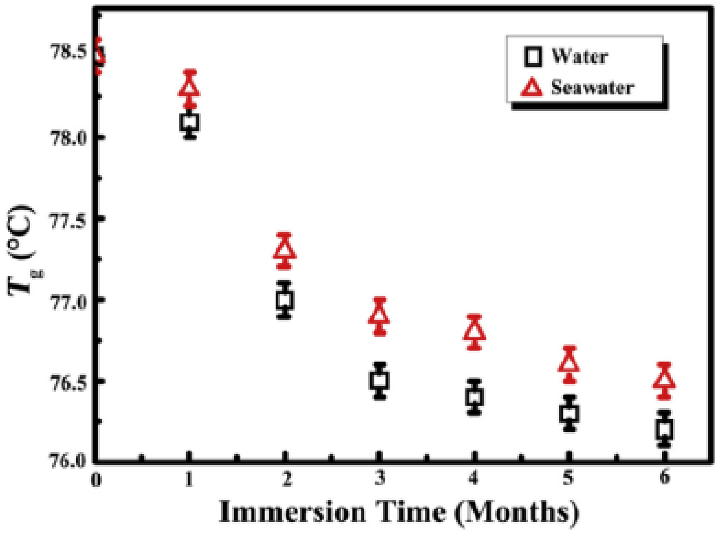

Figure 17. Glass transition values of GFRP composites as a function of immersion time for both water and seawater immersion [71].

Gu [83] and Chu *et al.* [66] performed DMTA tests and observed a decrease in T_g of GFRPs due to plasticization. Both studies reported an increase in the tan δ value, indicating a more viscous material as a result of the moisture penetration (Figure 18a, which shows the influence of aging time on the tan δ value). Gu [83] reported a significant deterioration of the GFRP's mechanical resistance after 60-days immersion in saltwater and its T_g value decreased from 134°C to 128°C after 10 days, 125°C after 60 days and 122°C after 120 days of aging (Figure 18b). Chu *et al.* [66] claim that the higher the aging temperature, the higher the tan δ value and the stronger the plasticization effect. Therefore, the higher the temperature, the greater the T_g loss. The tensile tests supported this plasticizing phenomenon, since a stronger decrease in tensile strength at high temperatures after 70 days was observed, being more significant in the first 10 days. Other studies also reported the plasticization effect [10,17,26,29,60].

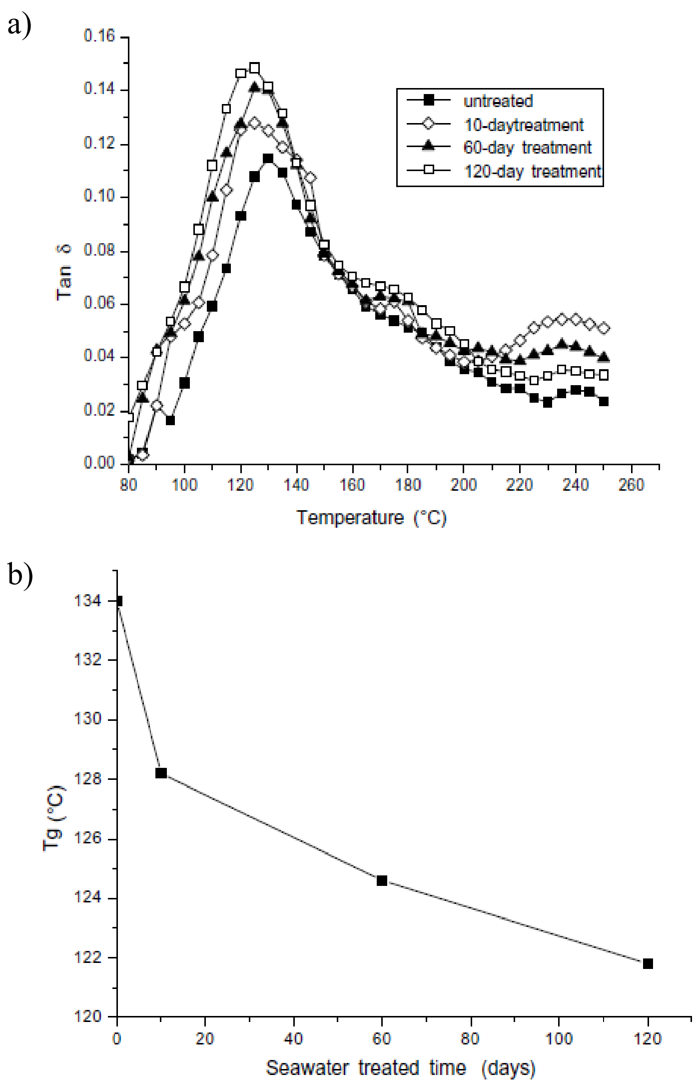

Figure 18. Variation of (a) tan δ values and (b) T_g values of GFRP with immersion time in saltwater solution [83].

Besides plasticization, another moisture-induced effect on the composite material is the matrix swelling due to the filling of the free space between the polymeric chains by water [13,36,84,85]. Swelling can also be caused by thermal expansion when the composite is subjected to high temperatures (>50-70°C). The expansion forces caused by swelling create residual stresses on the fiber/matrix interface due to the mismatch of both moisture absorption capacities and thermal expansion coefficients of fiber and matrix. The swelling profile is directly related to the moisture content, as shown in Figure 19 [83,86].

These residual stresses caused on the fiber/matrix interface lead to the formation of interfacial microcracks and flaws, causing the debonding of fibers, accelerating the degradation of mechanical properties and integrity of the composite [13,69]. The transverse intralaminar crack is the major damage mechanism in unidirectional laminates submitted to out-of-plane load, because it is often followed by debonding at the plies interface. Therefore, one of the best experimental methods to evaluate interfacial debonding is the transverse tensile test, which will be further discussed. A transverse crack is generally followed by the debonding at the laminae interface (delamination) [6,13,18]. Huang and Sun [13] studied this mechanical behavior in GFRPs immersed in water and observed that the resistance decreased immediately when the matrix cracks, swelling-induced debonding and resin degradation progressed. Figure 19 illustrates all the ways of water penetration and the degradation mechanisms that can be found in a composite subjected to hygrothermal aging.

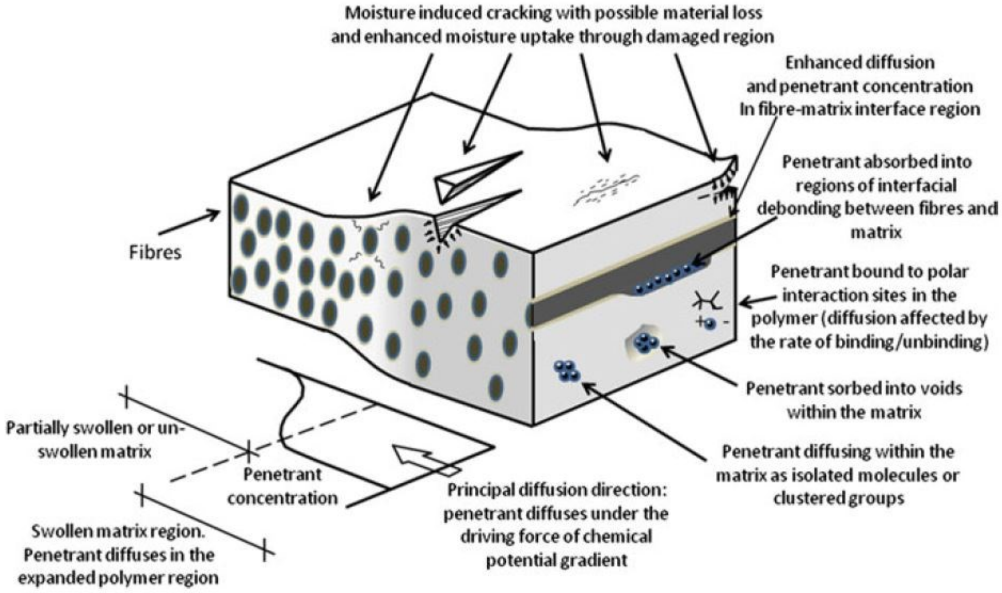

Figure 19. Ways of penetration of water molecules in the polymer and degradation mechanisms polymeric composites can suffer [16].

An efficient test to evaluate interface degradation is ILSS (Interlaminar Shear Strength), in which a short-span flexural test is performed, also named SBS (Short Beam Shear). Some authors have reported degradation analyses with ILSS tests [12,26,29,36,87]. Figure 20 shows examples of typical curves obtained in this test, in which the loss of interlaminar shear strength indicates adhesion loss, promoting delamination. In Figure 20a, there was an abrupt decrease in adhesion in the first three thermal cycles, presenting a decrease in strength by 13.5%. Figure 20b makes it clear that the increase in temperature accelerates the delamination process. The same behavior was observed by Shamsuddoha *et al.* [12]. Additionally, according to Costa *et al.* [26], the more moisture the material absorbs, the greater the interlaminar adhesion loss.

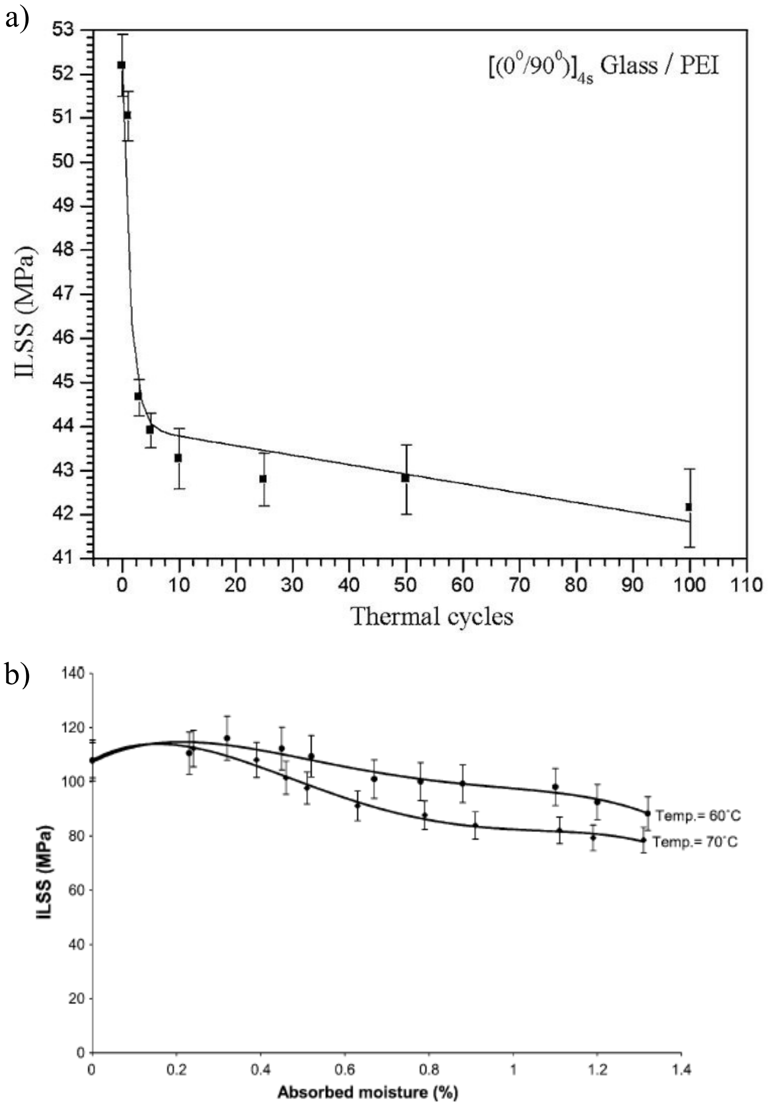

Figure 20. a) Variation of ILSS values of a PEI/glass fiber composite subjected to thermal cycles from 0 to 100°C [29] and b) Decrease in ILSS value as a function of temperature [36].

Pomiès *et al.* [6] performed transverse tensile tests in composites aged in distilled water and saltwater, allowing them to analyze the interface degradation. A sharp decrease in the fiber/matrix interface strength could be noted as a result of the detrimental effect of moisture on this region, plasticizing it and generating fiber debonding. Scanning Electron Microscope (SEM) analyses on the composites' fractured surfaces have been performed to assess the fiber/matrix debonding [6,13,29,35,71]. Figure 21 depicts the fractured surfaces of both unaged and aged Polyetherimide (PEI)/glass-fiber composite after ILSS test reported by Yilmaz and Sinmazcelik [29]. In this figure, it is noticed that the unaged specimen (Figure 21a) presents a stronger integrity and a better fiber/matrix adhesion, while the aged specimen (Figure 21b) presents bare fibers with no matrix chunk attached to it, indicating fiber/matrix debonding. Besides, it can also be noticed that the matrix lost integrity due to plasticization. Figure 22 shows a more detailed impact fracture surface of an epoxy-matrix CFRP before (Figure 22a) and after (Figure 22b) 90 days of aging in saltwater at room temperature obtained by Jesthi and Nayak. [35]. It is visible that the unaged composite exhibits excellent adhesion and shear cusps caused by the impact test. After the aging, the fiber/matrix debonding phenomenon is clear.

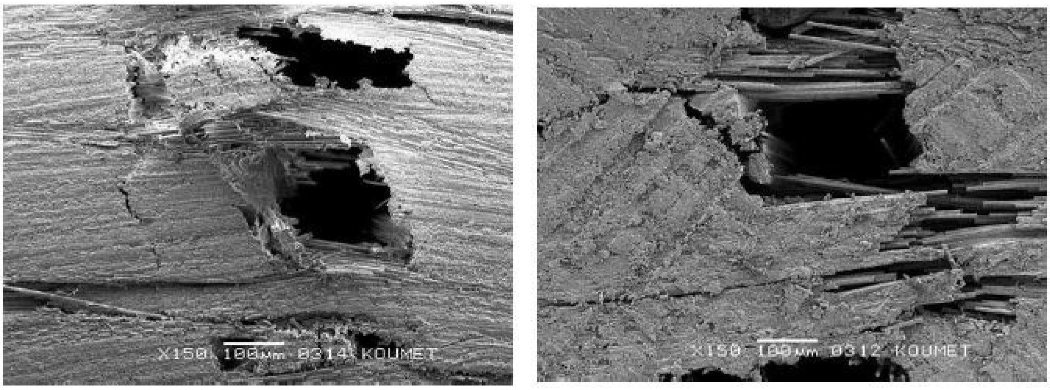

a) b)

Figure 21. Fracture ILSS surfaces of PEI/glass fiber composite a) before and b) after hygrothermal aging [29].

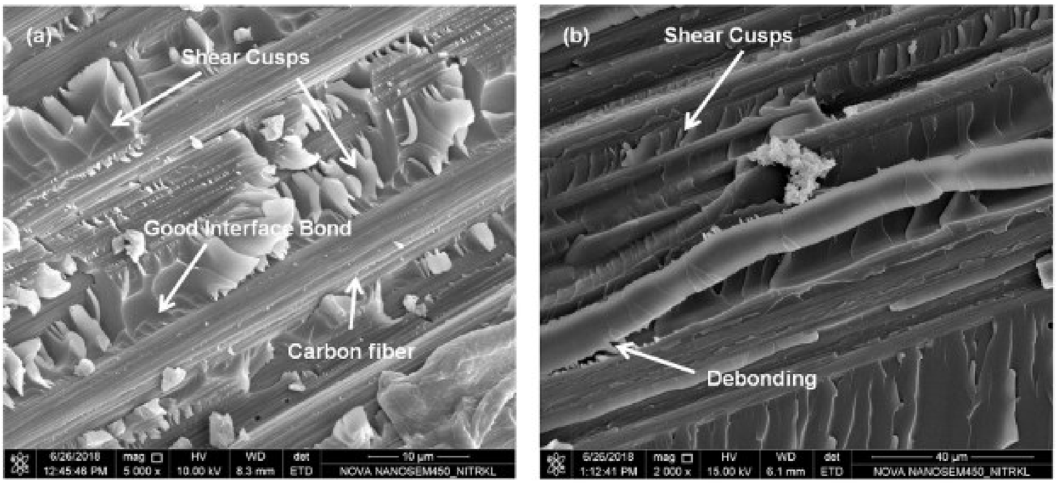

Figure 22. Fracture surfaces of a) dry and b) aged CFRP [35].

Other authors have reported degradation in distilled water and/or saltwater by means of longitudinal tensile tests and reported that both tensile strength and elastic modulus are gradually decreased with immersion time and temperature, showing that the composites lost both resistance and stiffness, as a result of the plasticization and interface degradation [13,30,34,83,88,89]. The same trend could be observed from flexural tests [13,29,34,58,65,85].

Conversely, the composites' properties can be improved by the cure and post-cure processes. Goertzen and Kessler [23] observed from DMTA analyses that epoxy-matrix CFRP composites suffered post-cure when exposed to temperatures close to the T_g range of the material. In this process, crosslinks were formed due to the thermally activated diffusional mechanisms, increasing both T_g and stiffnesses of the composites, decreasing their loss modulus. Other researchers have also reported this enhancement of properties induced by post-cure at high temperatures [72,90,91].

2.3.7.2. Chemical degradation

Even though the short-term physical degradation mechanisms, such as plasticization, may cause severe property losses of materials, these can be reversible and recovered after the drying of the specimen. However, the long-term effects are generally driven by chemical changes, such as hydrolysis or crack growth, promoting irreversible changes in material and are commonly caused by long-term exposure to harsh conditions, including temperature [17,26,34,85,92,93]. The chemical damage is caused by hydrolysis reactions in both matrix and interface, which can weaken the interfacial and interlaminar adhesions [69].

2.3.7.2.1. Chemical degradation of resins

Among the most commonly used FRP resins, the polyester and vinyl ester resins are more prone to suffer hydrolysis degradation due to the fact that the ester group is the weakest bond of these resins and is highly likely to undergo hydrolysis. As there are less ester groups in vinyl ester's backbone than in polyester's, the former is less susceptible to hydrolysis. Kootsookos and Mouritz [85] confirmed this behavior by immersing polyester- and vinylester-based composites in saltwater and observing a longer durability of vinylester composites, since the polyester one experienced hydrolysis after a short-term exposure, even though the flexural properties of both resins were similarly degraded.

On the other hand, the epoxy resin is less affected by hydrolysis, since there is no ester group in its chemical structure [64]. Although, it has already been reported that hydrolysis can be fostered in epoxy-based composites depending on the hardener used in the cure process, especially if it is an anhydride [94–96]. According to Krauklis *et al.* [93], the leaching degradation that may occur in the epoxy matrix is related to additives, unreacted hardener or some byproducts from degradation being diffused out of the epoxy. Aiming to experimentally quantify the hydrolysis degree that epoxy may undergo, Yagoubi *et al.* [94] carried out FTIR (Fourier-Transform Infrared Spectroscopy) analyses in anhydride-cured epoxy composites and observed a decrease in the absorbance peaks related to anhydride groups after water aging, indicating a lower anhydride content, which indicates the occurrence of hydrolysis. In addition, they found out that the reaction kinetics is related to the epoxy/hardener ratio, i.e., the higher the ester-rich hardener fraction, the greater the hydrolysis loss suffered by the material.

2.3.7.2.2. Chemical degradation of fibers

Among the most widely used fibers in fiber reinforced polymeric composites, the glass fiber is the most susceptible one to hydrolysis. This process may be driven by two processes: the scission of the Si-O-Si structure done by the hydroxyl ions (Equation 16), causing material loss; or the diffusion of alkali ions, like Na^+, into the glass structure (Equation 17). Carbon fibers are more resistant to chemical degradation [64].

$$(\equiv Si - O - Si \equiv) + OH^- \leftrightarrow (\equiv Si - OH) + (\equiv Si - O^-) \qquad (16)$$

$$(\equiv Si - ONa) + H_2O \rightarrow (\equiv Si - OH) + OH^- + Na^+ \qquad (17)$$

Berketis *et al.* [84] could detect from sorption tests the non-Fickian behavior of the polyester-matrix GFRP shown in Figure 23. This figure shows that after approximately 14-months immersion in water at 65°C there was a decrease in the specimen's mass, indicating the occurrence of hydrolysis in either the resin or the glass fiber. Fang *et al.* [71] reported the same behavior for both distilled water and seawater environments, attributing it to a possible hydrolysis reaction in the polyester-based composites. Schutte [97] conducted FTIR analyses with E-glass fibers aged in water at 80°C for 600h and it was possible to notice the presence of SiOH groups, which is the byproduct of the hydrolysis reaction of the Si-O-Si group.

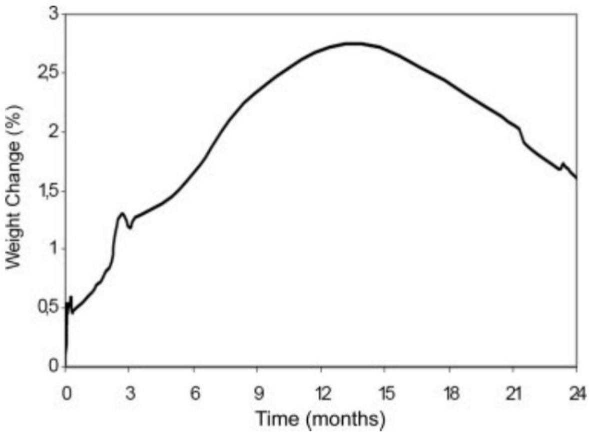

Figure 23. Absorption curve of GFRP immersed in water at 65°C for 24 months [84].

2.3.8. Swelling

As previously discussed, when the composites are exposed to high temperature and/or moist environment, its constituents undergo dimensional and stress state changes due to the mismatch of the thermal and moisture-induced volumetric expansions. These changes added to the relaxation of the polymer may induce non-Fickian absorption behavior. Therefore, the study of the swelling phenomenon is made necessary to estimate the correlation between the structural changes in the polymer and the absorption mechanisms [43,98–100].

The volumetric swelling of the composite is measured by the sum of the linear swelling of each dimension of the sample. Equation 18 shows the measurement of the linear swelling strains ($\varepsilon_{l,w,t}^{sw}(\%)$) based on the relative changes of length (*l*), width (*w*) and thickness (*t*) of the specimen [99]:

$$\varepsilon_l^{sw} = 100 \times \frac{l_t - l_0}{l_0}, \varepsilon_w^{sw} = 100 \times \frac{w_t - w_0}{w_0}, \varepsilon_t^{sw} = 100 \times \frac{t_t - t_0}{t_0} \qquad (18)$$

where the subscripts *t* and *0* refer to the dimensional changes of the sample after aging time *t* and time *t* = 0, respectively. Consequently, the volumetric swelling strain is a sum of the linear strains [99]:

$$\varepsilon_v^{sw} = \varepsilon_l^{sw} + \varepsilon_w^{sw} + \varepsilon_t^{sw} \qquad (19).$$

Figure 24 illustrates the results found in the work of Starkova *et al.* [99] for the volumetric strains of the neat epoxy. The swelling kinetic was found to be similar to that of the Berens-Hopfenberg absorption model (to be discussed in Section 2.4.1), presenting an initial linear increase, followed by a decrease in the swelling rate. A diffusion-relaxation model analogous to the BH model was applied (Equation 20), where ε_F^{sw} and ε_R^{sw} represent swelling strains induced by Fickian diffusion and relaxation, respectively. The calculations were made using the D and τ_R values obtained in the sorption test, and the total swelling was obtained by the sum of both equilibrium strains.

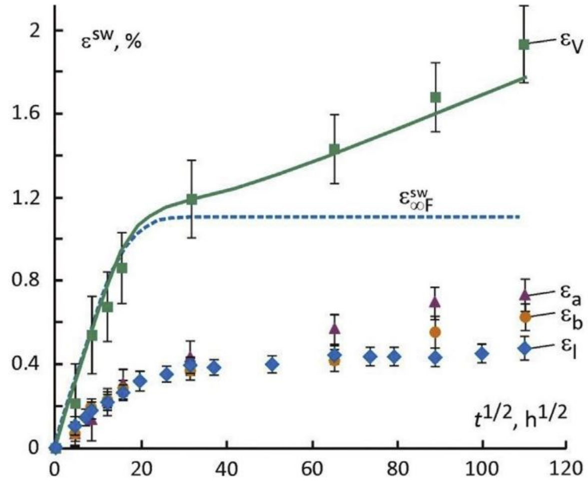

Figure 24. Swelling strains of epoxy as a function of the square root of time. The symbols are the experimental data, while the dashed line the calculation applying Fickian diffusion and the solid line is the diffusion-relaxation model [99].

$$\varepsilon^{sw}(t) = \varepsilon_F^{sw}(t) + \varepsilon_R^{sw}(t) \tag{20}$$

It was found that the relaxation-induced volumetric strain was slightly greater than the Fickian one ($\varepsilon_{\infty R}^{sw}$ = 1.20% and $\varepsilon_{\infty F}^{sw}$ = 1.11%), while the relaxation-related absorption was lower than the Fickian one. This can be explained by the free volume content of the polymer, which was found to be 0.5%. This free volume is occupied by the free water molecules during the Fickian absorption process, explaining the higher Fickian water absorption. Then, it plays a major role in the relaxation-driven swelling process [99].

Aniskevich *et al.* [98] carried out sorption tests of glass-fiber reinforced composites with different dimensions in distilled water. It was observed that, as discussed in section 2.3.4, the absorption kinetic varied with the dimension, where the sample with higher superficial area presented higher absorption rate and a slightly lower saturation level than the other samples. In addition, the absorption behaviors were measured (Figure 25) and the swelling in the z direction (through-thickness direction) was found to be greater than in other directions, corroborating with the edge effect mentioned in section 2.3.4. It was also observed that the swelling reached an equilibrium, while the water uptake was still increasing. The specimen tested in Figure 25b has larger length (x) and width (y) than the specimen in Figure 25a, reflecting in its more considerable swelling percentage.

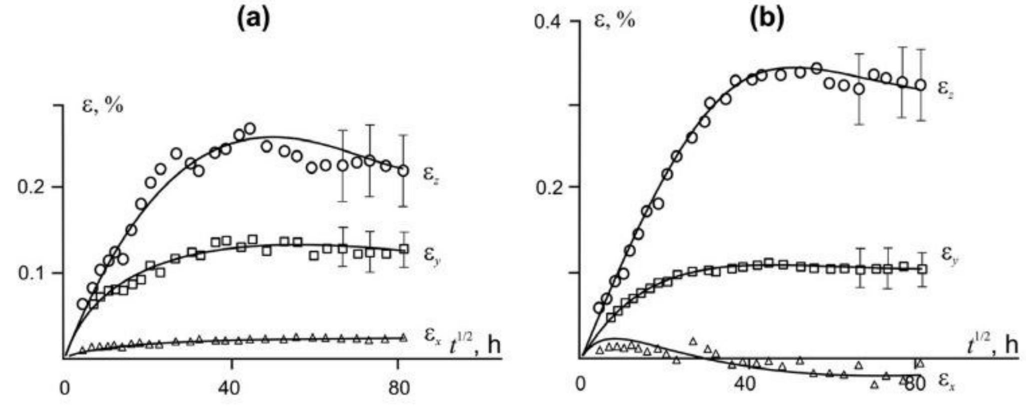

Figure 25. Swelling strains in the three main dimensions of a pultruded GFRP as a function of the square root of time (length = x, width = y, thickness = z). Dimensions of (a): *l* x *w* x *t* = 16 x 157 x 10 mm and (b) 155 x 15 x 10 mm [98].

Santos [101] performed immersion tests of sisal-fiber reinforced polyester composites with two different thicknesses (3 and 6 mm) in distilled water at 25, 50 and 70°C. While the temperature did not promote significant differences in the saturation moisture contents for both composites, the volumetric strain increased with temperature. This can be explained by the combined effect of temperature and moisture, which accelerates the material's deterioration. For the 3-mm thick composite, the increase in volume at 25, 50 and 70°C after 817-hours immersion was 19.77%, 21.77% and 31.34%, respectively. Conversely, for the 6-mm thick composites, after 848-hours immersion, the volumetric changes were 15.95%, 17.25% and 21.32%. The significant increase in swelling at 70°C can be related to the proximity of this temperature to the material's T_g, which enhances the expansion of polymeric chains, fostering a higher mobility, reflecting in the increase in the sample's volume. It is noteworthy that the thinner the composite is, the greater the swelling percentage, which can be due to the stronger water uptake observed in the 3-mm thick composite, which was associated by the authors with the difference in the fiber content among the composites.

A typical graph used for the analysis of the swelling behavior of the material is the relative volumetric swelling of the sample *vs*. volume of water absorbed. The volume of water absorbed is calculated from Equation 21, where V_0 is the sample's initial volume, M is the water content and ρ_{sample} and ρ_{H_2O} are the densities of sample and water (1.0 g/cm^3), respectively. Figure 26 shows a graph plotted by Starkova *et al.* [99] after aging neat epoxy, epoxy/EG (expanded graphite) and epoxy/GnP (graphite nanoplatelets). The solid line corresponds to the ideal mixture law with slope equal to 1, i.e., when the volume of sample and water are corresponding.

$$\frac{\Delta V_{H_2O}}{V_0} = M \cdot \frac{\rho_{sample}}{\rho_{H_2O}} \tag{21}$$

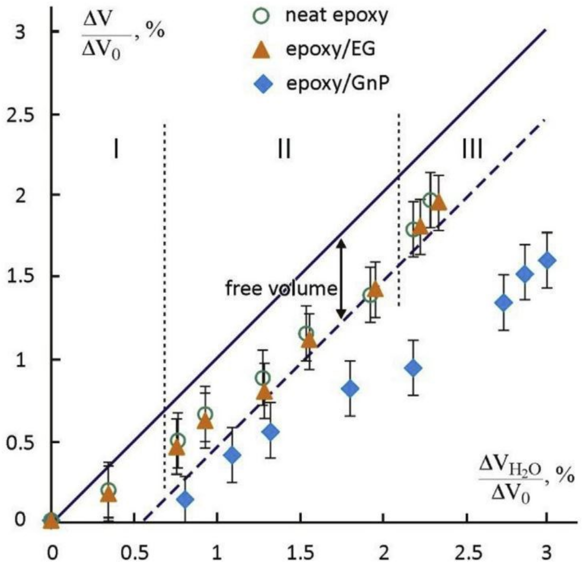

Figure 26. Swelling profile of samples as a function of the volume of water absorbed. The solid line corresponds to the ideal mixture law with slope equal to 1 [99].

It is visible that the swelling profile of polymer and polymer composites can be divided into three regions. The experimental data show that initially water causes a negligible swelling (Region I), followed by Region II, where swelling increases linearly with the volume of water absorbed and begins to increase at a higher rate than the volume of water absorbed (Region III) [43,98–100]. The dashed line was drawn to help calculate the difference between the curves. Regions I and II are associated with the diffusion-controlled absorption and the difference between the experimental curve and the solid line in Region II corresponds to the apparent free volume content of the polymer. The appearance of non-Fickian mechanisms in the water absorption behavior can be proved by the increase in the swelling rate in Region III [99].

The initial swelling with little moisture absorbed occurs at a slow rate provided that at this stage the diffused water molecules are the free ones, which only fill the existing voids, not interacting with the polymeric network, resulting in a slight volumetric gain. Afterwards, as moisture absorption continues, the molecules promote more interaction with the polymer (bound molecules), resulting in a more significant swelling, increasing the curve slope in the intersection between

Region I and II, making it closer to a line parallel to that of the ideal mixture law [43,100]. In Figure 27 this behavior is made evident, where the authors immersed epoxy resin in water at 74°C (Figure 27a) and 40°C (Figure 27b). In these graphs the transition between Regions I and II is determined by a difference in the slope of the curve. Furthermore, it was needed a stronger water absorption for the specimens at 40°C to shift to Region II if compared with those at 74°C, suggesting that more easily accessible free volume is available at the lower temperature. According to the authors, the difference in the measured free volume (3.02% at 40°C and 2.64% at 74°C) suggests that the free volume ratio increases as the temperature goes further below T$_g$. More importantly, the authors claim that the free volume ratio at 74°C agrees with the theory that says that the free volume ratio for polymers below T$_g$ is about 1/40 (2.5%) of the total volume [43].

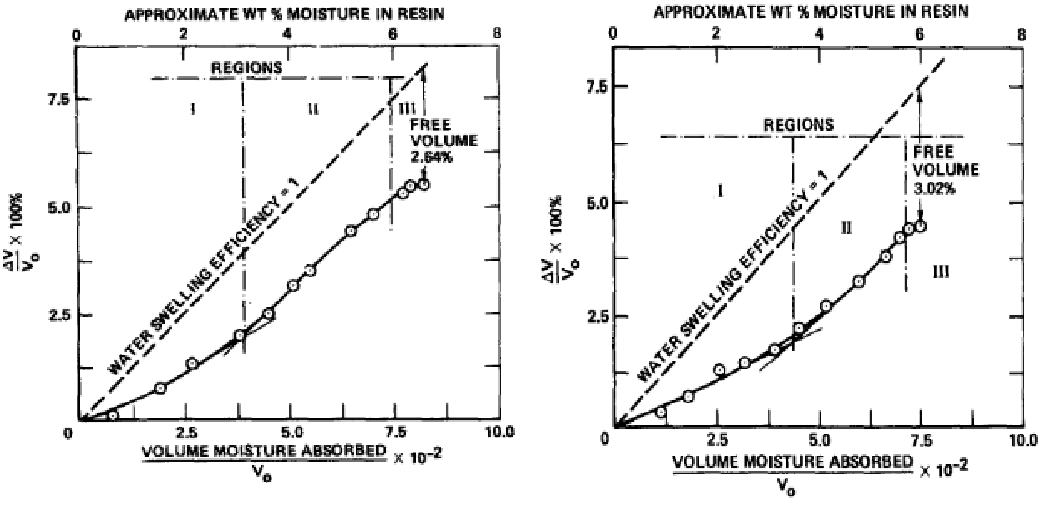

Figure 27. Swelling profiles of epoxy resin at a) 74°C and b) 40°C [43].

Aniskevich *et al.* [98] calculated the variation of free volumes in pultruded I-beams with different dimensions as a function of the weight gain using the equation:

$$v_p = M \cdot \frac{\rho_{sample}}{\rho_{H_2O}} - \frac{\Delta V}{V_0} \tag{22}$$

, which is basically the difference calculated in the graphs seen in Figures 26 and 27. The results can be found in Figure 28, in which Figure 28a depicts the variation of free volume content as a function of moisture absorbed at 20°C. This function is represented by two linear sections with an intersection point at w_p = 0.7%. In Figure 28b, there is the behavior of the same material for 66°C and 20°C as a function of immersion time. This behavior supports the results shown in Figure 27, since there was a higher free volume content at a lower temperature. The reduction in the free volume content at 66°C was attributed to a possible post-cure. These values were calculated considering that the filling of water in the pores initially does not induce swelling in the material.

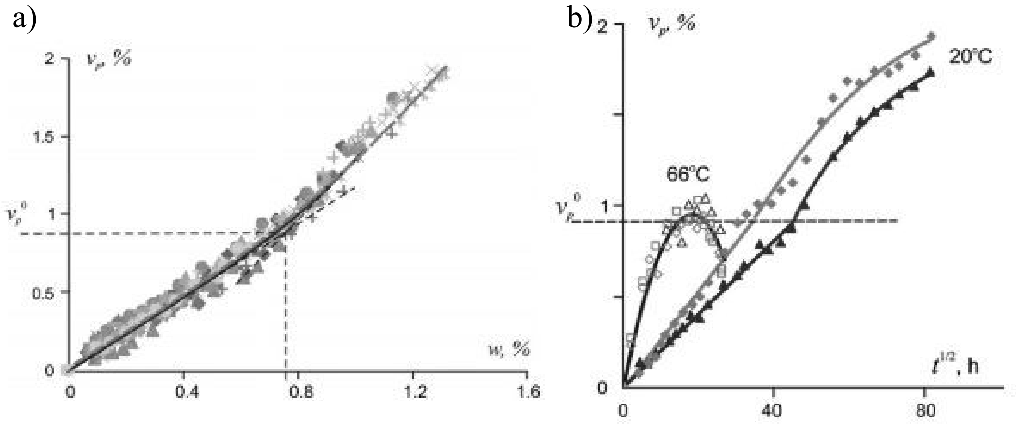

Figure 28. a) Volumetric pore ratio filled with water as a function of the weight gain at 20°C and b) the immersion time at 20 and 66°C. At figure 41b, the curves at 20°C represent two different sized profiles (♦ for profile with dimensions *l* x *w* x *t* = 155 x 15 x10 mm and ▲for 170 x 178 x 8 mm). In figure 41a, three different profiles are shown, including the two previous ones and □ for 16 x 157 x 10 mm [98].

Loh *et al.* [100] investigated the variation of swelling strains as a function of the moisture absorbed by the epoxy-based adhesive Araldite in different environments at 50°C (Figure 29a). The initial slow swelling could also be observed, becoming linear after reaching a relative absorption value (M_t/M_m) of 0.20. The swelling strains found for each environment agree with each other, meaning that the swelling is only a function of the absorbed moisture, instead of the moisture content of the environment to which the material is exposed. The swelling coefficients were determined using the Finite Element Method combining the absorption and swelling data obtained. A moisture-dependent elastic modulus was used together with an estimated swelling coefficient (α_{sw}). The swelling coefficient profile (Figure 29b) was found to be more satisfactory in the swelling prediction of the experimental data in Figure 29a than the linear coefficient of the solid line in Figure 29a (coefficient equal to 1).

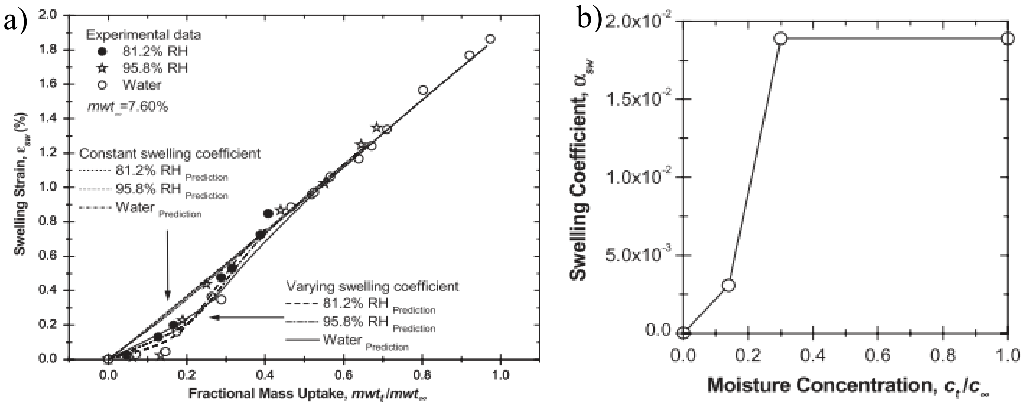

Figure 29. Variation of a) adhesive's swelling with moisture in different environments and b) swelling coefficient as a function of the relative moisture concentration [100].

From a Thermomechanical Analysis (TMA), Robert *et al.* [68] could calculate the variation in the coefficient of thermal expansion (CTE) of GFRP bars from the dimensional variation of specimen as a function of temperature. It was found that when temperature is close to the resin's T_g, its transversal CTE rapidly increases, which means that the material tends to expand faster at high temperatures (Figure 30). This analysis corroborates with the discussion in section 2.3.4 on the material's greater expansion at high temperatures, promoting a higher free volume content in the material, even though the results discussed in Figure 28 claim the opposite, where the composites exposed to a lower temperature presented a higher pore content. This phenomenon combined with the stiffness degradation on the material leads to a more porous material, enhancing its absorption capacity, which may lead to a non-Fickian behavior. Additionally, the authors found coefficients for resin and glass fiber to be $33x10^{-6}$ and $9x10^{-6}$ °C^{-1}, respectively. This expansion mismatch causes shear residual stresses at the fiber/matrix interface, which may lead to delamination.

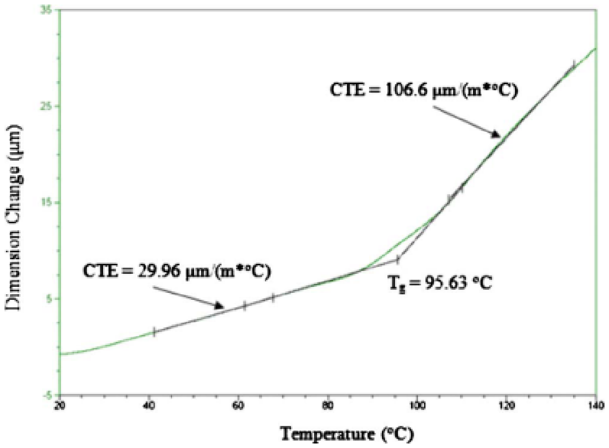

Figure 30. Dimension change of GFRP as a function of temperature [68].

2.4. Assessment of composites' hygrothermal behavior in marine environment

A number of analytical and numerical models for performance prediction of materials and components under different conditions, such as exposure to temperature, humidity and UV radiation can be found in literature [102–110]. For the hygrothermal aging of composite materials, two different yet concurring effects may occur:

1. Chemical and physical changes: both temperature and moisture alter the properties of composite and interface with time, as a result of hydrolysis, plasticization and post-cure, with the latter making a positive contribution to the material's performance. As previously discussed, moisture absorption is mainly affected by temperature, exposure time, loading conditions and nature of the materials, while the glass transition temperature is affected by plasticization. Consequently, there is a strong interaction between loading, temperature and moisture, which ultimately affects the composite's performance.
2. Additional stresses: the mismatch of thermal expansion coefficients of the materials involved leads to hydrothermal stresses, especially at the fiber/matrix and laminae interfaces. It needs to be stressed that the physical and elastic properties are modified with the aging time due to the phenomena mentioned in item (1). Therefore, the evolution of the stress distribution is completely non-linear.

As seen in the previous sections, the exposure media, constituents' properties, exposure time and temperature are major factors that influence the mechanical degradation of composites. It is noteworthy that as time and temperature increase, the degradation is more severe. Thus, it can be concluded that the composite materials generally follow an Arrhenius degradation model, where at high-temperature aging, the material's degradation reaches a certain level faster. Conversely, at low temperatures, the composites take longer to be degraded to the same level [111,112].

2.4.1. Analytical models for sorption behavior

Considering that the external load and temperature are constant and that the temperature is uniform throughout the material due to its significantly higher thermal diffusion compared to moisture diffusion, the water absorption is usually modeled using time-dependent diffusion, namely Second Fick's Law (Equation 2) [54].

Following an Arrhenius-type model, with time and the progress of the penetration front inwards the material, the hydro-thermo-mechanical properties should be adjusted to consider the hydrolysis, plasticization and post-cure phenomena, as well as the damages caused by matrix swelling [98,113–116]. It is known that the interaction between these phenomena is complex, therefore several relations and parameters are required for an appropriate simulation. In order to overcome these limitations, a simplified procedure needs to be adopted, by applying non-Fickian diffusion models, which describe the anomalous behavior that may be present in the composites [48].

The non-Fickian behavior reveals eventual relaxation processes and interactions between moisture and polymer, like the formation of hydrogen bonds (bound water molecules). This approach is based on the viscoelastic nature of polymers and relaxation of the polymer network, which is boosted by water and can be found in plasticization and post-cure effects [99]. Overall, if exposure time is lower than the time required for the relaxation process to occur, then only the Fickian transport is to be considered. Conversely, if the composite is exposed long enough to undergo relaxation, both Fickian and non-Fickian behaviors need to be considered [48].

In general, there are three different types of diffusional behaviors: Case I, or Fickian diffusion, Case II and Case III, known as non-Fickian or anomalous diffusion. All three diffusion cases can be theoretically distinguished by the absorption profile, which is represented by the empiric equation [117]:

$$\frac{M_t}{M_m} = kt^n \qquad (23),$$

where M_t is the moisture content at time t, M_m is the moisture content in the saturation level and k and n are constants. The value of the coefficient n represents the different behaviors between the cases:

- Case I (Fickian diffusion, $n = 0.5$): The relaxation of the polymer is much faster than the water diffusion, therefore diffusion is ruled by an instantaneous system response, resulting in the Fickian behavior. In this case, diffusion is governed by diffusivity [27].
- Case II ($n = 1$): Diffusion rate is much faster than the relaxation rate. In this case, there is a sharp penetration front, which separates the highly swollen region from the glassy one. This front progresses inwards the polymer at a constant rate, making the absorption increase linearly with time. This is when the polymer's swelling happens [27,54,118]. The characteristic of this behavior is the constant advancement of a penetration front that moves linearly with time, separating the swollen polymer from the dry (glassy) [54,118].
- Case III (non-Fickian diffusion, $0.5 < n < 1$): In this condition, the diffusion rate is equal to the relaxation rate. Unlike the previous cases, the non-Fickian behavior needs at least two parameters to fully describe the diffusion and relaxation processes in the material [27,54].

In Figure 31 it can be seen the possible moisture x square root of time curves for the water absorption of a composite. The curve (0) represents the classic Fickian diffusion, while the curve (1) represents the dual-phase diffusion, with a decrease in the absorption rate with time, and the curve (2) represents the two-stage diffusion. On the other hand, the curves (3) and (4) illustrate two cases of material degradation. While curve (3) shows a fast increase in moisture absorbed, which is generally induced by crack and damage growth in the material, curve (4) exhibits a weight loss, related to a change in the chemical structure of the material, like hydrolysis [67]. Thus, curves (3) and (4) are associated with irreversible damages in the material, while curves (1) and (2) are associated with reversible or nearly reversible changes in the material, which can become irreversible with the increase in media temperature, water acidity or exposure duration [119]. It is noteworthy that all behaviors shown in Figure 31 present an initial short-term linear increase of moisture absorbed.

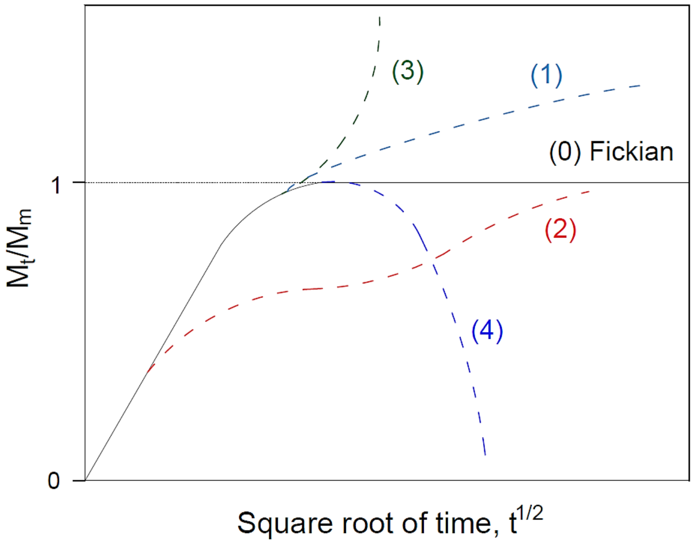

Figure 31. Illustrative curves representing different types of absorption x time curves (Adapted from Ref. [67]).

To evaluate the presence of non-Fickian processes, the dimensionless Deborah number is usually used, defined by the equation:

$$D_e = \frac{\lambda_m}{\theta_D} \tag{24}$$

where θ_D is the characteristic diffusion time, while λ_m is the characteristic relaxation time [27].

Figure 32 illustrates the relation between the Fickian and non-Fickian diffusion processes, the exposure times and Deborah numbers ($(DEB)_D$). In this representative graph, T_E is the temperature below which polymers admit an elastic solid behavior, T_g is the glass transition temperature and T_V is the temperature above which polymers act as a viscous fluid. The Fickian behavior generally occurs either above T_V or below T_E. In the latter, the polymeric segments instantaneously return to their original positions after the diffusion of a particle, resulting in an unchanged matrix. Therefore, it can be said that T_g is not the limiting temperature between Fickian and non-Fickian behaviors, as once thought, but there is a range of temperature where the non-Fickian behavior can happen [27].

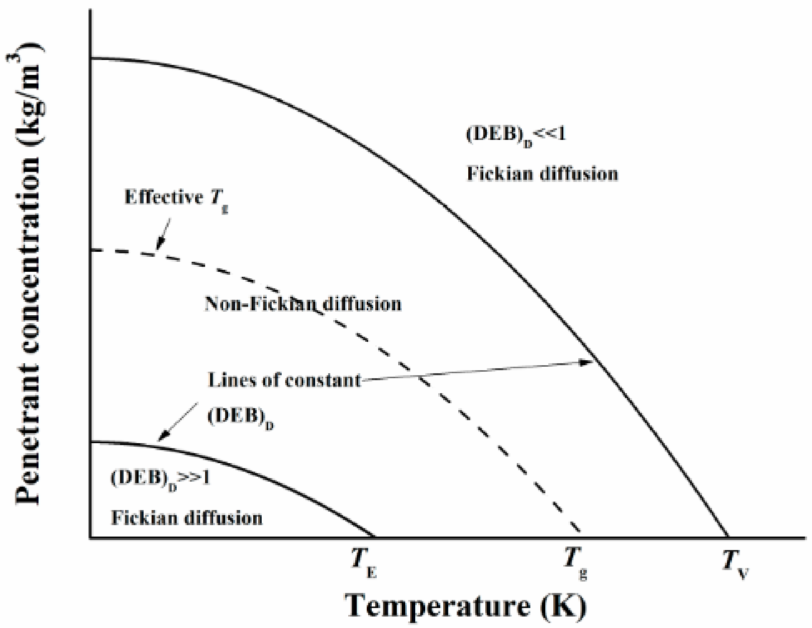

Figure 32. Schematic figure of different diffusion zones, separated by constant Deborah number $(DEB)_D$ lines, related with the penetrant concentration and temperature [27].

In the following sections, brief descriptions of some non-Fickian diffusion models that describe the changes that may happen to the material in study are presented.

2.4.1.1. Langmuir Model

Carter and Kibler [120] developed a non-Fickian diffusion model considering the chemical interaction between the polar water molecules and the polar sites of the polymer (bound molecules), as previously discussed, namely Langmuir Model [120,121]. In this model, the free, or mobile, molecules can be trapped in the macroscopic free volumes, like voids, and the physical absorption mechanism of these molecules can be easily described by the initial Fickian behavior. Afterwards, these free molecules can be displaced and temporarily retained in polymeric sites, becoming immobile [67]. In other words, these interactions force the water molecules to bond to the polymer and, therefore, the absorption continues to take place until the equilibrium between the bound and free molecules is reached [121].

Mobile molecules are diffused and absorbed, becoming immobile, with a probability γ per unit of time. Molecules are released from the immobile phase, becoming mobile, with a probability β per unit of time. The moisture content is close to the equilibrium when the number of mobile molecules by volume unit η and the number of immobile molecules by volume unit N get close to values that satisfy the equation $\gamma\eta = \beta N$ [120]. Assuming that diffusivity is independent of the concentration, for a unidirectional case, it can be written:

$$D\frac{\partial^2\eta}{\partial z^2} = \frac{\partial\eta}{\partial t} + \frac{\partial N}{\partial t}, \quad \frac{\partial N}{\partial t} = \gamma\eta - \beta N \tag{25}$$

The dimensionless non-Fickian diffusion model, for cases where 2β and 2γ $\ll \frac{D\pi^2}{h^2}$ and h is the thickness of the composite, it can be written [122]:

$$M_{\%} = M_m\left\{\frac{\beta}{\gamma+\beta}e^{-\gamma t}\left[1 - \frac{8}{\pi^2}\sum_{i=1}^{\infty}\frac{1}{i^2}e^{-\left(\frac{\pi t D i^2}{h^2}\right)}\right]\right\} + M_m\left\{\frac{\beta}{\gamma+\beta}\left(e^{-\beta t} - e^{-\gamma t}\right) + \left(1 - e^{-\beta t}\right)\right\} \tag{26}$$

Considering the following boundary conditions [55],

$$\gamma \ll \frac{D\pi^2}{h^2}\ e\ \beta \ll \frac{D\pi^2}{h^2} \tag{27}$$

equation 26 can be written as:

$$\frac{M_{\%}}{M_m} = \left[1 - \frac{\beta}{\gamma+\beta}exp(\gamma t) - \frac{\gamma}{\gamma+\beta}\cdot\frac{8}{\pi^2}exp\left(-\frac{Dt}{h^2}\right)\right] \quad (28).$$

For very short exposure times, Equation 28 can be even more simplified as:

$$M_{\%} = \frac{4}{\pi^{3/2}}\left(\frac{\beta}{\beta+\gamma}\right)M_m\sqrt{\frac{D\pi^2 t}{h^2}}, \qquad 2\beta, 2\gamma \ll \frac{D\pi^2}{h^2}, t < \frac{0.7h^2}{D\pi^2} \tag{29}$$

$$M_{\%} = M_m\left[1 - \frac{\gamma}{\gamma+\beta}exp(-\beta t)\right], \qquad 2\beta, 2\gamma \ll \frac{D\pi^2}{h^2}, t \gg \frac{h^2}{D\pi^2} \quad (30).$$

Figure 33 depicts this absorption behavior in an epoxy/glass fiber composite immersed in saltwater at 34°C, which consists of an initial linear behavior (Region I), followed by a typical curve of the behavior (1) from Figure 31 (Region II). After three-years aging, the absorption behavior shifted to curve (3) from Figure 31 (Region III), caused by degradation in the material’s interlaminar cohesion [119].

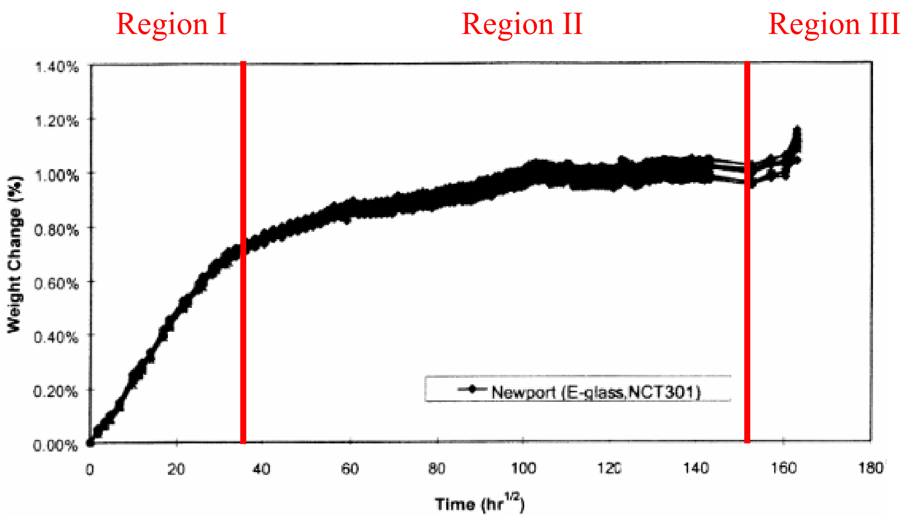

Figure 33. Weight change *vs.* square root of time curve of an epoxy/glass fiber composite exposed to seawater for four years at 34°C, showing the Langmuir-type model, followed by a degradation (Adapted from Ref. [119]).

This model was used by Boukhoulda *et al.* [123] to adjust the absorption behavior of isophthalic polyester/glass fiber composites exposed to a 95% RH environment at 50°C for 289 days. Figure 34 shows the results obtained by the authors. The authors used the equation 26, where the first part describes the Fickian behavior (free water) and the second term describes the diffusion of bound water molecules. Curve (1) represents the Fickian sorption, which is characterized by the diffusion of the free molecules inwards the material, while curve (2) represents the redistribution of the bound molecules. The curve (1) + (2) is simply the sum of the two previous curves. The fine curve fitting with the experimental data shows the complexity of the absorption and distribution of free and bound molecules.

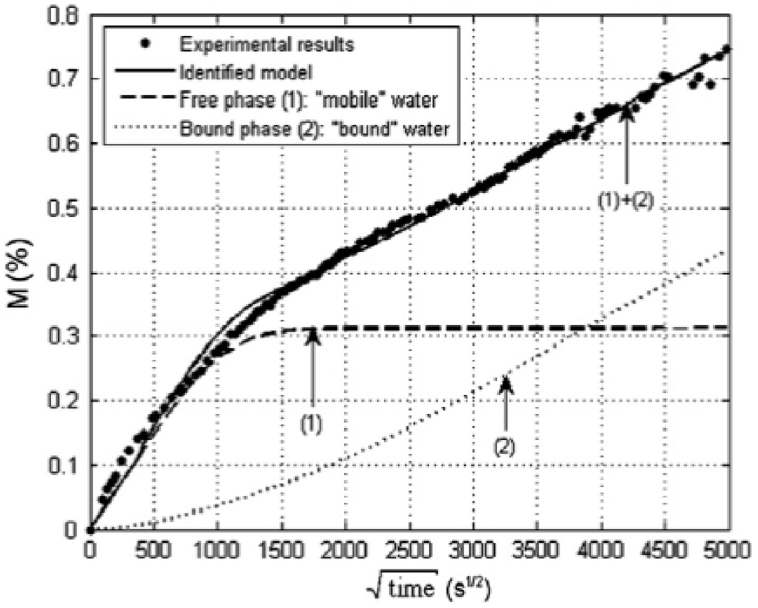

Figure 34. Absorption curves of the free and bound phases of water and the Langmuir Model curve [123].

Surathi and Karbhari [124] immersed E-glass/Vinylester composites in deionized water at 23 and 40°C and compared Fickian Model with Langmuir Model (Equation 28). For both temperatures the Langmuir model best fitted the absorption behavior. This comparison is shown in Figure 35.

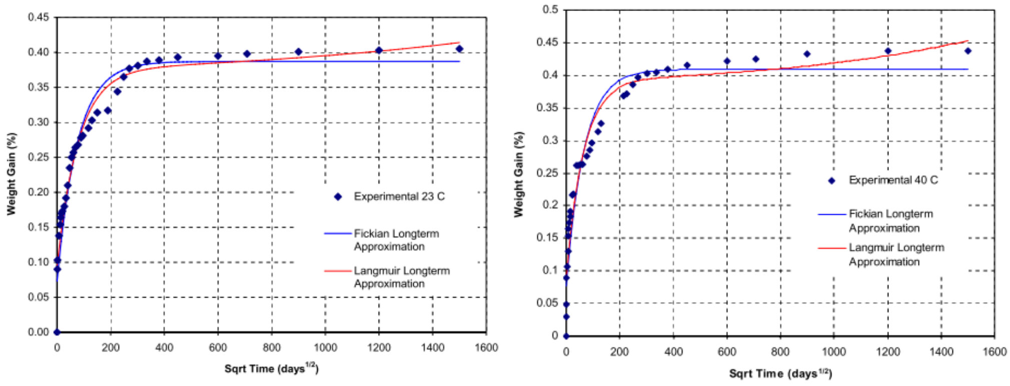

a) b)

Figure 35. Comparison between Fickian and Langmuir models for GFRPs immersed in deionized water at a) 23°C and b) 40°C [124].

Grace and Altan [125] put forward a tridimensional diffusion model, entitled by the authors as 3D HDM (*three-dimensional hindered diffusion model*), which is simply the extension of the Langmuir model previously described, but including the anisotropic diffusion and edge effect described in section 3.1. Then, the simplified equation is as follows:

$$M(t) = \frac{\beta}{\gamma+\beta}[M_F(t)] + M_m\left(1 - \frac{\gamma}{\gamma+\beta}e^{-\beta t} - \frac{\beta}{\gamma+\beta}\right) \tag{31}$$

where $M_F(t)$ is the Fickian gain mass, including D_x, D_y and D_z (Equation 32) [125]:

$$M_F(t) = M_m - \frac{512M_m}{\pi^6}\sum_{i=0}^{\infty}\sum_{j=0}^{\infty}\sum_{k=0}^{\infty}\frac{1}{(2i+1)^2(2j+1)^2(2k+1)^2}e^{-\alpha t} \tag{32}$$

where $\alpha = \pi^2\left(\frac{D_x(2i+1)^2}{h^2} + \frac{D_y(2j+1)^2}{w^2} + \frac{D_z(2k+1)^2}{l^2}\right)$.

The resulting behavior is plotted in Figure 36. Since the composite to be simulated was unidirectional, the D_y value in the fiber direction was higher than those perpendicular to the fibers (D_x and D_z), resulting in a model more complex than the one previously discussed. The authors performed an initial estimate using formerly known parameters for the materials used (Figure 36), except for the experimental diffusivity, and conducted further adjustments to the parameters until they could reach a perfect fitting (Final Estimate).

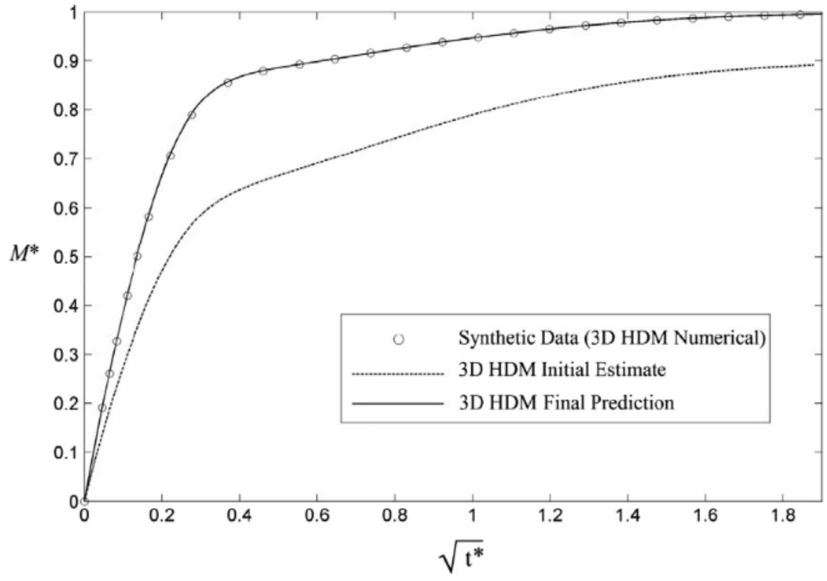

Figure 36. Non-Fickian behavior and 3D modeling [125].

To illustrate the effect of the variables β and γ on the material's absorption behavior, Guloglu [126] plotted schematic graphs showing the resultant absorption behavior from changes in these two terms. Figure 37 shows the effect of change in β (Figure 37a) and γ (Figure 37b) on the moisture absorption, while Figure 38 shows the effect of change in β (Figure 38a) and γ (Figure 38b) on the bound and unbound moisture absorption. It can be seen that the lower the values of β and γ, the longer it would take for the material to saturate.

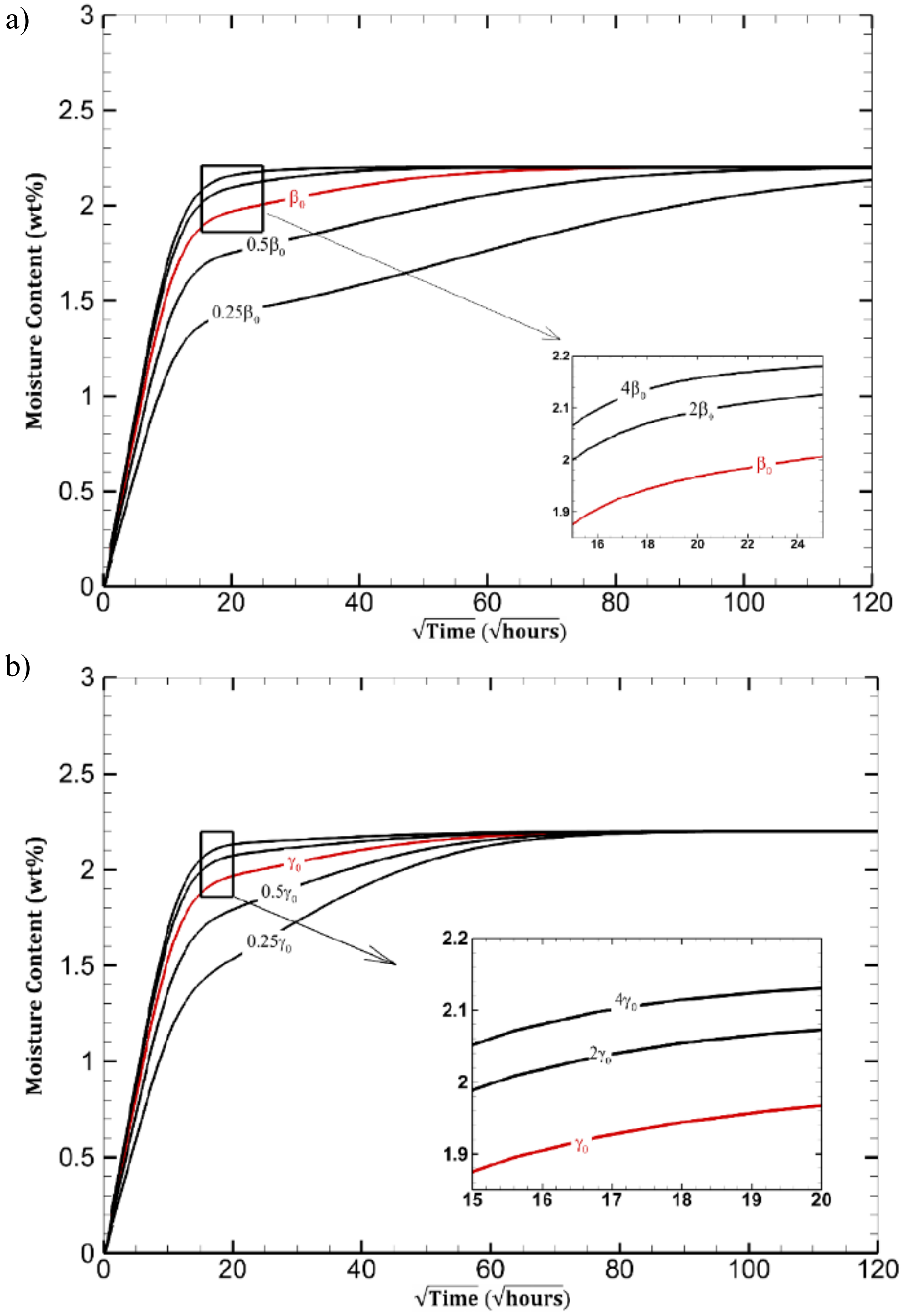

Figure 37. Effect of β (a) and γ (b) on the moisture absorption behavior [126].

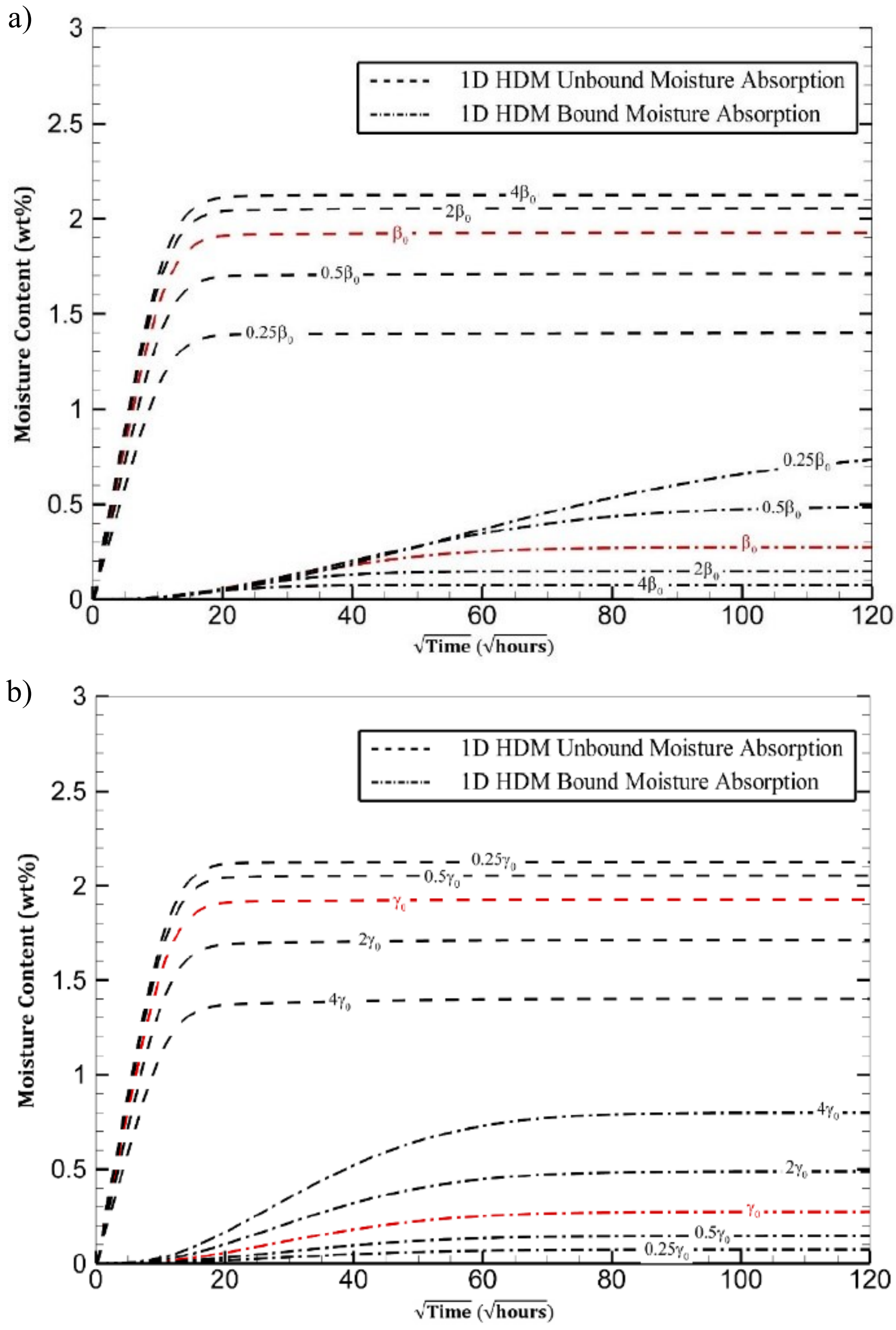

Figure 38. Effect of β (a) and γ (b) on the unbound and bound molecules absorption [126].

2.4.1.2. Jacobs-Jones Model

The Langmuir-type model considers that the water absorbed can be divided into mobile and bound molecules. However, while this model can be applicable for some polymeric systems, an additional factor to be taken into consideration is the presence of a dispersed phase. Therefore, Jacobs and Jones [127,128] developed an absorption model considering that polymer has two coexisting phases: a highly crosslinked phase and a less crosslinked phase, where each one presents a different diffusivity rate. In this case, the absorption curve has two major regions, as shown in Figure 39.

Region I is attributed to the moisture sorption in both less and highly dense phases of the material, while region II is attributed only to the absorption of the dense phase. Considering that initially both phases absorb moisture, but the less-dense phase reaches the equilibrium faster, the following water absorption is related to the absorption of the dense phase. Then, by subtracting the slope in region II (m_d) from the slope in region I (m_x), the slope corresponding to the absorption of the less-dense phase can be obtained (m_l) [127].

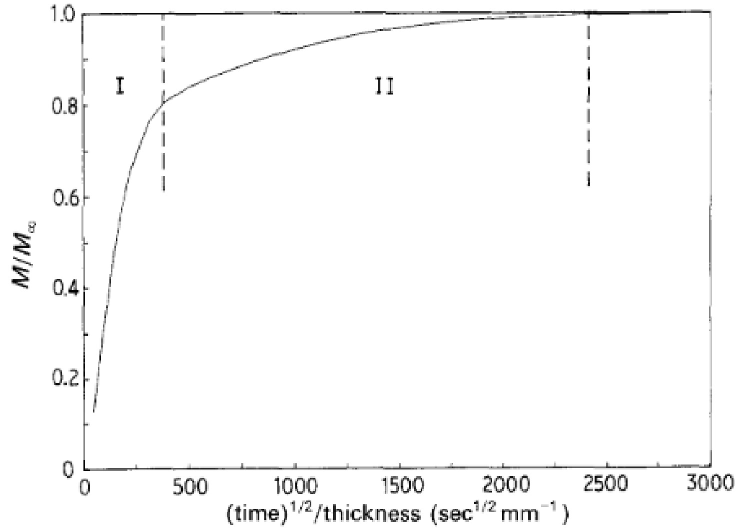

Figure 39. Representative sorption curve of a biphasic resin system, showing both dense and less dense phases (Region I) and the dense phase (Region II) [128].

In order to formulate this model, the equation used considers that diffusion is governed by a Fickian behavior in both phases (Equation 33) [127,128]:

$$\frac{M_{\%}}{M_{\infty}} = V_d\left\{1 - exp\left[-7{,}3\left(\frac{D_d t}{h^2}\right)^{0{,}75}\right]\right\} + (1 - V_d)\left\{1 - exp\left[-7{,}3\left(\frac{D_l t}{h^2}\right)^{0{,}75}\right]\right\} \quad (33)$$

where D_d and D_l are the diffusivities of the dense and less-dense phases, respectively, and V_d is the volume fraction of the dense phase.

The nominal diffusivities of the resin as a whole (D_x), the dense phase (D_d) and the less-dense phase (D_l) can be calculated, following the following equations [128]:

$$D_x = \pi\left(\frac{m_x h}{4M_m}\right)^2 \quad (34)$$

$$D_d = \pi\left(\frac{m_d h}{4(M_m - M_l)}\right)^2 \quad (35)$$

$$D_l = \pi \left(\frac{(m_x - m_d)h}{4M_l} \right)^2 \tag{36}$$

where M_m is the total moisture content absorbed by the resin, M_l is the moisture absorbed by the less-dense phase and m_x and m_d are the slopes of the curve $M(t)$ *vs.* $(time)^{1/2}/thickness$ of region I and region II (Figure 39), respectively. The value of M_l is obtained from the extrapolation of the curve of region II (m_d) to the $M(t)$ axis, while the equilibrium moisture content of the dense phase (M_d) can be a result of the subtraction of M_l from M_m [127].

Jacobs and Jones [128] exposed some unsaturated polyester resin specimens to 96% RH and 75% RH and immersed other specimens in distilled water. All exposure media were kept at 50 ± 1°C. The experimental data was accurately fitted with the theoretical equations 33 – 36 (Figure 40). The values for D_x, D_d, D_l and V_d were found to be the same for all conditions tested, as seen in Table 1, therefore for the RH environment, it can be said that the diffusion is independent of moisture concentration.

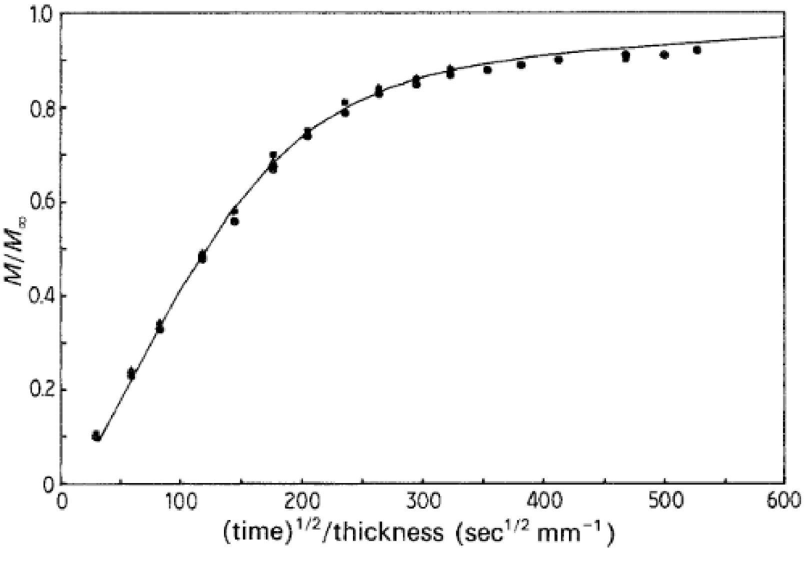

Figure 40. Comparison of the theoretical and experimental moisture absorption curves. (●) Immersion, (▲) 96% RH, (■) 75% RH [128].

Table 1. Moisture diffusion coefficients from absorption data for polyester resins exposed to different environments at 50°C [128].

	75% RH	96% RH	Immersion
D_x (10^{-5} mm^{2}s^{-1})	8	8	8
D_d (10^{-5} mm^{2}s^{-1})	0.6	0.6	0.6
D_l (10^{-5} mm^{2}s^{-1})	10	10	10
V_d	0.16	0.16	0.16

2.4.1.3. Modified Jacobs-Jones Model

The previous model considers that in each phase the diffusion is only controlled by its density. However, the possible formation of hydrogen bonds between the water and hydroxyl groups of the resin is neglected. The Modified Jacobs-Jones model also considers the polymer structure as one phase, where most of water is absorbed (phase 1), and another phase with different density and hydrophilicity from phase 1 (phase 2) [55,129].

This behavior is also called two-stage diffusion (curve (2) in Figure 31), where there is a pseudo-saturation, followed by a new increase in absorption. This behavior is generally reported in materials immersed in high-temperature environments and can be attributed to the relaxation of the polymer. This model can be represented by the sum of two Fickian stages, where the total moisture content (M_m) is written as the sum of the absorption of the first phase in the first stage (M_1) and the second phase in the second stage (M_2) [17,55,69,129]:

$$M_t = M_1 \left\{1 - exp\left[-7{,}3\left(\frac{D_1 t}{h^2}\right)^{0{,}75}\right]\right\} + M_2 \left\{1 - exp\left[-7{,}3\left(\frac{D_2 t}{h^2}\right)^{0{,}75}\right]\right\} \quad (37)$$

where D_1 and D_2 are the diffusivity values of both phases.

Figure 41 shows both mechanisms and their contributions to the water absorption of a DGEBA epoxy resin immersed in water at 40°C. The results in Figure 41 show that, in some cases, the absorption process requires more than one diffusivity coefficient. Also, the total moisture saturation content observed in the experiment is the sum of M_1 and M_2 (Equation 37). The overlap of modes 1 and 2 results in the solid curve [129]. This behavior could also be observed in Figures 9 and 12.

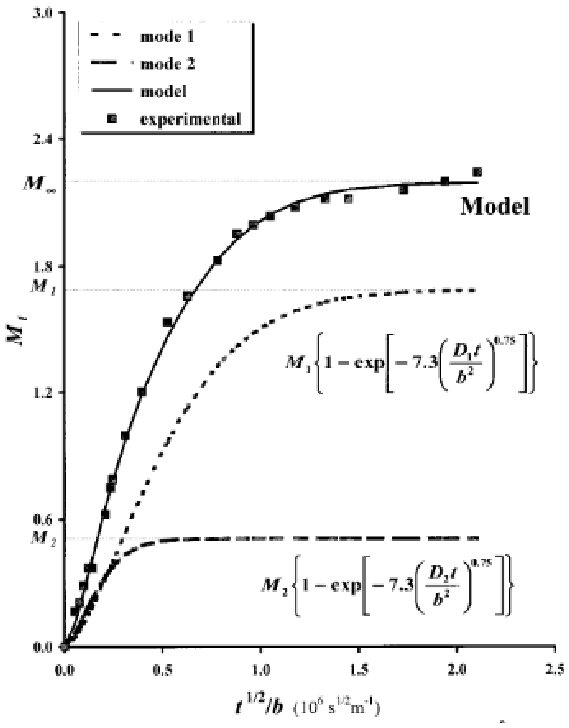

Figure 41. Representative description of the evolution of two diffusion ways and their contributions to the total diffusion process [129].

Heshmati *et al.* [17] found the same behavior for GFRP immersed in distilled water at 45°C. Figure 42 shows that the modeling implemented using a two-stage model resulted in a finer correlation (R^2) in relation to the Fickian model. Additionally, Du Plessix *et al.* [67] found that this behavior was more prominent at higher temperatures.

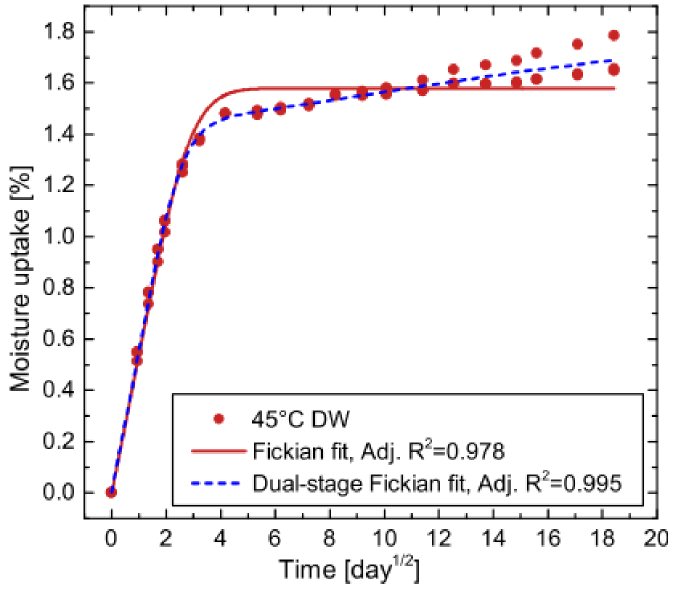

Figure 42. Experimental absorption curve of an epoxy sample immersed in distilled water at 45°C and the comparison of Fickian and Two-Stage theoretical curves [17].

This two-stage diffusion model has also been applied for the fitting of the moisture absorption behavior of epoxy at 60°C in 85% RH and at 85°C in 85% RH [130]. The authors found that the M_1 value (Equation 37) was independent of the exposure temperature, and the diffusivity value on the first stage was found to be two orders of magnitude greater than that on the second stage. Moreover, the diffusivities in both stages, as well as the saturation contents were increased with temperature.

Bao *et al.* [131] put forward a modification to this model when trying to better adjust the behavior observed for bismaleimide resin (BMI) after long-term immersion in distilled water at 70°C. Since the BMI resin is well-known as a glassy polymer, the relaxation takes place much slower than the diffusion process. Then, the concentration profile is made uniform throughout the specimen. This means that any increment in the saturation content would promote equilibrium in the material at a time scale shorter than the time scale of the structural relaxation. Given that the mass gain during the second stage increased linearly with $\sqrt{t}$ (Figure 43), it was suggested that the saturation content follows a function linear with $\sqrt{t}$:

$$M = M_0 + k\sqrt{t} \qquad (38)$$

where the term k is a constant obtained from the experimental data fitting.

Equation 38 could, therefore, be rewritten as:

$$M_t = M_m \left\{1 - exp\left[-7{,}3\left(\frac{D_x t}{h^2}\right)^{0{,}75}\right]\right\} + k\sqrt{t} \cdot M_m \left\{1 - exp\left[-7{,}3\left(\frac{D_x t}{h^2}\right)^{0{,}75}\right]\right\} \qquad (39)$$

where the first term refers to the diffusion-driven stage, while the second describes the relaxation process.

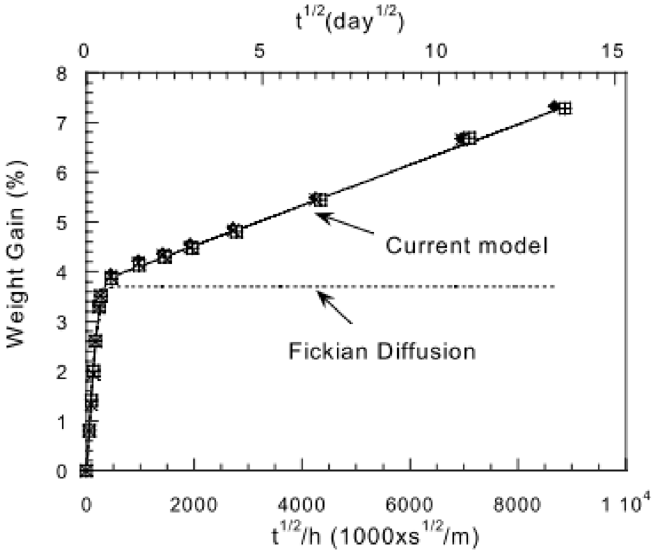

Figure 43. Weight gain of BMI resin t 70°C. The dash line shows the curve fitting with Fickian diffusion model, while the solid one shows the fitting using the model of equation 29 [131].

2.4.1.4. Berens-Hopfenberg Model (BH Model)

Berens and Hopfenberg [132] developed an analytical water absorption model in glassy polymers based on two phenomena: Fickian diffusion and time-dependent polymeric relaxation. The Berens-Hopfenberg (BH) Model allows the calculation of the diffusivity from absorption data, in which long relaxation times may overshadow a rapidly reached Fickian diffusion, with the aid of just few parameters. Thus, these two processes may coexist and can be combined, by making use of a simple linear superposition. As a result, the weight gain with time is given by the sum of the absorption related to the Fickian diffusion ($M_F(t)$) and the relaxation-related absorption ($M_R(t)$) [99,132]:

$$M_{BH}(t) = M_F(t) + M_R(t) \tag{40}$$

The first term has already been discussed and is shown in Equation 41, while the second one is shown in Equation 42 [99]:

$$M_F(t) = M_{m,F}\left\{1 - exp\left[-7.3\left(\frac{Dt}{h^2}\right)^{0.75}\right]\right\} \tag{41}$$

$$M_R(t) = M_{m,R}\left[1 - exp\left(-\frac{t}{\tau_R}\right)\right] \tag{42}$$

where $M_{m,F}$ is the Fickian saturation moisture content, $M_{m,R}$ is the saturation content related to the polymeric relaxation and τ_R is the first-order relaxation term, which corresponds to the time in which all the structure reorganizations of the polymeric network are complete and, therefore, $M_R(t) = M_{m,R}$. The term $M_{m,R}$ can only be determined if the total moisture (M_{BH}) and the Fickian equilibrium moisture ($M_{m,F}$)

are known values. It is worth mentioning that the stronger contribution of the term τ_R intensifies the deviations from the Fickian model [99].

Following the same hypothesis, the total weight gain (M_{BH}) is given by the sum of the total Fickian absorption ($M_{m,F}$) and the relaxation-related absorption ($M_{m,R}$):

$$M_{BH} = M_{m,F} + M_{m,R} \qquad (43)$$

Figure 44 schematically represents a typical BH Model curve resulting from equations 40 to 43.

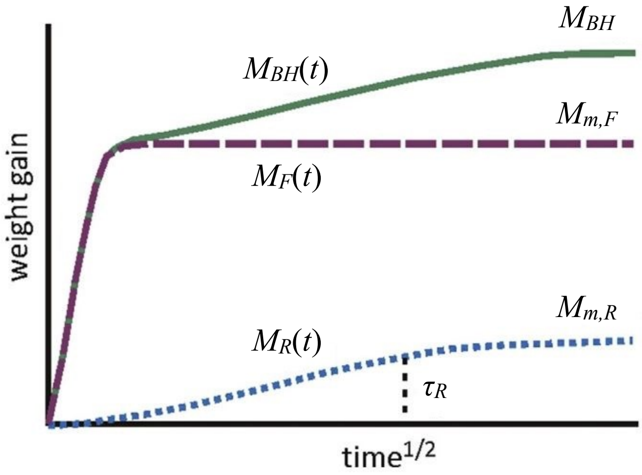

Figure 44. Schematic representation of the BH model, including the contributions of diffusion and polymeric relaxation [99].

Starkova *et al.* [99] performed immersion tests using epoxy-based nanocomposites reinforced with carbon nanoparticles (expanded graphite (EG), carbon black (CB), multi-walled carbon nanotube (MWCNT) and graphite nanoplatelets (GnP)) in distilled water at 20, 50 and 70°C. The non-Fickian behavior was modeled using BH model and the total absorption value for each material was found to be independent of immersion temperature, since the sum values of both types of absorption for each material are roughly the same (Table 2). The graphs in Figure 45 illustrate the absorption behavior of the neat epoxy (45a) and the epoxy/MWCNT composite (45b). A small deviation from the Fickian behavior for the epoxy/MWCNT samples (Figure 45b) at 70°C indicates that the relaxation processes had not been completed yet at this temperature within the aging time. Either a higher temperature or a longer exposure time must be needed to reach full saturation, therefore it is assumed that the total water content to be absorbed by each material is its value at 70°C, where $M_{BH} = M_{m,F}$ [99].

Table 2. Water absorption parameters on epoxy nanocomposites [99].

Material	T (°C)	$M_{m,F}$ (%)	$M_{m,R}$ (%)	τ_R (10^3h)
Pure Epoxy	20	1.38	0.89	70
	50	1.70	0.57	15
	70	2.27	——	——
EG	20	1.46	0.77	70
	50	1.75	0.48	30
	70	2.23	——	——
CB	20	1.60	0.90	70
	50	1.93	0.57	30
	70	2.50	——	——
MWCNT	20	1.60	0.87	150
	50	1.80	0.67	60
	70	2.47	——	——
GnP	20	n/a	——	n/a
	50	2.35	0.85	30
	70	n/a	——	n/a

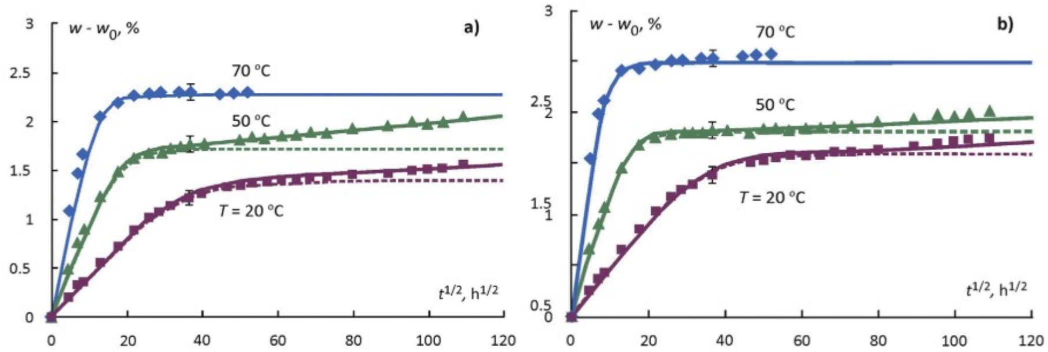

Figure 45. Water absorption curves of (a) pure epoxy and (b) epoxy/MWCNT composites at 20, 50 and 70°C [99].

From Table 2, what can be confirmed is that the relaxation times for the epoxy/MWCNT composites are twice greater than those of the neat epoxy, indicating a retarded relaxation caused in the polymeric structure by the nanofillers. It can be also observed that the higher the temperature the shorter the relaxation time [99].

It is known that viscoelastic processes in polymers are generally described by a distribution of relaxation times. Therefore, a more general expression for the relaxation-induced absorption process is as follows [132]:

$$M_R(t) = \sum_i M_{m,i}\left[1 - exp\left(-\frac{t}{\tau_i}\right)\right] \tag{44}$$

where $M_{m,i}$ represents the equilibrium content of the *i*th relaxation process, while τ_i refers to the respective relaxation time. Therefore, the characteristic equation for BH model that accounts for the relaxation spectra derives from the substitution of Equation 44 into equation 40:

$$M_{BH} = M_{m,F}\left\{1 - exp\left[-7.3\left(\frac{Dt}{h^2}\right)^{0.75}\right]\right\} + \sum_i M_{m,i}\left[1 - exp\left(-\frac{t}{\tau_i}\right)\right] \quad (45)$$

According to Bond and Smith [133], generally no more than two relaxation processes are required to obtain an acceptable fit.

2.4.1.5. Weight loss modelling

Krauklis *et al.* [93] developed a reliable model for the prediction of the behavior in curve (4) from Figure 31 and could successfully predict the weight loss rate of a GFRP immersed in distilled water. The diffusivity of the components leached out of the epoxy matrix has been based on the a Fickian model used to fit the water absorption (Equation 46), where $M_{leaching}(t)$ is the material content leached out of the composite, $M_{leaching}^0$ is a material's constant, $D_{leaching}$ is the hydrolysis diffusivity, *h* is the material's thickness and *t* the immersion time. The authors precisely fitted the weight loss with time, following the gravimetric tests, and the hydrolysis diffusivity was found to be 6.0 x 10^{-5} mm^2/h. The dissolution of the glass fibers was also evaluated with the aid of Equation 47, where K_0 is the dissolution rate of the glass and *S(t)* the exposure area of glass surface.

$$M_{leaching}(t) = M_{leaching}^0\left\{1 - exp\left[-7.3\left(\frac{D_{leaching}t}{h^2}\right)^{0.75}\right]\right\} \quad (46)$$

$$\frac{\partial m}{\partial t} = K_0 S(t) \quad (47)$$

2.4.2. Mechanical degradation prediction

Several empirical and theoretical models have been put forward for prediction of FRP's long-term mechanical performance. A description of some of the most used prediction models can be found in the following subsections.

2.4.2.1. Arrhenius Model

In order to estimate the long-term mechanical degradation of composites, Chen *et al.* [111] and Bank *et al.* [112] employed a predictive Arrhenius model for deterioration of mechanical properties, similar to that of diffusivity. This model can be found in Equation 48, where *k* is the degradation rate (*1/time*), *A* is a material's constant, E_a the activation energy, *R* the universal gas constant and *T* the temperature in kelvin. In this model, it is assumed that the dominant degradation mechanism in the material does not change with time and temperature during aging, although the degradation rate is increased with temperature [111].

$$k = Aexp\left(\frac{-E_a}{RT}\right) \tag{48}$$

Equation 48 can be written as:

$$\frac{1}{k} = \frac{1}{A}exp\left(\frac{E_a}{RT}\right) \tag{49}$$

In Equation 49, the degradation rate k can be expressed as the inverse of the time required for a material's property to reach a specific value [111]. Then, graphs relating time, property retention and time can be plotted, based on experimental data, like the graphs in Figure 46. All regression curves must have nearly the same slope, otherwise the degradation mechanism is dependent on temperature.

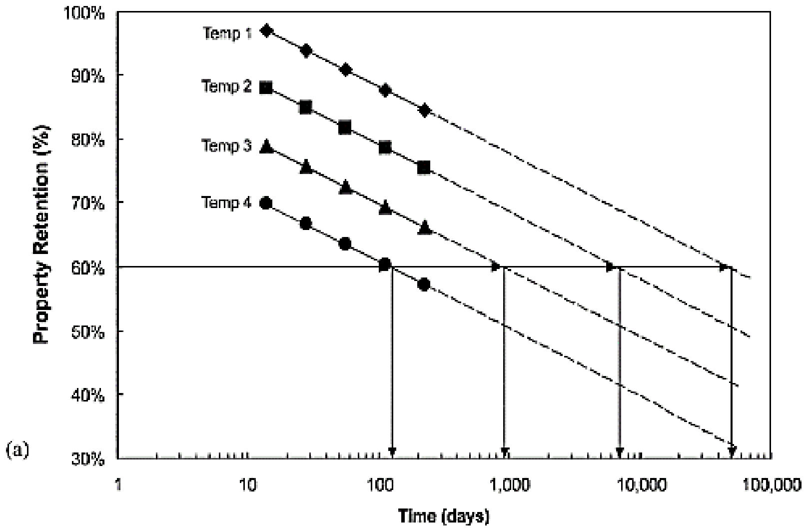

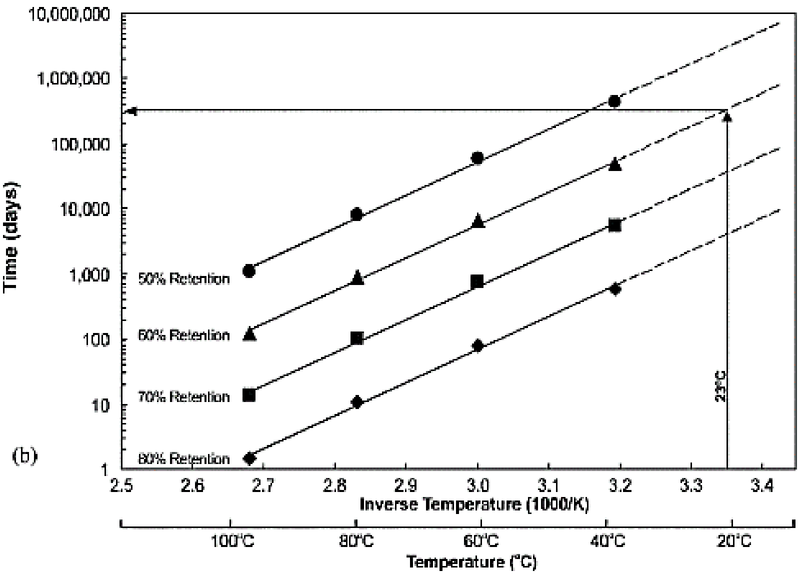

Figure 46. a) Property retention curve as a function of time and b) Arrhenius lifespan as a function of temperature and percentage retention with Temperature 4 > Temperature 3 > Temperature 2 > Temperature 1 [112].

2.4.2.2. Phani and Bose Prediction Model

Phani and Bose [134] investigated the degradation of glass-fiber reinforced polyester laminates immersed in water through flexural tests. From the results obtained by the characterization of the hydrothermal aging of the composite by means of acoustic and ultrasound tests the authors came up with a relation between mechanical property (σ_t) and exposure time t given by:

$$\sigma_t = (\sigma_0 - \sigma_\infty)exp(-t/\tau) + \sigma_\infty \tag{50}$$

where σ_0 and σ_∞ are the initial strength and the strength at infinite time, respectively, and τ is a temperature-dependent characteristic time [134,135].

It was found that the strength degradation of laminates follows a relation, in which the rate constant follows the Arrhenius equation [136]:

$$\frac{1}{\tau} = \frac{1}{\tau_0} exp\left[\frac{-E_a}{RT}\right] \tag{51}$$

where $1/\tau$ is the degradation rate constant and $1/\tau_0$ is a constant. Obviously, this constant is nothing but the diffusion coefficient. The percentage retention data are fitted to equation 49 using regression analysis. These analyses result in relationships between flexural strength and time at different temperatures. By plotting $1/\tau$ *vs.* $1/T$ graphs, the E_a and $1/\tau_0$ values can be found. With the aid of these parameters, it is possible to plot the property retention at other temperatures. After having calculated the constants values, the equations 50 and 51 can be combined to calculate the degradation with time and temperature (Equation 52) [124,136].

$$\sigma_t = (\sigma_0 - \sigma_\infty)exp\left(-t/\tau_0\, exp\left(-\frac{E_a}{RT}\right)\right) + \sigma_\infty \qquad (52)$$

Equation 52 can be manipulated into:

$$\sigma_{r_T} = \sigma_t - \sigma_\infty = (\sigma_0 - \sigma_\infty)exp(-t/\tau) \qquad (53),$$

given that for each individual system, the term $(\sigma_0 - \sigma_\infty)$ is constant. In order to implement this model, it is needed to estimate an initial value for σ_∞ prior to data fitting. Generally, this estimation is done from the data at the highest test temperature. Then, the data can be fitted through least square sum method, for instance, and the value of σ_∞ can be adapted until the best correlation is found [136]. The curves the authors fitted to the experimental data obtained at 50, 60, 80 and 100°C can be seen in Figure 47a. The mean value of $(\sigma_0 - \sigma_\infty)$ could be calculated, leading to a σ_0 value close to the measured value in the mechanical tests. The authors could also observe from the curve equations that the characteristic time τ decreases as temperature increases. This behavior can be seen in Figure 47b, since the inverse of τ increases at a higher temperature [136].

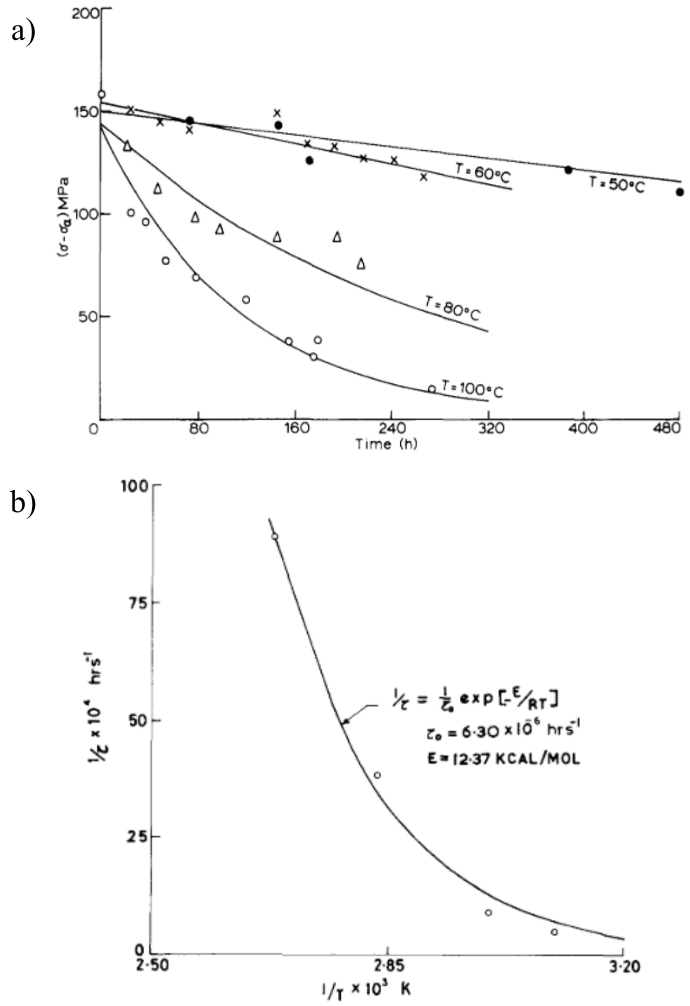

Figure 47. a) Plot of ($\sigma - \sigma_\infty$) versus aging time and b) Arrhenius plot of $1/\tau$ versus $1/T$ [136].

This model also allows the creation of a master curve for the aging process at the temperatures tested. To do so, a time/temperature superposition is required. This is only possible when two conditions are satisfied: (i) the temperature influences only the rate constant ($1/\tau$), and (ii) the degradation process is a function of t/τ. Then, the data must be shifted along the time axis by the amount calculated by Equation 54, where $ln\ a_D$ is the shift distance and $1/\tau_R$ is the rate constant at the reference temperature T_R, which can be one of the temperatures tested. Combining equations 54 and 51, the relationship between $ln\ a_D$ and temperature is written as Equation 55 [136].

$$ln\frac{\tau_R}{\tau} = -lna_D \tag{54}$$

$$lna_D = -E/R\,(1/T - 1/T_R) \tag{55}$$

The values of $ln\ a_D$ calculated by the authors are shown in Figure 48. In this master curve, it is necessary to perform experiments only at one temperature, then estimations of the degradation rate at other temperatures can be made using the shift distance [136].

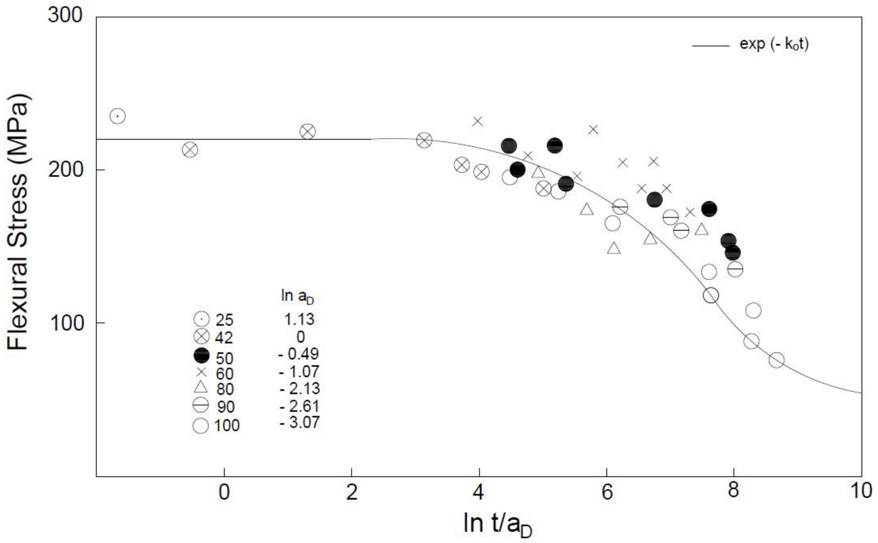

Figure 48. Master curve for flexural strength degradation using 42°C as a reference temperature (Adapted from Ref. [136]).

In addition, Wang *et al.* [135] added the following term to Equation 52 to include the initial strength gain due to the post-cure of samples:

$$Y_1 = \alpha exp[-\beta(1-\mu)^2] \quad (56),$$

where Y_1 is the percentage increment to the property retention due to post-cure and α, β and μ are constants.

The degradation prediction can also be made by combining Arrhenius and Phani and Bose model. To do so, Equation 52 can be simplified to [72,111]:

$$PR(t) = 100e^{-kt} \tag{57}$$

The experimental property retention values *vs.* aging time allow the determination of degradation rate k through linear regression. The results reported by Chen *et al.* [111] show that the degradation rate k is enhanced with temperature.

After the obtaining of k by linear regression, the equation for each temperature is obtained. Then, arbitrary retention values are input in equation 57 and the time required to reach a determined retention value for each temperature is calculated. Afterwards, it is possible to obtain a Time Shift Factor (*TSF*) with the calculated values, which relates the material's degradation rate between two different temperatures and follows an Arrhenius relationship Equation 58). For this, it is necessary to arbitrarily set a temperature as reference, which will have *TSF* value as 1.0 [72,111].

$$TSF = \frac{t_1}{t_2} = \frac{c/k_1}{c/k_2} = \frac{k_1}{k_2} = \frac{A\,exp\left(\frac{-E_a}{RT_1}\right)}{A\,exp\left(\frac{-E_a}{RT_2}\right)} = exp\left[\frac{E_a}{R}\left(\frac{1}{T_1} - \frac{1}{T_2}\right)\right] \tag{58}$$

where *TSF* is the time shift factor, t_1 and t_2 are the times required for a property to reach a certain value at the temperatures T_1 and T_2, respectively, c is a constant and k_1 and k_0 are the degradation rates at the temperatures T_1 and T_2, respectively.

Silva *et al.* [72] found that the time shift factor is increased with temperature. Figure 49a shows the retention curves at each temperature and Figure 49b shows the relationship between *TSF* and temperature in relation to the reference temperature 35°C ($\mathrm{TSF}_{35^{\circ}\mathrm{C}} = 1.0$). From the fitted equation shown in Figure 49b, the value of *TSF* for a temperature out of the test temperature range can be obtained, like 10°C for instance. For the example, in the work of Silva *et al.* [72], the prediction for 10°C resulted in a time equal to 3254 hours for strength retention of 80%.

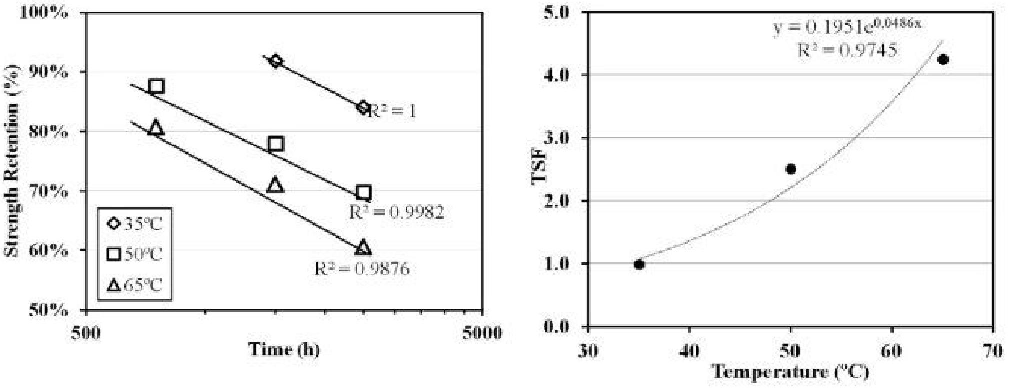

a) b)

Figure 49. a) Tensile strength retention *vs*. log of time and b) relation between TSF and temperature [72].

To calculate the degradation time in an immersion test at 10°C, for example, by applying the Equation 58 to compare 10°C with 65°C, the relative TSF at this temperature was found to be 20.74. Therefore, aiming to calculate the time required to reach 61% retention at 10°C, one can simply multiply 2500 hours of aging at 65°C (Figure 49a) by the relative TSF of 20.74, thereby obtaining 6-years aging prediction at 10°C. Similarly, in order to predict the retention after 25 years at 10°C, the ratio 25/20.74 indicates that the experimental data should be obtained for at least 1.2 years. Figure 50 shows the prediction curve plotted by the authors for 10, 14 and 18°C (50a) and the material's Arrhenius in-service lifespan curve (50b) [72].

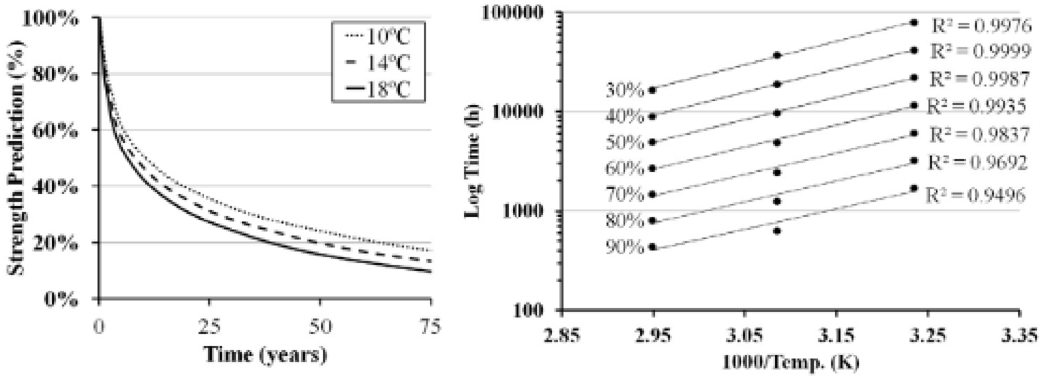

a) b)

Figure 50. a) Estimated tensile strength retention for a GFRP and b) In-service lifespan as a function of temperature and retention [72].

2.4.2.3. Time-Temperature Superposition Principle

The Time-Temperature Superposition Principle (TTSP) is a well-known method that works for certain types of viscoelastic materials and relates the effects of time and temperature. TTSP was originally developed to characterize properties related to the stiffness of polymers and is based on the viscoelastic theory. However, this method can be extended for the prediction of strength properties [137].

Firstly, it is necessary to understand the viscoelastic strain model based on time and temperature. Figure 51 shows the Maxwell Model for the deformation of a viscoelastic material under constant load. The deformation rate is higher at high temperatures, reducing the time needed to reach certain deformation [137].

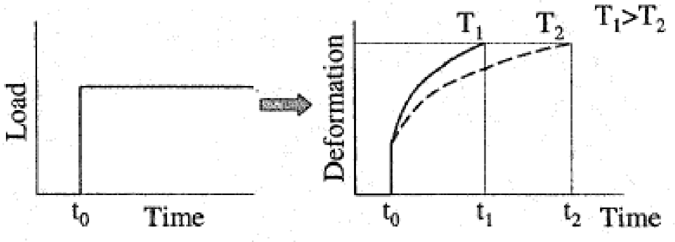

Figure 51. Deformation dependent on time and temperature [137].

Substituting the Time axis by a function of time and temperature, these curves can be merged to form a single curve (Figure 52). From this curve, the deformation can be predicted for a wide range of temperature and time. This is the basis of the TTSP method, where the scales of time and temperature become one single scale [137].

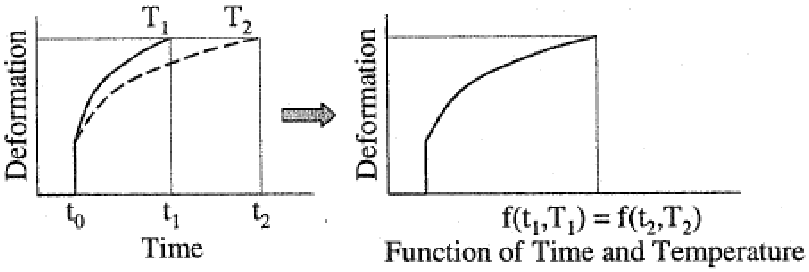

Figure 52. Merged deformation curve [137].

In the TTSP method, a master curve is obtained by plotting the property *vs.* the logarithmic scale of time. This master curve makes it possible to determine the strength at any temperature if the activation energy of the process is known. Figure 53 shows the strength graph *vs.* logarithm of time for different temperatures. The TTSP method assumes that these curves are superposed when horizontally shifted. This curve is called master curve and is applicable for any temperature within the range of temperatures tested [124,137].

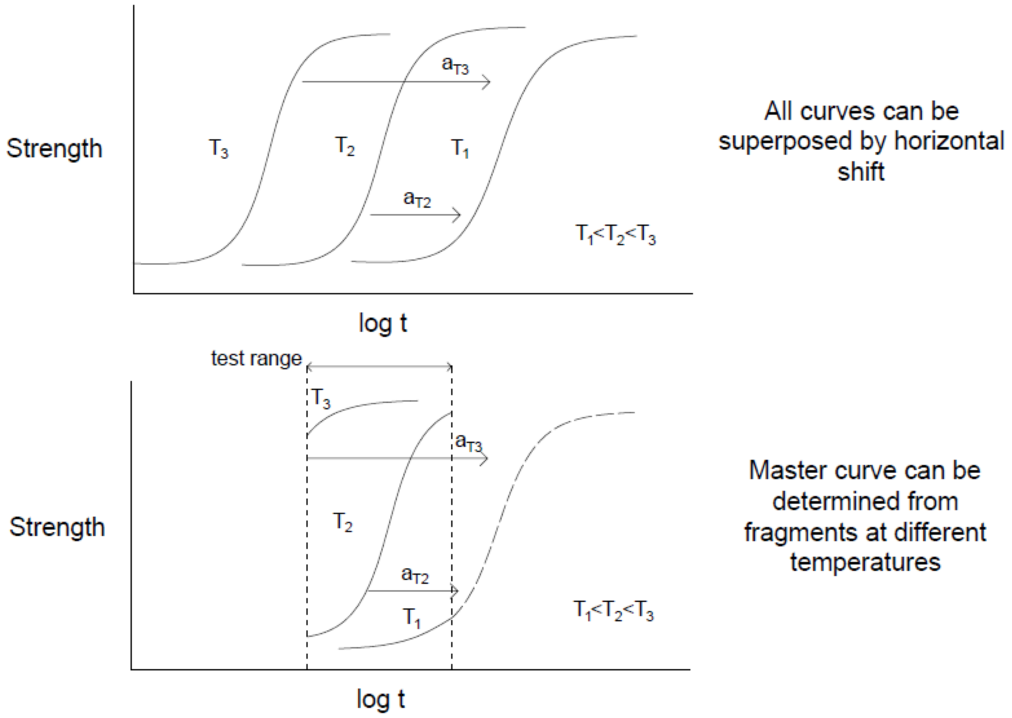

Figure 53. Time-Temperature Superposition Principle (Adapted from Ref. [137]).

A temperature must be chosen to be a reference temperature (T_0) so that the shift coefficients (a_T) of each temperature could be calculated in order to fit the different curves to the master curve [124,137]. The equation for the shift coefficient (a_{T0}) is an Arrhenius-type equation:

$$log a_{T0}(T) = \frac{E_a}{2.303R}\left(\frac{1}{T} - \frac{1}{T_0}\right) \qquad (59)$$

where E_a is the activation energy, R the universal gas constant and T_0 the reference temperature.

Krauklis *et al.* [138] proposed a modification to the TTSP model by including the plasticization effect, creating the time-temperature-plasticization superposition principle (TTPSP). In this proposed model, the authors first applied Equation 59 to determine the master curve of creep compliance of epoxy before and after the immersion in water at 60°C. Then, they used Equation 60 to plot a master curve to include the unaged and aged polymers. In this equation, $T_{g_{dry}}$ is the T_g value of the unaged polymer and $T_{g_{plast}}$ the T_g value of the plasticized material.

$$log a_{dry-to-plast} = \frac{-E_a}{2.303R}\left(\frac{1}{T_{g_{plast}}} - \frac{1}{T_{g_{dry}}}\right) \qquad (60)$$

Figure 54 shows the master curves found for the dry (54a) and aged (54b) epoxy. The reference temperature chosen was 26°C (log a_t = 0).

After the application of Equation 60, it was possible to create the master curve for the compliance of both dry and aged polymers (Figure 55) from the curves in Figure 54. It was observed that the curves could be quite well superposed, therefore it can be said that the viscoelastic processes are the same for the dry and saturated epoxy [138].

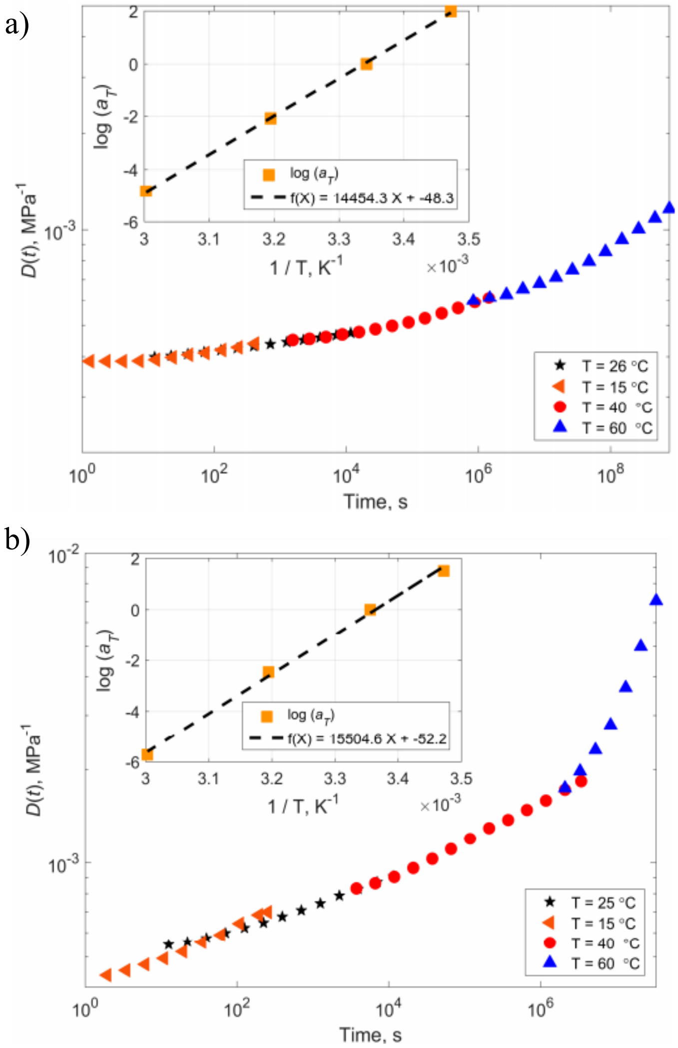

Figure 54. Master creep compliance (D(t)) curves of a) dry and b) saturated epoxy under creep at 10 MPa [138].

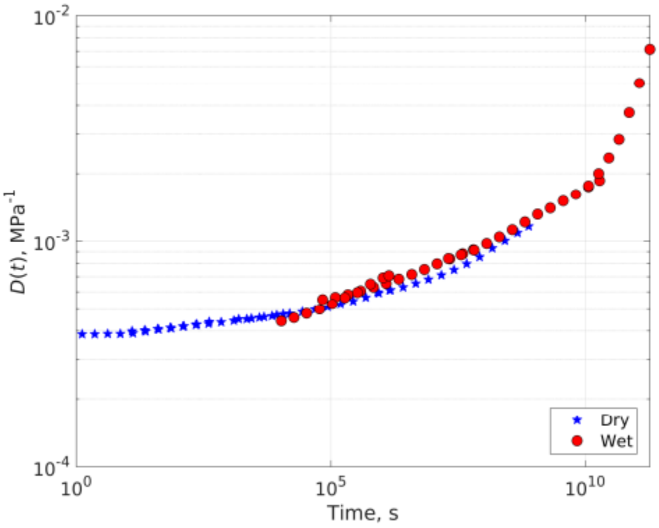

Figure 55. Master compliance curve of dry and aged epoxy. The dry material was set as a reference [138].

It is noteworthy that this superposition is merely an approximation, therefore an extrapolation for long-term exposures out of the temperature range used in the experiments is unreliable [124]. Moreover, TTSP principle does not work if there are other degradation processes. Regarding the test time needed, this principle works better with accelerated tests during a limited time, since for long-term exposures this method will generate multiple curves [124].

2.4.2.4. Pritchard and Speake Predictive Model

Pritchard and Speake [139] proposed a predictive model for the degradation of mechanical properties of polyester/glass fiber composites after immersion in water at a temperature range from 30 to 100°C, which includes temperatures higher than the composite's T_g (74°C). The authors demonstrated in their work that the properties' degradation is a function of the moisture content absorbed and independent of the immersion temperature, even at temperatures over the material's T_g.

According to Pritchard and Speake [139], the first step for prediction of material's properties would be the determination of the model that would best describe the composite's absorption behavior at the temperatures tested (Fickian or non-Fickian), as previously discussed. Then, from Arrhenius analyses (Figure 10), it would be possible to predict the absorption kinetic and the saturation level at temperatures out of the temperature range used. For example, the authors used a model similar to the Berens-Hopfenberg model (section 2.4.1.4), with a modification made to the term referred to the relaxation-caused absorption: $M_R =$

$M_{m,R}\left(1 - e^{-kt^2}\right)$, where k represents the relaxation rate. After plotting the curve *1/D vs. 1/T* and M_m *vs. T* for the test temperatures, they could predict both total moisture absorbed and the relaxation-induced moisture absorbed at 15°C, as well as the time required for them to be reached.

The second step is the development of empirical relationships between moisture absorbed and property retention. To do so, the authors conducted mechanical tests at the temperatures tested during aging and plotted the mechanical properties values *vs.* water content (Figure 56). This figure shows the independence of the degradation from the water content, although at higher water content the samples immersed at 60 and 70°C showed a stronger degradation than at other temperatures. The solid line was obtained from the average values of all temperatures [139].

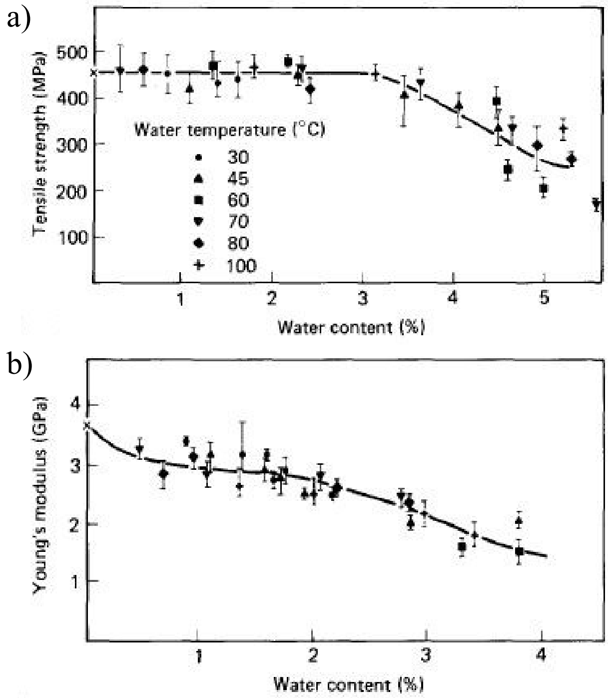

Figure 56. a) Unidirectional tensile strength of composite *vs.* water absorbed and b) Young Modulus of resin *vs.* water absorbed [139].

A curve fitting algorithm was used to compare the different shaped curves with the experimental results. The fitting pointed to a general empirical equation for this model:

$$p = a\left(1 - e^{-b\exp[-cM_t]}\right) + d \qquad (61)$$

where p is the residual property, M_t the moisture content at time t and a, b, c and d are empiric constants. This equation can be used to predict the residual mechanical properties at various temperatures [139].

2.5. Non-Destructive Testing (NDT)

Non-Destructive Tests (NDT) are of great importance for inspection of large and expensive components, as in aerospace, food, nuclear and offshore industries. The main goal of NDT techniques is to provide quantitative and qualitative defect characteristics from their detection, localization and dimensioning [140]. Among the most commonly used methods for defect detection, one can mention thermography, radiography, impulse excitation technique and ultrasound [84].

2.5.1. Impulse Excitation Technique

This technique uses the concept of acoustic emission (AE) to determine the dynamic elastic properties of the material from their natural vibration frequencies. A basic diagram of this technique can be found in Figure 57. The impulse excitation is originated by the application of a weak mechanical impact on the sample, generating a measurable mechanical vibration, but not too strong to damage the material [141]. The probe captures this vibration and, through a Rapid Fourier Transform calculation, obtains the frequency response function (FRF). The peak locations in the frequency response spectrum are identified as the natural frequencies of the specimen [142,143].

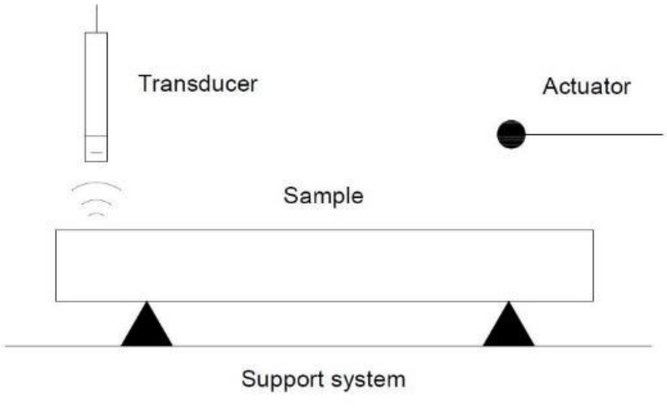

Figure 57. Diagram of a typical IET test [142].

The dynamic Young Modulus for rectangular test specimens can be then estimated to follow the following equation [141,144]:

$$E = 0.9465 \frac{m f_f^2 L^3}{b t^3} T_1 \qquad (62)$$

where E is the Young Modulus (Pa), m is the specimen's mass (g), b is the specimen's width (mm), L is the specimen's length (mm), t is the specimen's thickness (mm), f_f is the fundamental frequency for the specimen in flexural mode (Hz) and T_1 is a correction factor, defined as [141]:

$$T_1 = 1 + 6.585(1 + 0.0752\mu + 0.8109\mu^2)\left(\frac{t}{L}\right)^2 - 0.868\left(\frac{t}{L}\right)^4 - \left[\frac{8.340(1+0.2023\mu+2.173\mu^2)\left(\frac{t}{L}\right)^4}{1+6.338(1+0.1408\mu+1.536\mu^2)\left(\frac{t}{L}\right)^2}\right] \qquad (63)$$

, where μ is the Poisson's ratio.

In addition, the damping factor $tan(\varphi)$ is calculated from the relation between the loss modulus (E'') and storage modulus (E') (Equation 64) and measures the material's viscous contribution to its mechanical response [144]:

$$\tan(\varphi) = \frac{E''}{E'} \qquad (64).$$

Batista *et al.* [145] analyzed the shear and elastic moduli of PEI/carbon fibers composites using the impulse by excitation technique before and after exposing the samples to 90% RH at 80°C for eight weeks. They found out that the elastic and shear moduli decreased by 2.70% and 20.90%, respectively, after saturation. Cheour *et al.* [146] conducted acoustic test by impulse on flax fiber reinforced epoxy composite after immersion in tap water at room temperature for 180 days. The bending modulus presented a sharp decrease in the first 4-days exposure with subsequent slighter degradations until saturation. This was attributed to the plasticization and swelling of the natural flax fibers. Moreover, the loss factors of the composites increased with aging time. Paolino *et al.* [147] compared the IET results with the tensile tests performed on CFRP in two conditions: before (undamaged) and after the introduction of a damage (damaged). In the undamaged condition, the IET could accurately measure the Young modulus in comparison with the destructive tests. Some slight differences from the two techniques were attributed to the heterogeneity of the material. Conversely, in the damaged condition, there was a higher difference between the results of the techniques. Therefore, the IET provides an overall value for the property, which means that a very localized damage may not significantly change the overall Young modulus of the material according to the IET technique.

2.5.2. Colorimetry

The evaluation of the material's color change during aging is one of the most widely used methods to assess the material's degradation, since a color change may indicate the occurrence of chemical reactions in the polymer due to thermal-oxidation [148] and/or hydrolysis processes [149]. The former is related to chemical degradation of polymeric structures at high temperatures, which could lead to the increase in crosslink density and the embrittlement of the material [150]. Therefore, a correlation can be done between color change and structural degradation with aging time and temperature.

The color analysis was made by using the *Commision Internationale de l'Eclairage* (CIE) CIELAB color system. According to the CIELAB color system, there are three parameters for color, namely lightness ($L*$) and two chromaticity coordinates ($a*$ and $b*$). In this system, +$a*$ and –$a*$ denote red and green, respectively, +$b*$ and –$b*$ denote yellow and blue, respectively, and $L*$ varies from black (0) to white (100). Another important parameter to be calculated from the CIELAB system is the human perceptibility to color difference between objects. This is done by calculating the variable ΔE^*, which is calculated from the mean ΔL^*, Δa^* and Δb^* values for a set of specimens (Equation 65). For ΔE^* values lower than 1, the color difference is imperceptible to the human eye, for values between 1 and 3.3, it is perceptible to the trained eye and for values over 3.3, it is perceptible to everyone [151,152].

$$\Delta E^* = \sqrt{(\Delta L^*)^2 + (\Delta a^*)^2 + (\Delta b^*)^2} \qquad (65)$$

Among other renown non-destructive techniques for defect inspection in FRP, there are Ultrasound, Terahertz, Shearography and Microwave techniques.

2.6. Summary

In this chapter, the main water absorption mechanisms were reviewed and it is clear from the literature that water ingress into fiber-reinforced composites and their degradation mechanisms are very complex and involve numerous variables, like temperature, exposure environment, curing degree, nature of the polymer matrix and reinforcements, fabrication methods and material's T_g. Therefore, to investigate the absorption and degradation of the GFRP used in this work at different temperatures, the Fickian and non-Fickian models discussed in this chapter were implemented. In addition, post-curing and hydrolysis effects were assessed. An absorption model including post-curing effects was proposed, which has not been seen in the literature.

The volumetric and linear swelling bevahiors discussed in this chapter were investigated in the composite used in this work and similar results were observed. The orthotropy of the composite was evident. A Fickian-like model was proposed to estimate the swelling front penetrating the composite.

A methodology to predict the service-life of the repair at room temperature after long-term environment exposure was proposed based on accelerated aging tests. This methodology differs from those in literature, because it is more valid for long-term experimental results, rather than the short-term ones commonly found in the literature. Moreover, no property prediction under salt spray environment was found in previous works. This is particularly useful in real-life applications to predict the degradation level at low temperatures, which would be achieved experimentally at much longer time.

In this literature review chapter, it was also seen that the non-destructive techniques are widely applied in industry to monitor property loss and defects. Thus, the Impulse Excitation Technique (IET) and colorimetry tests were performed on the materials tested to monitor the effects of moisture and temperature on the material degradation.

3. Experimental Procedure

The methodology used basically consisted in the exposure of composite samples to a salt fog environment in order to periodically evaluate its physical and mechanical characteristics through destructive and non-destructive techniques. All samples were fabricated by a renowned offshore composite repair company in Brazil. The flowchart shown in Figure 58 summarizes the procedure used in the research, which will be explained in details in the following sections.

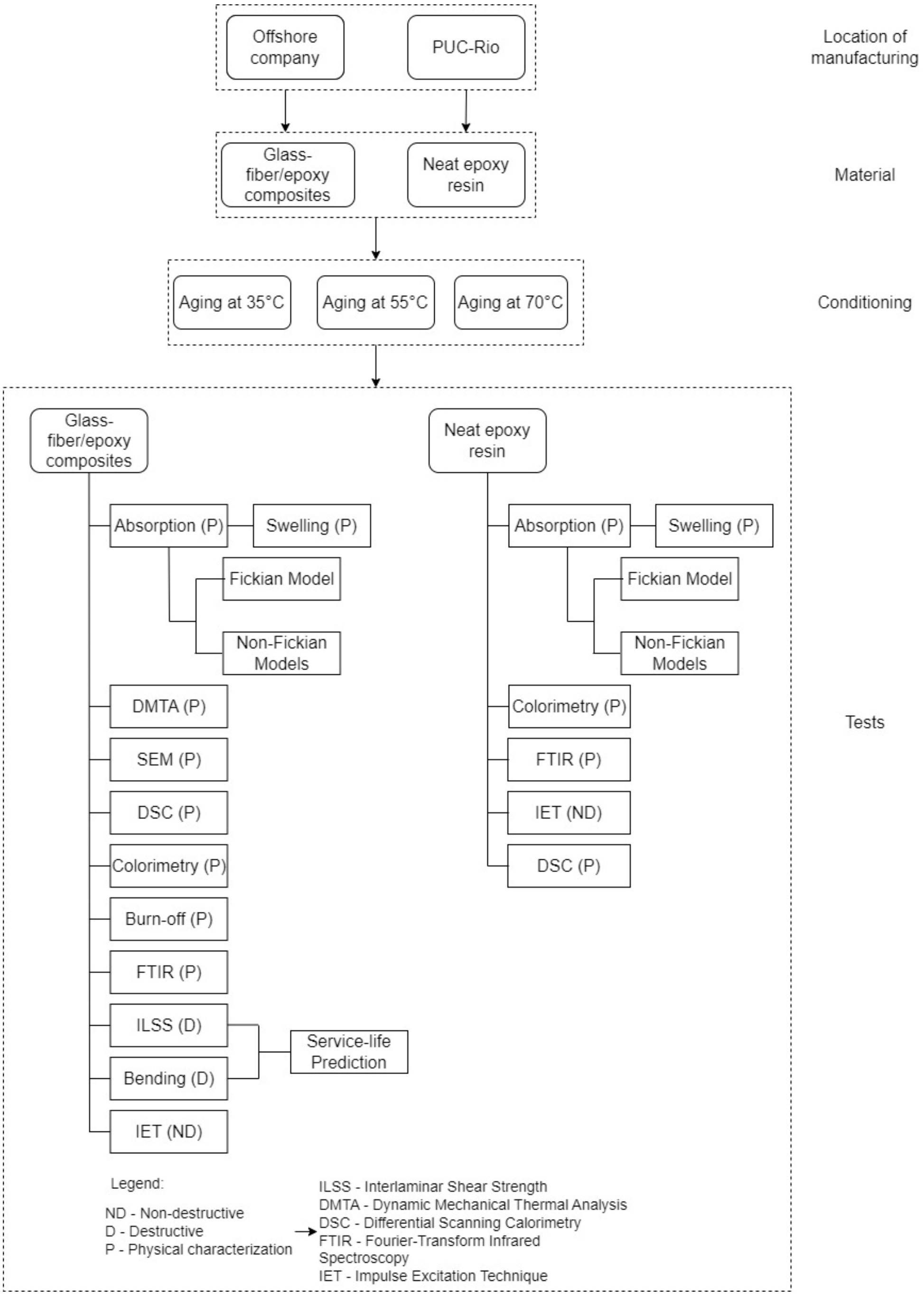

Figure 58. Flowchart of the experimental procedure used.

3.1. Materials

3.1.1. Composite samples

The composite used in this work was fabricated using the same fabrication method as the conventional composite repair systems (hand lay-up lamination), consisting in a bidirectional glass-fiber woven embedded to an epoxy matrix. The woven has a 2:1 weft (66% longitudinal fibers and 33% transverse fibers) and a weight of 365 g/m^2. The laminates consist of twenty epoxy + glass fiber layers, for a total nominal thickness of 6 mm. The typical properties of the glass fibers used are listed in Table 3 [153]. The glass fibers were fabricated by Owens Corning. According to a datasheet provided by the manufacturer, the glass fibers were coated with a type of sizing to improve fiber/matrix adhesion [154]. The nature of the sizing was not specified.

Table 3. Typical properties of the glass fiber used in the repairs [153].

Property	Unit	E-glass
Density	g/cm^3	2.55
Failure strain	%	2.00
Young modulus	GPa	72
Tensile strength	MPa	2000

A PIPEFIX bicomponent epoxy resin (Component A + Component B) was used. Component A is the DGEBA (*Diglycidyl ether of bisphenol A*) epoxy resin and component B consists of a polyamide-based hardener plus additives. This is a low-temperature cure resin, having a curing time of approximately 6 hours at 25°C. According to the Dynamic-Mechanical Thermal analysis (DMTA) results carried out by the manufacturer [153], this repair system has a T_g of 116°C.

The PIPEFIX repair laminates were initially fabricated in plates, and afterwards, they were cut in the PUC-Rio facilities in the desired samples' dimensions for each test. The manufacturing of the composites are detailed in Appendix A [155].

According to a report sent by the manufacturer, the cured laminate presented the characteristics listed in Table 4 [155]:

Table 4. Characteristics of the fabricated and cured laminates. These data were obtained from the Type Approval ABS process [155].

Property	Value	Unit
Each layer's thickness	0.30	mm
Circumferential Young Modulus (E_c) (longitudinal fibers direction)	23.10	GPa
Axial Young Modulus (E_a) (transverse fibers direction)	12.40	GPa
Poisson Coefficient (ν_{12})	0.16	——
Shear Modulus (G_{12})	3.75	GPa
Circumferential thermal dilation coefficient (α_c)	11.60×10^{-6}	$°C^{-1}$
Axial thermal dilation coefficient (α_a)	11.60×10^{-6}	$°C^{-1}$
Energy release rate (γ_{LCL})	146.44	J/m^2
Glass transition temperature (T_g)	116	°C
Cure time (25°C)	24	hours

Table 5 shows the cure parameters of the epoxy resin and its properties after the curing process [155]. The acceptable values follow a Qualification Certificate from the supplier company.

Table 5. Cure parameters and the mechanical properties of the cured DGEBA epoxy resin [155].

Cure parameters			
Temperature (°C)	**Application Time (min)**	**Initial Cure (Gelation) (min)**	**Functional Cure (hours)**
25	30	100	24
35	25	80	24
Cured epoxy properties			
Tests		**Acceptable Values**	**Measured Values**
Tensile Strength – ASTM D638 (MPa)		45 – 55	51.4
Hardness – ASTM D2240 (Shore D)		>70	75

3.1.1.1. Samples Fabrication

The samples to be fabricated and cut from the composite plates are destined to absorption, destructive and non-destructive tests described in Figure 58. The nominal dimensions of the samples for each test can be found in Table 6. All these dimensions follow the recommendations of the ASTM standard of the respective test. To obtain more reliable results, each actual dimension of each specimen was measured using a 0.01- mm precision caliper.

Table 6. Nominal dimensions of the composite's dimensions for the mechanical tests and the ASTM standard for each test.

Test	Width (mm)	Length (mm)	Nominal Thickness (mm)	ASTM standard
Absorption	25.4	76.2	6	ASTM D570
Bending	10	120	6	ASTM D790
Interlaminar Shear Strength (ILSS)	12	36	6	ASTM D2344
Dynamic-Mechanical Thermal Analysis (DMTA)	10	50	6	ASTM D4065

3.1.2. Epoxy samples fabrication

Epoxy resin samples were also fabricated aiming to study the effect of the addition of glass fibers on the material's absorption behavior from the comparison between the absorption curves of neat epoxy and composite. The samples were fabricated with the same dimensions specified in Table 6 for the composite absorption samples (76.2 mm x 25.4 mm x 6 mm).

To make these samples, a two-component silicon-based mold was produced with the aid of the composite samples for making the cavities (Figure 59). The mixture of the DGEBA bicomponent epoxy in a mass ratio of 5.7A:1B was poured in the mould's cavities and cured at room temperature (23 ± 2°C) for 24 hours.

In addition to the periodic weight measurements, the specimens' dimensional changes were also measured as a function of the exposure time in order to evaluate the swelling behavior of the materials.

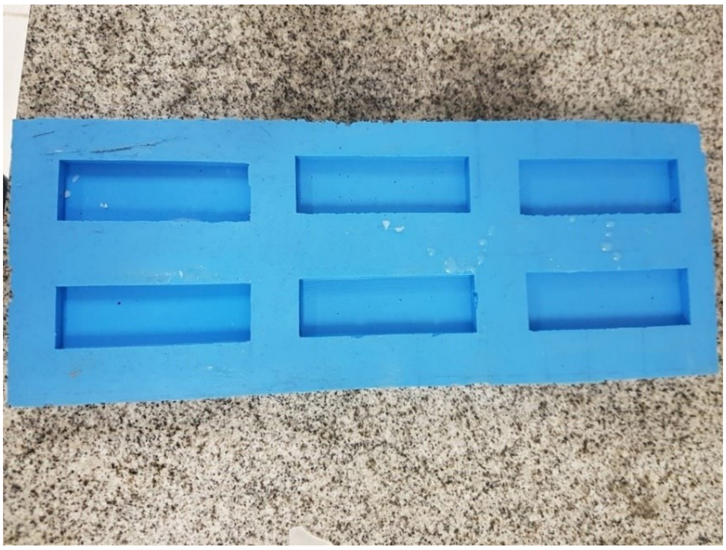

Figure 59. Silicon mold used to fabricate the epoxy specimens for absorption tests.

3.2. Methods

3.2.1. Aging

The composites and epoxy samples were subjected to aging using three independent salt spray (SS) heating chambers EQUILAM SSEQ-Walk-In (Figure 60), working at temperatures of 35°C, 55°C and 70°C. All the temperature values adopted are higher than room temperature so as to accelerate the hygrothermal aging of the materials (Accelerated Arrhenius Aging Methodology [111]). For practical purposes, a terminology was adopted for each chamber: Chamber A (35°C), Chamber B (55°C) and Chamber C (70°C) (Figure 60). The salt concentration in the solution used for the SS chambers was 5.0 wt%, according to the recommendations of ASTM B117 standard [156].

Figure 60. Salt-spray chambers and identification adopted.

Figure 61 shows the moving average of the daily temperature variation of each chamber during the total duration of the aging test. The temperature drops and the gaps in the graph represent the occasional openings of the chambers and failure in the heating element, respectively. The latter occurred especially in chamber C, resulting in a momentary decrease in the aging temperature. Despite this, during these periods the chambers were kept closed so that the moisture concentration inside the chambers would remain constant, so the aging continued during these interruptions. After approximately 7000 hours of aging, the temperature inside Chamber C decreased to nearly 60°C and operated at this temperature throughout the rest of the aging, due to limitations of the heating resistance, decreasing the maximum operational temperature of this chamber. However, the nominal temperature adopted for Chamber C herein is 70°C.

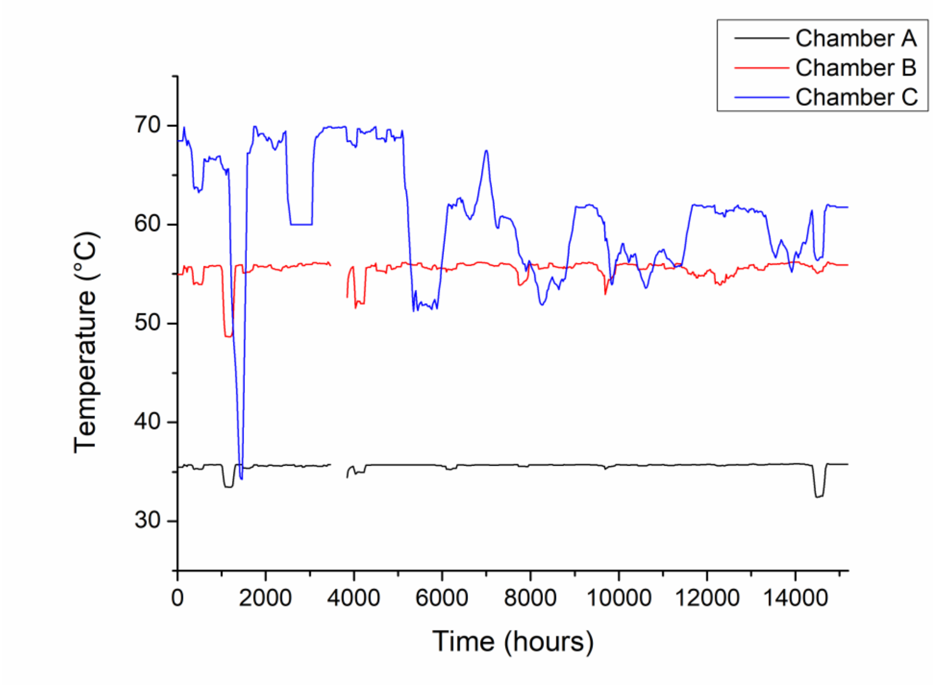

Figure 61. Moving average temperature *vs*. time graphs for the aging chambers.

Whenever the chambers were opened, the NaCl solution was collected and its pH was measured, according to the methodology described by the ASTM B117 standard [156]. It was thus verified that the pH was maintained within the optimal pH range recommended by the standard, which is from 6.5 to 7.2.

3.2.1.1. Absorption Test

In total, three different groups of samples were subjected to absorption test: the composites, the neat epoxy and the composites with the edges coated with epoxy resin. The latter group was fabricated in order to simulate the practice adopted by repair industries, which is the coverage of the exposed edges with hydrophobic painting. The epoxy applied on the edges was the same one used to fabricate the neat DGEBA epoxy and the composite (section 3.1.1). The epoxy was mixed and manually applied to the edges with a wooden stick. In summary, it was evaluated whether the application of epoxy on the samples' edges hindered the diffusion through the edges, limiting it to the through-thickness direction. Each group of absorption specimens consisted of three specimens for each chamber. Figure 62 shows the pictures of a schematic figure showing the specimens' nominal dimensions, the composite and the neat epoxy.

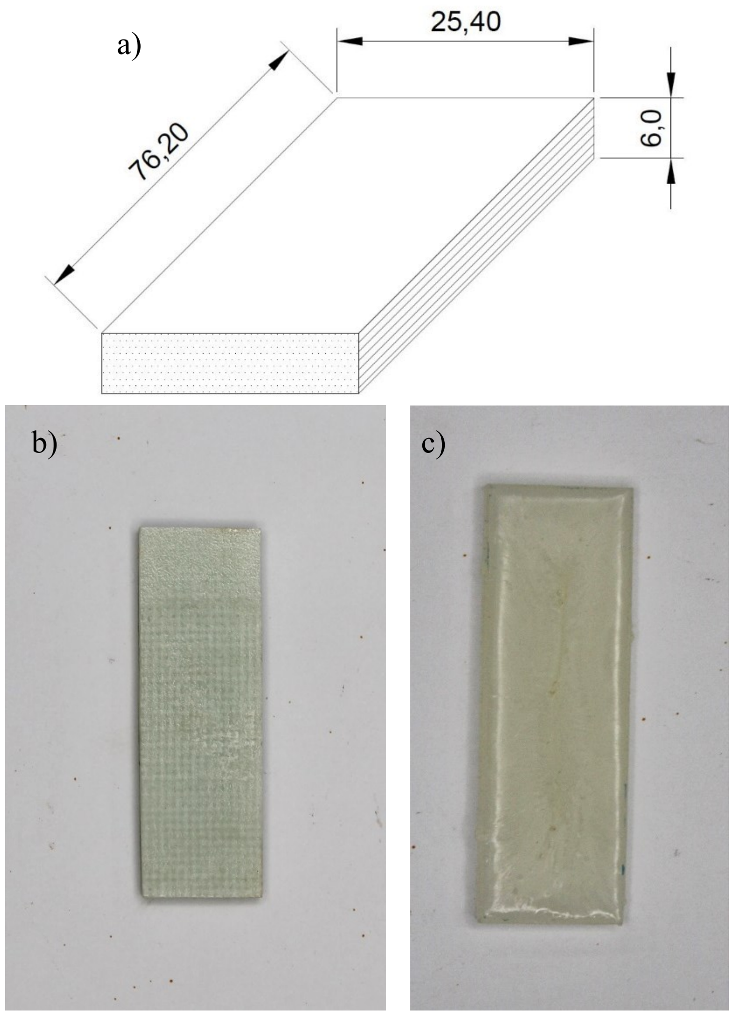

Figure 62. (a) Schematic figure showing the dimensions of the absorption specimens, (b) an uncoated FRP specimen and (c) a neat epoxy specimen.

Table 7 summarizes the materials whose weight gain was measured, as well their quantities and dimensions to be adopted in this work. Each sample in Table 7 had its dimensions and masses measured before they were introduced in the chambers, i.e., the unaged condition. During aging, the samples were periodically weighted and measured to assess their moisture absorption following the gravitational method (Equation 1) and following the ASTM D570 standard [157] within the period of 15171 hours (~21 months) of aging. The first weight gain acquisition was obtained after 570 hours of aging, and then periodically in each two weeks. The weighting was performed using an analytical balance GEHAKA AG200 (Figure 63) with the precision of 0.0001 g. Following the standard's recommendation, the samples had their surfaces softly wiped immediately before being weighted in order to remove the superficial moisture. Besides, the samples were wrapped up in a plastic film immediately after being taken out of the chambers and transported to the balance in order to minimize desorption.

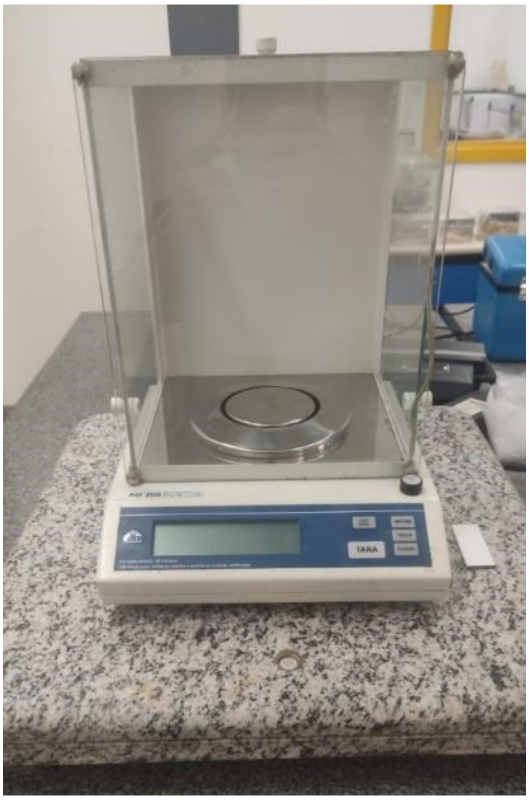

Figure 63. Weighing balance used int he gravimetric tests.

Table 7. Terminology, dimensions and number of specimens of each material designated for the weight gain test.

	Material	**Number by chamber**	**Total number**	**Dimensions (l x w x t) (mm x mm x mm)**
Epoxy/Glass Fiber composite	FRP	3	9	76.2 x 25.4 x 6
Epoxy/Glass Fiber + Epoxy coating on edges	Coated FRP	3	9	
Neat Epoxy resin	Epoxy	3	9	
Total			**27**	

The dimensions of these samples were also measured in order to assess the swelling behavior of the composite using the equations 18 and 19 for the calculations. Dimensional changes were measured using a Mitutoyo caliper with an accuracy of 0.01 mm, with the same periodicity as the weight measurements.

3.2.2. Destructive Tests

In order to measure the influence of the hygrothermal aging on the main mechanical properties of the composite and couple this degradation with the moisture content absorbed, destructive tests were performed in the GFRP specimens.

The destructive tests were performed in according to the schedule shown in Table 8, where the letter *R* in the terminology column stands for round. The destructive tests were performed within the period of 10170 hours (~14 months) of aging.

Table 8. Aging times for the destructive tests.

Terminology	Aging time (hours)	Aging time ($h^{1/2}$)
R0	Unaged (0 h)	0 $h^{1/2}$
R1	570 h	23.87 $h^{1/2}$
R2	1820 h	42.66 $h^{1/2}$
R3	3490 h	59.07 $h^{1/2}$
R4	5160 h	71.83 $h^{1/2}$
R5	6830 h	82.64 $h^{1/2}$
R6	8500 h	92.19 $h^{1/2}$
R7	10170 h	100.85 $h^{1/2}$

The destructive tests performed on the composites were:

- Bending ASTM D 790 [158] (15 specimens/temperature/aging period);
- Interlaminar Shear Strength (ILSS) ASTM D 2344 [159] (15 specimens/temperature/aging period);

Table 9 summarizes the total amount of composite samples for each test and for each removal from the chambers, in addition to the initial ones (unaged). All tests were performed at room temperature (25 ± 2°C).

Table 9. Number of laminate specimens designated for the destructive mechanical tests.

	Bending	ILSS
Samples/aging period	15	15
Chambers	3	3
Aging Periods	7	7
Unaged	15	15

Total	**330**	**330**

3.2.2.1. Bending Test

The three-point bending tests were performed on a universal testing machine MTS 810-500 with a servo hydraulic actuator with a capacity of 500 kN, shown in Figure 64. A total of 15 tests, according to the ASTM D790 standard [158], were performed in the composite specimens after each aging period and in the unaged condition. The tests were performed at room temperature at a displacement rate of 2.4 mm/min. The span-to-thickness ratio used for all bending tests was 16:1, as recommended by the ASTM D790 standard. A 10 mm displacement transducer and a 2.5 kN load cell were used as external instrumentation.

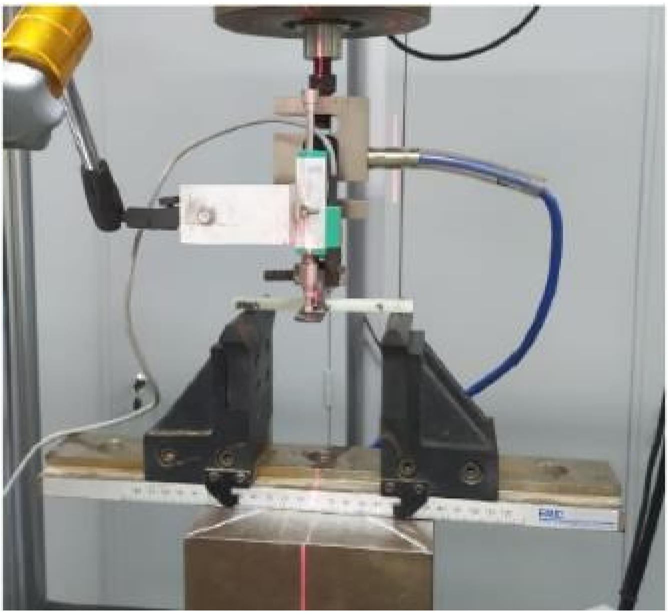

Figure 64. Experimental setup of three-point bending test.

To identify the samples to be tested, a standard terminology was established referring to the conditioning time and the sample identification number. The characters used are described as follows:

- First number: aging period identification (0 for the unaged specimens);
- A, B and C: indicate in which chamber the specimen is being aged (A = 35°C, B = 55°C and C = 70°C);
- Letter *M*: indicate the manufacturer;
- Last number: specimen's identification number.

For example, sample *1BM-2* refers to the specimen number 2 tested after the first aging period in the hygrothermal aging chamber at 55°C.

3.2.2.2. Interlaminar Shear Strength (ILSS) Test

The ILSS tests were performed using a servo hydraulic actuator MTS 810-500 with capacity of 500kN at a displacement rate of 1 mm/min (Figure 65). A total of 15 tests, ruled by the ASTM D2344 standard [159], were performed in the composites specimens after each removal and in the unaged condition.

A 26-mm span was used between the supports and no displacement instrumentation was used.

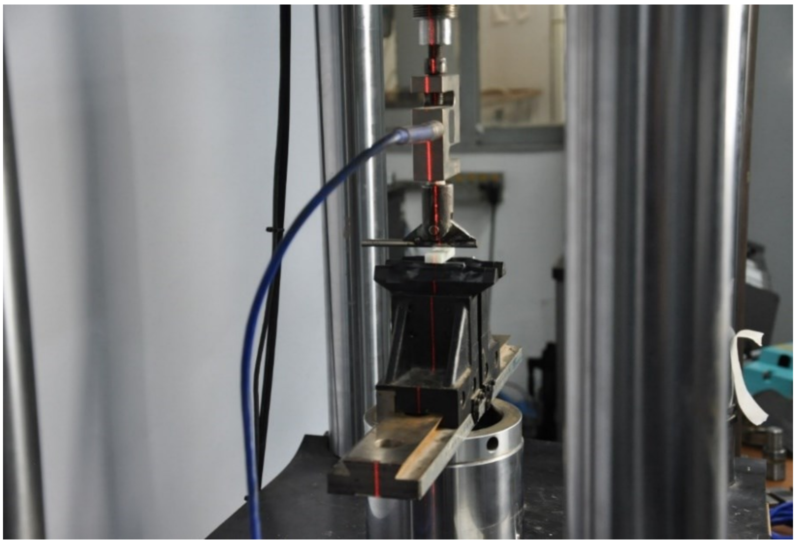

Figure 65. Experimental setup of ILSS test.

3.2.3. Physical Characterization

3.2.3.1. Dynamic Mechanical-Thermal Analysis (DMTA)

To evaluate the T_g values of the composites, DMTA analysis was performed in a three-point bending configuration with a frequency of 1 Hz and a heating rate of 5.0°C/min with the temperature ranging from 20°C to 150°C under constant N_2 flow. The tests were conducted using a Q800 T.A. Instruments DMTA equipment. Additionally, it was possible to evaluate the elastic and viscous contribution to the material's performance by assessing the storage modulus (E'), loss modulus (E'') and tan δ.

The DMTA analyses were performed following recommendations of the ASTM D 4065 standard [160]. For the unaged tests three composite samples were used, while for the aged composites, one specimen for each chamber for four aging periods (R1 – R4) were used.

3.2.3.2. Differential Scanning Calorimetry (DSC)

To validate the T_g values of the unaged composite found by the DMTA analysis, DSC analysis was performed. Additionally, the same as-manufactured composite specimen analyzed was aged in an oven for eight days at 85 ± 5°C aiming at the analysis of a possible post-cure suffered by the material.

The DSC analyses were performed using a Perkin-Elmer Simultaneous Thermal Analyzer STA 6000 (Perkin-Elmer, Waltham, MA, USA) under N_2 flow (20 mL min^{-1}) at heating rate of 5°C/min in the temperature range of 25-200°C.

3.2.3.3. Burn-off Test

In order to better assess the volume fractions of fibers, matrix and voids, a burn-off test was carried out. The muffle furnace used was a Nabertherm L 3/12 and the temperature range used in the test was from 27 to 450°C in order to degrade solely the epoxy matrix. The tests followed the recommendations of the ASTM D3171 standard [161]. They were weighted before and after the matrix digestion. The sample dimensions were also measured, using a caliper with 0.01 mm accuracy, in order to estimate the densities of the composites. Three unaged specimens were used in the analyses and their dimensions were the same as those of the DMTA specimens.

The initial and final mass of the specimen, along with the constituents' densities and the estimated composite density were introduced in equations 66 to 68 to calculate the volume fraction of the fibers (V_f - Eq. 66), matrix (V_m – Eq. 67) and voids (V_v – Eq. 68), following the Procedure G described by ASTM D3171 [161]. In these equations, V is the volume fraction of the constituent, M is the mass, ρ is the density and the subscripts f, m and v refer to fiber, matrix and void, respectively.

$$V_f = \left(M_f/M_i\right) \cdot 100 \cdot \rho_c/\rho_f \tag{66}$$

$$V_m = \left(M_i - M_f\right)/M_i \cdot \rho_c/\rho_m \cdot 100 \tag{67}$$

$$V_v = 100 - \left(V_f + V_m\right) \tag{68}$$

3.2.3.4. Scanning Electron Microscopy (SEM)

The fibers distribution in the composites was analyzed with a Hitachi TM3000 SEM microscope (Hitachi, Japan) with electron beam energy of 15 kV. The dry samples used in this test were the remaining from the cutting process of the bending specimens due to their small size (10mm x 15mm). The samples' surfaces were sanded and polished to produce a smooth and clean surface prior to SEM imaging.

This analysis allowed the assembly of images along the thickness of the sample to evaluate the distribution of fibers in the composite. Moreover, the fiber, voids and matrix volume fractions could be estimated from image segmentation. The ratio between longitudinal and transverse fibers could also be calculated. Additionally, the visual quality of the fiber/matrix was evaluated.

3.2.3.5. Fourier-Transform Infrared Spectroscopy (FTIR)

A FTIR analysis was performed on the unaged and 11550-hours aged FRP and epoxy materials in order to characterize the changes made to the chemical structure of the materials by aging, like moisture sorption, hydrolysis and post-cure.

The FTIR analysis was run on a Bruker Alpha II spectrometer scanning the average infrared region between 4000 and 400 cm^{-1} in the Analytical Center of the Chemistry Department at PUC-Rio. All samples were analyzed in the solid form. The aged specimens were removed from the aging chambers, weighted and taken to the laboratory for analysis. The analysis was performed with the ATR accessory, with 31 scans/min.

3.2.4. Non-Destructive Testing (NDT)

The NDTs were used as complementary tests to monitor the progress of degradation, corroborating then with the results from the destructive tests.

The non-destructive tests performed were Impulse by Excitation Technique and Colorimetry.

3.2.4.1. Impulse Excitation Technique (IET)

As explained earlier, the IET test is a non-destructive technique of impulse excitation, which allows the determination of elastic coefficients, like Dynamic Young Modulus, from the natural vibration frequency of the sample. This technique follows the recommendations of ASTM E1876 standard [141]. This test consists of the excitation of the specimen by means of a slight mechanical impact made by an actuator, generating vibration frequencies that are captured by a sensitive microphone. Afterwards, the signal captured is decoded by a software that, through Fast Fourier Transform, obtains the frequency spectra. Then, from equations relating the frequencies and material’s dimensions and weight, the software determines the material’s dynamic properties, such as damping factor (*tan δ*), shear modulus and Young modulus.

The IET test was performed using a *Sonelastic*® equipment (Figure 66). The samples used for this test were the bending FRP specimens and absorption neat epoxy samples. For the FRP samples, the measurements were periodically taken before the destructive bending tests and the measurements on the neat epoxy specimens were taken after their withdrawal from the heating chambers. At least 20 measurements were taken from each specimen at laboratory temperature (23 ± 2°C). In this work, focus was given on the determination of the Young’s Modulus and tan δ, whose equations were described in Section 2.5.1.

Figure 66. *Sonelastic*® equipment used for IET test.

3.2.4.2. Colorimetry

The external surfaces of the absorption samples were analyzed with a DeltaVista 450G colorimeter from *DeltaColor*. The data were taken from at least five different points of each sample. The parameters obtained in this test are *L*, *a* and *b*, which denote lightness (black – white), the spectrum red – green and the spectrum yellow – blue, as explained in Section 2.5.2. Afterwards, these parameters of the aged specimens are compared with those of the unaged ones and Equation 65 (Section 2.5.2) is applied to determine the parameter ΔE, which indicates the magnitude of the material’s color change, indicating some ongoing process, like thermal-oxidation, for example.

The measurements were taken in five aging times, namely: unaged, 672 hours, 2535 hours, 10149 hours and 15171 hours.

4. Results

4.1. Unaged Composites' Characterization

4.1.1. Assessment of composite's fiber volume fraction

From the SEM analysis, it was possible to assess the fibers' distribution within the composite. Several images were taken from both longitudinal and transverse directions for segmentation purposes. Moreover, an assembly was made with the images across the thickness. Figure 67 shows the schematic figure of the fabric in the composite, as well as sample images taken in each direction. From these images, it is visible that the fabric used is a plain woven-type, since longitudinal and transverse fibers are interlaced.

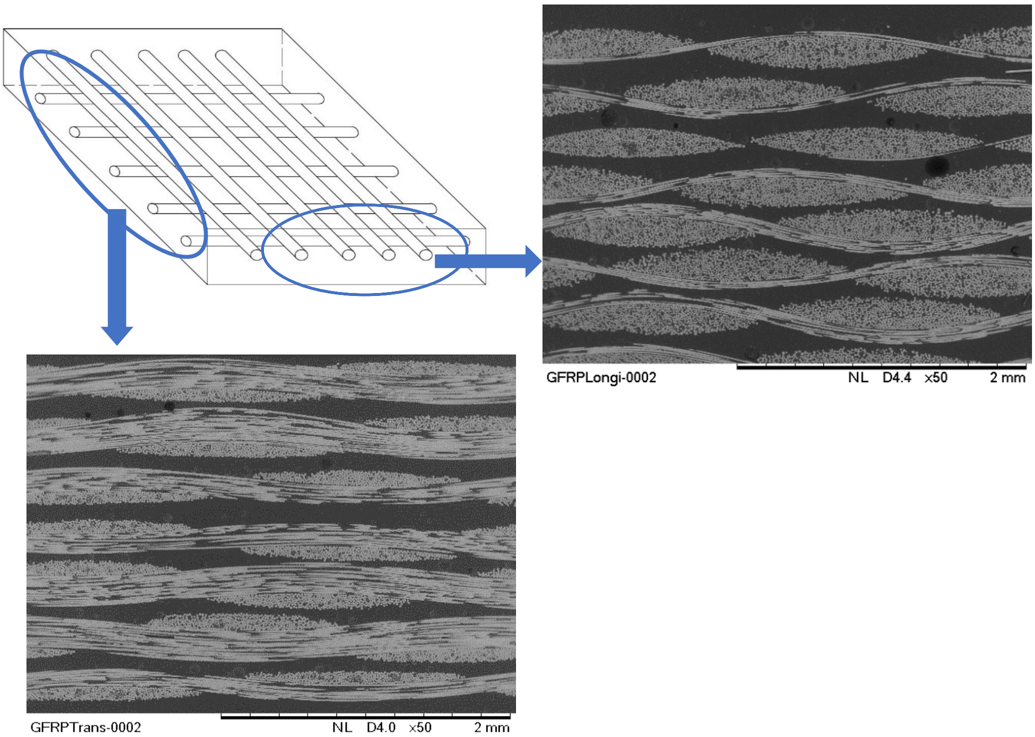

Figure 67. Schematic figure of the fibers' distribution in the composite (top left), longitudinal view of the fibers (top right) and transverse view of the fibers (bottom left).

In order to take a single picture of the full thickness of the composite, which would show the twenty layers of the fibers, three images were captured along the material's thickness in the longitudinal direction using a magnification of 50x. With the aid of a software called Fiji ImageJ® [162], it was possible to stich the images into one, using its unique feature to find the patterns the images have in common. Figure 68 shows the composite in the through-thickness direction. The twenty layers of glass fibers embedded in the epoxy matrix, although the 13th and 14th layers were overlaid probably due to a bad pattern in the shared top and middle images.

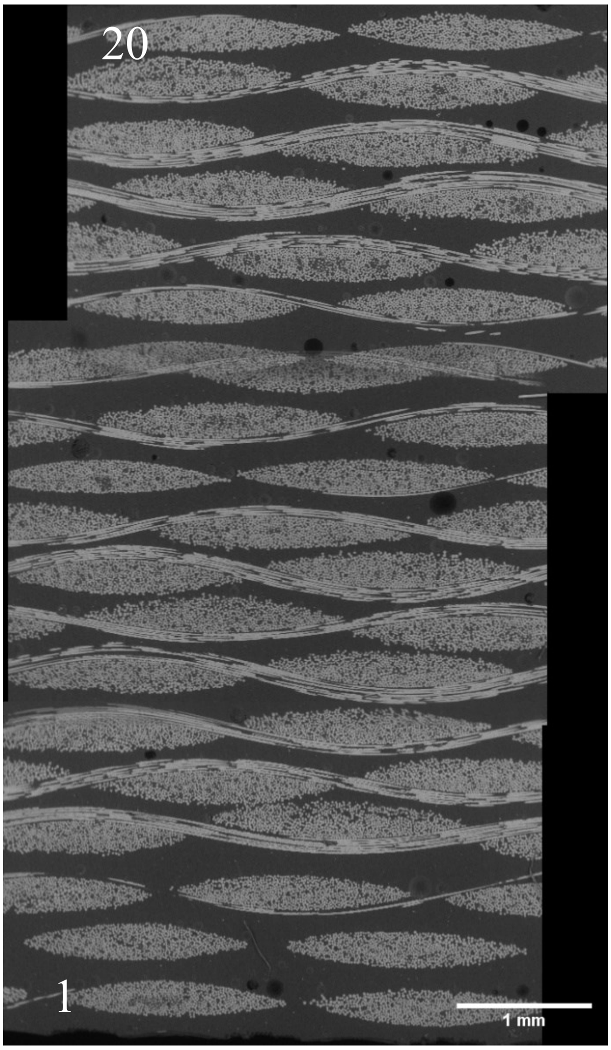

Figure 68. Image of the fibers disposition through the composite's thickness.

Since the manufacturer did not provide the glass fiber volume fraction used in the fabrication of the composites, it is necessary to calculate this property. A practical way to assess the fiber fraction in the material is from the mixture rule for density (Equation 69), where ρ_c is the composite's density, ρ_m is the matrix's density, ρ_f is the fiber's density and V_f the fiber volume fraction.

$$\rho_c = \rho_m(1 - V_f) + \rho_f V_f \tag{69}$$

From the weighting and measurement of the absorption samples' dimensions, it was possible to obtain the apparent density of both composite and epoxy resin. The fiber's density can be found in Table 3. Table 10 shows the average values and standard deviations of the weight, volume and density of unaged absorption composite and epoxy samples. Therefore, it can be established that, since all composite samples are made of the same material, the composites' density is 1.71 g/cm^3 and epoxy's density is 1.06 g/cm^3.

Table 10. Average values and standard deviations of the weight, volume and apparent density of absorption composites and epoxy samples measured from three specimens each.

	Material	Weight (g)	Volume (cm^3)	Density (g/cm^3)
Chamber A (35°C)	FRP	22.23 ± 0.26	12.97 ± 0.21	1.71 ± 0.01
	Epoxy	13.55 ± 0.50	12.67 ± 0.17	1.07 ± 0.03
Chamber B (55°C)	FRP	22.35 ± 0.10	13.07 ± 0.04	1.71 ± 0.002
	Epoxy	13.55 ± 0.86	12.68 ± 0.16	1.07 ± 0.05
Chamber C (70°C)	FRP	22.28 ± 0.09	13.01 ± 0.13	1.71 ± 0.01
	Epoxy	13.41 ± 0.56	12.89 ± 0.24	1.04 ± 0.03
Average	**FRP**	**22.29 ± 0.18**	**13.02 ± 0.15**	**1.71 ± 0.01**
	Epoxy	**13.51 ± 0.67**	**12.74 ± 0.22**	**1.06 ± 0.04**

Then, by applying the average values for the constituents' densities in Equation 69, the fiber volume fraction was found to be 43.62%.

However, this procedure does not take the void volume fraction into account. Therefore, image processing and segmentation was considered to be more reliable. Thus, eight SEM images were taken from both sample directions with magnifications ranging from 50x to 150x. It was possible to quantify the fiber fraction in both directions and, therefore, in the whole material.

As the SEM analysis generates 2D surface images, their segmentation results in the superficial area fraction. Then, considering the surface distribution to be homogeneous throughout the specimen and all the fibers to have the same length, it can be shown that the volume fraction is the same as the cross-sectional area fraction, as explained by equations 70 to 74, where $\%V_{f,L}$ is the longitudinal fiber volume fraction, v_f the fibers' volume, v_c the composite's volume, A_c the composite's surface area, A_f the fiber's cross-section area, $n_{f,L}$ the number of longitudinal fibers and l the composite's length. Similarly, the same logic was used to calculate the transverse volume fraction and the void volume fraction.

$$\%V_{f,L} = \frac{v_f}{v_c} \tag{70}$$,

$$\%V_{f,L} = \frac{A_f \cdot n_{f,L} \cdot l}{A_c \cdot l} \tag{71}$$,

$$\%V_{f,L} = \frac{A_f \cdot n_{f,L}}{A_c} \tag{72}$$,

But $\%A_{f,L} = \frac{A_f \cdot n_{f,L}}{A_c}$ (73).

Therefore,

$$\%V_{f,L} = \%A_{f,L} \tag{74}$$.

The result obtained for the longitudinal and transverse fiber fractions were 27.64 ± 1.67% and 13.39 ± 2.40%, respectively. Therefore, the longitudinal/transverse ratio is 2.06, which confirms the woven fiber ratio given by the manufacturer (2:1). Since the total fiber volume within the composite is equal to the sum of the fiber volume in each direction, the composite's fiber volume fraction follows the same relation. Then, $V_f = 41.03 \pm 2.93\%$. Therefore, it can be concluded that both techniques used to quantify the material's composition resulted in similar results, with the images segmentation considering the voids fraction.

Similarly, segmenting the voids and flaws in the material (black areas in Figure 69) with eleven selected images taken from both directions with magnification varying from 50x to 300x, the voids volume fraction was found to be 1.06 ± 0.59%.

Regarding the fiber/matrix interface in the unaged composites, it can be seen from Figure 69 that, apparently, the fibers are well-adhered to the matrix, probably indicating a good interface adhesion, with few imperfections (microcracks), indicated by the yellow arrows. Moreover, the fibers surfaces are slightly damaged, probably caused by the surface preparation methods, such as grinding.

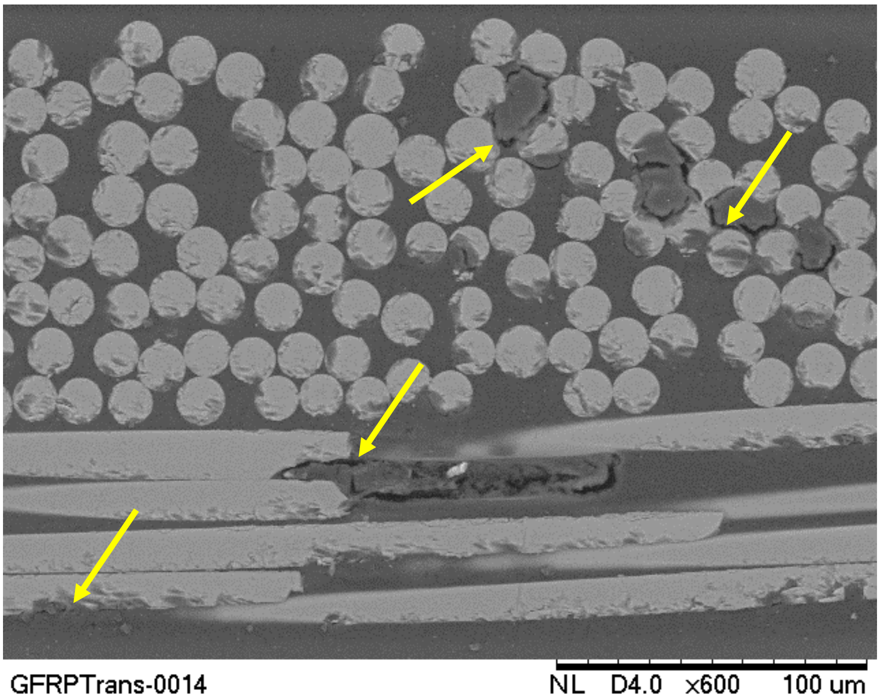

Figure 69. SEM picture of the dry composite indicating good interface adhesion.

Table 11 shows the burn-off results with the average and standard deviations values of the fibers (V_f), matrix (V_m) and voids (V_v) volume fractions calculated with Equations 66 – 68. It can be seen that, indeed, the previous two methods of determining the composite's contents are accurate, given that the fiber fraction found in the burn-off test is within the experimental error of the other techniques. However, the void volume fraction was found to be negative, which indicates an experimental error, perhaps due to the presence of some residual matrix in the burned specimen, due to to the low maximum temperature used (450°C). Thus, the fiber volume fraction to be used throughout the study will be $V_f = 41.03 \pm 2.93\%$, obtained from the SEM analysis. Consequently, the matrix volume fraction is $V_m = 57.91\%$.

Table 11. Burn-off results on the composites.

V_f (%)	**V_m (%)**	**V_v (%)**
42.72 ± 3.60	58.81 ± 8.66	-1.53 ± 5.06

4.1.2. Thermal Properties

With respect to the thermal properties of the composites, DMTA analysis was performed in three samples of the unaged material following the description in Section 3.2.3.1. The results can be found in Figure 70. Unlike the T_g value provided by the composite supplier (116°C [153]), the T_g value found fits in the range 86.7 – 100.2°C, according to the tan δ peak values, indicating that either the composites were not fully cured or the information provided by the supplier was not accurate.

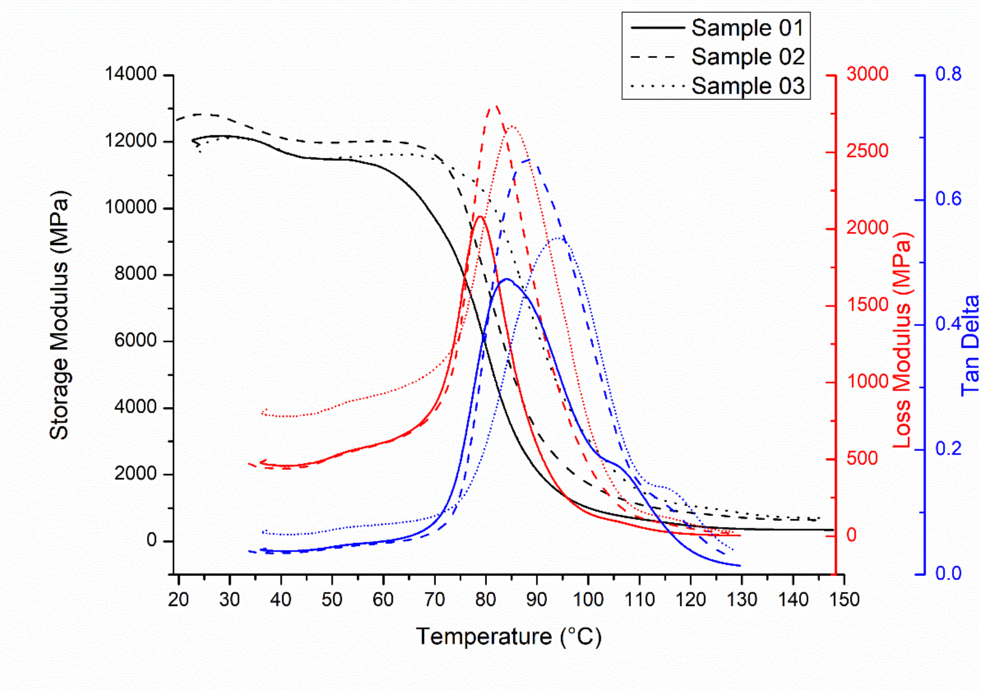

Figure 70. DMTA analysis of the dry composite materials.

To investigate the curing degree of the as-manufactured composites, a DSC analysis was undertaken before and after subjecting the material to aging in an oven for eight days at 85 ± 5°C. Figure 71 shows the endothermal heat flow *vs.* temperature plots for the as-manufactured FRP specimen (Figure 71a) and the post-cured one (Figure 71b). The same specimen was used for both analyses. The curves do not show a clear peak, as it is expected from a traditional DSC curve for thermoset polymers [30], which may be attributed to the overshadowing caused by the fibers content on the test resolution. However, it was still possible to notice a subtle change in the curve slope of the uncured specimen (Figure 71a) at ~79.39°C, which would be assigned as the material's T_g. An inset is shown in both graphs in Figure 71, showing two tangent lines (colored); the intersection of these lines leads to the determination of the T_g. This value is lower than the temperature range found in the DMTA analysis (Figure 70), however is close to the lowest T_g value found from DMTA (86.70°C). Considering that different specimens were used in the techniques, it can be inferred that the value of 79.39°C is within the experimental range. After the exposure to 85°C, the specimen showed an apparent T_g of

128.48°C, an increment of 61.83%, corroborating with the previously presented hypothesis that the as-manufactured composites were not fully cured before exposure to hygrothermal aging. This means that after exposure to high temperatures (55 and 70°C) in the aging chambers the composites will likely undergo post-cure, particularly in the first days of aging, and later, moisture-induced plasticization.

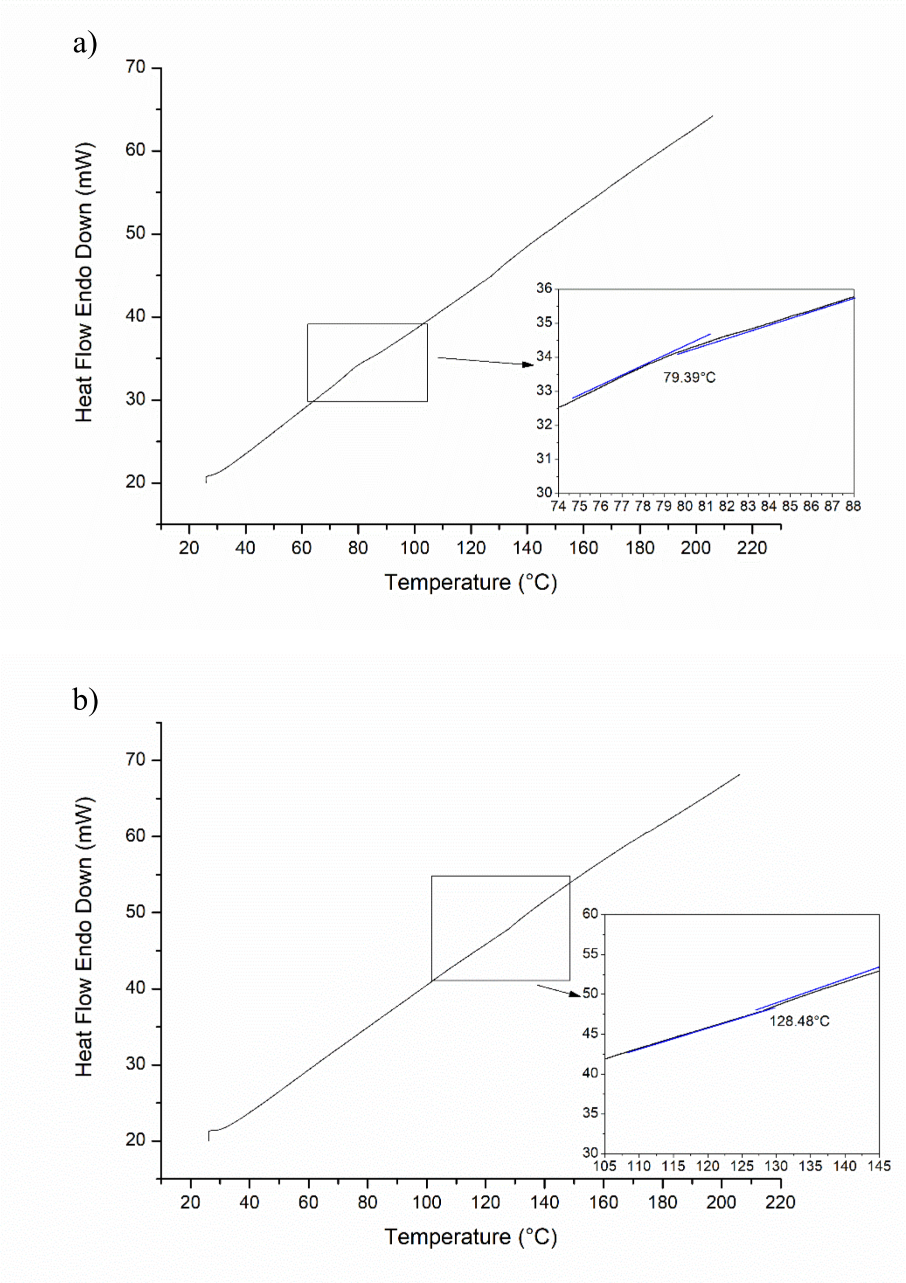

Figure 71. DSC curve for the (a) unaged as-fabricated and (b) post-cured FRP.

Considering the low resolution on the peaks in the DSC spectrograms above, a DSC test was also performed on the neat epoxy resins to investigate the test's accuracy. Furthermore, the effects of temperature on the post-curing of the neat epoxy system were analyzed. The neat epoxy sample was subjected to the same temperature aging as the FRP specimen. Figure 72 shows the DSC curves for the as-fabricated (Figure 72a) and the post-cured (Figure 72b) neat epoxy systems. Indeed, there was a depreciation of the DSC signal in the results shown in Figure 71, since the T_g peaks are much more noticeable for the neat epoxy resin (Figure 72). Furthermore, the effects of post-curing can also be seen for the neat epoxy, since there was an increase from 71.79°C to 119.18°C after exposure to temperature, an increase of 66.01%.

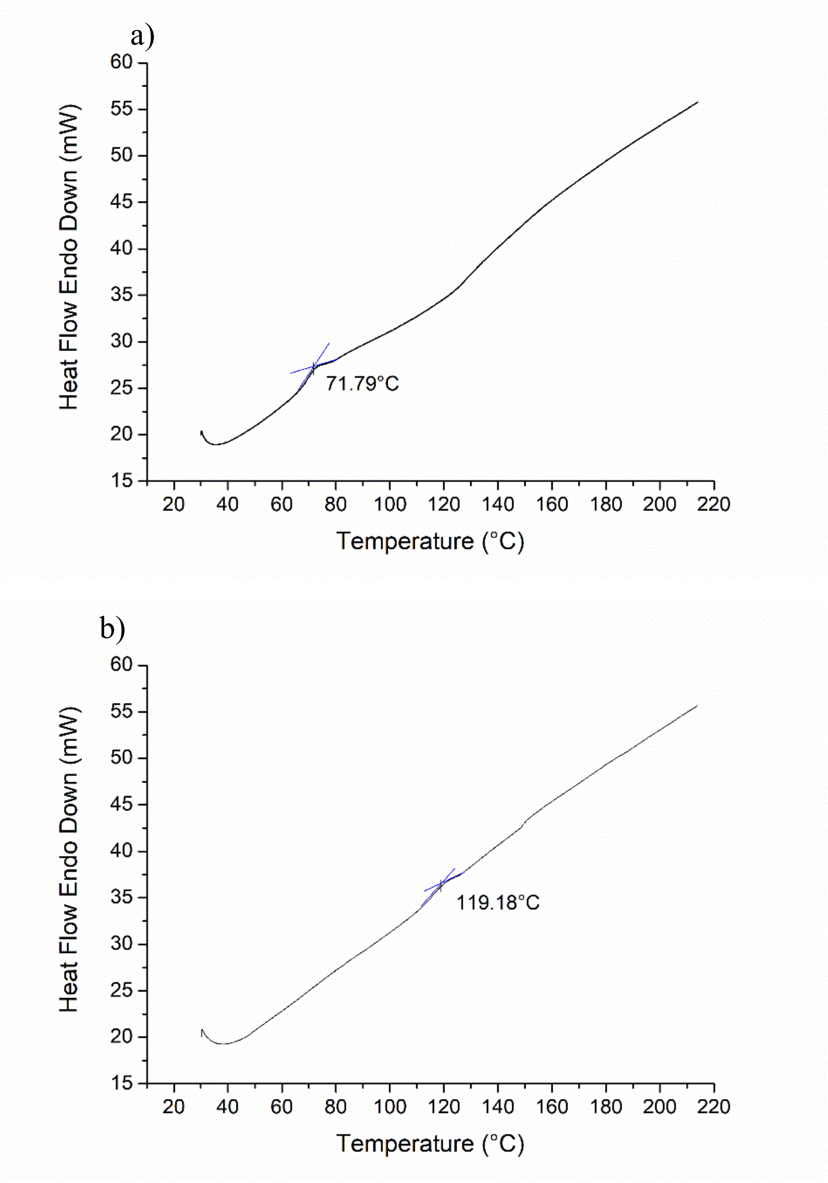

Figure 72. DSC curve for the (a) unaged as-fabricated and (b) post-cured neat epoxy system.

It is noteworthy that the FRP presented a higher T_g value in both as-manufactured (79.39°C for the FRP and 71.79°C for the neat epoxy) and post-cured conditions (128.48°C for the FRP and 119.18°C for the neat epoxy). This increase in T_g with the addition of fibers has already been reported in literature [163,164] and is credited to the restriction of the matrix relaxation process imposed by the fibers owing to the increase in the number of chain segments.

4.1.3. Fourier Transform Infrared Spectroscopy (FTIR)

Figure 73 shows the infrared (IR) spectroscopy of the unaged neat epoxy and FRP specimens. It is noteworthy that both spectra are nearly the same, except that the peaks in the epoxy specimen are stronger due to the lower matrix fraction in the composites. A broad peak can be spotted in the wavenumber range 2997 – 3600 cm^{-1} in both specimens, which is the stretching vibration of hydroxyl groups (-OH) present in amine-cured DGEBA epoxy systems, which can be associated with the presence of alcohol, amine or carboxylic acid [165,166]. It can be seen that the hydroxyl maximum peak was shifted from 3313 cm^{-1} on the epoxy specimen to 3340 cm^{-1} on the FRP, which may indicate that the hydroxyl groups present in the epoxy resin interacted with the glass fibers in the composite [167]. Aliphatic C-H stretching vibrations can be spotted in the range 3000 – 2700 cm^{-1} for both materials [167]. The characteristic C=C stretching vibration of benzene ring is observed at 1578, 1605 and 1615 cm^{-1} [168]. For both C-H and C=C vibrations there was no significant changes seen among both materials. An aromatic peak can be seen at 1506 cm^{-1}, also present in the DGEBA epoxy's backbone [94]. A small peak at 1749 cm^{-1} can be assigned to the carbonyl group that belongs to the ester present in the epoxy [94]. A O-Si-O bending vibration can be seen at 414 cm^{-1} in the composite's spectrum, being attributed to the glass fibers [169]. A small peak was observed at 919 cm^{-1} corresponding to either an anhydride group or an unreacted epoxide group. According to literature [94,170,171], the presence of this peak might mean that the material is not fully cured before their input into the aging chambers. The intensity of this peak in the FRP spectrum was smaller than in the epoxy system, owing to either the matrix proportion or the composite's higher curing degree.

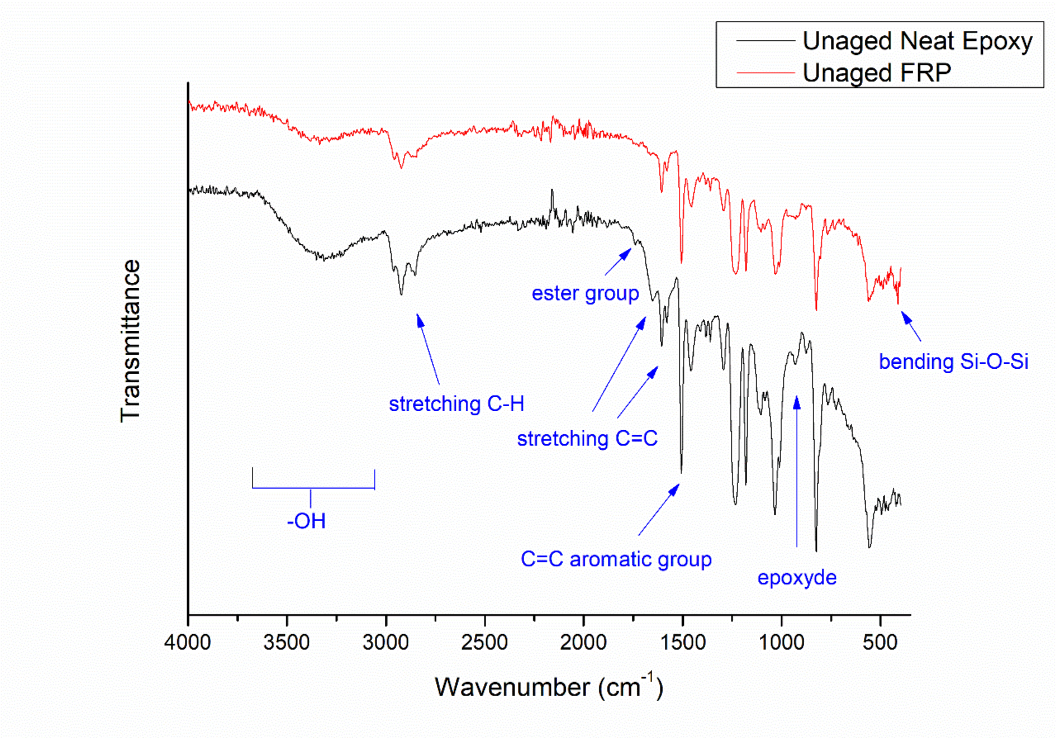

Figure 73. Infrared spectra of the unaged neat epoxy and FRP specimens.

4.2. Absorption

Figure 74 shows the comparison between the absorption profiles of the uncoated FRP and the neat epoxy resin. Each experimental data point is the mean value of three specimens. As expected, the neat epoxy resin specimens absorbed a larger absolute moisture content than the FRP. This means that the addition of hydrophobic glass fibers prevented the material from absorbing a high amount of moisture.

It can be noted from Figure 74 that the average moisture absorbed by the neat epoxy resin exposed to 55°C surpasses that of samples exposed to 70°C at $t^{1/2} = 70$ $h^{1/2}$ after having presented a pseudo-plateau at $t^{1/2} = 60$ $h^{1/2}$. This may be attributed to mass loss from hydrolysis at 70°C [36,85] or post-curing suffered at high temperature, which would increase the crosslinking density, thereby decreasing the free volume content to be occupied by water molecules [172]. For the FRP specimens, the ones at 70°C presented a pseudo-plateau after $t^{1/2} = 24$ $h^{1/2}$, presenting a new increase afterwards, while the specimens at 35 and 55°C showed a pseudo-plateau at $t^{1/2}$ equal to 52 and 48 $h^{1/2}$ respectively. This can be explained by the occurrence of non-Fickian behavior at all temperatures, which will be discussed later. In addition, the moisture absorbed by the epoxy samples is in accordance with literature, which states that the epoxy resin can absorb up to 3.0 – 4.0% of its own weight [173,174].

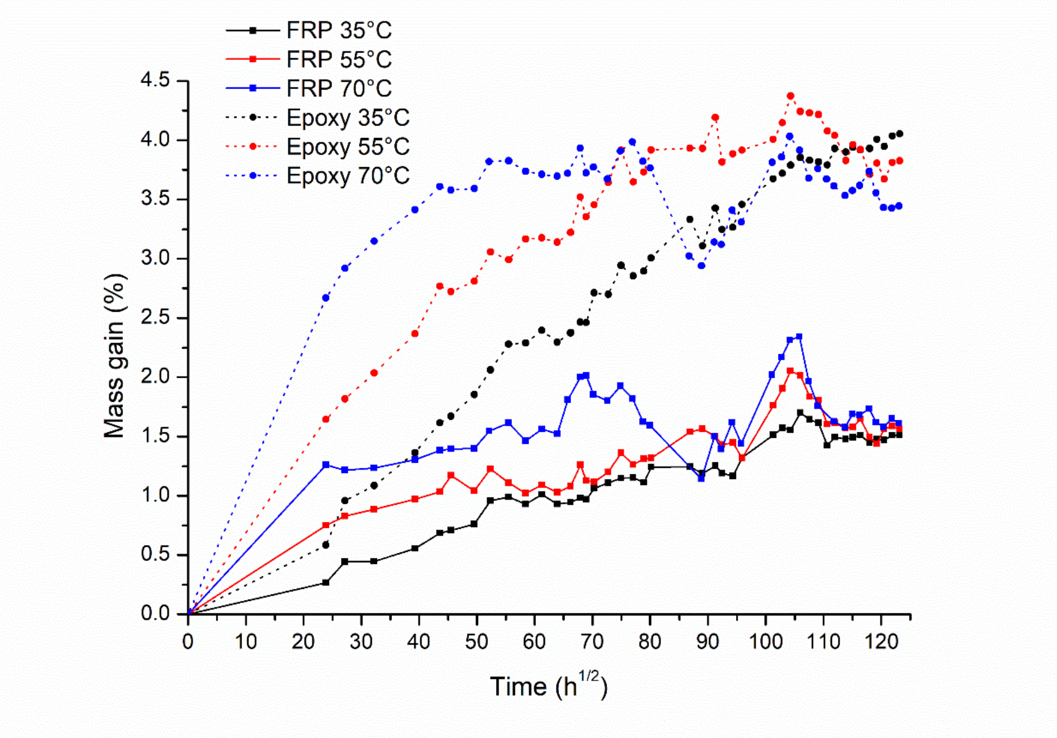

Figure 74. Moisture absorption profile of the neat epoxy resin and the uncoated composite at 35, 55 and 70°C.

The effect of temperature on absorption in Figure 74 is evident. The higher the temperature, the faster the absorption, owing to the temperature-dependent diffusivity (equation 11). Regarding the saturation content, it can be seen that for the FRP the total moisture absorbed increased with temperature, while for the neat epoxy, there was an increase from 35 to 55°C, followed by a lower value at 70°C, which could indicate the occurrence of mass loss from hydrolysis or the post-cure at high temperature [85,93,175]. The hydrolysis investigation was done by carrying out FTIR analysis and will be further discussed (Section 4.2.2). From these graphs, it can be stated that for all temperatures there was not a visible plateau in the absorption content, and this increase in the absorption after long-term exposure is stronger at 70°C, especially for the FRP specimens. This may be due to the polymer relaxation at high temperatures, as discussed in section 3.7.1, since 70°C is closer to the T_g value of the amine-cured DGEBA epoxy found by the DSC analysis (~80°C). In literature this property varies within the range 141 – 166°C for the DGEBA epoxy [176–178]. This increases the thermal expansion coefficient, inducing a stronger matrix swelling, increasing the free volume density, resulting in a stronger absorption capacity of the composite [67,68]. For both materials, the samples exposed to 55 and 70°C exhibited similar maximum moisture absorbed after approximately $t^{1/2} = 100\ h^{1/2}$ for the composites and $t^{1/2} = 75\ h^{1/2}$ for the epoxy samples.

The FRPs exposed to 35°C, 55°C and 70°C presented an initial plateau at $t^{1/2} = 55h^{1/2}$, $t^{1/2} = 50\ h^{1/2}$ and $t^{1/2} = 24\ h^{1/2}$, respectively, and afterwards a new increase in the moisture absorption at a lower rate, similar to curve (1) in Figure 31 (Section 2.4.1). At 70°C, after exposure time equal to 4086h (~64 $h^{1/2}$), there was a new increase in the moisture absorption at a higher rate, similar to curve (3) in Figure 31 (Section 2.4.1). This may indicate a non-Fickian absorption process caused by the high temperature on the epoxy resin. Both Fickian and non-Fickian behaviors will be further discussed. On the other hand, for the neat epoxy specimens, this continuous increase in the absorption curve after a pseudo saturation was more prominent in the specimens exposed to 35 and 55°C.

A sudden decrease in the absorption curve for all specimens at 70°C between $t^{1/2} = 78$ and 95 $h^{1/2}$ was attributed to an electrical damage in the heating resistance in the chamber C (70°C), causing a decrease in temperature during that period ($t^{1/2} = 78 - 95\ h^{1/2}$) (Figure 61). The sudden increase in all absorption curves between 100 and 114 $h^{1/2}$ was due to the lack of salt provision from the supplier in this time period, momentarily increasing the absorption, as explained in Section 2.3.5, decreasing again after $t^{1/2} = 95\ h^{1/2}$ with the return of salt provision. Despite this drawback, the absorption results shown by the materials were consistent with the expectations about the effect of temperature on absorption.

Aiming to investigate whether one of the three specimens of each material was inducing a deviation in the average absorption curves, the absorption curve of each specimen of FRP and epoxy is plotted in Figure 75. Interestingly, all the specimens of each group presented the same trend, i.e., all three specimens of each group changed their mass at the same rate at the same time interval. This proves that the atmosphere inside the heating chambers can be considered uniformly concentrated around all samples. The FRP curve at 70°C presented the most pronounced difference in moisture absorption among the samples, reflecting in the peaks and valleys observed in Figure 74.

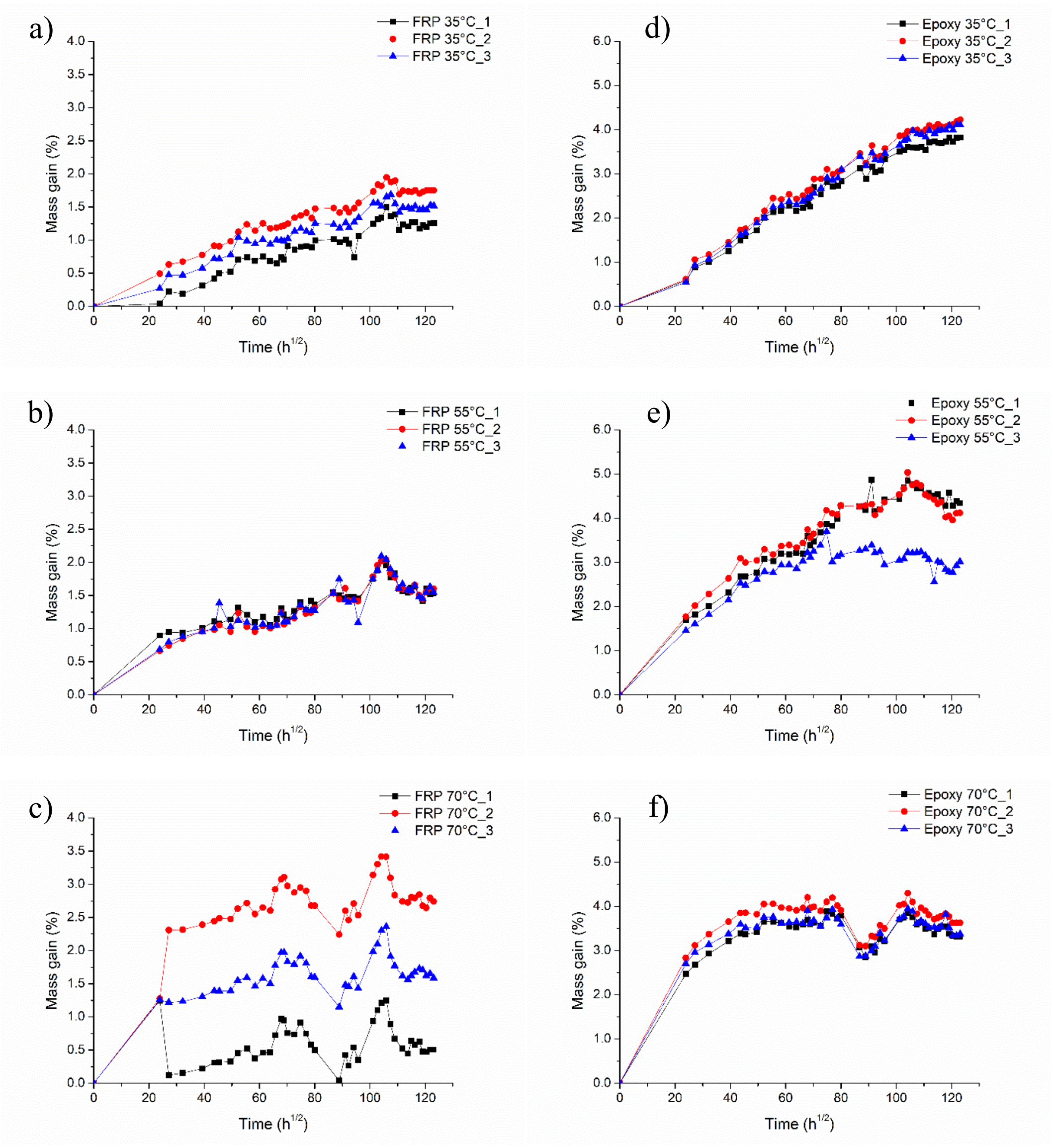

Figure 75. Moisture absorption curves for each sample for FRP at a) 35°C, b) 55°C and c) 70°C and for epoxy at d) 35°C, e) 55°C and f) 70°C.

The comparison between the absorption profile of the uncoated FRP and the coated FRP is shown in Figure 76. The epoxy coating on the composite's edges fulfilled its purpose, hindering the ingress of moisture inwards the material, since both absorption rate and total moisture content of the coated FRP are lower than those of the uncoated FRP. The anisotropic moisture absorption was also evaluated to ensure that the epoxy coating in the coated FRPs fulfilled its purpose of preventing the water penetration through the exposed edges of the composites.

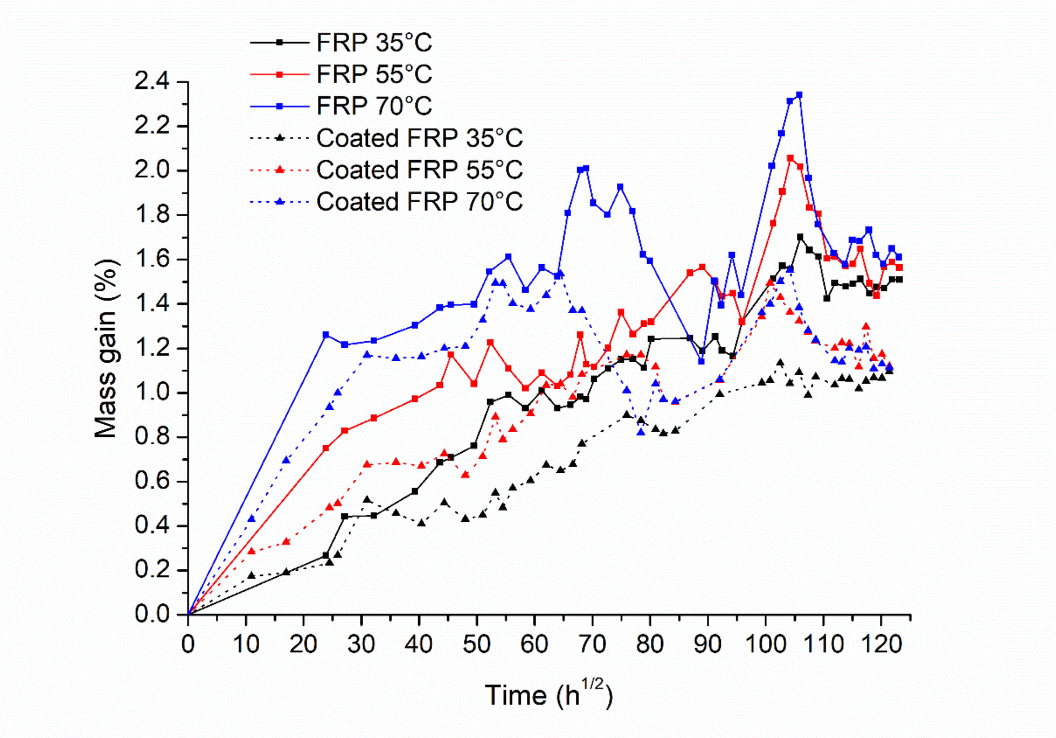

Figure 76. Moisture absorption profile of the coated and the uncoated composites at 35, 55 and 70°C.

4.2.1. Fickian Diffusion Model

Table 12 shows the fitting results of the 1D Fickian (Equation 6 – Section 2.3.4, Page 41) and 3D Fickian (Equations 6 and 10) models for the average weight gain of the FRP specimens, where M_m is the saturation moisture content, D_x is the diffusivity through the thickness, D_y and D_z are the transverse diffusivities in the directions parallel to length and width, respectively, as shown in Figure 9, Section 2.3.4. The graphs with the fitted Fickian curve are shown in Figure 76. It is worth mentioning that the results between $t^{1/2} = 78$ h$^{1/2}$ and $t^{1/2} = 95$ h$^{1/2}$ in the 70°C curve were removed from the modelling to avoid a low correlation factor, provided that this period corresponds to the time span that the salt spray chambers went through technical problems. The effect of temperature is clear, since the 1D diffusivity value increased with temperature. For the tridimensional diffusion, it can be seen that for 55 and 70°C the through-thickness diffusivity value (D_x) was higher than the transverse ones (D_y and D_z), meaning that the capillarity flow through the composite's sides at these temperatures was not the preferential pathway for the moisture ingress, though it was not negligible. On the other hand, at 35°C the transverse diffusivities values were found to be higher than the through-thickness one, indicating a more uniform distribution of moisture penetration on all sides of the samples and a more significant capillarity flow at this temperature. It can also be seen that the saturation contents attained by the composites slightly decreased from 35 to 55°C, increasing at 70°C. The saturation levels at low temperatures can be considered nearly the same, while at 70°C the composites presented a higher absorption capacity due to its proximity to T_g, inducing a stronger viscous behavior in the matrix, which may increase the polymer's free volume content, leading to a higher absorption capacity [67,68]. From Figure 77 and Table 12, it can be seen that the saturation content calculated for 35 and 55°C are beyond the levels attained experimentally. This could be credited to the lack of enough experimental data, meaning that at a longer experiment time, the saturation time would have been reached.

In Figure 77 the 1D and 3D Fickian curves are overlapped, owing to their equal correlation factors shown in Table 12. The equations were fitted to the experimental data by using the least squares method incorporated in the Trust-region-reflective optimization algorithm [179].

Table 12. 1D and 3D Fickian model parameters for the FRP specimens.

	1D Fickian			3D Fickian				
	M_m (%)	D ($\times 10^{-13}$ m^2/s)	**R^2**	M_m (%)	D_x ($\times 10^{-13}$ m^2/s)	D_y ($\times 10^{-13}$ m^2/s)	D_z ($\times 10^{-13}$ m^2/s)	**R^2**
35°C	1.726	1.73	**0.9481**	1.726	1.05	4.17	3.33	**0.9481**
55°C	1.681	3.33	**0.7652**	1.681	2.56	2.11	2.14	**0.7652**
70°C	1.813	9.72	**0.7159**	1.813	8.06	2.04	2.64	**0.7159**

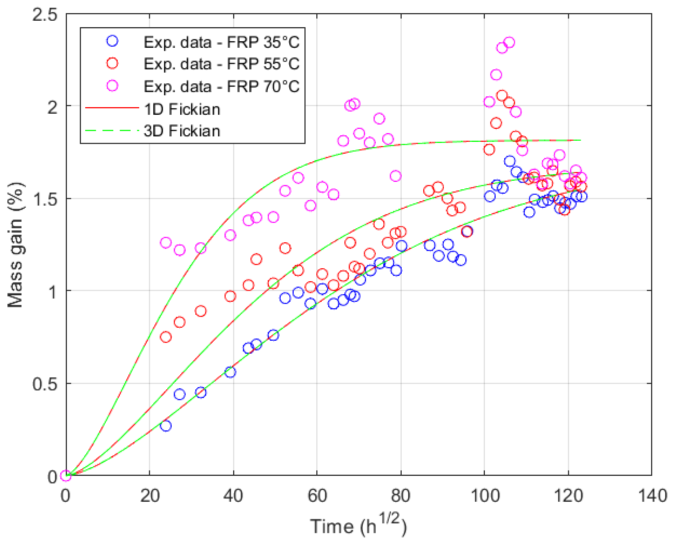

Figure 77. Fitted curves from the Fickian models to the FRP samples.

Table 13 shows the fitting results of the 1D and 3D Fickian models for the epoxy specimens. Once again, the diffusivity values increased with temperature and a small capillarity phenomenon was spotted (D_y, $D_z < D_x$). The neat epoxy presented higher saturation content values than that of the FRP specimens for all temperatures, due to the higher matrix proportion. It is also seen that, for 35°C, the diffusivity values of the epoxy material were lower than that of the FRP at the same temperature, which means that, at low temperatures, the effect of temperature on moisture penetration is less pronounced than at high temperatures. Indeed, at 55 and 70°C, the diffusivity values for the neat epoxy specimens are greater than those for the composites.

It was also found that the saturation content decreased with temperature, which could be associated with either polymer mass loss through hydrolysis or post-cure at high temperatures [36,85,172]. The hypothesis of hydrolysis will be investigated in the Section 4.2.2 with FTIR analyses. The increase in the crosslinking density due to post-curing may lead to a decrease in the availability of hydrogen-bonding sites in the polymeric structure [180], although Chen *et al.* [181] claim the opposite. However, this phenomenon is highly dependent on the nature of the polymer. Previous works on epoxy curing [182,183] state that in the curing reaction between DGEBA epoxy resin and an amine-based hardener, the C-O bonds in each epoxide group (functional group present in unreacted epoxy resin) are broken to form a reactive -CH_2 site, becoming capable of crosslinking to the hardener reactive molecules. Then, under appropriate thermal activation, the molecules' mobility increases and the covalent bonds are formed between C and N atoms. Therefore, for the resin in this study, the availability of hydrophilic sites is diminished. In addition, post-curing increases the polymer's density, reducing the amount of free volume, making the material more resistant to moisture gain [172,180,184]. This decrease in absorption content with temperaturewas not observed in the composites (Table 12), but it is likely that the FRP specimens also suffered post-curing. However, the curing effects on moisture absorption on the FRP were outweighed by the presence of voids and interface, which enhanced the absorption capacity with temperature.On the other hand, Rajaram *et al.* [185] claim that post-curing increases the availability of free volume in the polymer, especially when aging at high-temperatures, thus increasing moisture absorption. The occurrence of post-cure after aging will be discussed in Section 4.2.3 with DMTA analyses.

The epoxy specimens presented more acceptable fitting for high temperatures than the FRP, due to the higher regularity present in the epoxy's absorption curve. The Fickian curves fitted to the experimental values can be found in Figure 78.

Table 13. 1D and 3D Fickian model parameters for the neat epoxy specimens.

	1D Fickian			3D Fickian				
	M_m (%)	D (x 10^{-13} m^2/s)	**R^2**	M_m (%)	D_x (x 10^{-13} m^2/s)	D_y (x 10^{-13} m^2/s)	D_z (x 10^{-13} m^2/s)	**R^2**
35°C	4.794	1.31	**0.9927**	4.793	1.13	0.14	0.27	**0.9927**
55°C	4.041	5.00	**0.9551**	4.041	4.17	0.50	0.75	**0.9551**
70°C	3.728	20.83	**0.9516**	3.728	18.33	1.81	3.61	**0.9516**

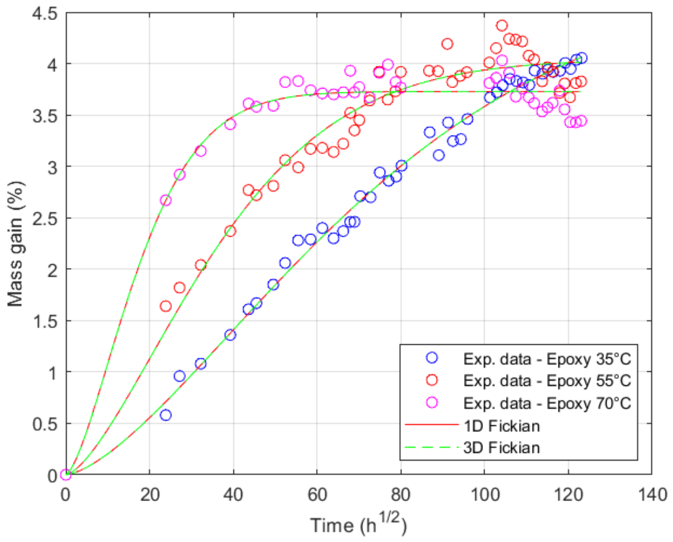

Figure 78. Fitted curves from the Fickian models to the epoxy samples.

The comparison between the saturation moisture contents absorbed by the composites and epoxy samples are shown in Table 14, as well as the ratio between them. Proportionally, the saturation moisture absorbed by the FRP is equivalent to 36.00%, 41.60% and 48.64% of those of the neat epoxy resin at 35°C, 55°C and 70°C, respectively (Table 14). According to the segmentation made from the SEM images (Section 4.1.1), the matrix volume fraction in the composites is approximately 58.97%. As the epoxy matrix is the only component that absorbs moisture, it can be stated that the composites absorbed less than expected for all temperatures. This could be attributed to the different degrees of cure of the materials, leading to different free volume contents in the bulk matrix, essential factor for water diffusion, according to the free volume theory [175]. Moreover, if post-cured, the material will increase the crosslink density, thereby decreasing the amount of hydrophilic sites, as explained earlier, reducing moisture ingress [180]. Hence, the matrix volume fraction is not the only factor that influences the absorption capacity of the composites.

It could also be noted that the absorption ratio between FRP and neat epoxy increased with temperature. As it will be discussed in the non-Fickian models, the higher the temperature, the shorter the relaxation time, which implies a stronger viscous behavior, leading to an increase in the absorption capacity of the composite [186].

Table 14. Comparison of the saturation moisture content absorbed by the composites and neat epoxy samples and the absorption ratio for all temperatures.

	35°C	**55°C**	**70°C**
		M_m (%)	
FRP	1.726	1.681	1.813
Epoxy	4.794	4.041	3.728
M_{FRP}/M_{epoxy}	0.3600	0.4160	0.4864

Tables 15 and 16 show the comparison of the diffusivity and saturation content values between the materials used in this work and in literature for the epoxy-based GFRP and neat epoxy, respectively. The fiber volume content, temperature and the exposure media are also described in the tables. It is noticeable that both diffusivity and saturation content found in this work follow the same order of magnitude found in literature for both materials.

Table 15. Experimental and literature values of the diffusivity and saturation content for epoxy-based GFRPs.

Reference	**Fiber volume content**	**Temperature (°C)**	**Environment**	**Diffusivity (m^2/s)**	**Saturation (%)**
Experimental values	**42%**	**35**	**SS**	**1.73E-13**	**1.73**
		55		**3.33E-13**	**1.68**
		70		**9.72E-13**	**1.81**
[187]	39%	35	SS	6.30E-13	1.10
[60]	48%	50	DW	4.50E-13	0.86
[60]	48%	90	DW	2.10E-12	1.02
[74]	30%	40	DW	9.74E-13	1.50
[74]	58%	40	DW	1.85E-13	1.00
[74]	60%	40	DW	4.00E-14	1.00
[76]	60%	23	DW	2.60E-14	0.71

[76]	60%	23	DW	2.20E-14	0.52
[34]	50%	24	DW	1.12E-12	0.35
[34]	50%	70	DW	1.90E-12	2.87
[34]	50%	90	DW	2.40E-12	5.41
[95]	70%	23	DW	1.19E-14	0.23
[95]	70%	50	DW	1.05E-14	0.30
[86]	28%	23	DW	4.26E-14	3.07
[86]	28%	38	DW	7.25E-14	3.77
[86]	48%	50	DW	8.57E-13	1.19
[86]	48%	50	DW	7.68E-13	1.19
[188]	not informed	25	DW	1.92E-12	3.11
[188]	not informed	70	DW	2.08E-12	3.62
[93]	60%	60	DW	5.83E-12	0.96
[189]	57%	40	DW	1.20E-13	1.50
[189]	57%	60	DW	6.50E-13	1.92
[190]	40%	26	SW	6.09E-13	1.57
[35]	not informed	25	SW	3.15E-13	1.20
[59]	34%	30	SW	6.50E-13	0.34
[59]	44%	30	SW	7.70E-13	0.44
[191]	35%	20	RH 50%	1.35E-13	0.15
[191]	35%	40	RH 95%	1.96E-13	0.69
[191]	35%	20	RH 50%	1.54E-13	0.14
[191]	35%	40	RH 95%	2.38E-13	0.71
[191]	35%	20	RH 50%	2.83E-13	0.087
[191]	35%	40	RH 95%	5.20E-13	0.63

SS = Salt Spray; DW = distilled water; SW = seawater; RH = relative humidity

Table 16. Experimental and literature values of the diffusivity and saturation content for epoxy resin systems.

Reference	**Temperature (ºC)**	**Environment**	**Diffusivity (m^2/s)**	**Saturation (%)**
Experimental values	**35**	**SS**	**1.31E-13**	**4.79**
	55		**5.00E-13**	**4.04**
	70		**2.08E-12**	**3.73**
[192]	50	DW	1.90E-13	7.60
[193]	20	DW	4.69E-14	7.00
[193]	40	DW	2.20E-13	8.40
[193]	60	DW	1.15E-12	8.00
[193]	20	SW	8.02E-14	4.60
[193]	60	SW	1.38E-12	4.40
[194]	45	DW	3.13E-13	6.80
[194]	60	DW	6.61E-13	6.80
[194]	75	DW	1.15E-12	6.80
[194]	90	DW	2.35E-12	6.80
[194]	45	DW	3.35E-13	3.35
[194]	60	DW	7.93E-13	3.35
[194]	75	DW	1.35E-12	3.35
[194]	90	DW	3.14E-12	3.35
[194]	45	DW	2.08E-13	6.95

[194]	60	DW	5.03E-13	6.95
[194]	75	DW	8.96E-13	6.95
[194]	90	DW	1.34E-12	6.95
[17]	45	DW	3.70E-13	1.77
[17]	45	DW	2.43E-13	1.76
[17]	20	DW	3.47E-14	1.66
[17]	20	DW	3.47E-14	1.43
[195]	20	DW	8.40E-14	2.03
[74]	40	DW	1.23E-12	3.00
[196]	37	DW	1.26E-12	1.11
[180]	20	DW	1.50E-13	2.74
[180]	40	DW	4.30E-13	3.05
[180]	70	DW	5.70E-13	5.32
[180]	100	DW	2.32E-12	6.21
[180]	20	DW	1.20E-13	5.12
[180]	40	DW	4.60E-13	5.06
[180]	70	DW	1.39E-12	5.52
[180]	100	DW	9.25E-12	4.82
[197]	40	DW	6.45E-12	1.50
[59]	30	SW	5.80E-13	0.75
[198]	23	SW	1.46E-13	2.44
[198]	50	SW	2.93E-13	2.78
[198]	60	SW	3.85E-13	2.97
[198]	70	SW	3.68E-13	3.26
[61]	45	DW	3.70E-13	1.77
[61]	45	SW	4.28E-13	1.34
[61]	20	DW	3.47E-14	1.66
[61]	20	SW	3.47E-14	1.36
[61]	45	RH	6.02E-13	1.10

SS = Salt Spray; DW = distilled water; SW = seawater; RH = relative humidity

As discussed in Section 2.3.4, the diffusivity *D* is a temperature-dependent property, which follows the Arrhenius relationship described in Equation 75, where D_0 is the material constant, *Q* is the activation energy, *R* the universal gas constant and *T* the temperature in Kelvin [20]. According to Serpe *et al.* [199], the saturation value can also be modeled by the Arrhenius law, following equation 76, where $M_{m,0}$ and ΔH are a material constant and the mixing enthalpy, respectively. Figure 79 shows the Arrhenius plots for the diffusivities and saturation moisture contents for the FRP and neat epoxy systems from literature listed in Tables 15 and 16 and the ones found in this work. These graphs are in logarithmic scale of diffusivity (*D*) and saturation content (M_m) *vs*. inverse temperature in Kelvin. The equations used for the fitting are shown in the graphs. These graphs also include the 95%

confidence curves. The data scattering is due to different aging environments used in literature, manufacturing methods, curing degree and fiber volume fraction, in the case of the composites. However, the fitting is consistent with the expected trend.

$$D = D_0 exp\left(\frac{-Q}{RT}\right) \tag{75}$$

$$M_m = M_{m,0} exp\left(-\frac{\Delta H}{RT}\right) \tag{76}$$

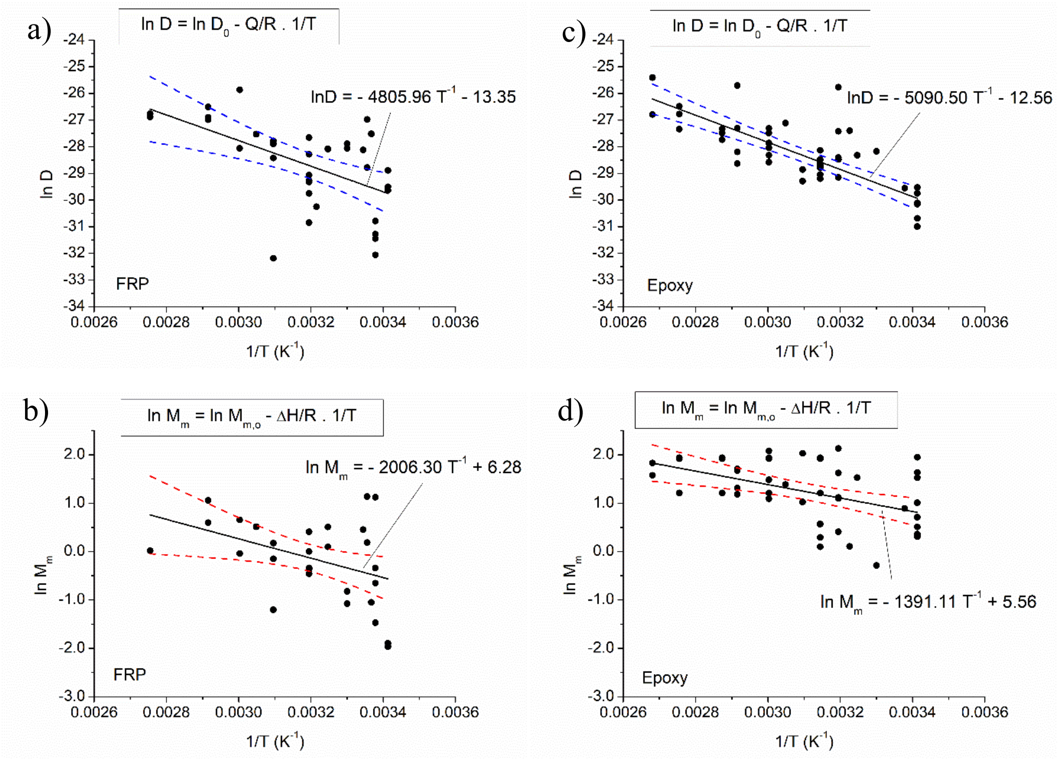

Figure 79. Arrhenius plots for diffusivity values and saturation moisture content: a) and b) FRP; c) and d) epoxy.

The graphs in Figure 79 show that both diffusivity value and saturation content increase with temperature, as reported in literature [20,34,199]. By applying linear regression, representative values of Q, D_0, ΔH and $M_{m,0}$ were estimated for FRP and neat epoxy systems and are shown in Table 17. Both activation energy and mixing enthalpy of FRP and neat epoxy systems were similar to each other and in agreement with literature [34,194,200,201]. On the other hand, the values for $M_{m,0}$ for both materials are extremely high and are unattainable for any existing material and can be attributed to the large data scattering that increased the curve slope. Regarding the enthalpy and diffusion activation energies found, Zhou and Lucas [194] found a mixing enthalpy value of 19.50 kJ/mol for neat epoxy resin after immersion in distilled water, while Guermazi *et al.* [34] found 35.00 kJ/mol for

GFRP in distilled water. For the diffusion activation energy, Chateauminois *et al.* [60] found values of 29 and 21 kJ/mol for epoxy resin and GFRP, respectively, after immersion in distilled water, Bao and Yee [202] found 38 kJ/mol for woven carbon-fiber composites after immersion in water and Nogueira *et al.* [180] found 47.7 kJ/mol for neat epoxy resin after immersion in deionized water.

Table 17. Values of D_0, Q, $M_{m,0}$ and ΔH for FRP and epoxy systems in literature.

System	D_0 (m^2/s)	Q (kJ/mol)	$M_{m,0}$ (%)	ΔH (kJ/mol)
FRP	1.59E-06	39.98	534.96	16.69
Neat epoxy	3.50E-06	42.35	258.89	11.57

The logarithm of diffusivity *vs*. the inverse temperature in Kelvin for the FRP and neat epoxy specimens are shown in Figure 80. The slope of the fitted curve is greater for the epoxy material than for the composite, resulting in a higher activation energy, as shown in Table 18. The values of the constant D_0 and activation energy Q for both materials are shown in Table 18. The values found for the activation energy were consistent with previous works in literature, such as 40.71 kJ/mol for neat epoxy systems [194], 51.00 kJ/mol for neat epoxy specimens immersed in distilled water [200] and 10.43 kJ/mol for GFRP specimens immersed in distilled water [34]. Some works in literature state that if the activation energy of a composite is different from its neat resin, it is suggested that additional diffusion mechanisms, such as void penetration and interface diffusion, are present [184,202]. Judd [184] claims that the void content also plays a role in the diffusion activation energy. The author found that higher void contents induce lower the activation energies, facilitating the water ingress. However, this is more accurate when comparing the same material with different void contents. When comparing two different materials, even if the matrix is the same, this is no longer valid, since the activation energy is an intrinsic property of the material, indicating the minimum energy required for solute penetration to occur. It can be said then that the difference in activation energy might indicate different curing degrees. Therefore, the composite might present a lower curing degree than the neat epoxy, as the composite’s activation energy was lower than that of the neat epoxy. In addition, the resin matrix closest to the fibers, i.e., the interphase, generally presents a lower curing degree than the bulk matrix [203].

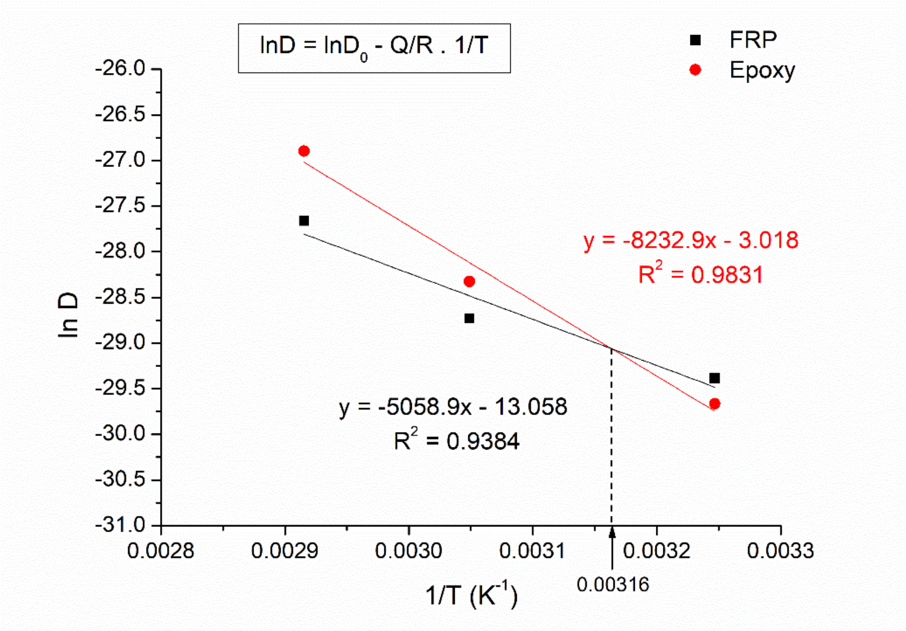

Figure 80. Arrhenius plot for diffusivity values of the FRP and neat epoxy samples.

Table 18. Arrhenius diffusivity constant D_0 and diffusion activation energy Q obtained for the FRP and neat epoxy.

	D_0 (m^2/s)	**Q (kJ/mol)**
FRP	2.13×10^{-6}	42.09
Epoxy	4.89×10^{-2}	68.49

In order to extrapolate these results to ambient temperature (25°C) to simulate a real application, the inverse of 25°C was substituted in the equations shown in Figure 80. The diffusivity values found for the FRP and epoxy specimens for this temperature were 9.04×10^{-14} and 4.91×10^{-14} m^2/s, respectively. These values have the same order of magnitude as the values found in the literature for 25°C [34,35,198], even though these works performed aging experiments different from salt spray. Surprisingly, the extrapolated diffusivity value for the FRP at 25°C was higher than that of the neat epoxy for this temperature (~84.17% higher). Thus, it can be deduced that at low temperatures the addition of fibers does not significantly impair moisture absorption. This behavior can be observed for temperatures lower than the intersection point in Figure 80, which is 43.12°C (1/T = 0.00316 K^{-1} in Figure 80).

Figure 81 shows the Arrhenius plot of the saturation content of FRP and epoxy materials as a function of the inverse temperature. The fitted values of $M_{m,0}$ and ΔH are shown in Table 19. For the neat epoxy specimens, there was a deviation in the graph curve with an increasing slope, provided that generally this curve is characterized by a negative decreasing slope with the saturation content increasing with temperature [34,199–201]. Consequently, the mixing enthalpy for the neat epoxy resin was found to be negative, which deviates from all the works in literature found by the author, although none of these works accounted for the cure effects on the moisture absorption capacity.

On the other hand, for the FRP specimens, the mixing enthalpy was found to be 1.05 kJ/mol, which is a value more consistent with literature, even though higher values are cited, such as 19.50 kJ/mol for epoxy coating for pipelines [201], 35.00 kJ/mol for GFRP [34], 4.50 kJ/mol for PA11 immersed in acid solutions [199] and 3.20 kJ/mol for both the neat epoxy and nanocomposites with multi-walled carbon nanotubes (MWCNT) immersed in distilled water [200]. The low correlation factor obtained for the FRP specimens is due to the decrease in saturation content from 35 to 55°C followed by an increase at 70°C.

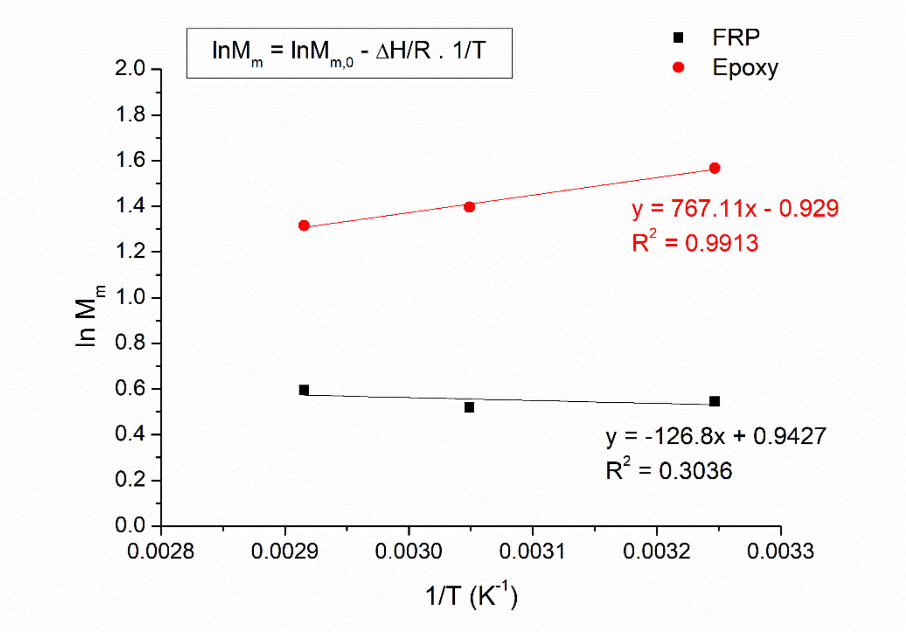

Figure 81. Arrhenius plot for the saturation content of FRP and epoxy materials.

Table 19. Arrhenius saturation constant $M_{m,0}$ and enthalpy energy ΔH for FRP and epoxy.

	$M_{m,0}$ (%)	**ΔH (kJ/mol)**
FRP	2.57	1.05
Epoxy	0.39	-6.38

From the Arrhenius plot in Figure 81 the saturation moisture content could be estimated for 25°C. Table 20 displays the values found for the saturation contents extrapolated to 25°C. This table also includes the estimation of the diffusivity values previously discussed. It appears that at 25°C the composite would absorb approximately 32.40% of the amount of moisture absorbed by the neat epoxy, 9.60% lower than the fiber volume fraction ($V_f \approx 42\%$, Section 4.1.1), while its diffusivity value would be 1.84 times higher than that of the epoxy samples. According to Table 15, where the diffusion parameters for the FRP from literature are compared, the diffusivity values for the FRP at 25°C found in Table 18 are consistent with most values from literature, with the exception of the works from Oguz *et al.* [188], Jesthi and Nayak [35], Guermazi *et al.* [34] and Jiang *et al.* [191], where the former found a value of 19.20 x 10^{-13} m^2/s for GFRP immersed in distilled water at 25°C, the second found 3.15 x 10^{-13} m^2/s for GFRP immersed in seawater, the third found 1.12 x 10^{-12} m^2/s for GFRP immersed in distilled water and the latter found 2.83 x 10^{-13} m^2/s for GFRP exposed to 50% RH. The saturation content was also found to be higher than those from literature. The same trend was found for the saturation content of the neat epoxy (Table 15). Regarding the neat epoxy's diffusivity, it was found to be lower than most values from literature.

Table 20. Prediction of the saturation moisture content and diffusivity values at 25°C.

	At 25°C	
	M_m (%)	**D (x 10^{-13} m^2/s)**
FRP	1.68	0.90
Epoxy	5.18	0.49
FRP/Epoxy ratio	0.324	1.842

4.2.1.1. Moisture profiles

In order to evaluate the progress of moisture diffusion in the thickness direction, the moisture profiles of FRP and epoxy were assessed. For this, the 1D diffusivity values and saturation contents found in Tables 12 and 13 were inserted into equation 77 [54]. To calculate the time needed to reach such saturation level, equation 78 was employed, by using the specimen's thickness (h) and diffusivity (D). This equation describes the time taken to reach 99.9% of the saturation level [53]. Both equations were already discussed in section 2.3.4.

$$\frac{c-c_i}{c_m-c_i} = 1 - \frac{4}{\pi}\sum_{n=0}^{\infty}\frac{1}{(2n+1)} sin\frac{(2n+1)\pi x}{h} exp\left[-\frac{(2n+1)^2\pi^2 D_x t}{h^2}\right] \quad (77)$$

$$t_{99.9} = \frac{0.67h^2}{D} \quad (78)$$

The saturation times found for the FRP were 47944, 25288 and 8593 hours ($t^{1/2}$ = 218.96, 159.02 and 92.68 hours$^{1/2}$) at 35, 55 and 70°C, respectively. For the specimens exposed to 35 and 55°C, the time required to saturate the composites was found to be higher than the experimental time (t = 15171 hours, section 3.2.1.1). Figure 82 shows the progress of the relative moisture concentration as a function of the relative thickness of the composites (x/h, where x is the position and h is the thickness) at all temperatures. The boundary condition applied was:

At $x/h = 0$ and $x/h = 1 \rightarrow M_t/M_m = 1$ during the whole aging time, where M_t and M_m are the moisture uptake at time t and saturation moisture content, respectively.

As expected, the moisture concentration through the specimen's thickness follows a parabolic trend, with the exposed edges being the ones with the highest moisture concentration, and the profile tends to stabilize at the saturation value over time. It can be highlighted that the moisture contents from the absorption curves (Figure 74) are average values from the curves in Figure 82 [100]. The time taken to reach the saturation moisture level decreased with temperature, as expected.

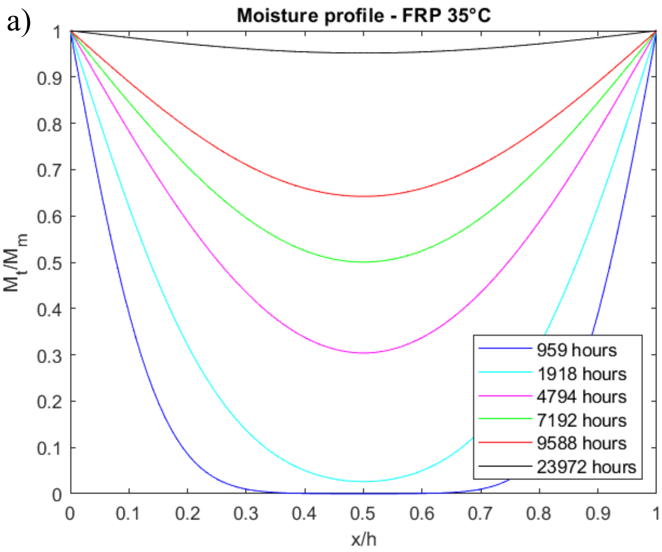

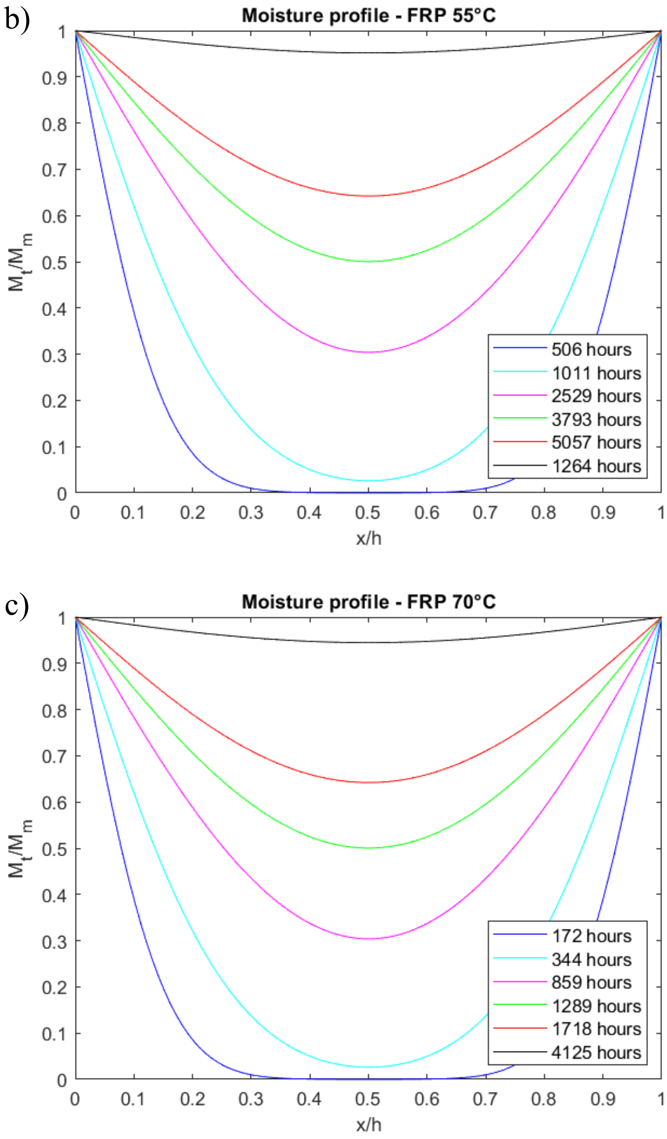

Figure 82. Moisture profile of the FRP at (a) 35, (b) 55 and (c) 70°C.

For the epoxy specimens, the time taken to reach the saturation level was found to be 61795, 16411 and 3938 hours ($t^{1/2}$ = 248.58, 128.10 and 62.75 hours$^{1/2}$) for 35, 55 and 70°C, respectively. Saturation times for 55 and 70°C were lower than for FRP, evidencing the higher susceptibility of moisture penetration experienced by the neat resin. Figure 83 shows the moisture profiles of the epoxy specimens at 35, 55 and 70°C.

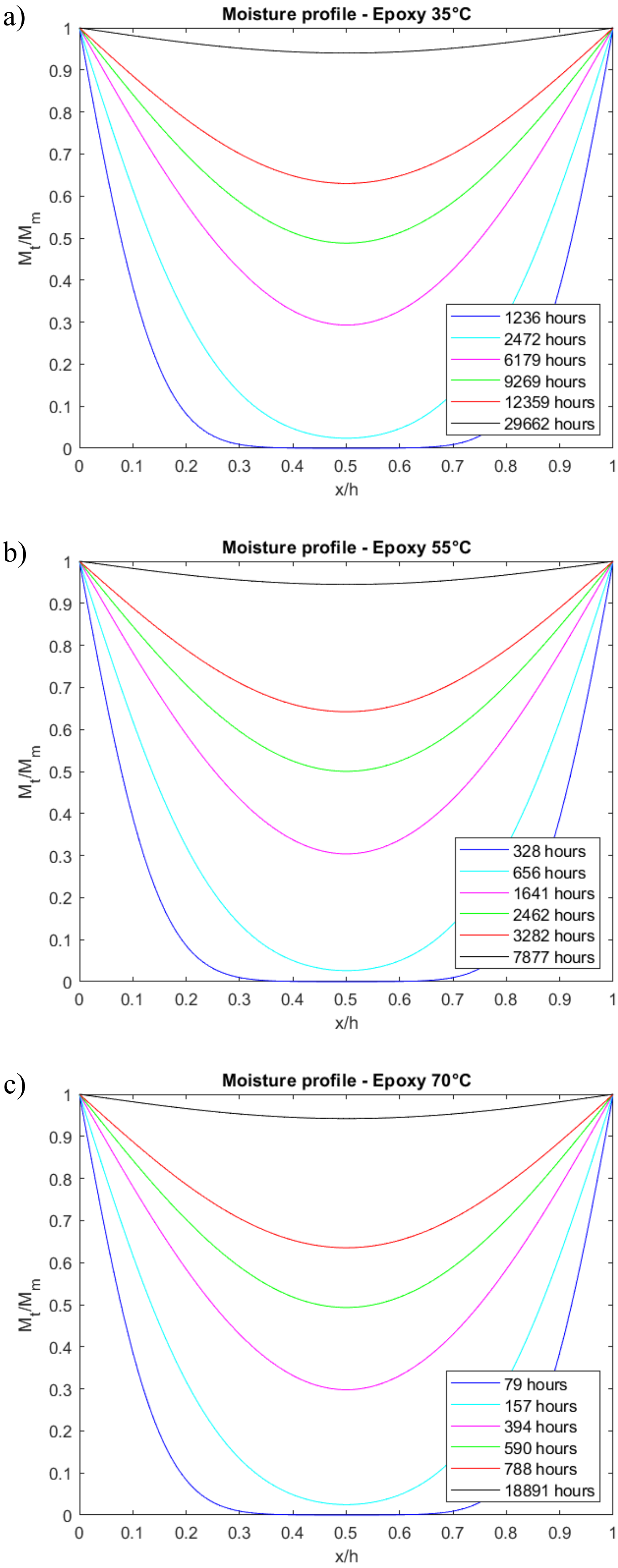

Figure 83. Moisture profile of the neat epoxy at (a) 35, (b) 55 and (c) 70°C.

4.2.1.2. Effectiveness of the epoxy coating on FRP’s exposed edges

To evaluate the effectiveness of the coating of the composite’s exposed edges with an epoxy layer, the moisture absorption behavior of the coated FRP specimens was also determined. It is expected that the diffusion will be predominantly unidirectional in the through-thickness direction. Table 21 shows the comparison between the Fickian model results of the coated and uncoated FRP, with the latter being the regular FRP discussed in Section 4.2.1.1. The graph with the fitted curves can be seen in Figure 84. It can be seen that the saturation contents of the coated FRP were lower than those of the uncoated FRP for all temperatures, meaning that the epoxy coating fulfilled its purpose of hindering water penetration.

Table 21. 1D and 3D Fickian results of the uncoated and coated FRP specimens.

Coated FRP								
	1D Fickian			3D Fickian				
	M_m (%)	D (x 10^{-13} m^2/s)	**R^2**	M_m (%)	D_x (x 10^{-13} m^2/s)	D_y (x 10^{-13} m^2/s)	D_z (x 10^{-13} m^2/s)	**R^2**
35°C	1.251	1.62	**0.9591**	1.251	1.24	0.95	0.95	**0.9591**
55°C	1.291	3.89	**0.9152**	1.291	3.06	2.03	2.10	**0.9152**
70°C	1.317	21.39	**0.8409**	1.317	16.67	10.28	10.56	**0.8409**
Uncoated FRP								
	1D Fickian			**3D Fickian**				
	M_m (%)	D (x 10^{-13} m^2/s)	**R^2**	M_m (%)	D_x (x 10^{-13} m^2/s)	D_y (x 10^{-13} m^2/s)	D_z (x 10^{-13} m^2/s)	**R^2**
35°C	1.726	1.73	**0.9481**	1.726	1.05	4.17	3.33	**0.9481**
55°C	1.681	3.33	**0.7652**	1.681	2.56	2.11	2.14	**0.7652**
70°C	1.813	9.72	**0.7159**	1.813	8.06	2.04	2.64	**0.7159**

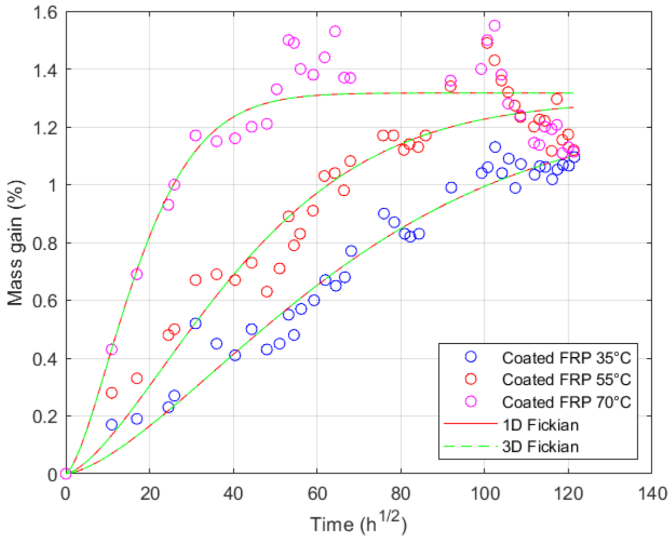

Figure 84. Absorption curve and Fickian fitted curves of the coated FRP specimens.

Regarding the diffusivity, the diffusion of water molecules through the exposed edges (D_y and D_z) on the coated FRP was higher at 70°C and lower at 35 and 55°C in comparison with the uncoated FRP. Therefore, the epoxy coating seems to be more efficient at low temperatures. To confirm this assumption, the Arrhenius plot for diffusivity values of coated FRP was plotted together with that of the uncoated FRP (Figure 85).

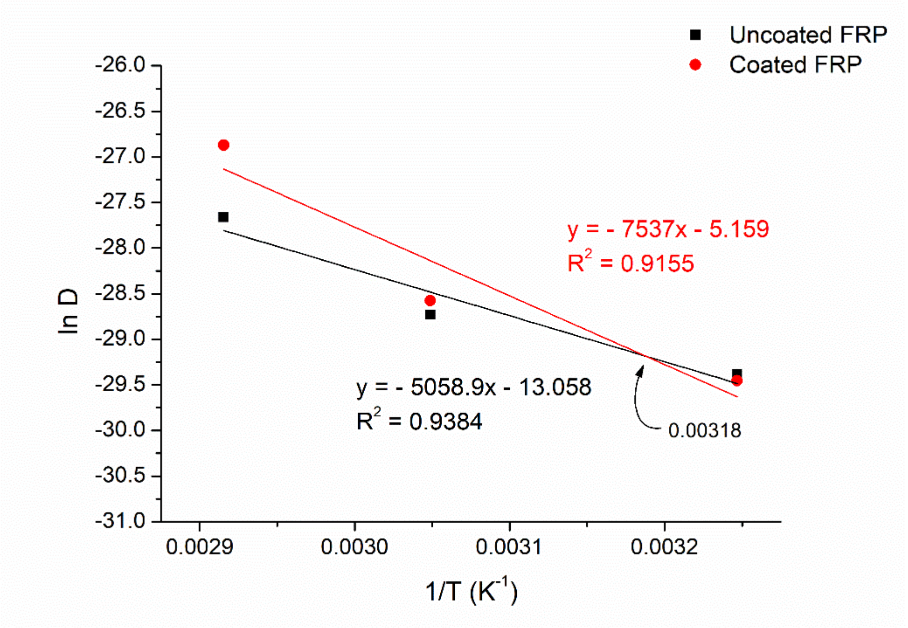

Figure 85. Arrhenius plot for diffusivity of both coated and uncoated FRP.

By applying the Arrhenius relationship (Equation 73), the extrapolation of diffusivity values to 25°C yielded a lower value for the uncoated FRP, corroborating with the hypothesis that the epoxy coating is more effective at lower temperatures. Moreover, the activation energy (*Q*) for the coated FRP was higher than the uncoated FRP (Table 22), meaning that the water penetrated the uncoated FRP more easily [184,202]. According to the Arrhenius plot in Figure 85, the intersection of the two curves occurs at 40.7°C (1/T = 0.00318 in Figure 85), meaning that the effectiveness of the epoxy coating is higher for temperatures lower than this value.

Table 22. Extrapolated diffusivity value for coated and uncoated FRP at 25°C and their activation energies (*Q*).

	D (x 10^{-13} m^2/s) (at 25°C)	**Q (kJ/mol)**
Coated FRP	0.59	62.70
Uncoated FRP	0.90	42.09

4.2.2. Hydrolysis investigation

In order to investigate the occurrence of hydrolysis during aging, a FTIR test was done on the FRP and epoxy specimens after 11550 hours of aging ($t^{1/2} \approx 107.47$ $h^{1/2}$). A clear indication of a hydrolysis reaction in the polymer is weight loss after a certain aging time [93,204]. However, from the absorption graphs it was not possible to notice such phenomenon. Figure 86 shows the infrared spectra of the FRP (86a) and epoxy (86b) for all temperatures. It can be seen that no additional peak appeared after 11550-hours aging, meaning that there was no thermal-oxidation process, since this phenomenon is often associated with either the appearance of amide groups (~1656 cm^{-1}) or carbonyl groups (~1736 cm^{-1}), characterized by the increase in the peak intensity in the wavenumber range 1550 – 1850 cm^{-1} [205].

Yagoubi *et al.* [94] state that the hydrolysis in epoxy resin occurs mainly in the ester and/or epoxide groups. Therefore, the peaks assigned to these groups would be the most important ones to analyze in order to investigate hydrolysis. In Figure 86 it can be seen that there was a decrease in intensity of the peak located at 919 cm^{-1} associated to the unreacted epoxide groups [94,170,171] with aging for both materials. This means that the exposure to temperature completed the curing reaction of the matrix, promoting a post-cure. Indeed, as explained in Section 4.2.1, the bond C-O is broken to form -CH_2 and react with the hardener during curing. Therefore, the hypothesis presented in Section 4.2.1 regarding the possibility of mass loss by hydrolysis to explain the decrease in saturation content with temperature observed in the neat epoxy specimens is proven wrong; the most likely event would be post-cure suffered at high temperatures.

Furthermore, there was no significant change in the intensity of the carbonyl peak, present in the ester group of the epoxy, at 1744 cm^{-1} with temperature, although it experienced a slight decrease. This might indicate a reaction between the water and the ester group [94], but since there was no weight loss, this event can be associated with the chemical bond of water molecules to the ester polar sites within the epoxy chain (bound molecules) [94].

The moisture absorption is characterized by the increase in the peak intensity of the hydroxyl group (-OH) in the range 2997 – 3600 cm^{-1} [165,166]. Therefore, it would be expected to notice an increase in the peak intensity of this chemical group. In fact, it was possible to see an increase in this peak intensity for the FRP after aging, but without a significant change with temperature. On the other hand, it could not be observed for the epoxy specimens, but this may be attributed to the low resolution of the spectra caused by the translucency of the epoxy specimens. It can be said, then, that there was an overlap between the hydroxyl from the water absorbed and that present in the DGEBA epoxy matrix.

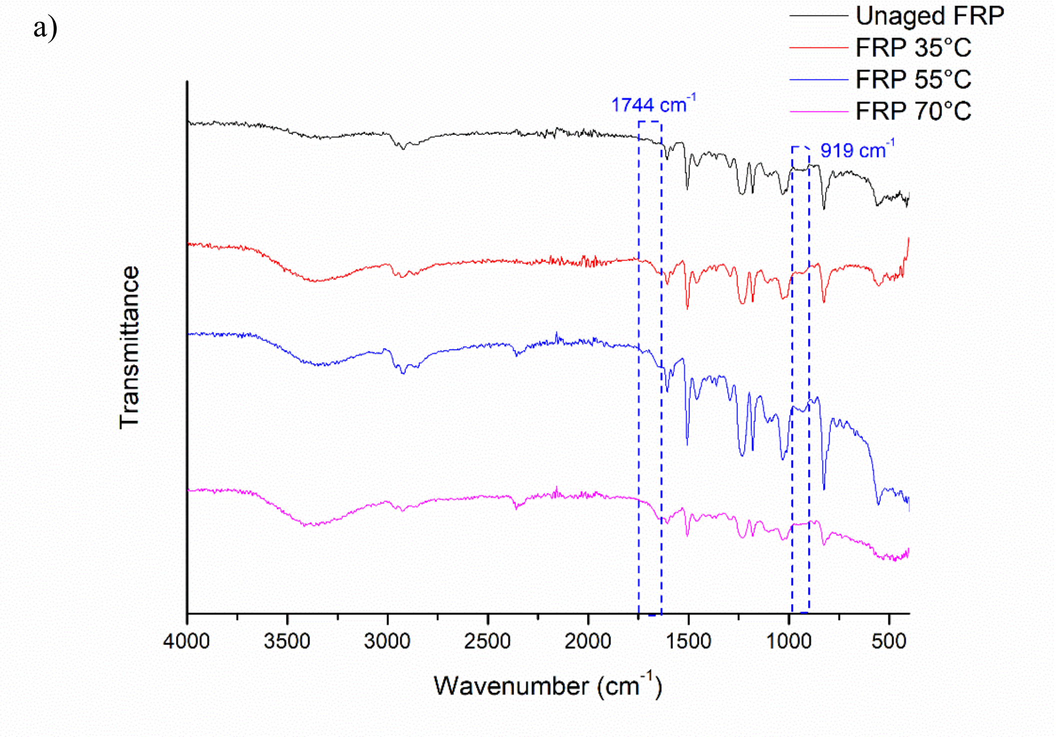

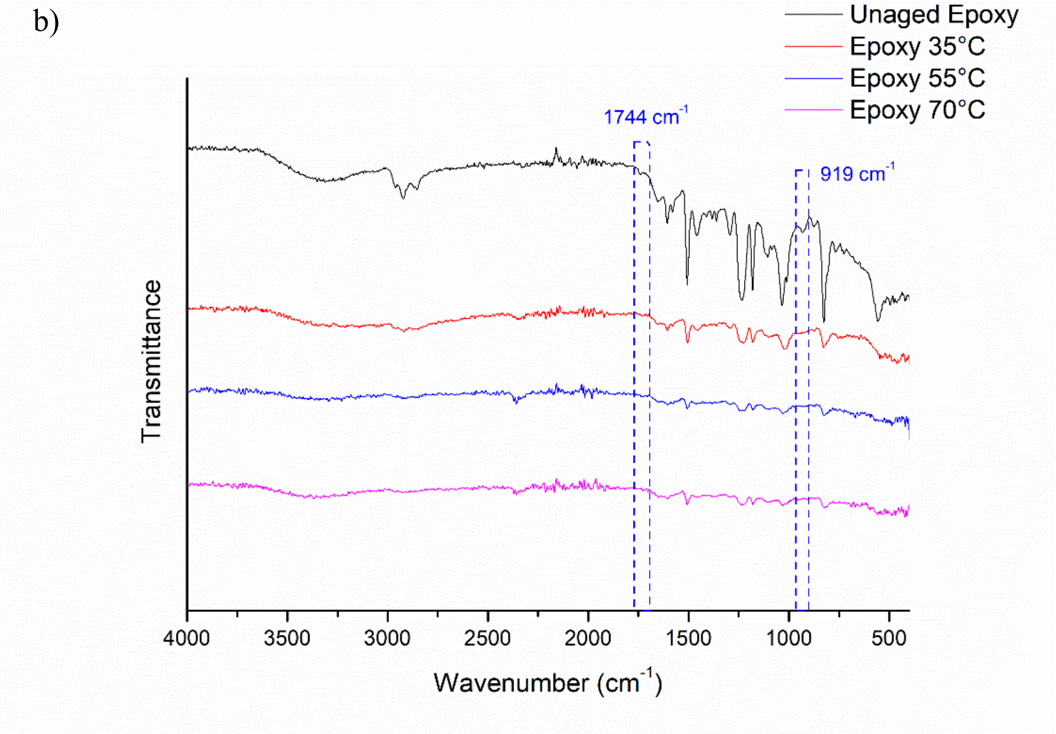

Figure 86. IR spectra for the (a) FRP and (b) epoxy specimens after 11550-hours aging.

4.2.3. Dynamic properties evaluation

Figure 87 shows the T_g value for the composites as a function of aging time. These values were obtained by the tanδ peak value. The behavior shown confirms the post-cure hypothesis at high temperatures, since the increase in T_g was more prominent at 70°C. At 55°C there was an initial enhancement of T_g followed by a slow decrease with time. On the other hand, at 35°C there was an initial decrease in T_g caused by plasticization, followed by an increase to a level above the value for the unaged specimens.

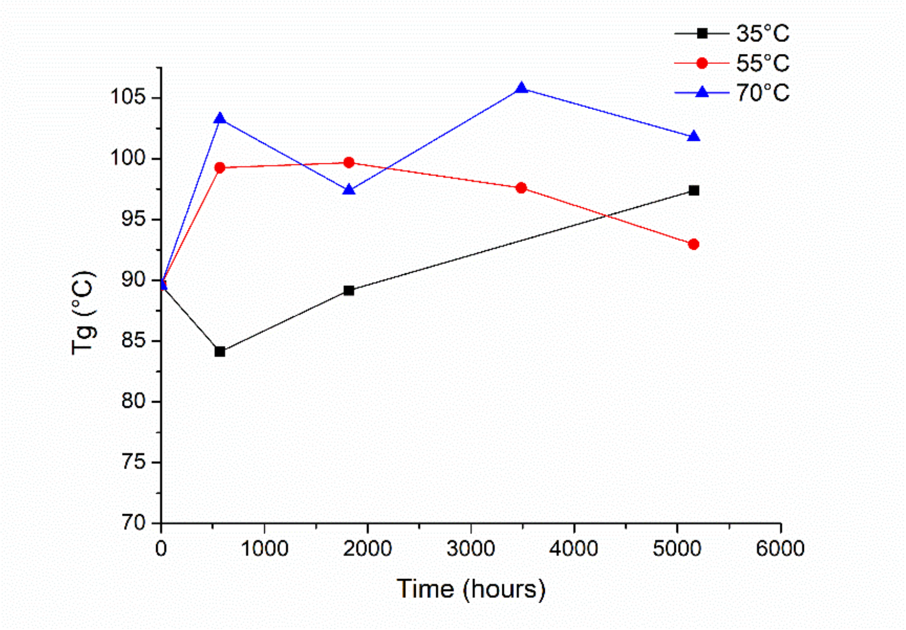

Figure 87. Evolution of T_g with aging time for the three temperatures.

Figure 88 shows the tan δ graphs for each temperature. Firstly, it should be noted that the tan δ values decreased with aging time, which is characteristic of the post-cure process [23,185]. This decrease is more significant at higher temperatures.

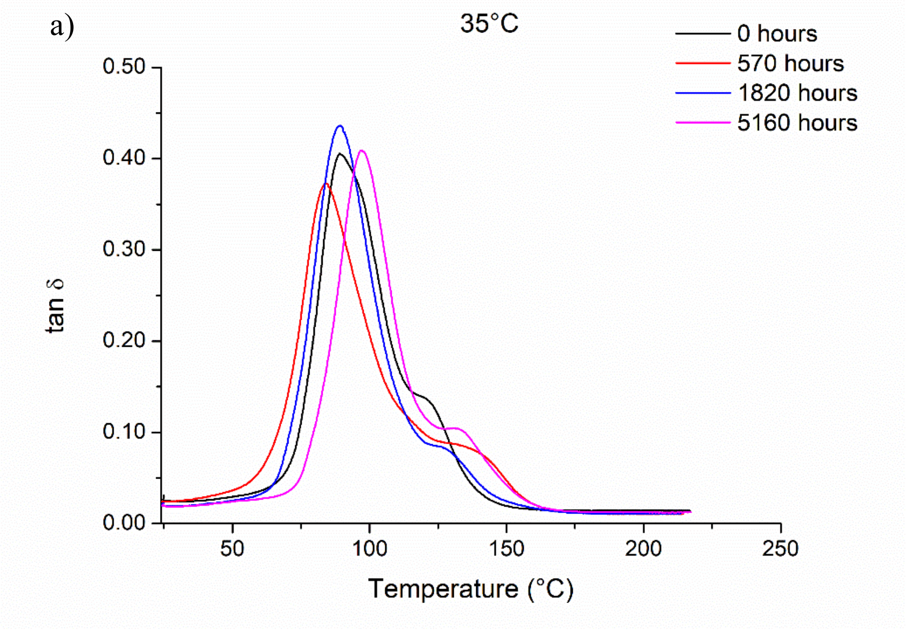

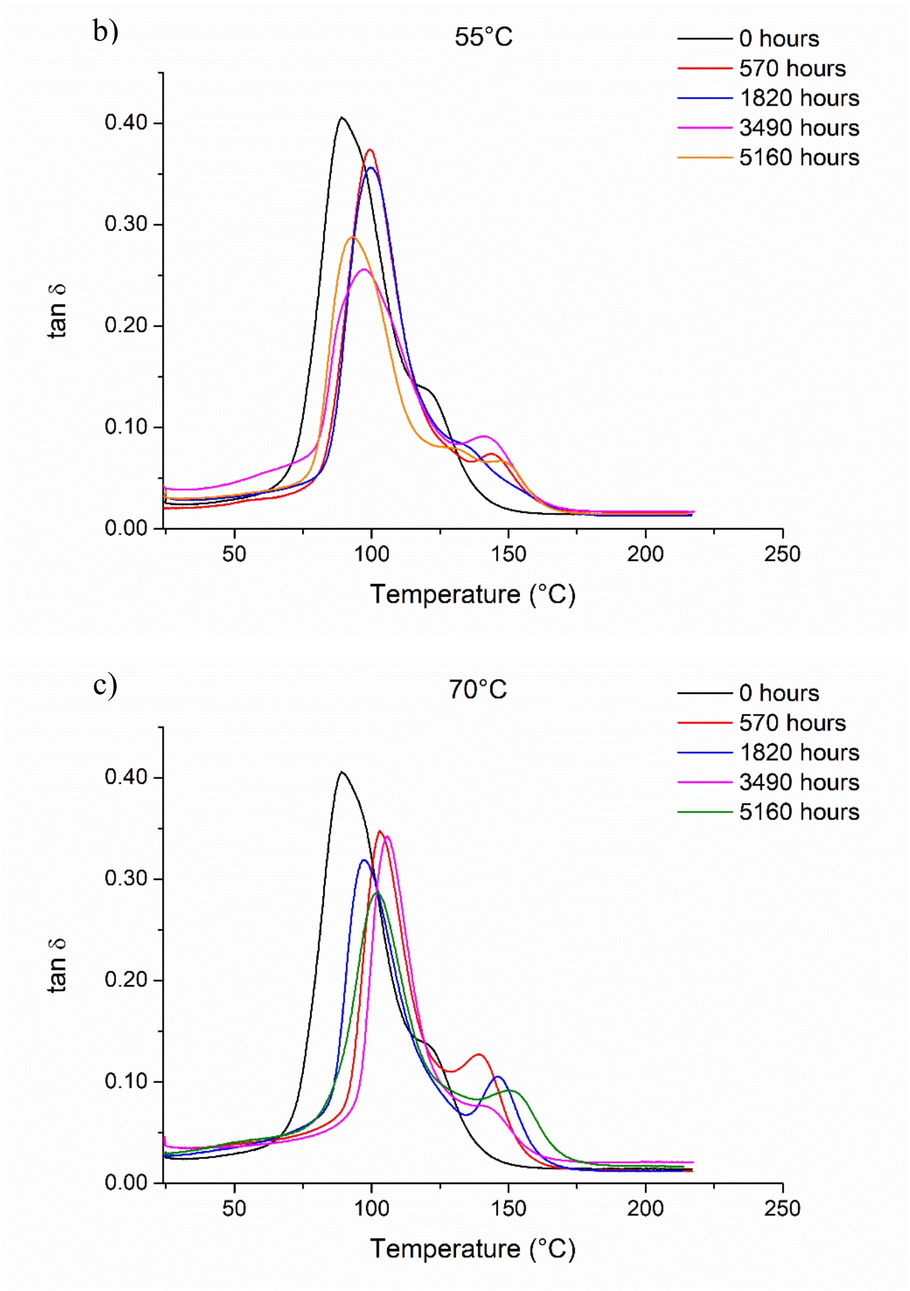

Figure 88. Evolution of tan δ with the aging time for (a) 35°C, (b) 55°C and (c) 70°C.

Other remarkable event is the appearance of a second peak with a smaller value than the main peak. Thomason [206] also observed this behavior for GFRPs and associated this effect to at least one of the following phenomena: (i) incomplete cure of the matrix, i.e., composites not fully cured, (ii) drying of the sample during heating, and (iii) the presence of an interphase region around the fiber with a higher T_g.

The first hypothesis is acceptable, but the sample should increase its curing degree the more it was exposed to high temperature. Moreover, for the DSC analysis performed on the unaged specimen before and after the exposure to high temperature (Section 4.1.2), the T_g peak for the as-manufactured specimen cannot be found in the specimen after the thermal cure in oven. To investigate whether this second peak was related to the curing degree, a DMTA test was performed on an as-manufactured specimen and three runs were taken in order to expose the material to cyclic temperature (from room temperature to 150°C). The time span between the runs was approximately two weeks. Figure 89 shows the tan δ curves for the specimen after the three runs. It can be seen an increase in the intensity of the second peak. A post-cure would reflect in either a disappearance or a decrease in this peak.

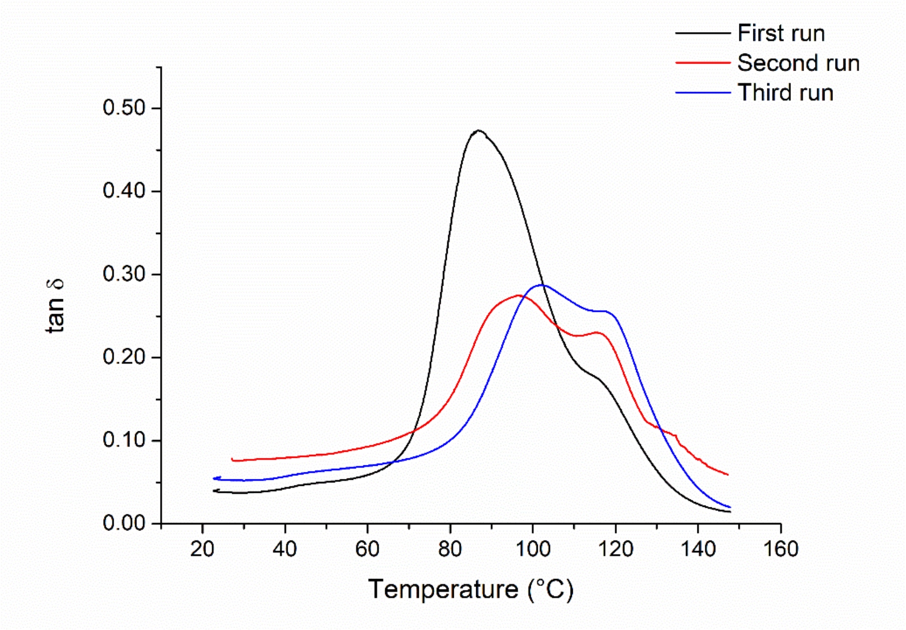

Figure 89. Three runs on the composite sample to investigate its curing degree.

The second hypothesis should not be feasible for the composites in this work, since the samples were not dried prior to DMA tests. The only possible hypothesis is the third one, where the fibers present an interphase around them with a higher T_g. This is plausible, provided that the fibers were coated with a sizing during manufacturing in order to improve matrix adhesion (Section 3.1.1) [154].

Even though the nature of the sizing was not provided by the manufacturer, some previous works in literature state that some sizing agents, especially silane, have chemical groups that are reactive with the matrix constituents and act to reduce the crosslinking density of the interphase, reducing its T_g [207,208]. In this work, the fiber sizing must have increased the crosslinking density on the fiber interphase, leading to increased local T_g, reflected in the second peak displaced to a higher temperature in the DMA graphs.

4.2.4. Non-Fickian Models

The non-Fickian models discussed in section 2.4.1 were also fitted to the experimental data of FRP and neat epoxy specimens in order to assess the phenomena involved in water absorption, such as polymer relaxation and polymer-water interaction. The curve fitting was also done by employing the least squares method into the trust-region-reflective algorithm.

4.2.4.1. Dual-Stage Model (Modified Jacobs-Jones Model)

Table 23 shows the Dual-Stage Model parameters for FRP and epoxy specimens, where M_T is the total absorbed moisture, which is the sum of M_1 and M_2. The graphs with the fitted curves are shown in Figure 90. It can be seen that the equations fit better to the epoxy than to the composites due to the deviations spotted in the composite's absorption curve, such as valleys and peaks in Figure 74. Nevertheless, this non-Fickian model adjusted better to the FRP absorption curve than the Fickian one. This non-Fickian model presented no significant difference in the correlation factor (R^2) for the neat epoxy specimens at different temperatures, while for the FRP the lower the temperature, the higher the correlation.

Table 23. Dual-Stage Fickian parameters for FRP and epoxy specimens at all temperatures.

			FRP			
	M_1 (%)	**D_1 (x 10^{-13} m^2/s)**	**M_2 (%)**	**D_2 (x 10^{-13} m^2/s)**	**M_T (%)**	**R^2**
35°C	1.667	1.28	0.166	12.22	1.833	**0.9492**
55°C	1.450	0.99	0.590	176.39	2.039	**0.8242**
70°C	1.184	5.56	0.658	1490	1.842	**0.7382**
			Epoxy			
	M_1 (%)	**D_1 (x 10^{-13} m^2/s)**	**M_2 (%)**	**D_2 (x 10^{-13} m^2/s)**	**M_T (%)**	**R^2**
35°C	4.726	1.09	0.268	7.50	4.994	**0.9928**
55°C	3.658	4.17	0.427	1309	4.085	**0.9579**
70°C	1.864	20.83	1.864	20.83	3.728	**0.9516**

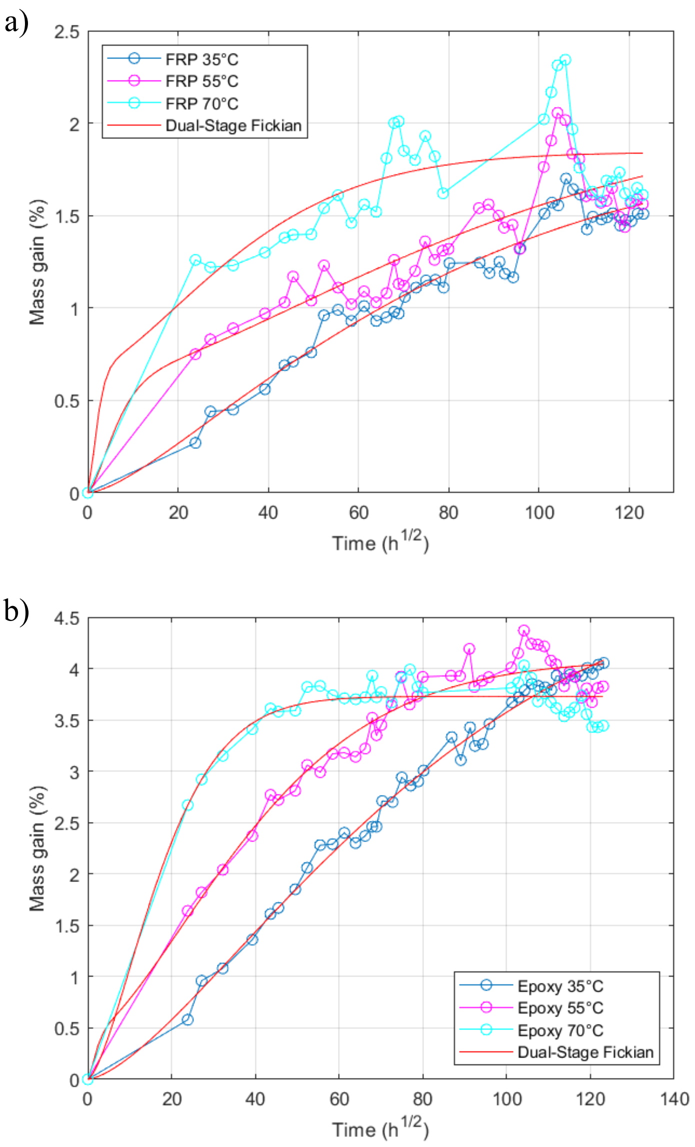

Figure 90. Dual-Stage curves for (a) FRP and (b) neat epoxy resin.

The second-stage saturation content (M_2) and diffusivity (D_2) increased with temperature, agreeing with some works from literature [129,130], although the D_2 value for the epoxy resin at 55°C was higher than at 70°C. For both materials the specimens exposed to 70°C presented the lowest Fickian saturation (M_1) and the highest second-stage saturation content (M_2), meaning that the relaxation-dominated component of the moisture diffusion is enhanced at high temperatures.

Placette *et al.* [130] exposed neat epoxy resin to relative humidity at 60 and 80°C and found out that the parameter D_2 was lower than D_1 for both temperatures. Therefore, they claimed that the Fickian behavior is dominant in the beginning of the absorption, which is widely supported by literature [67,99,120]. Conversely, in this work it was found that the second-stage diffusivity is higher than the first-stage.

An explanation to this phenomenon is pointed out by Maggana and Pissis [129], who studied the absorption behavior of epoxy systems and found similar results to this work ($D_2 > D_1$) and stated that when this happens, it means that the diffusion is controlled by the formation of hydrogen bonds between water and hydrophilic sites. This is because, according to the authors, D_1 refers to the diffusion rate in the less polar dense phase, which is mostly bonded to the free water, therefore is controlled by the initial Fickian diffusion process, while D_2 refers to the dense polar phase (bound water). Consequently, there is a strong bond between the water molecules and the polar sites of the resin matrix in both FRP and epoxy systems in this study. This will be corroborated with the Langmuir and Jacobs-Jones models in the subsequent sections. Furthermore, at 70°C the neat epoxy resin presented same values for D_1 and D_2. This may indicate a balanced diffusion process at higher temperatures for the neat resin due to the temperature's equal contribution to both diffusion mechanisms.

Regarding the differences between the materials studied, it can be highlighted that at 35°C the neat epoxy was less affected by the second stage than the FRP. Moreover, the second-stage absorption content (M_2) was higher in the neat epoxy than in the FRP, due to the neat resin's higher matrix proportion, resulting in more polar sites. Finally, the D_2 value for the neat epoxy specimens was lower than for the FRP, except for 55°C, which can suggest that the addition of fibers induced a stronger non-Fickian response.

4.2.4.2. Bao-Modified Dual-Stage Model

Table 24 shows the Bao-Modified Dual-Stage model results for FRP and epoxy specimens. The graphs with the fitted curves are shown in Figure 91.

Despite the relatively good fitting found for the materials and temperatures tested, there is no clear correlation between the diffusivity values of different temperatures. Besides, unlike the original Dual-Stage Model, this model does not consider an ultimate equilibrium moisture content, i.e., the material absorbs moisture endlessly [131]. Therefore, this model does not result in a valid physical behavior and no significant contribution can be made to the study by this model. Thus, it will be discarded from the material behavior assessment (item 7.2.1.3).

Table 24. Fitting results from the Bao-Modified Dual-Stage Fickian Model.

FRP

	M_1 (%)	**D_1 (x 10^{-13} m^2/s)**	**k**	**R^2**
35°C	1.169	3.89	0.0039	**0.9472**
55°C	0.608	120.28	0.0153	**0.8158**
70°C	1.835	16.39	2.22E-14	**0.7277**
		Epoxy		
	M_1 (%)	**D_1 (x 10^{-13} m^2/s)**	**k**	**R^2**
35°C	1.619	7.22	0.0133	**0.9910**
55°C	4.186	7.22	2.22E-14	**0.9545**
70°C	3.741	39.17	2.22E-14	**0.9467**

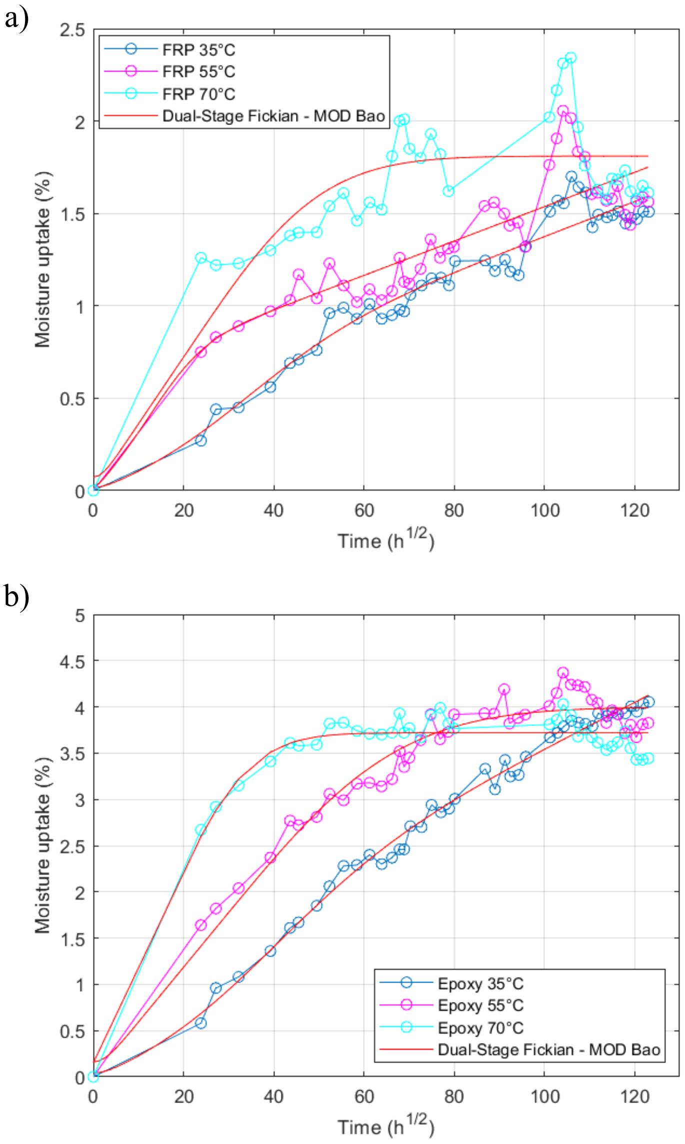

Figure 91. Bao-Modified Dual-Stage curves for (a) FRP and (b) neat epoxy resin.

4.2.4.3. Berens-Hopfenberg (BH) Model

Table 25 shows the BH Model fitting results for FRP and epoxy specimens, where M_T stands for the total moisture absorption, which is the sum of the Fickian (M_F) and relaxation-related (M_R) sorption. For both materials, the relaxation time (τ) decreased with temperature, agreeing with reports in literature [99,209]. In fact, it is already well-established in literature that at higher temperatures there is a stronger molecular motion on the polymeric segments, promoting a stronger relaxation process, decreasing the τ value, inducing a higher viscous contribution to the polymer's mechanical behavior [186].

The relaxation time for the neat epoxy was found to be lower than for the FRP for 55 and 70°C. This observation agrees with reports in literature [210–212], which state that the addition of fibers slows the polymeric relaxation process by restraining the molecular flow in the polymer next to the interface. Additionally, Obaid *et al.* [211] affirm that covalent bonds between fiber and matrix at the interface restrains the polymer mobility and relaxation, therefore the addition of sizing to the fibers to strengthen the interface also slows the polymer relaxation. At 35°C the relaxation time for the neat epoxy specimens was higher than for the FRP, which might indicate that at low temperatures the molecular movement restriction around the fibers is less affected.

Regarding the relaxation-related saturation content (M_R), its value decreased with temperature for both materials. Starkova *et al.* [99] found the same results for epoxy resin immersed in distilled water. The authors found that at 70°C there was no M_2, leading to the assumption that at this temperature the relaxation processes were fully completed. For the materials in this study, the exposure to 70°C fostered a stronger and faster relaxation, but a higher temperature would be needed for a full relaxation of the matrix. Furthermore, the relaxation-related moisture content of the FRP was lower than the neat epoxy. This is likely related to the short relaxation time presented by the neat epoxy, being significantly lower than the aging time, except for 35°C, promoting a stronger non-Fickian moisture absorption.

The graphs with the fitted curves for the BH Model are shown in Figure 92.

Table 25. BH Model results for FRP and epoxy specimens.

			FRP			
	M_F (%)	**D (x 10^{-13}m^2/s)**	**M_R (%)**	**τ (h)**	**M_T (%)**	**R^2**

35°C	0.466	10.56	1.253	7344	1.719	**0.9497**
55°C	0.707	83.06	1.130	7077	1.837	**0.8298**
70°C	0.906	2966	0.931	2189	1.837	**0.7478**
			Epoxy			
	M_F (%)	**D (x 10^{-13} m^2/s)**	**M_R (%)**	**τ (h)**	**M_T (%)**	**R^2**
35°C	1.249	6.67	3.431	8719	4.680	**0.9929**
55°C	1.140	81.39	2.889	2740	4.029	**0.9615**
70°C	1.279	1671	2.446	682	3.725	**0.9525**

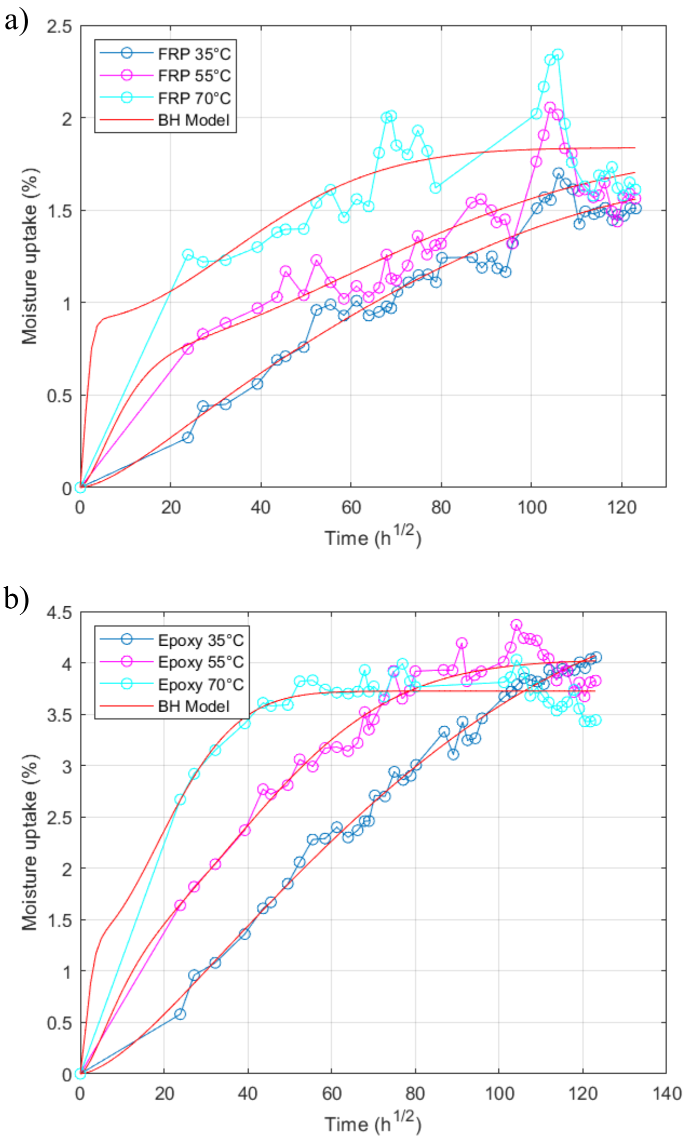

Figure 92. Berens and Hopfenberg (BH) curves for (a) FRP and (b) neat epoxy resin.

Jiang *et al.* [209] reported similar results for relaxation times for a polyester-based composite, where the samples immersed in distilled water at 20 and 40°C presented relaxation times equal to 1786 and 328 hours, respectively. Similarly, Yin *et al.* [213] immersed two different cycloaliphatic epoxy resins in deionized water at 80°C and found out that the relaxation time varied from 96.88 and 228.75 hours; such range includes the value found in this work for a similar temperature (70°C).

In order to investigate the heterogeneity of the relaxation processes in the polymer, a curve fitting of the experimental data to the Equation 45 (Section 2.4.1.4 – Page 87) for multiple relaxation times, namely expanded BH model, was also performed using two relaxation processes was done. The results are shown in Table 26. The fitted curves for the Expanded BH model can be seen in Figure 93.

For both materials, it can be seen that the values of τ_1 and τ_2 were similar to each other, indicating the same relaxation process for different polymeric segments. Furthermore, the relaxation-related saturation contents M_1 and M_2 were found to be different from each other, except for the FRP at 35°C. Even though the different polymeric phases presented different total moisture absorption, it was shown that the bulk matrix presented a homogeneous relaxation behavior, considering the same relaxation times. This may indicate that there is a uniformity in the moisture diffusion within the material. Therefore, the absorption behavior experienced by the composite and neat resin is already perfectly described by the original BH model (Table 25).

Table 26. BH model parameters with two relaxation times.

FRP								
	M_F (%)	**D (x 10^{-13}m^2/s)**	**$M_{R,1}$ (%)**	**τ_1 (h)**	**$M_{R,2}$ (%)**	**τ_2 (h)**	**M_T (%)**	**R^2**
35°C	0.466	10.42	1.15	7343	0.098	7346	1.718	**0.9497**
55°C	0.707	81.78	0.705	7076	0.425	7077	1.837	**0.8298**
70°C	0.906	616.10	0.681	2189	0.250	2189	1.837	**0.7478**
Epoxy								
	M_F (%)	**D (x 10^{-13} m^2/s)**	**$M_{R,1}$ (%)**	**τ_1 (h)**	**$M_{R,2}$ (%)**	**τ_2 (h)**	**M_T (%)**	**R^2**
35°C	1.248	6.79	3.319	8732	0.112	8425	4.680	**0.9929**
55°C	1.140	81.97	2.089	2741	0.799	2741	4.029	**0.9615**
70°C	1.280	616.08	2.112	682	0.333	683	3.725	**0.9525**

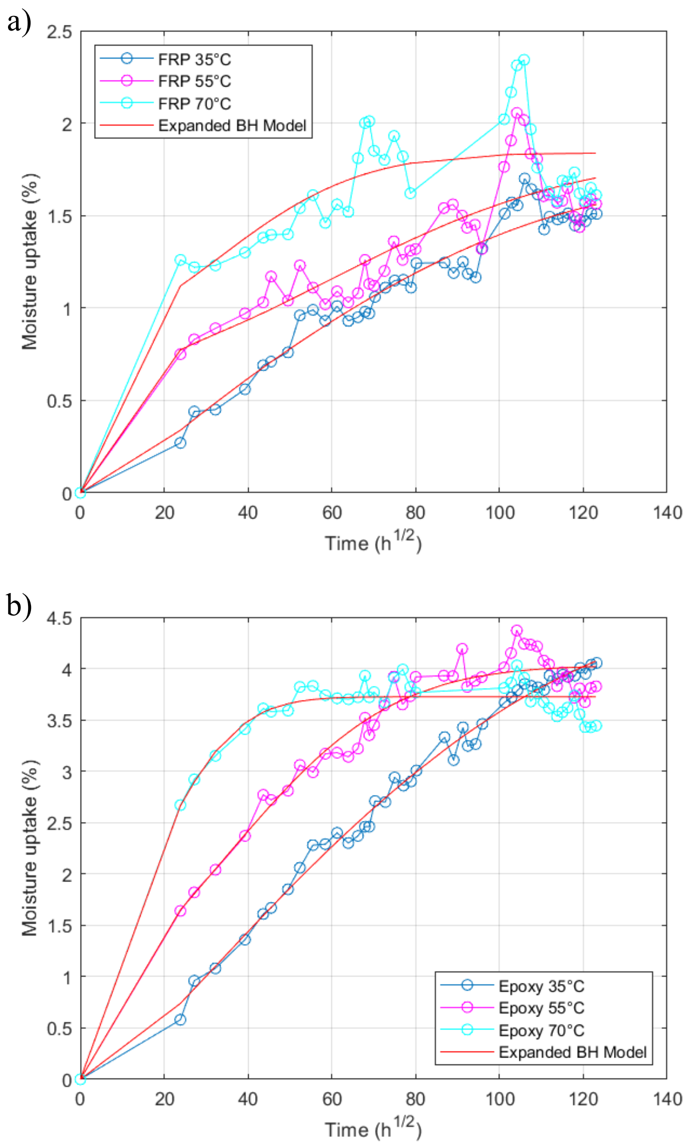

Figure 93. Expanded BH Model curves for (a) FRP and (b) neat epoxy samples.

4.2.4.4. Langmuir Model

Table 27 shows the fitting results of the Langmuir Model for the FRP and neat epoxy specimens. The graphs with the fitted curves can be seen in Figure 94.

It can be seen that the diffusivity, β and γ values increased with temperature for both materials, which means that temperature affects the mobility of water molecules, providing a more intense movement between free and bound molecules. This behavior is in accordance with the results found by Surathi and Karbhari [124].

According to Guloglu [126], the lower the values of β and γ, the longer it would take for the material to saturate, as explained in Section 2.4.1.1. Indeed, as seen in Section 4.2.1.1, the materials exposed to 35°C reached the saturation level at a longer time compared with higher temperatures. An increase in the β and γ

values implies in more bound and unbound water molecules. This happens at higher temperatures, as shown in Table 27, reflecting in the higher moisture absorbed. Since the bound molecules are characteristic of the second-stage Fickian absorption, these results support the increase in the saturation content related to the dense polar phase (M_2) with temperature (Table 23).

Additionally, it can be seen that both β and γ values of the neat epoxy resin are higher than those of the FRP. It may indicate that the addition of fibers hindered the penetration of both free or bound molecules, decreasing the total moisture content absorbed. Therefore, proportionally, the neat epoxy resin has much more free and bound molecules in their polymeric sites than the FRP.

Table 27. Langmuir Model results for FRP and epoxy specimens.

			FRP		
	M_m (%)	**β**	**γ**	**D (x 10^{-13} m^2/s)**	**R^2**
35°C	1.714	4.22E-04	1.40E-04	13.33	**0.9500**
55°C	1.838	2.24E-04	1.41E-04	67.22	**0.8296**
70°C	1.837	4.73E-04	4.58E-04	351.39	**0.7474**
			Epoxy		
	M_m (%)	**β**	**γ**	**D (x 10^{-13} m^2/s)**	**R^2**
35°C	4.327	1.30E-03	1.68E-04	2380	**0.9909**
55°C	4.028	9.68E-04	3.68E-04	2158	**0.9614**
70°C	3.724	3.10E-03	1.50E-03	1875	**0.9523**

a)

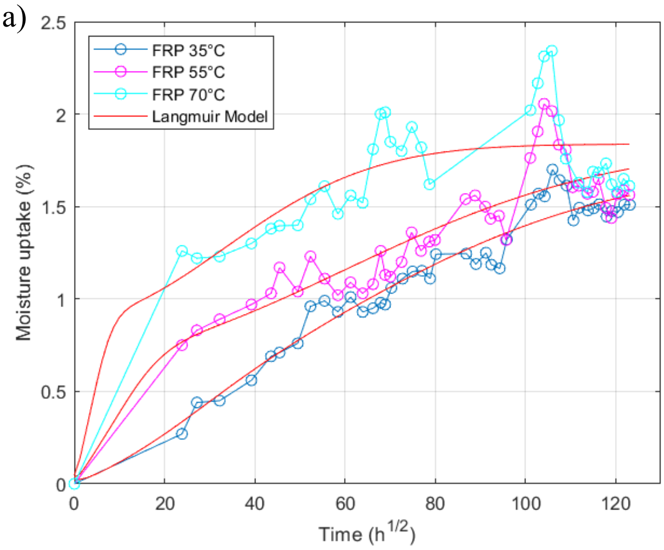

b)

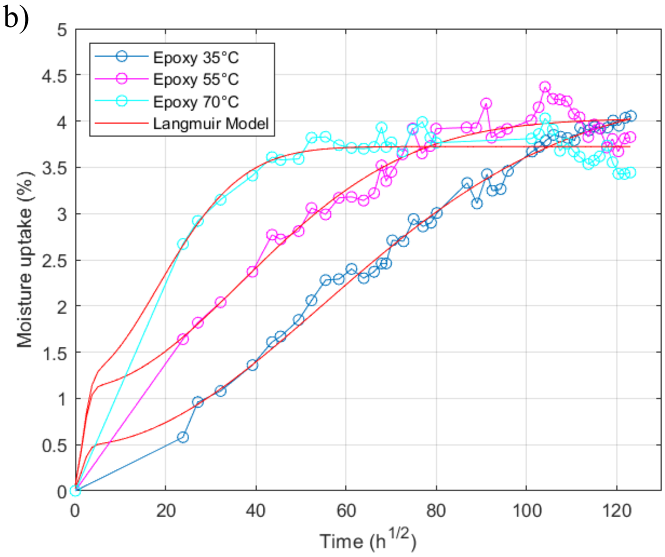

Figure 94. Langmuir curves for (a) FRP and (b) neat epoxy resin.

4.2.4.5. Jacobs and Jones Model

Table 28 shows the Jacobs-Jones Model results for the FRP and epoxy specimens. The graphs with the fitted curves can be found in Figure 95.

The results show that for the FRP specimens the volume fraction of the highly crosslinked dense phase (V_d) of the material exposed to 70°C was the lowest among all temperatures tested. This means that structural changes occurred from the exposure to high temperature. As seen in the Langmuir model, high temperatures promote a larger number of molecules bonded to the polymeric sites, therefore the network presents higher mobility, decreasing the crosslink density. On the other hand, an increase in the V_d value was found for the neat epoxy system, which corroborates with the hypothesis that the neat epoxy resin suffered post-cure, thereby increasing its crosslinking density, promoting a lower moisture absorption capacity.

Furthermore, it can also be observed that the diffusivity values for the less densely crosslinked phase (D_l) are much higher than those for the densely crosslinked phase (D_d) for both materials at all temperatures. Correlating the results with the Modified Jacobs-Jones model (Dual-Stage Model – Section 4.2.4.1), where the higher diffusivity value occurred in the dense polar region of the polymer, then it can be supposed that the less-densely crosslinked phase (D_l in Jacobs-Jones Model) consists of the highly polar region of the epoxy matrix.

Table 28. Jacobs-Jones Model results for FRP and epoxy specimens.

FRP

	M_m (%)	V_d	D_d (x 10^{-13} m^2/s)	D_l (x 10^{-13} m^2/s)	R^2
35°C	1.833	0.909	1.29	12.22	**0.9492**
55°C	2.040	0.711	0.99	176.39	**0.8242**
70°C	1.842	0.643	5.55	871.11	**0.7382**

Epoxy

	M_m (%)	V_d	D_d (x 10^{-13} m^2/s)	D_l (x 10^{-13} m^2/s)	R^2
35°C	4.994	0.946	1.12	7.78	**0.9928**
55°C	4.085	0.896	4.17	1760	**0.9579**
70°C	3.728	1.000	21.11	27784	**0.9516**

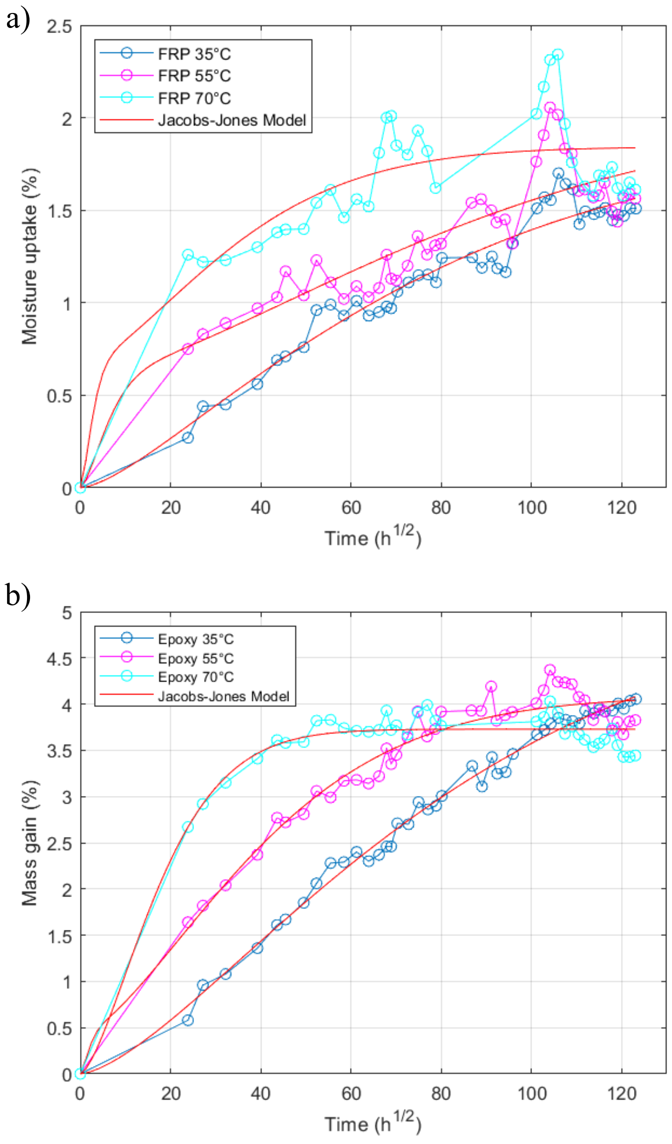

Figure 95. Jacobs-Jones curves for (a) FRP and (b) neat epoxy resin.

4.2.4.6. Goodness of fit and absorption parameters' correlation

The composites' absorption behavior showed a better fit for the non-Fickian models compared to the Fickian model, mainly for 55 and 70°C. This result demonstrates that the non-Fickian behavior is more prominent at high temperatures, as previously explained. On the other hand, for the neat epoxy specimens there was no significant difference between the adjustment of the models. This indicates that the neat epoxy can be modeled by the Fickian behavior, but the non-Fickian models provide important information regarding the physical modifications promoted in the resin matrix by temperature and moisture. Table 29 summarizes the output parameters of the most important models previously shown. Figure 96 summarizes all the results in Table 29 in graphs for both FRP and neat epoxy materials, which emphasizes the good correlation for all the non-Fickian models.

Table 29. Summary of the most important absorption models aforementioned for FRP and epoxy systems.

<table>
<tr><th colspan="7">1D Fickian</th></tr>
<tr><th colspan="7">FRP</th></tr>
<tr><th></th><th colspan="2">M_m (%)</th><th colspan="2">D (x 10^{-13} m^2/s)</th><th colspan="2">R^2</th></tr>
<tr><td>35°C</td><td colspan="2">1.726</td><td colspan="2">1.73</td><td colspan="2">0.9481</td></tr>
<tr><td>55°C</td><td colspan="2">1.681</td><td colspan="2">3.33</td><td colspan="2">0.7652</td></tr>
<tr><td>70°C</td><td colspan="2">1.813</td><td colspan="2">9.72</td><td colspan="2">0.7159</td></tr>
<tr><th colspan="7">Epoxy</th></tr>
<tr><th></th><th colspan="2">M_m (%)</th><th colspan="2">D (x 10^{-13} m^2/s)</th><th colspan="2">R^2</th></tr>
<tr><td>35°C</td><td colspan="2">4.794</td><td colspan="2">1.31</td><td colspan="2">0.9927</td></tr>
<tr><td>55°C</td><td colspan="2">4.041</td><td colspan="2">5.00</td><td colspan="2">0.9551</td></tr>
<tr><td>70°C</td><td colspan="2">3.728</td><td colspan="2">20.83</td><td colspan="2">0.9516</td></tr>
<tr><th colspan="7">Dual-Stage Fickian</th></tr>
<tr><th colspan="7">FRP</th></tr>
<tr><th></th><th>M_1 (%)</th><th>D_1 (x 10^{-13} m^2/s)</th><th>M_2 (%)</th><th>D_2 (x 10^{-13} m^2/s)</th><th>M_T (%)</th><th>R^2</th></tr>
<tr><td>35°C</td><td>1.667</td><td>1.28</td><td>0.166</td><td>12.22</td><td>1.833</td><td>0.9492</td></tr>
<tr><td>55°C</td><td>1.450</td><td>0.99</td><td>0.590</td><td>176.39</td><td>2.039</td><td>0.8242</td></tr>
<tr><td>70°C</td><td>1.184</td><td>5.56</td><td>0.658</td><td>1490</td><td>1.842</td><td>0.7382</td></tr>
<tr><th colspan="7">Epoxy</th></tr>
<tr><th></th><th>M_1 (%)</th><th>D_1 (x 10^{-13} m^2/s)</th><th>M_2 (%)</th><th>D_2 (x 10^{-13} m^2/s)</th><th>M_T (%)</th><th>R^2</th></tr>
<tr><td>35°C</td><td>4.726</td><td>1.09</td><td>0.268</td><td>7.50</td><td>4.994</td><td>0.9928</td></tr>
</table>

55°C	3.658	4.17	0.427	1309	4.085	**0.9579**
70°C	1.864	20.83	1.864	20.83	3.728	**0.9516**
			BH Model			
			FRP			
	M_F (%)	**D (x 10^{-13}m^2/s)**	**M_R (%)**	**τ (h)**	**M_T (%)**	**R^2**
35°C	0.466	10.56	1.253	7344	1.719	**0.9497**
55°C	0.707	83.06	1.130	7077	1.837	**0.8298**
70°C	0.906	2966	0.931	2189	1.837	**0.7478**
			Epoxy			
	M_F (%)	**D (x 10^{-13} m^2/s)**	**M_R (%)**	**τ (h)**	**M_T (%)**	**R^2**
35°C	1.249	6.67	3.431	8719	4.680	**0.9929**
55°C	1.140	81.39	2.889	2740	4.029	**0.9615**
70°C	1.279	1671	2.446	682	3.725	**0.9525**
			Langmuir Model			
			FRP			
	M_m (%)	**β**	**γ**	**D (x 10^{-13} m^2/s)**	**R^2**	
35°C	1.714	4.22E-04	1.40E-04	13.33	**0.9500**	
55°C	1.838	2.24E-04	1.41E-04	67.22	**0.8296**	
70°C	1.837	4.73E-04	4.58E-04	351.39	**0.7474**	
			Epoxy			
	M_m (%)	**β**	**γ**	**D (x 10^{-13} m^2/s)**	**R^2**	
35°C	4.327	1.30E-03	1.68E-04	2380	**0.9909**	
55°C	4.028	9.68E-04	3.68E-04	2158	**0.9614**	
70°C	3.724	3.10E-03	1.50E-03	1875	**0.9523**	

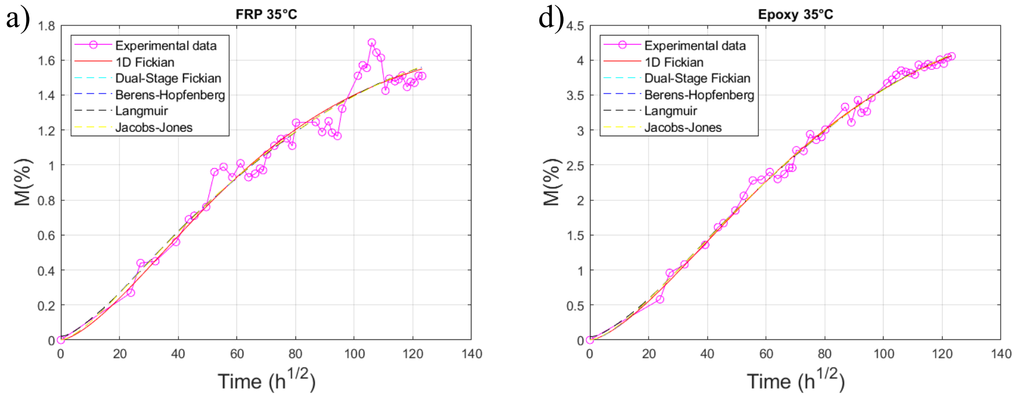

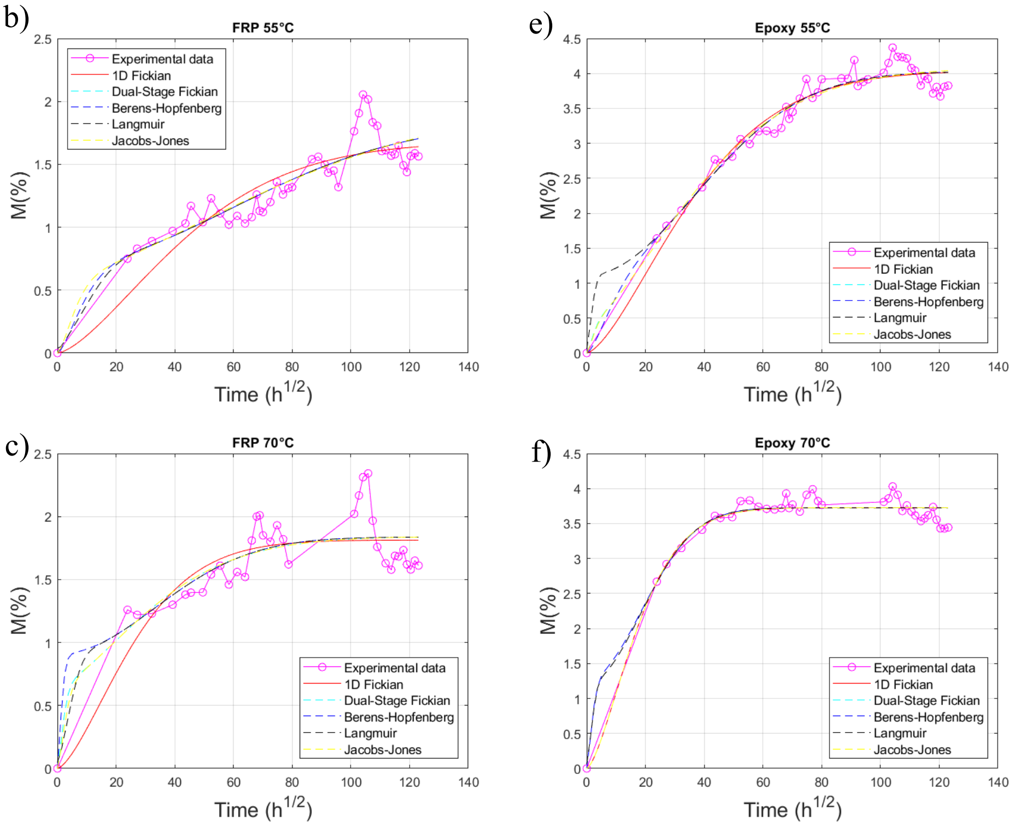

Figure 96. Fickian and non-Fickian fitted curves for the FRP at 35°C (a), 55°C (b) and 70°C (c) and for the neat epoxy at 35°C (d), 55°C (e) and 70°C (f).

Aiming to correlate the most important factors that would affect the moisture absorption of the materials, Arrhenius graphs for the Dual-Stage diffusivities were plotted (Figure 97). The correlation graphs with temperature for the relaxation time (Figure 98) and relaxation-related absorption (Figure 99) were also plotted. The curve fitting along with the mathematical relationships are included on the graphs.

Theactivation energies calculated from the Arrhenius equation displayed in the graphs of Figure 97 are shown in Table 30. Q_1 and Q_2 stand for the activation energy of D_1 and D_2, respectively. For the FRP the second-stage absorption (Q_2) was higher than the first-stage (Q_1), indicating that the diffusion-controlled stage is not only easier to occur but also predominant, especially at the early stages of absorption. This might be credited to a higher content of voids that increase the trap of free water molecules. On the other hand, for the neat epoxy samples, Q_2 was found to be lower than Q_1, meaning a strong interaction between the bound water molecules and the polar sites , since the second-stage diffusion is controlled by the formation of hydrogen bonds between polymer and water [129]. Table 31 shows the values of these diffusivities, alongside the relaxation-related relaxation time and moisture absorption, extrapolated to 25°C. Like the previous results for the FRP at

35°C, at 25°C the movement restriction imposed by the fibers on the bulk matrix is negligible, since the relaxation time for the neat epoxy resin is much higher than for the FRP. Consequently, the neat epoxy will absorb more relaxation-induced moisture (M_2).

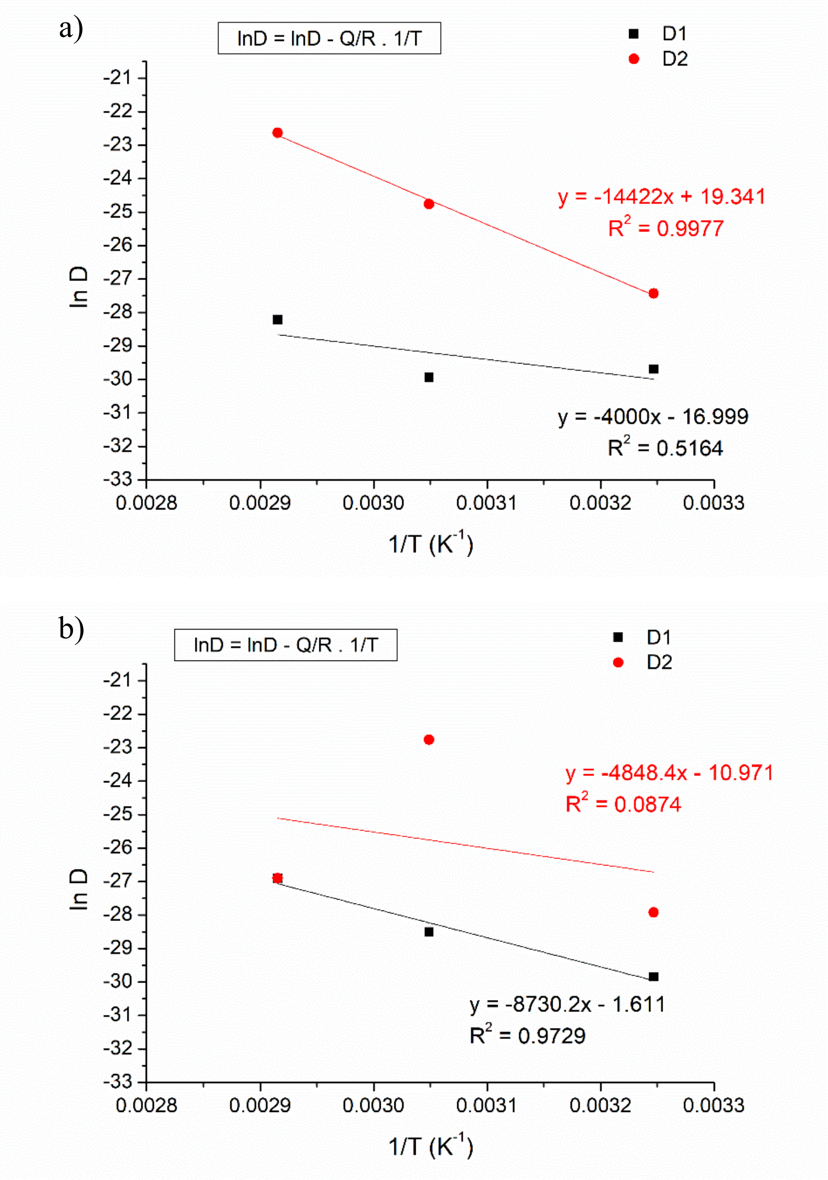

Figure 97. Arrhenius plots for the diffusivity values from the Dual-Stage Fickian model for the (a) FRP and (b) epoxy materials.

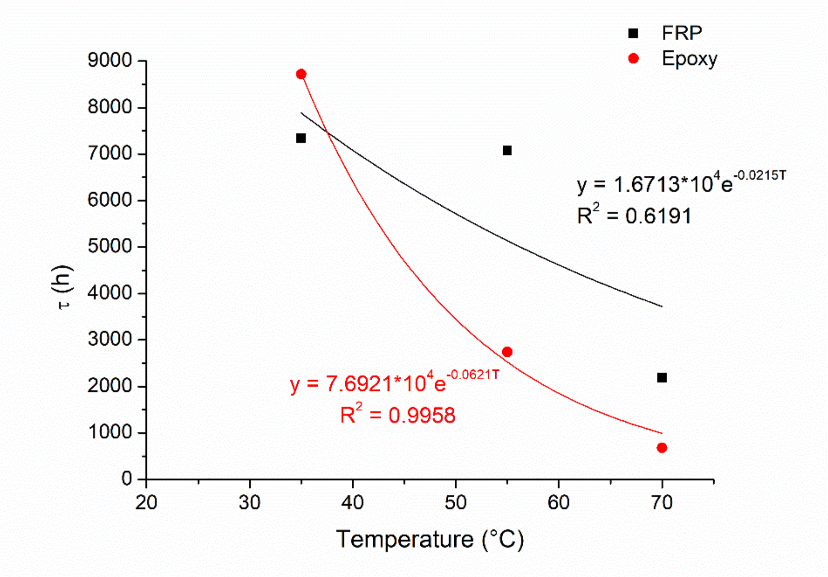

Figure 98. Relaxation time as a function of temperature for the FRP and epoxy systems.

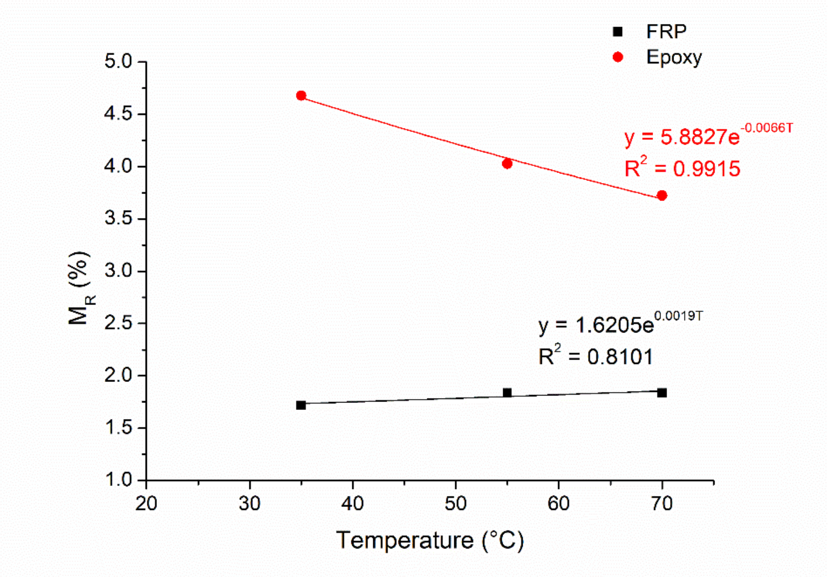

Figure 99. Relaxation-induced moisture absorption.

Table 30. Activation energy of both diffusion stages for FRP and neat epoxy resin.

	Q_1 (kJ/mol)	**Q_2 (kJ/mol)**
FRP	33.28	119.99
Epoxy	72.63	40.34

Table 31. Non-Fickian parameters at 25°C.

	25°C			
	D_1 (x 10^{-13} m^2/s)	**D_2 (x 10^{-13} m^2/s)**	**τ (h)**	**M_R (%)**
FRP	0.61	2.41	9764	1.69

Epoxy	0.38	14.77	16285	4.98

Considering the post-curing effects on the epoxy's absorption capacity (Table 32), this phenomenon should be incorporated into an analytical model to better assess the effects of moisture and temperature on the material. Therefore, a modification to a non-Fickian model is proposed. The BH Model is chosen to be adjusted, since it considers the polymer relaxation, a temperature-dependent parameter. Jiang *et al.* [209] proposed a modified BH Model to account for hydrolysis phenomenon they observed in pultruded GFRP bridge profiles exposed to RH at 40°C, by adding a third term to Equation 40, resulting in Equation 79. In this equation, the first two terms are the Fickian- and relaxation-related absorption mechanisms, already explained in Section 2.4.1.4, and the third term refers to mass loss, with M_3 is set to be negative and represents the mass lost from hydrolysis and k_2 represents the hydrolysis rate.

$$M_t = M_{m,F}\left\{1 - exp\left[-7.3\left(\frac{Dt}{h^2}\right)^{0.75}\right]\right\} + M_{m,R}\left[1 - exp\left(-\frac{t}{\tau_R}\right)\right] + M_3[1 - exp(-kt)] \tag{79}$$

However, this equation was attempted to model the post-curing effects on moisture absorption of the materials in this study, with M_3 being the moisture mass hindered by post-curing and k the rate of post-curing.

Good correlations were found for both composite and neat epoxy resin, as it can be seen in Table 32, where M_T is the total moisture absorbed, a sum of M_F, M_R and M_3. The fitted curves are shown in Figure 100.

Focus should be given to the parameters M_3 and k from Table 32. It can be seen that the post-curing rate k increases with temperature for both materials, which means that the cure reaction rate is thermally activated [214]. Also, the post-curing rates of the neat epoxy resin are significantly higher than those of the FRP, especially at 55 and 70°C, which were three orders of magnitude higher than the FRP. In other words, the neat epoxy resin suffered post-curing more easily, owing to the blockage of reactant movements within the bulk polymer matrix imposed by the fibers. This occurs due to the restrictions imposed by the fibers to the movements of the reactive curing groups in the bulk matrix. Moreover, the moisture mass hindered by post-cure (M_3) for the FRP was even higher than for the neat epoxy resin at all temperatures, showing that the composites also suffered post-curing in hygrothermal environment and it was not reflected on a decrease in the total moisture gain due to the fiber/matrix interface and the inclusion of voids and imperfections by the addition of fibers that fostered moisture ingress.

Table 32. Parameters for the post-curing modified BH Model.

FRP

Temperature (°C)	M_F (%)	D (x 10^{-13} m^2/s)	M_R (%)	τ (h)	M_3 (%)	k (h^{-1})	M_T (%)	R^2
35	0.467	10.83	1.778	9119	-0.99	2.88E-05	1.245	**0.9501**
55	0.697	96.39	1.657	8589	-1.00	3.14E-05	1.354	**0.8324**
70	0.890	1958	1.485	3298	-1.00	5.98E-05	1.375	**0.7841**

Epoxy

Temperature (°C)	M_F (%)	D (x 10^{-13} m^2/s)	M_R (%)	τ (h)	M_3 (%)	k (h^{-1})	M_T (%)	R^2
35	4.794	1.31	3.80E-14	6006	-4.44E-14	1.00E-10	4.794	**0.9927**
55	4.041	5.00	2.25E-14	5993	-2.22E-14	3.85E-02	4.041	**0.9551**
70	4.145	22.78	2.22E-14	5988	-0.42	5.60E-02	3.726	**0.9517**

a)

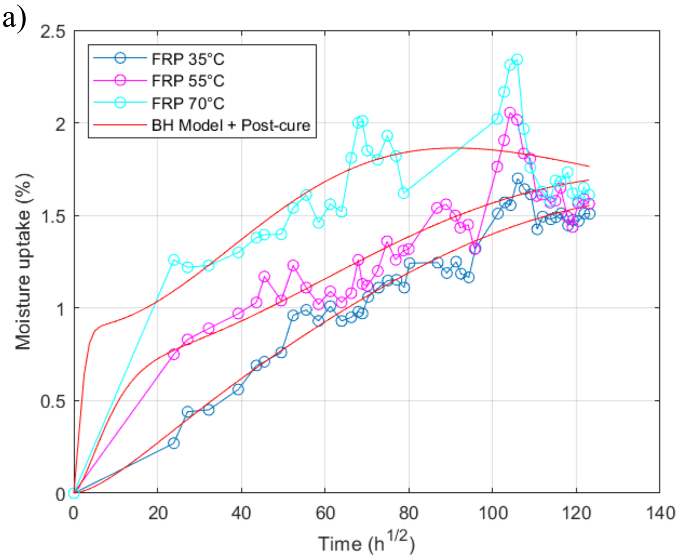

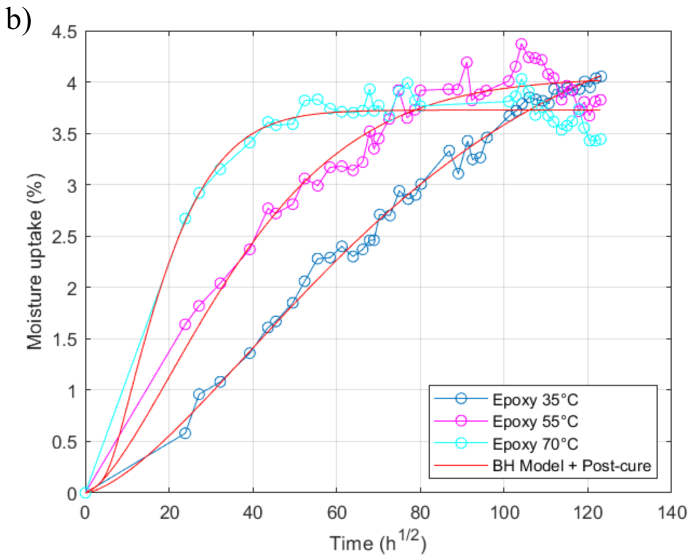

Figure 100. Post-cure modified BH Model for the (a) FRP and (b) neat epoxy samples.

4.3. Swelling

Figure 101 shows the volumetric swelling strains ($\Delta V/V_0$) *vs.* the volume of absorbed water ($\Delta V_{H2O}/V_0$) for FRP (101a), neat epoxy (101b) and the coated FRP (101c). The swelling data was acquired by measuring the specimens' dimensions with a caliper, as described in Section 3.2.1.1. Each data point is the average value from three specimens. The ideal behavior is represented by a solid line with slope equal to one, where the volumetric swelling and the volume of absorbed water are equal. The effects of thermal dilation were not considered in this analysis. Therefore, the samples were kept at room temperature after their withdrawal from the chambers for enough time to reach the thermal equilibrium with the laboratory environment, so that the only factor influencing the swelling strain would be the moisture absorption.

It can be seen that, except for some data points at 35°C for the FRP and neat epoxy, the experimental values are located at the lower portion of the graph, meaning that the swelling behavior of the polymeric materials is lower than the ideal one, as expected from literature [43,99,215]. This behavior is credited to the presence of free volumes, where water molecules are trapped and do not directly interact with the polymeric structure. However, Perrin *et al.* [215] partly disagree with this statement claiming that free volume is not totally accessible to water. Additionally, the materials' behaviors did not follow the trend explained in Section 2.3.8 with a slow initial swelling followed by an increase in the swelling rate. As it was seen in the non-Fickian models (Section 4.2.4), there was a strong diffusion of bound molecules in the polymer, contributing for this strong swelling. It is noticeable that there is a significant scattering in the data, which could, in part, be attributed to the intrinsic experimental error in the caliper readings. For the FRP there was a stabilization of the swelling value over time, which means it reached its saturation swelling. This indicates that the polymer chains stopped being displaced by the ingress of water, suggesting stabilization of the plasticization. In order to calculate the free volume content from the data, a polynomial fit was done to account for the data scattering. The fitted curves alongside their equations are shown in the graphs. The free volume contents calculated from the fitted curves are shown in the graphs from Figure 101. Table 33 summarizes the average values for the free volumes found for the FRP and epoxy. The data for the coated FRP (Figure 101c) fluctuated around the ideal behavior line, therefore it can be speculated that the coated composite showed an ideal swelling behavior, meaning that its swelling and the water volume absorbed were additive [99].

The composites presented an increase in the free volume with temperature, with the highest value at 55°C. This can be explained by the polymer relaxation at higher temperatures, causing the dilation of the free volumes and voids present in the material due to the proximity to the T_g of the material [68]. The same behavior was found in the neat epoxy specimens, although there was little difference between the values found for each temperature. For the exposure at 70°C there was a slight decrease in the average free volume value compared to 55°C, which can be related to the post-curing in both neat epoxy and FRP at high temperatures, which would increase the material's density and decrease its free volume content [172]. This corroborates with two events: the increase in the material's T_g observed in the DSC and DMTA analyses for the aged specimens (Sections 4.2.2 and 4.2.3) and the decrease in the saturation moisture absorption with temperature observed for the neat epoxy specimens (Section 4.2.1 – Table 13).

From the average free volume contents shown in Table 33, it can be said that, considering the scattering in Figure 101, there were no significant changes between FRP and epoxy, especially at 55°C.

a)

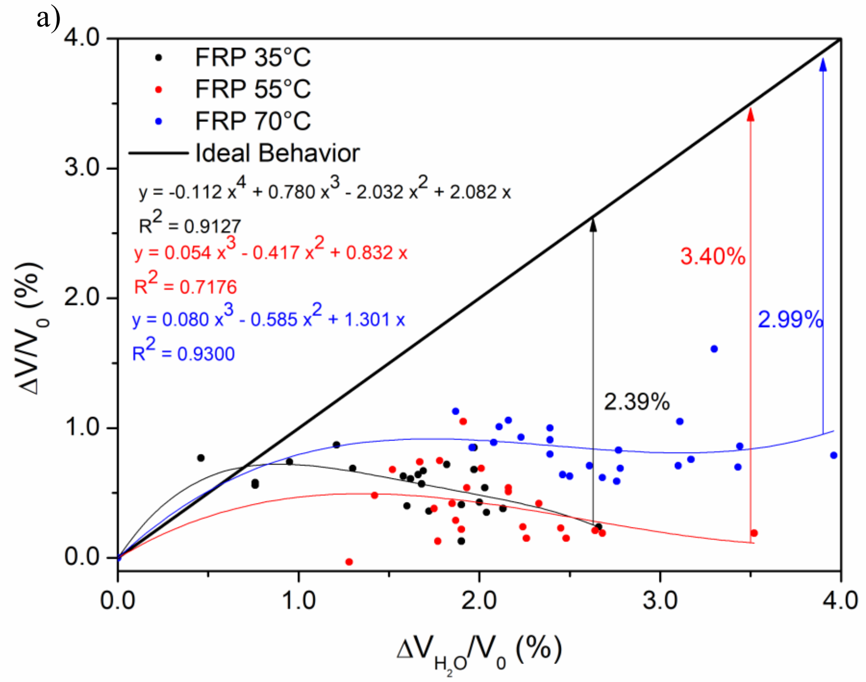
FRP 35°C
FRP 55°C
FRP 70°C
Ideal Behavior
y = -0.112 x^4 + 0.780 x^3 - 2.032 x^2 + 2.082 x
R^2 = 0.9127
y = 0.054 x^3 - 0.417 x^2 + 0.832 x
R^2 = 0.7176
y = 0.080 x^3 - 0.585 x^2 + 1.301 x
R^2 = 0.9300
3.40%
2.99%
2.39%
ΔV/V0 (%)
ΔVH2O/V0 (%)
0.0
1.0
2.0
3.0
4.0

b)

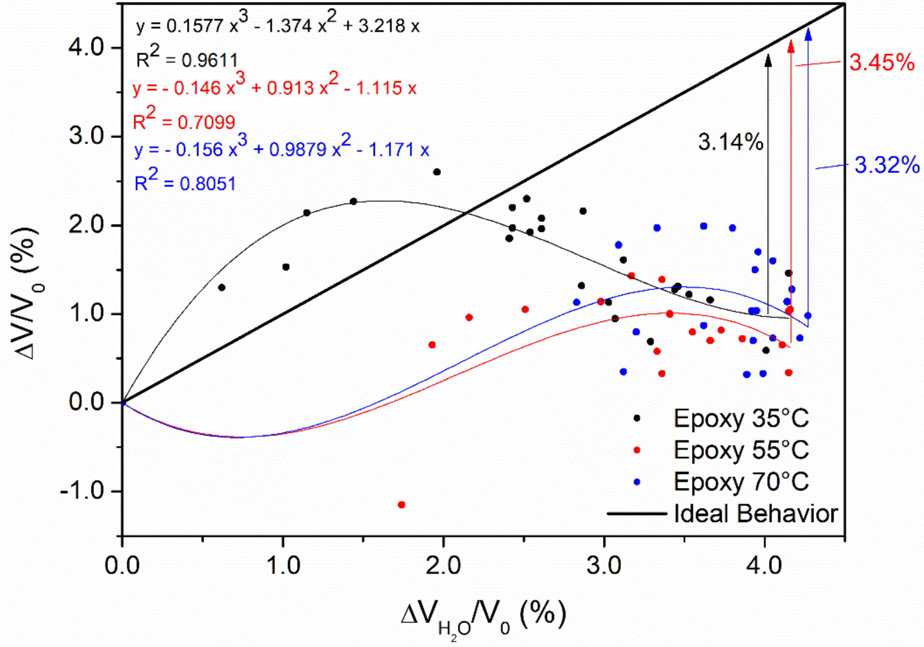
y = 0.1577 x^3 - 1.374 x^2 + 3.218 x
R^2 = 0.9611
y = - 0.146 x^3 + 0.913 x^2 - 1.115 x
R^2 = 0.7099
y = - 0.156 x^3 + 0.9879 x^2 - 1.171 x
R^2 = 0.8051
3.45%
3.14%
3.32%
Epoxy 35°C
Epoxy 55°C
Epoxy 70°C
Ideal Behavior
ΔV/V0 (%)
ΔVH2O/V0 (%)
-1.0
0.0
1.0
2.0
3.0
4.0

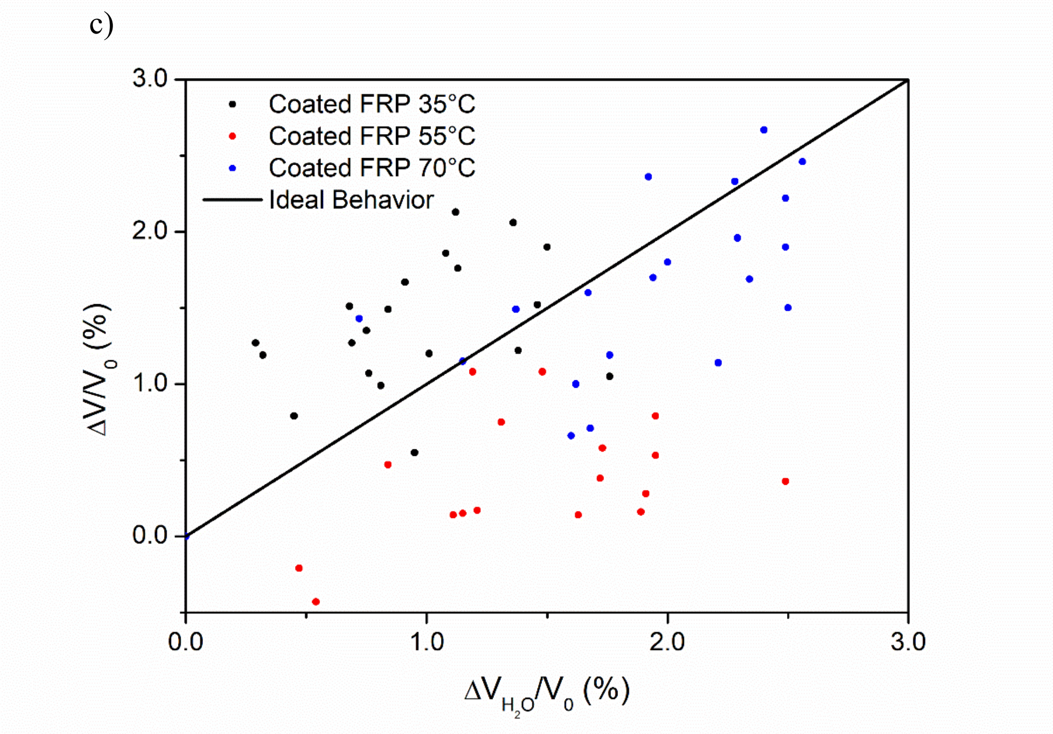

Figure 101. Volumetric swelling as a function of the volume of absorbed water of the (a) FRP, (b) epoxy and (c) coated FRP.

Table 33. Average free volume content for FRP and epoxy at all temperatures obtained from swelling analysis.

	Average free volume content (%)		
Material \ Temperature (°C)	**35**	**55**	**70**
FRP	2.39	3.40	2.99
Epoxy	3.14	3.45	3.32

Figure 102 shows the average values and standard deviations of the volumetric swelling strains as a function of the weight gain (M_t) for the FRP and neat epoxy at all temperatures. Each data point is the average value from three specimens. It is noticeable that for all dataset the standard deviation is considerably large, so it can be assumed that there was no significant variation with moisture absorption. Therefore, the materials presented a stabilization of the swelling with moisture absorption. It can be speculated that this behavior might be related to the plateau of mechanical degradation induced by plasticization. An in-depth investigation on the relationship between swelling and property degradation is suggested for future works. The effects of moisture on the matrix plasticization will be discussed in Section 4.4 with the analyses of the properties' degradation. This stabilization can also be credited to a stabilization of bound water molecules in the material, since this is the type of water molecule that directly interacts with the polymetric matrix, leading to physical effects, like plasticization and hydrolysis, for example [42,48].

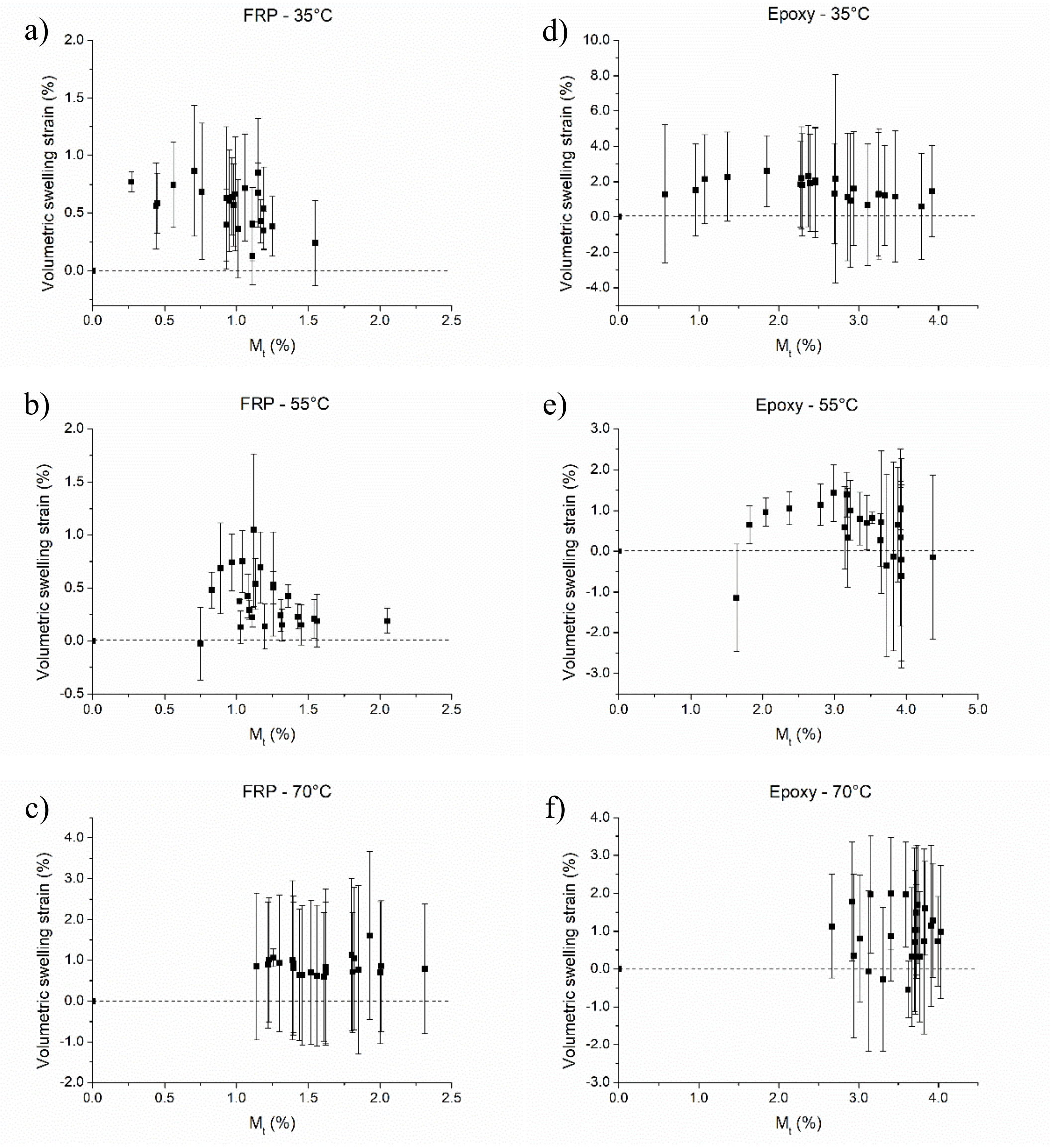

Figure 102. Average and standard deviation values for the volumetric swelling strain *vs*. mass gain at time *t* for FRP at (a) 35°C, (b) 55°C and (c) 70°C, and for neat epoxy at (d) 35°C, (e) 55°C and (f) 70°C.

To compare the effects of temperature on the volumetric swelling behavior of the materials, the average values of the swelling strains were calculated from the data points in Figure 102. The average swelling strains calculated were 0.56%, 0.39% and 0.87% for the FRP at 35°C, 55°C and 70°C, respectively, and 1.61%, 0.52% and 1.04% for the neat epoxy at 35°C, 55°C and 70°C, respectively. For both materials, there was a decrease in the volumetric swelling strain from 35 to 55°C, followed by an increase at 70°C. The volumetric strains for the epoxy specimens were found to be higher than those for the fiber-reinforced composite. This is due to the fact that the swelling occurs solely on the polymer matrix, since the water absorption of the glass fibers is negligible. Therefore, assuming that the fiber/matrix adhesion is good, there is a restriction of volumetric expansion caused by the fibers. The ratio between the average volumetric swelling of the FRP and neat epoxy resin was found to be 0.35, 0.76 and 0.83 for 35, 55 and 70°C, respectively. As it was expected, the ratio increased with temperature. The swelling ratio was lower than the fiber volume fraction ($V_f \approx 42\%$) only at 35°C, while it was higher at high temperatures. As it was seen in the non-Fickian models, both second-stage diffusivity and the probability of the mobile water becoming immobile increased with temperature, therefore at higher temperatures there is a higher number of bound water molecules, causing a stronger interaction between water and the polar sites of the polymer matrix. Thus, the swelling phenomenon is more prominent at higher temperatures.

Figure 103 shows the volumetric swelling strain of the FRP *vs*. those of the epoxy resin. To plot this graph, the volumetric swelling strains of the neat resin (x axis) were normalized in relation to the matrix volume fraction in the composite ($V_m \approx 57.91\%$). By normalizing these data, the comparison between the materials is more reliable, since the polymer matrix is the only constituent in the composite that swells from moisture absorption. Therefore, the only factor to influence the swelling correlation between the materials is the temperature. The fitted curves and their equations are shown on the graph. The boundary condition for the calculation of these curves was the intercept point on the y axis to be x = y = 0.00, represented by the dotted lines, because the only elastic strain present in the unaged specimens is the compressive strains due to the shrinkage during curing, which is not being considered herein [36,38]. The slopes of the curves represent the proportionality between the swelling capacity of the FRP and that of the neat epoxy resin. Therefore, it can be seen that there was an increase in the swelling capacity with temperature, for at 35°C the coefficient was 0.5344, at 55°C it was 0.7284 and at 70°C it was 1.0353. Thus, the higher the temperature, the stronger the relaxation on the polymer matrix, leading to a stronger matrix swelling. Indeed, at 70°C the slope was greater than 1.0, therefore the FRP swelled more than the neat resin. Moreover, it was observed that at 35°C the relationship between the composite's and the neat epoxy's swelling capacities was found to be similar to the matrix volume content

($V_m \approx 57.91\%$), whereas for higher temperatures this relationship was higher, meaning that stronger interchain distancing occurred as moisture was absorbed.

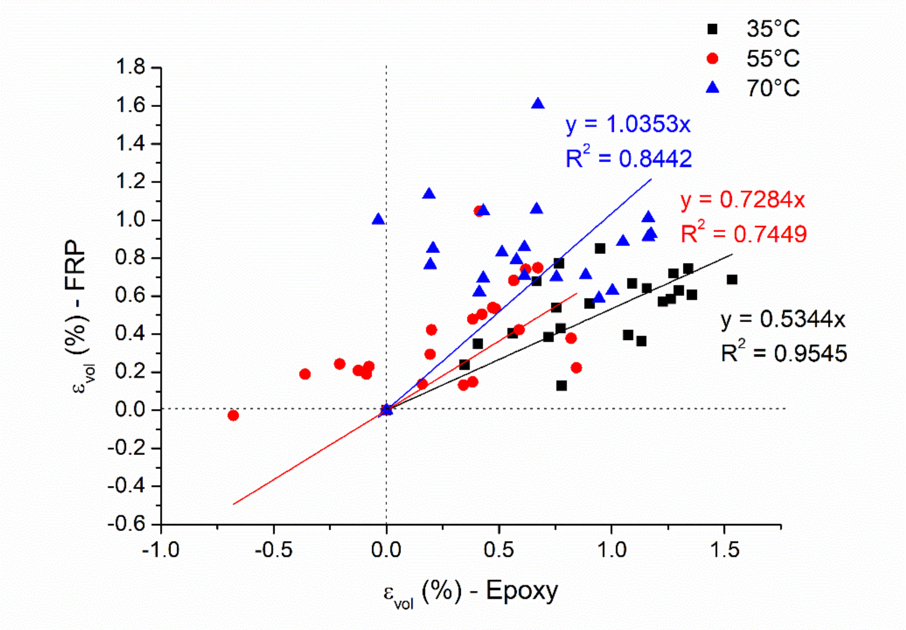

Figure 103. Swelling capacity of FRP *vs*. swelling capacity of the neat epoxy normalized with matrix volume fraction for all temperatures tested.

The swelling strain can be considered proportional to the moisture absorbed with a proportionality constant called swelling coefficient (β). This dimensionless coefficient measures the swelling capability of the material at a given weight gain. The relationship between the swelling strain and moisture follows a linear relationship (Equation 80), where the swelling strain is the elastic strain imposed on the material by the moisture absorbed. The subscript *i* refers to each experimental data point on the graphs of Figure 101.

$$[\varepsilon_i] = [\beta] \cdot [M_i] \qquad (80)$$

Figure 104 shows the swelling coefficient *vs*. mass gain graphs for both FRP and neat epoxy. Despite the scattering, it can be seen that there was a general trend of decrease in the swelling coefficient with mass gain. This might indicate a stabilization in the swelling driving force after the water molecules start bonding to the epoxy's polar sites. Consequently, the swelling is stronger at the beginning of the exposure to moisture, followed by a decrease in its value. This is in disagreement with literature [43,67,100]. Other authors state that the beginning of aging is characterized by a slow swelling due to the filling of voids by free water, followed by a stronger swelling owing to the bonding to bound immobile water.

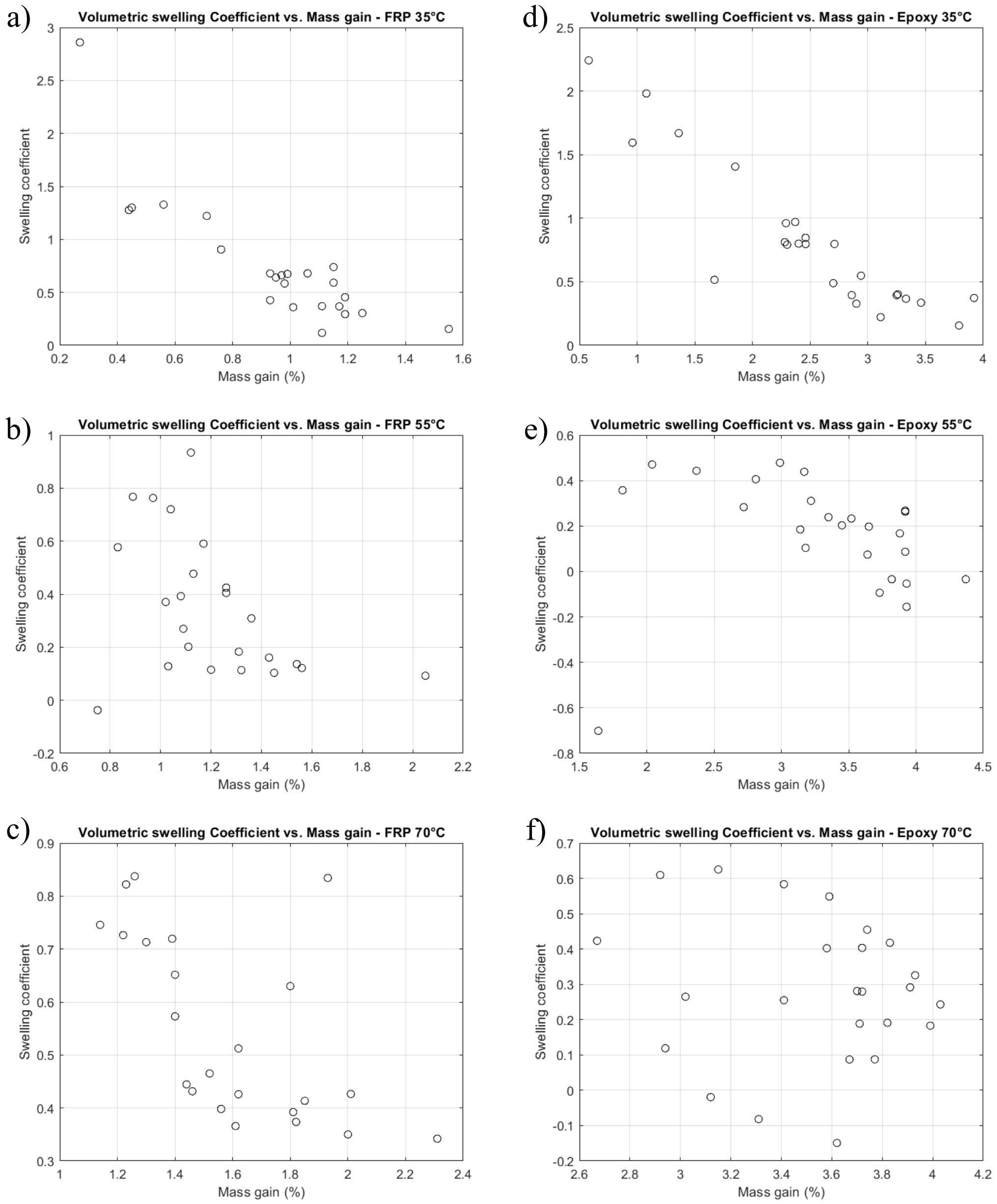

Figure 104. Volumetric swelling coefficient *vs*. mass gain for FRP at (a) 35°C, (b) 55°C and (c) 70°C, and for epoxy at (d) 35°C (e) 55°C and (f) 70°C.

The linear swelling also needs to be taken into account when evaluating moisture-induced swelling. Then, it can be correlated with the tridimensional diffusion phenomenon, since this behavior is different in the three directions of the specimens. Figure 105 shows the average linear swelling strains curves as a function of the aging time on the thickness (ε_t), length (ε_l) and width (ε_w) directions for FRP and neat epoxy at all temperatures. Each data point is the average value for three specimens. For the FRPs, it is clear that the swelling strain is orthotropic, since the swelling in the thickness direction (ε_t) is considerably higher than in the other two directions (ε_w in the width direction and ε_l in the length direction), with the thickness swelling contributing to most of the volume change. It can be explained by the restriction of movement imposed by the fibers. It is well-known that the swelling occurs exclusively on the polymer matrix, since the absorption of glass fibers is negligible. Therefore, since the composite in this work is reinforced by bidirectional fibers (longitudinal (ε_l) and transverse (ε_W)), the fibers restrain the swelling on the directions parallel to them, i.e., in the in-plane directions. In fact, during the exposure the swelling strains on the length and width directions of the FRP (Figures 105a, 105b and 105c) fluctuated around 0.0%, meaning that these directions were barely affected by moisture-induced swelling. Tanks *et al.* [189] and Aniskevich *et al.* [98] reported the same behavior for woven-fiber and unidirectional composites, respectively, with the fibers restraining swelling in the in-plane directions. On the other hand, for the neat epoxy resin the swelling on the thickness direction was not found to be higher than the other two. In fact, the absolute values of the swelling strains on the length and width directions were higher than on the thickness, especially in long-term exposure. This lack of dependency on the direction of the specimen is due to the epoxy's isotropy, while the FRP is orthotropic.

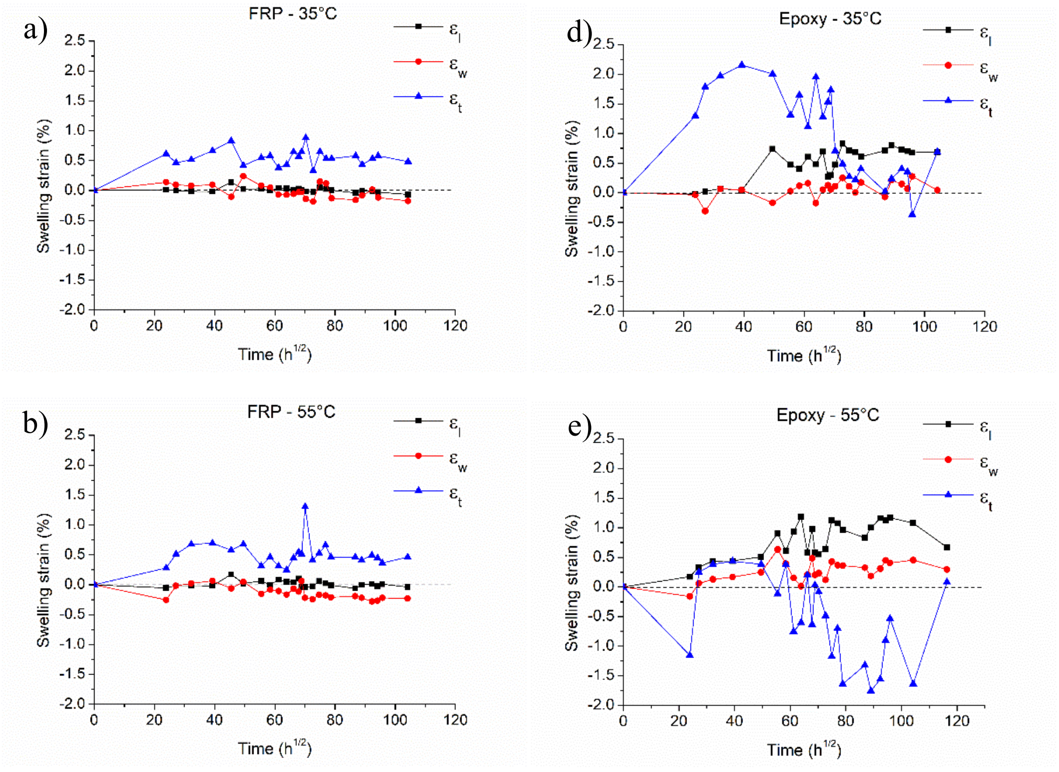

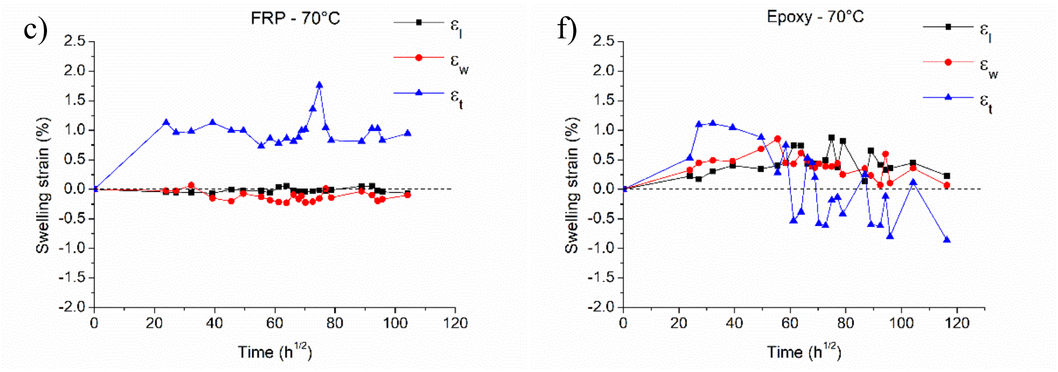

Figure 105. Linear swelling strain *vs*. aging time for FRP at (a) 35°C, (b) 55°C and (c) 70°C, and for epoxy at (d) 35°C, (e) 55°C and (f) 70°C.

It can be noticed that the curves of the thickness swelling of the FRP in Figures 105a, 105b and 105c are shaped like the Fickian absorption discussed previously (Section 4.2.1). Therefore, it can be estimated that the swelling behavior on the thickness direction might follow the relationship described by Equation 81, where ε_t is the swelling strain at time t, ε_m is the saturation swelling strain, h the sample's thickness and S is the swelling front progressing through the thickness of the composite, a parameter similar to the diffusivity in the absorption analysis. This parameter represents the swelling front progressing inwards the material. The thickness swelling of the neat epoxy will not be modeled with this equation because the neat epoxy's thickness swelling did not present a Fickian-like behavior on the experimental data.

$$\frac{\varepsilon_t}{\varepsilon_m} = 1 - \frac{8}{\pi^2}\sum_{n=0}^{\infty}\frac{exp\left[-(2n+1)^2\pi\left(\frac{St}{h^2}\right)\right]}{(2n+1)^2} \tag{81}$$

Firstly, a statistical analysis was done to the experimental data in order to investigate whether the temperature influences the swelling behavior. Figure 106 shows the average values calculated from the data in Figures 105a, 105b and 105c alongside their standard deviations. From Figure 106 it can be concluded that there was no statistical difference between the average swelling between 35 and 55°C. This may be credited to the material's T_g, since the proximity to the glass transition temperature leads to major changes in the polymeric matrix, by enhancing the viscous behavior of the polymer, making it more prone to a stronger swelling [216]. Therefore, in this model both low temperatures (35 and 55°C) will be considered as only one series of data.

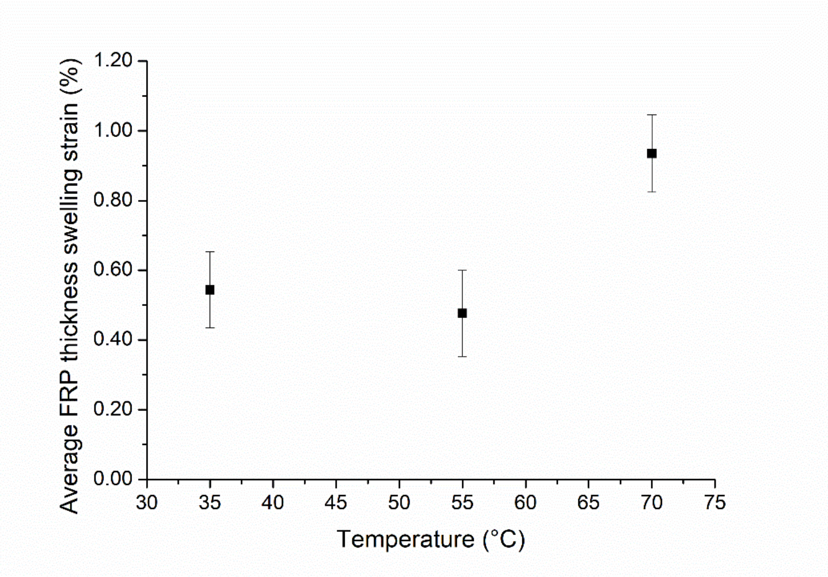

Figure 106. Average and standard deviation values of the FRP thickness swelling strain for all temperatures.

Then, by gathering the thickness swelling data for 35 and 55°C, the average swelling strain is 0.502 ± 0.112%. The average values will be assumed as the thickness swelling saturation value (Table 34) to be input into Equation 80.

By expanding Equation 81 in five terms (n = 0, 1, 2, 3 and 4) and applying the least square method, a curve fitting was performed on the experimental data and the resulting curves for the FRP are shown in Figure 107. Few data points were discrepant from the general experimental trends; therefore, they were considered as outliers and were removed from this analysis. The saturation thickness swelling strain and swelling front are shown in Table 34. It should be clear that due to the large data scattering, this analysis is only an assessment of the general swelling trend in the thickness direction. In addition, there is a lack of experimental data between 0 and 570 hours of aging, which casts doubt on the reliability of the swelling front and, therefore, the time required to reach the saturation will not be reliable, so this parameter will not be calculated. Thus, short-term data points are necessary for a better fitting. Despite this, it is clear that temperature plays an important role in moisture-induced swelling, since the low temperatures presented the same behavior and at 70°C both equilibrium thickness swelling strain and swelling front were the highest of all temperatures due to the enhancement in polymer relaxation. From the results obtained, the maximum strain on the thickness direction experienced by the composites was nearly 1.0% at 70°C. Additionally, Tanks *et al.* [189] state that the higher swelling strains in woven-fiber reinforced composites may lead to the increase in both spacing between yarns and fiber waviness angle, leading to decrease in interlaminar shear strength.

Table 34. Saturation thickness swelling strain and swelling front for the FRP at all temperatures tested.

Temperature (°C)	Saturation thickness swelling strain (%)	Swelling front (m^2/s)	R^2
35 + 55	0.502	1.83 x 10^{-11}	**0.3127**
70	0.935	1.72 x 10^{-10}	**0.6581**

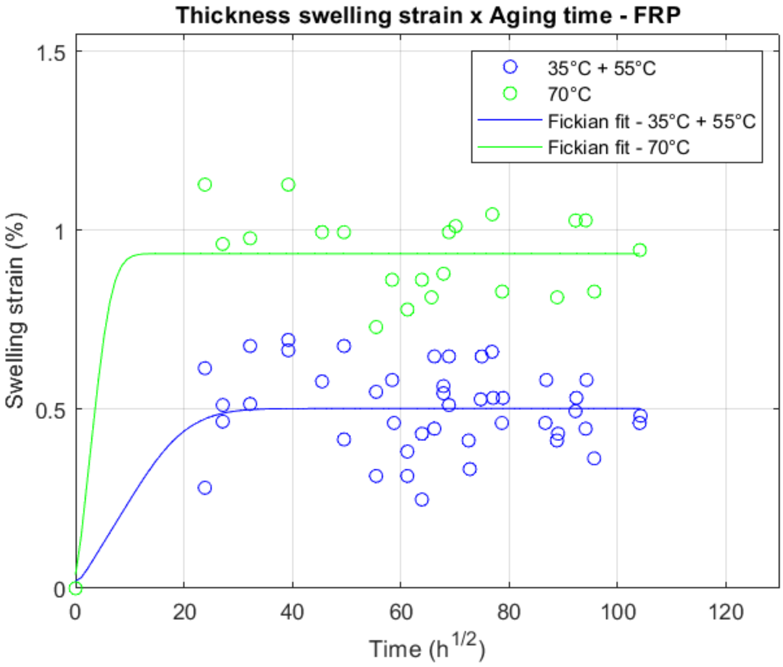

Figure 107. Composite’s experimental thickness swelling data and Fickian swelling curve fitting.

Comparing these values with the through-thickness diffusivity values (D_x) obtained in Section 4.2.1, the swelling front is three orders of magnitude higher. This might indicate that as moisture slowly penetrates the composite, it creates a stronger swelling front progressing through the material, so that the thickness swelling strain saturates at a shorter time scale than the moisture penetration. This might be due to the strong increase in the interchain spacing with a small amount of moisture absorbed. Graphically, this phenomenon could be represented by the schematic diagram in Figure 108 with both diffusion and swelling fronts progressing through the thickness by both directions. No similar investigation was found in literature.

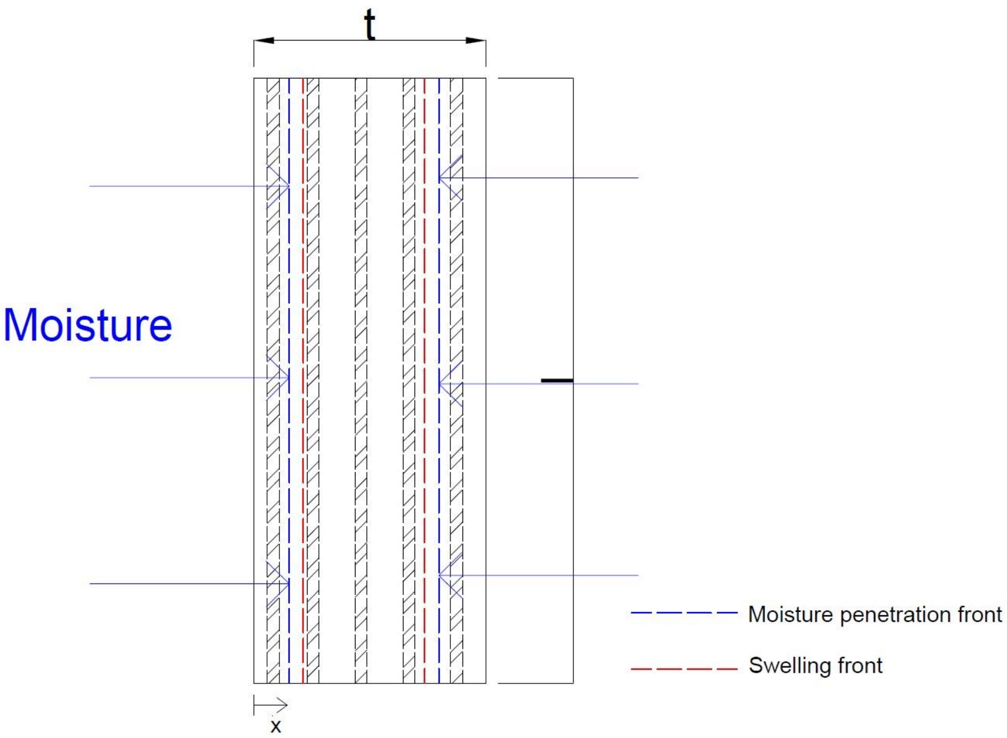

Figure 108. Schematic representation of both moisture and swelling fronts in a composite.

Considering the swelling coefficient previously discussed, equation 80 can be expanded to include the swelling capacity on the three directions of the specimen. Thus, considering the composites as orthotropic materials, equation 80 can be rewritten as:

$$\begin{bmatrix} \varepsilon_t \\ \varepsilon_l \\ \varepsilon_w \end{bmatrix}_i = \begin{bmatrix} \beta_t & 0 & 0 \\ 0 & \beta_l & 0 \\ 0 & 0 & \beta_w \end{bmatrix}_i \cdot [M_i] \qquad (82)$$

where the subscript *i* refers to each experimental data point.

Figure 109 shows the linear swelling coefficient *vs*. mass gain of the FRPs for the temperatures tested.

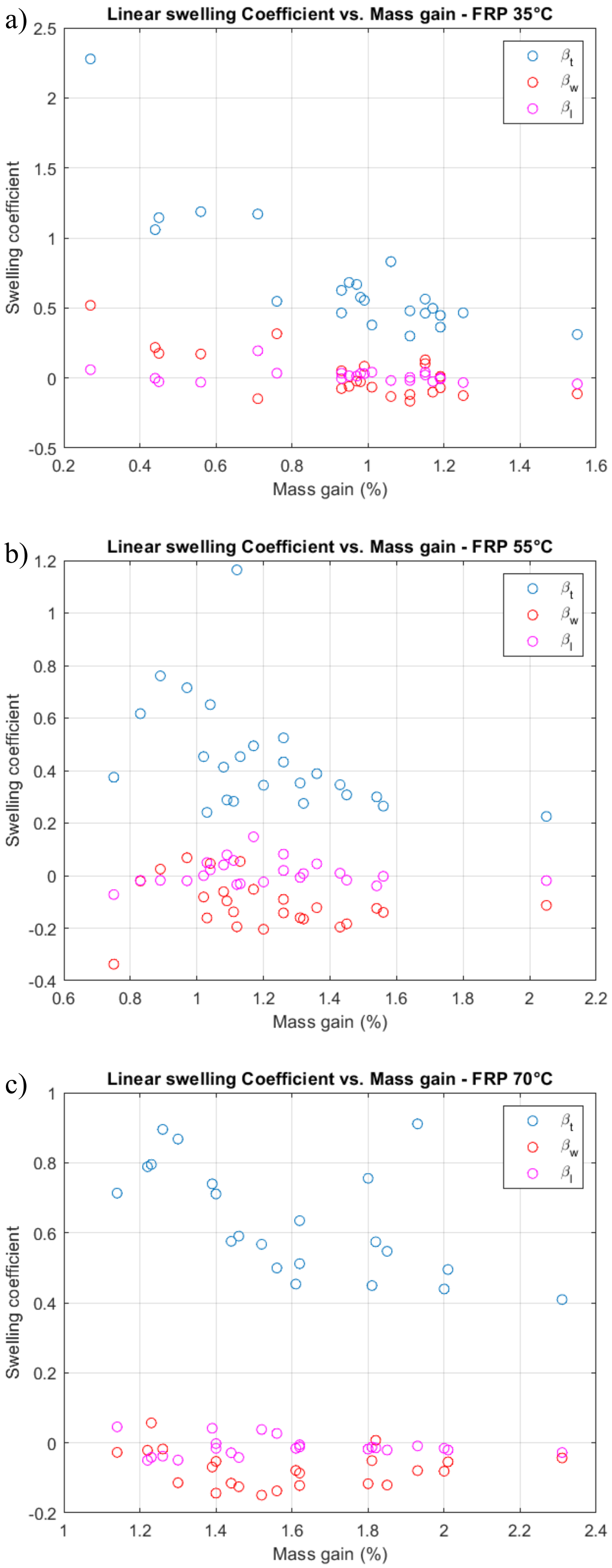

Figure 109. Linear swelling coefficient *vs*. mass gain for the FRP at (a) 35°C, (b) 55°C and (c) 70°C.

As expected, the swelling capacity on the thickness direction is higher than in the other directions. In fact, in the length and width directions the swelling capacity fluctuated around zero due to the restrictions imposed by the fibers. Through the thickness, the swelling phenomenon is directly dependent on the resin matrix, with lower movement restrictions from the fibers.

Average values for the swelling coefficients were calculated from the graphs in Figure 109. Table 35 shows the average swelling coefficients for all temperatures tested. Indeed, the average swelling coefficient in the thickness direction is the highest among all the sample's directions. Most of the swelling coefficients in the length and width directions were found to be negative, except for the β_l at 35°C, evidencing the strong swelling constriction imposed by the fibers, due to the composites' orthotropy. It can also be observed that the coefficient in the length direction was negligible for all temperatures, due to the stronger restriction in this direction owing to the higher number of fibers in the longitudinal direction.

Table 35. Average linear swelling coefficient for all temperatures in the thickness direction (β_t), width direction (β_w) and length direction (β_l).

Temperature (°C)	β_t	β_w	β_l
35	0.5545	-0.0265	0.0036
55	0.3814	-0.1234	-0.0013
70	0.5904	-0.0793	-0.0155

4.4. Mechanical Tests

The mechanical destructive tests were carried out according to procedures detailed in section 3.2.2. The aging times chosen to perform these tests were detailed in Table 8, and are shown in the moisture absorption curve in Figure 110. The aging times were the same for all temperatures.

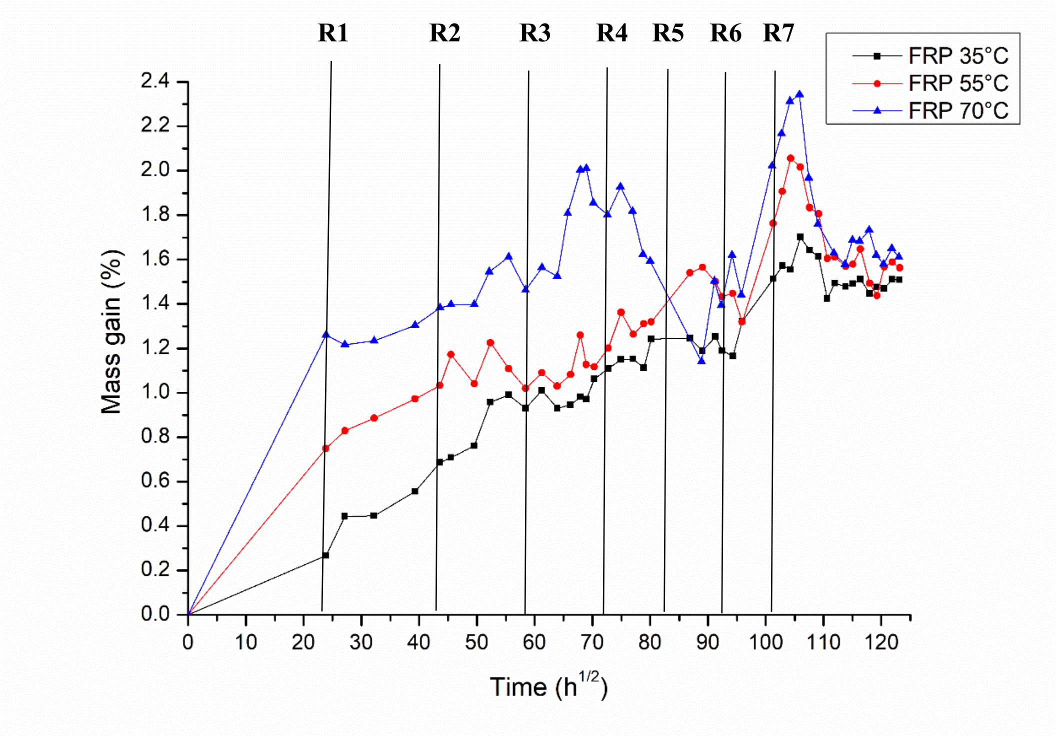

Figure 110. Moisture absorption curve with the aging times for the mechanical destructive tests.

4.4.1. Bending

Figure 111 shows the load *vs*. deflection curves for 35°C (111a), 55°C (111b) and 70°C (111c) as a function of moisture absorbed. The samples, whose test curves were plotted, were chosen according to their proximity to the average strength value. It can be seen that the curves present the same elastic linear shape, meaning that the results are comparable, since there was no shift in failure mode. With the increase in moisture absorbed, the curve slope decreased, reflecting in the decrease in stiffness. Moreover, the maximum load decreased with aging, resulting in strength loss.

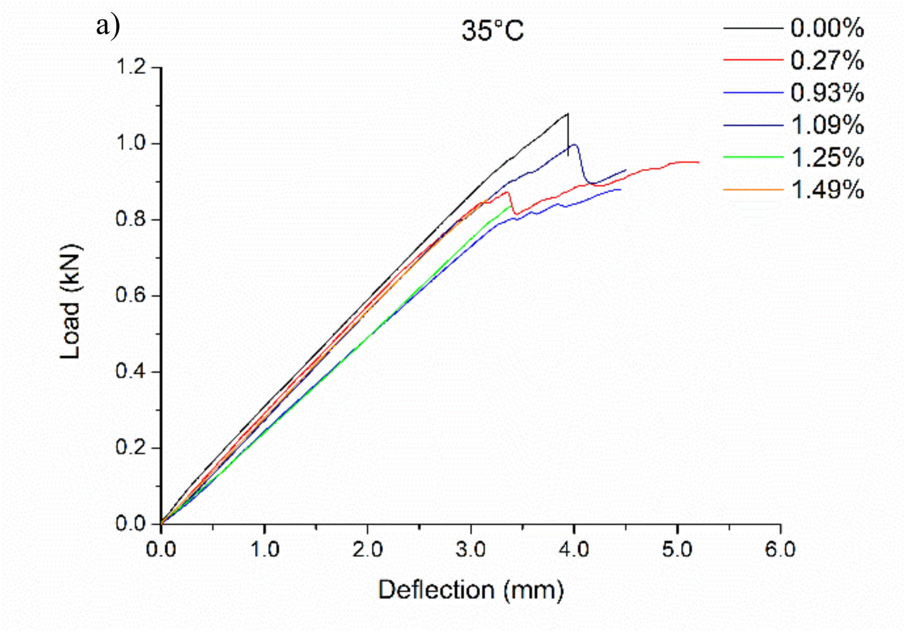
a)
35°C
0.00%
0.27%
0.93%
1.09%
1.25%
1.49%
Load (kN)
0.0
0.2
0.4
0.6
0.8
1.0
1.2
Deflection (mm)
0.0
1.0
2.0
3.0
4.0
5.0
6.0

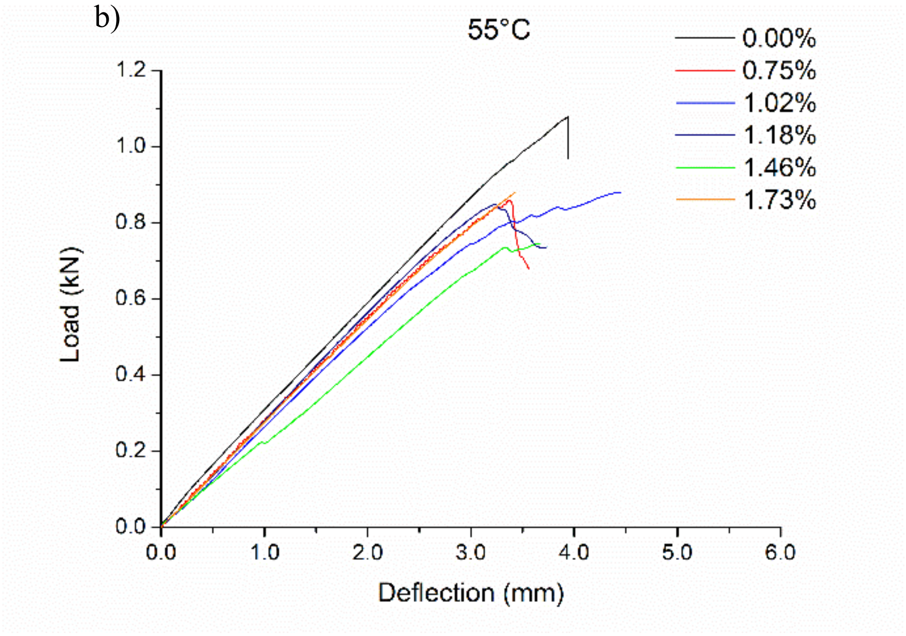
b)
55°C
0.00%
0.75%
1.02%
1.18%
1.46%
1.73%
Load (kN)
0.0
0.2
0.4
0.6
0.8
1.0
1.2
Deflection (mm)
0.0
1.0
2.0
3.0
4.0
5.0
6.0

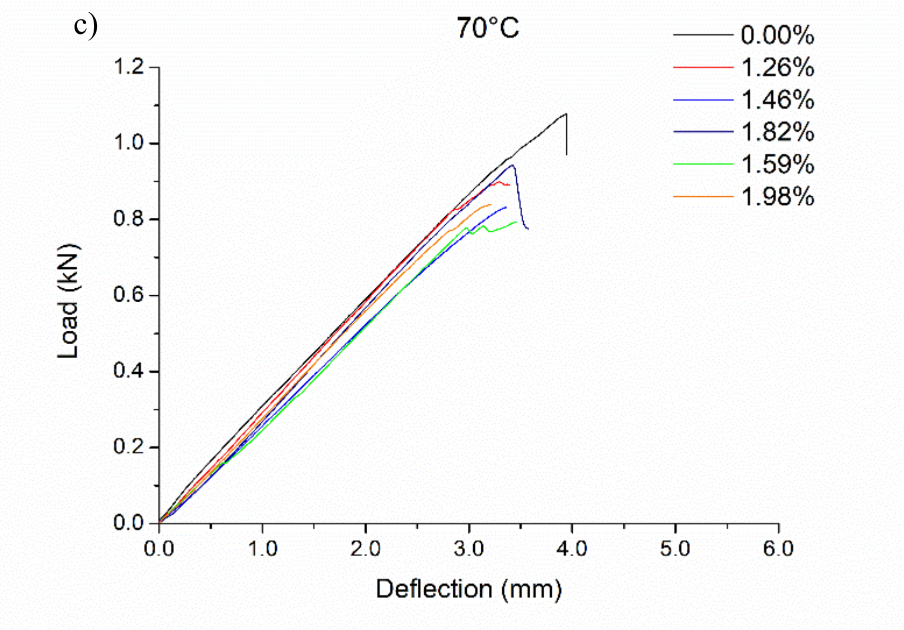

Figure 111. Bending load *vs*. deflection curves with moisture absorbed for (a) 35°C, (b) 55°C and (c) 70°C.

Figure 112 shows the average and standard deviation values of the flexural strength (Figure 112a) and modulus (Figure 112b) of the composite as a function of the aging time. Each value is an average of 15 (fifteen) specimens. It can be seen that the flexural strength presented a strong initial decrease in the first two aging times (R1: 570 hours and R2: 1820 hours) for all temperatures, being more significant at 55 and 70°C. This property loss is temperature dependent, as the higher the temperature, the stronger the strength degradation. Subsequently, there was a slower decrease in the rate of property loss in the following aging times, causing the material to reach an apparent strength plateau. This property loss is due to the plasticization effect induced by humidity and the attack of water onto the fiber/matrix interface [34,145,188]. From the DSC analysis on the post-cured composite (Section 4.1.2), a post-cure effect can be predicted for the samples exposed to high temperatures. However, this phenomenon could not be seen in Figure 112, since a post-cure would be characterized by an improvement in mechanical properties, leading to the apparent deduction that the samples might have undergone post-cure between 0 and 570 hours (R1) of aging, and then undergoing plasticization [135]. However, from the DMTA analysis in Section 4.2.3, the samples continued to undergo post-cure after this aging time, mainly at high temperatures; therefore, it can be said that two opposite, yet concomitant, effects were simultaneously happening to the material, which are post-cure and plasticization, with the latter being more strongly reflected in the mechanical property degradation behavior. The same analysis is valid for the other mechanical properties that will yet be discussed, since the degradation trends were similar.

Considering the standard deviation in Figure 112a, there was no considerable change in strength after R3 (3490 hours of aging) for each temperature, suggesting a degradation level plateau, which would be the lowest level that the material will reach. It is noteworthy that this degradation plateau decreases with increasing temperature, as expected, since temperature increases the moisture absorption kinetic, resulting in stronger plasticization and interface attack [36,145,201,217]. For the modulus (Figure 112b), there was a milder loss with time, owing to the less severe effect of temperature, since this is a fiber-dominated property [95].

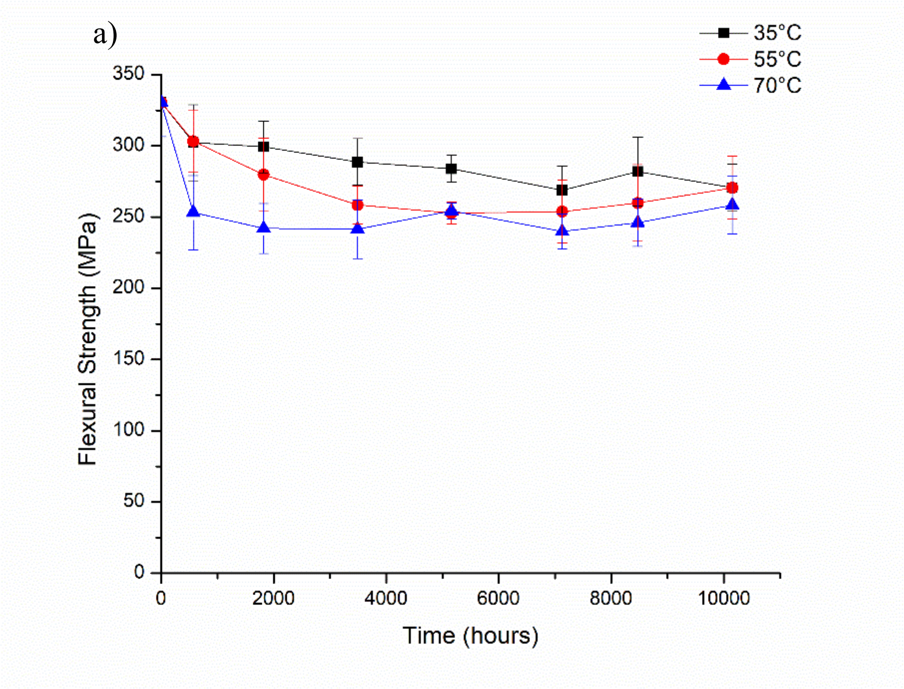

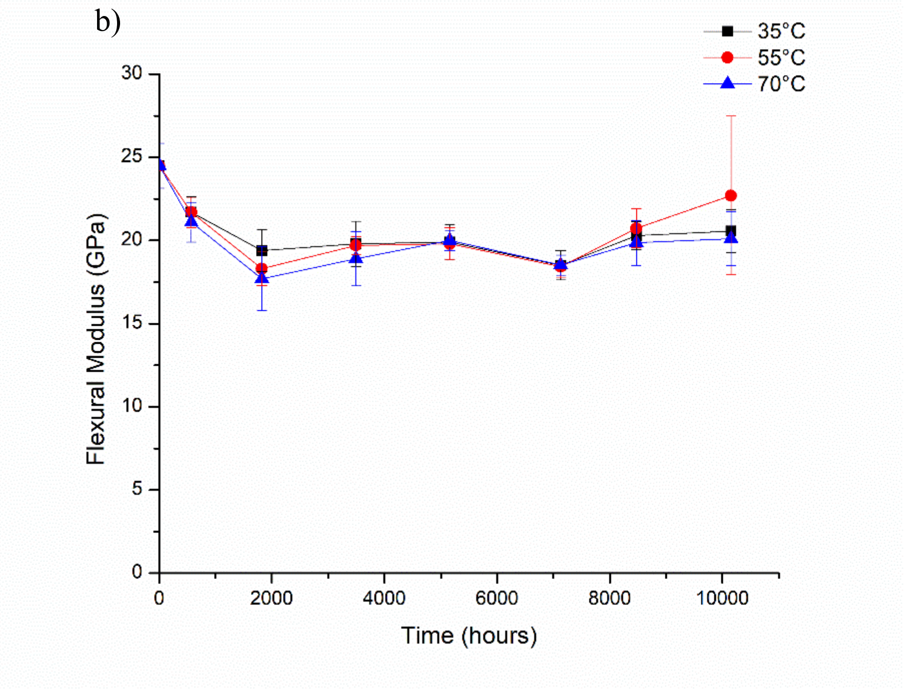

Figure 112. (a) Flexural strength and (b) flexural modulus as a function of aging time in hours.

After plasticization, the composite becomes more ductile, with greater deformability. Therefore, the bending deflections were also evaluated herein. The maximum bending deflections were normalized in relation to the thickness of each sample and the average values for each group are plotted in Figure 113. An ellipse was inserted in the graph highlighting the experimental data at 5160 hours of aging that stands out among the other aging times. These data are attributed to experimental error when capturing the displacement; therefore, this aging time will not be included in the discussion. A horizontal black line was drawn on the unaged value for better visualization of the deformation change with aging time. At 35°C there was an initial increase of 24% after 570h. It then remained statistically unchanged, decreasing after 6830h and remaining unchanged until 10170 hours. For 55°C, there was also an initial increase in deflection, with the final value after 10170 hours being a value lower than the unaged value. On the other hand, at 70°C the normalized deflection decreased after 570h, remaining unchanged until 10170 hours of aging. The initial increase observed in bending deflection evidences the plasticization effect, characterized by the weakening of the interchain secondary forces, facilitating the movement of the matrix, making the material more ductile [34,39,194]. Although for 70°C the values have remained practically the same, if the standard deviation is considered.

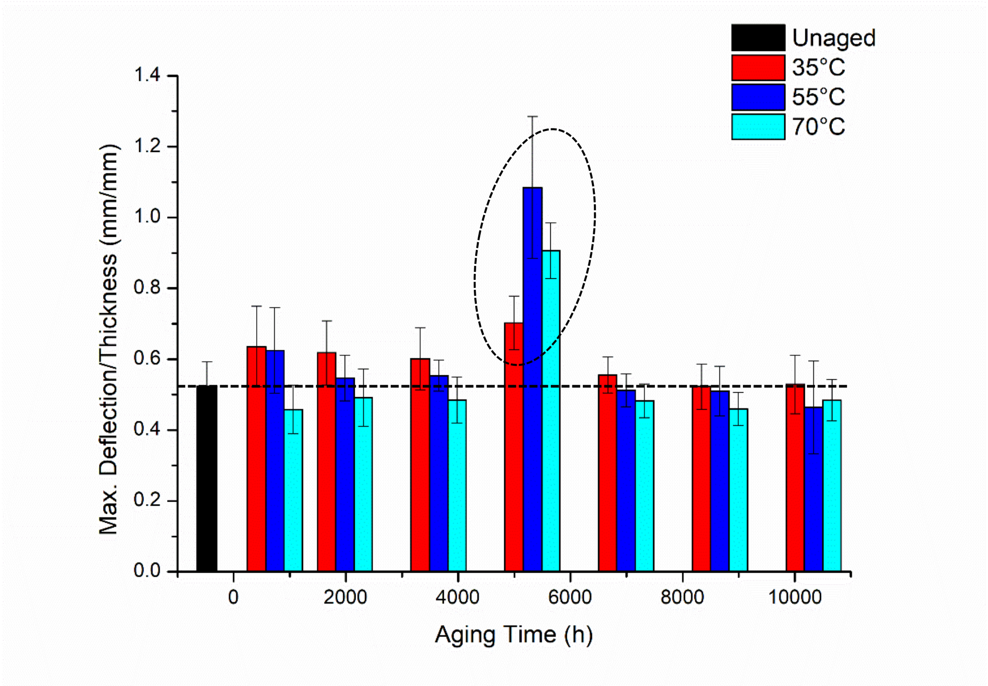

Figure 113. Average values for the normalized maximum bending deflection of the FRP as a function of aging time.

This increase in deformability, i.e., plasticization, followed by a decrease has already been reported by Prolongo *et al.* [39] after aging epoxy composites reinforced by carbon nanofillers. Zhou and Lucas [194] presented a possible explanation for this phenomenon. According to the authors, there is a change in the absorption mechanism during the aging time with a shift from Type I bound water to Type II bound water. Diffusion of the former occurs readily during aging and breaks interchain van der Waals forces, increasing chain mobility. As the aging progresses, the number of Type I bound water molecules increases significantly, saturating the polar sites of the epoxy. Then, Type II bound water occurs, which forms multisite binding complexes and makes little contribution to matrix plasticization. This leads to a high density of hydrogen bonds, leading to secondary crosslinking with hydrophilic groups of epoxy resin. The higher the temperature, the stronger the formation of Type II bound water molecules [39,194].

Figure 114 shows the retention levels of the flexural strength (Figure 114a) and modulus (Figure 114b) calculated in relation to the unaged properties. It is shown that the degrading effect of temperature is more significant on the strength than on the modulus, since the decrease in retention levels with temperature was more pronounced for the strength property, while there was not much difference between the modulus retentions of the three temperatures. This is mainly because the flexural modulus is a fiber-dominated property, while the polymer matrix is the composite's constituent to be the most affected by moisture absorption [218]. Moreover, if there had been a loosening and considerable debonding of the fibers from the matrix, there would have been a more significant drop in stiffness with moisture absorption [219].

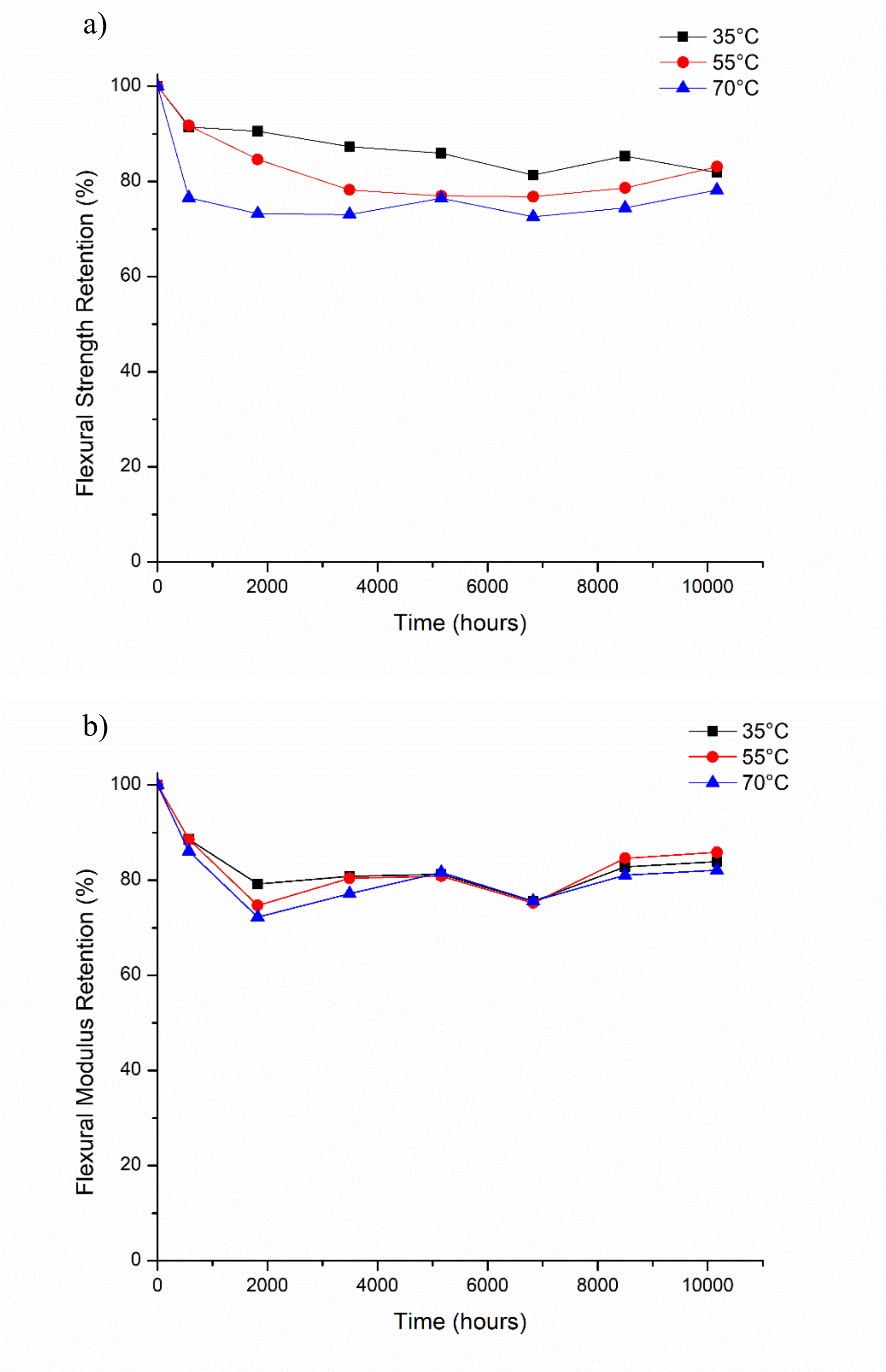

Figure 114. Retention curves for the flexural strength (a) and modulus (b) as a function of the aging time.

Table 36 shows the average and standard deviation values for the bending properties of the FRP.

Table 36. Flexural properties and their percentage retention as a function of aging time and temperature.

Aging time	Temperature (°C)	Flexural Strength (MPa)	Strength Retention (%)	Flexural Modulus (GPa)	Modulus Retention (%)
Unaged (R0)	**-**	330.60 ± 24.07	100.00	24.50 ± 1.35	100.00
570h (R1)	**35**	302.30 ± 26.60	91.44	21.70 ± 0.92	88.57
	55	303.30 ± 22.00	91.74	21.70 ± 0.91	88.57
	70	253.20 ± 26.10	76.59	21.10 ± 1.20	86.12
1820h (R2)	**35**	299.41 ± 18.13	90.56	19.40 ± 1.27	79.18
	55	279.82 ± 25.79	84.63	18.30 ± 1.01	74.69
	70	242.07 ± 17.56	73.23	17.70 ± 1.92	72.24
3490h (R3)	**35**	288.76 ± 16.33	87.34	19.80 ± 1.36	80.82
	55	258.56 ± 13.33	78.21	19.70 ± 0.52	80.41
	70	241.52 ± 20.48	73.06	18.90 ± 1.63	77.14
5160h (R4)	**35**	284.07 ± 9.60	85.93	19.90 ± 1.04	81.22
	55	252.83 ± 7.67	76.94	19.80 ± 0.97	80.82
	70	254.37 ± 5.38	76.48	20.00 ± 0.61	81.63
6830h (R5)	**35**	268.97 ± 16.91	81.36	18.51 ± 0.89	75.55
	55	253.92 ± 21.89	76.81	18.43 ± 0.69	75.22
	70	239.89 ± 12.42	72.56	18.52 ± 0.60	75.59

8500h (R6)	**35**	282.07 ± 24.14	85.32	20.29 ± 0.84	82.82
	55	259.97 ± 26.88	78.64	20.73 ± 1.17	84.61
	70	246.12 ± 16.71	74.45	19.86 ± 1.35	81.06
10170h (R7)	**35**	270.65 ± 16.53	81.87	20.56 ± 1.29	83.92
	55	270.57 ± 22.16	83.09	22.70 ± 4.77	85.84
	70	258.49 ± 20.14	78.19	20.11 ± 1.63	82.08

To investigate whether the bending properties degradation is more affected by moisture or by temperature, the relationships between the retention levels and moisture absorbed are plotted in Figures 115 and 116. Figure 115 shows the bending strength *vs*. moisture absorbed, while Figure 116 shows the modulus *vs*. moisture absorbed by the composites. Figures 115a and 116a show the exponential fit to each temperature individually, while Figures 115b and 116b show the exponential fit to the data obtained for all temperatures together, with the temperatures being colored differently. The fitted equations and their correlation factors are displayed in the graphs, where S is the property retention and M_t is the moisture absorbed.

It is noted that the higher the moisture content the higher the property loss, due to the stronger moisture-induced plasticization, with the flexural strength presenting a retention level lower than the modulus. For the flexural strength, the curve for each individual temperature (Figures 115a) was better fitted, i.e., has a higher R^2, than when all temperatures are plotted together. This indicates that the property loss is not only dependent on the moisture absorbed, but also on the exposure temperature, indicating a deleterious thermal effect on the composite. The same trend was found in literature [85,201,220]. For the flexural modulus, the same trend was observed, however, since the modulus is a fiber-dominated property, the moisture absorbed by the matrix has little influence on this property, as explained earlier. Additionally, the curve adjustments were worse than those for the flexural strength.

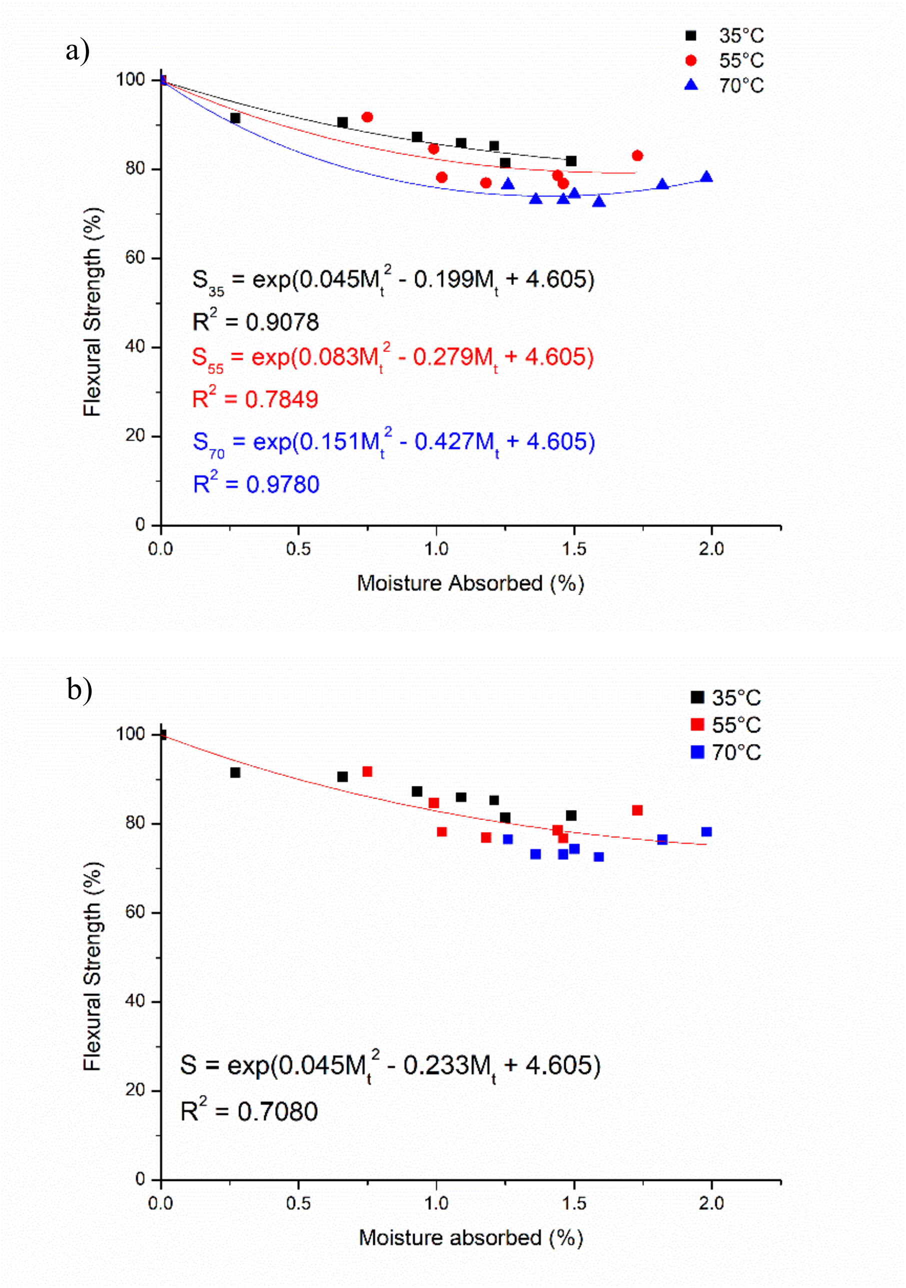

Figure 115. Flexural strength retention as a function of moisture absorbed with exponential fitting for (a) each temperature individually and (b) all temperature data assembled.

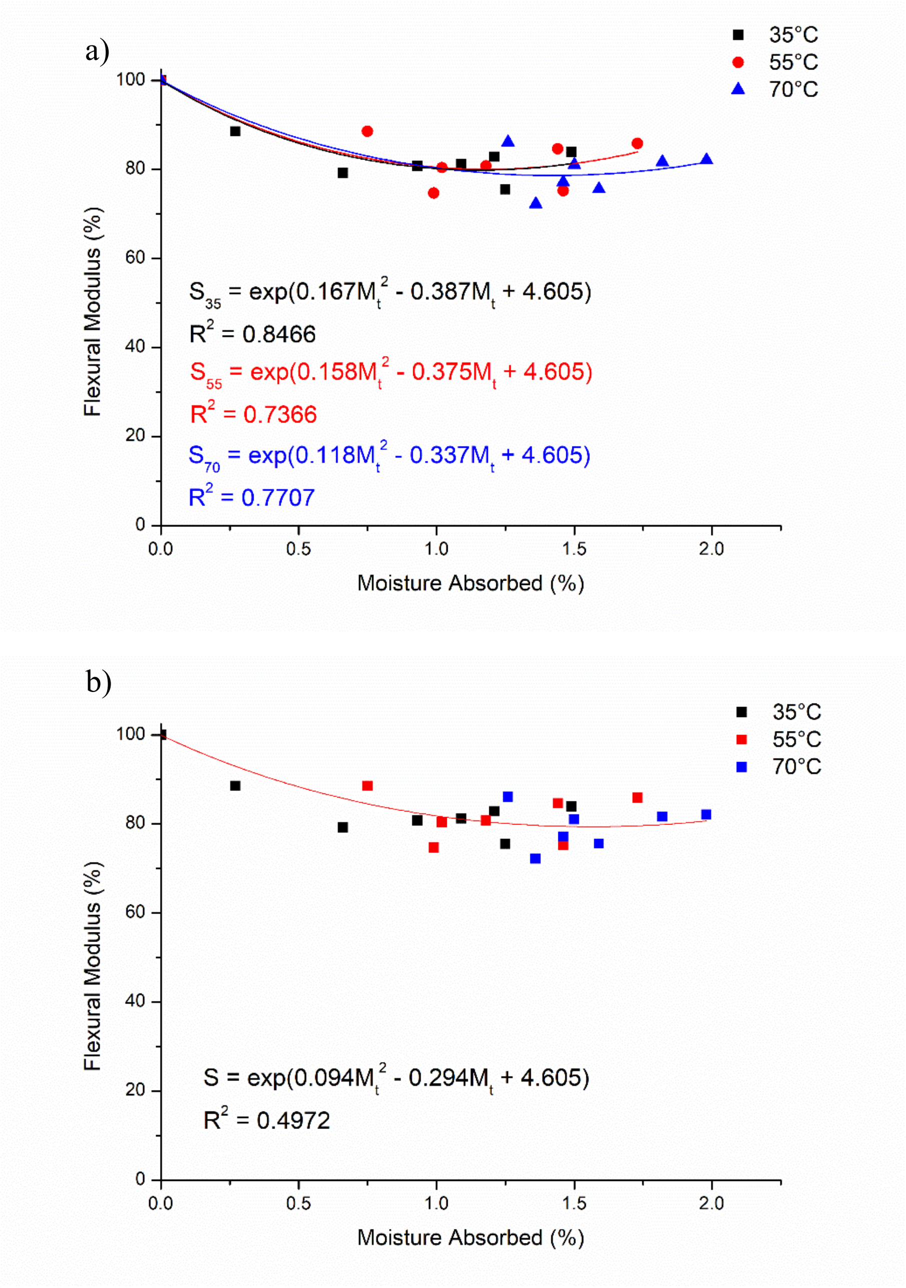

Figure 116. Flexural modulus retention as a function of moisture absorbed with exponential fitting for (a) each temperature individually and (b) all temperature data assembled.

Figure 117 shows typical failure modes observed in bending specimens. The representative pictures of the failure modes for each temperature and aging period are shown in Appendix B. The dominant failure mode was the compression of the upper fibers and traction of the outer fibers at the bottom of the specimens, failing by normal stresses, as seen in Figure 117a. Other failure modes can be observed, as in Figure 117b with a specimen aged after 5160 hours, where the crack propagated diagonally through the thickness of the specimen towards the outer fibers on the tensile side. In Figure 117c the specimen presented shear fiber fracture mode [221].

Another common failure mode is shown in Figure 117d, where the compressed fibers on the top presented buckling [222], as indicated by an arrow, followed by the transverse crack propagation towards the opposite tensile face, where the sample ultimately failed. The fiber buckling is a characteristic failure of continuous fiber reinforced composites when submitted to compressive loading, which can be more significant if there is a fiber waviness [221], which is the case of the woven-fiber composite in this study. Fiber buckling was observed for all specimens, especially the aged ones. This is especially promoted by moisture absorption, due to the softening of the matrix caused by plasticization [219]. Moreover, the compressive stress concentration in the pin load contact region foster this behavior [223].

Figure 117. Typical failure modes observed in the bending specimens in these conditions: (a) unaged, (b) 5160-hours aged at 55°C, (c) 3490-hours aged at 70°C and (d) 10170-hours aged at 70°C. All figures show failure by tensile stress on the outer fibers with the crack propagating from the compressive side. The black arrow on Fig. 107d indicates the fiber compressive buckling.

Eventually, other less common failure modes were observed with aging. Figure 118a shows a sample aged after R7 (10170 hours) at 70°C, which presented a combination of failure modes: fiber buckling in the compressive zone, crack propagation through the specimen's thickness and delamination in the direction perpendicular to the load. This happens due to the attack of moisture onto the interlaminar and fiber/matrix interfaces, weakening them, generating a preferable path for crack growth [36,188]. Nevertheless, the delaminated specimens represented a small portion of the specimens tested. The few samples that presented delamination failure mode were not considered in the calculation of the flexural properties discussed previously. Figure 118b shows a specimen aged after 570 hours at 70°C, which presented a delamination-like failure mode. However, this perpendicular crack propagation occurred after the specimen reached its maximum bending stress, in other words, after the load drop; therefore, delamination was not the composite's main failure mode. Table 37 summarizes the changes in bending failure modes observed with aging.

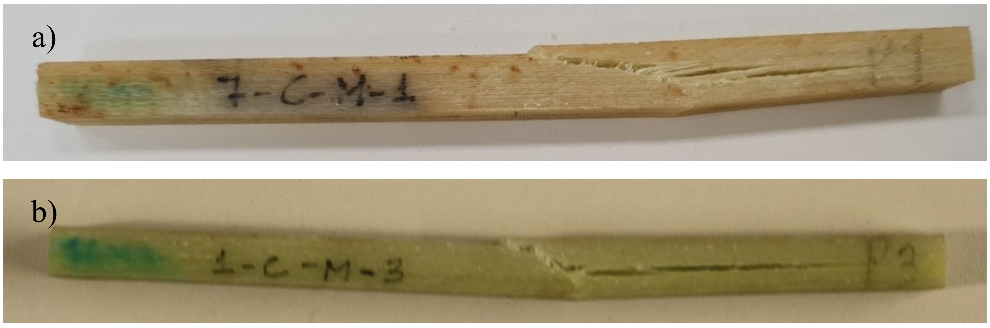

Figure 118. Delamination failure modes observed in few specimens. (a) 10170-hours aged specimen (R7) at 70°C and (b) 570-hours aged specimen (R1) at 70°C.

Table 37. Typical bending failure modes for each aging period and temperature.

Aging period (hours)	**Temperature (°C)**	**Main failure modes**		
		Tensile failure on the outer fibers	Fiber buckling on the compressive zone	Few delaminations
R0 (0 hours)	-	✓		
R1 (570 hours)	35	✓		
	55	✓		
	70	✓		
R2 (1820 hours)	35	✓		
	55	✓		
	70	✓		
R3 (3490 hours)	35	✓		
	55	✓		
	70	✓		
R4 (5160 hours)	35	✓	✓	
	55	✓	✓	
	70	✓	✓	

R5 (6830 hours)	35	✓	✓	✓
	55	✓	✓	✓
	70	✓	✓	
R6 (8500 hours)	35	✓	✓	✓
	55	✓	✓	✓
	70	✓	✓	✓
R7 (10170 hours)	35	✓	✓	✓
	55	✓	✓	✓
	70	✓	✓	✓

4.4.2. Interlaminar Shear Strength (ILSS)

Figure 119 shows representative interlaminar shear load *vs*. deflection curves for 35°C (Figure 119a), 55°C (Figure 119b) and 70°C (Figure 119c) as a function of the moisture absorbed. The ultimate strength decrease is evident with the increase in moisture absorbed for all temperatures tested. Moreover, the slope of the curves also decreased with moisture ingress, indicating a more ductile behavior presented by the aged composites.

All curves initially presented a non-linear region, followed by a linear region, with greater slope, and culminating in failure. For the unaged specimens and those after short-term exposure, the curves presented an abrupt drop in load at failure. According to Daniels *et al*. [224], such a mechanical response would be indicative of a tensile failure mode for carbon-fiber reinforced composites, but for high-strength glass-fiber reinforced composites, a shear failure can be characterized by a curve of this shape. Additionally, in the graphs in Figure 119, it can be noticed that for some groups of samples there was a variation from curves with a sharp peak to curves with a smooth peak, followed by a slow decrease in the load. This kind of behavior means that, at this stage, the fibers could still support a lower post-peak load after matrix failure.

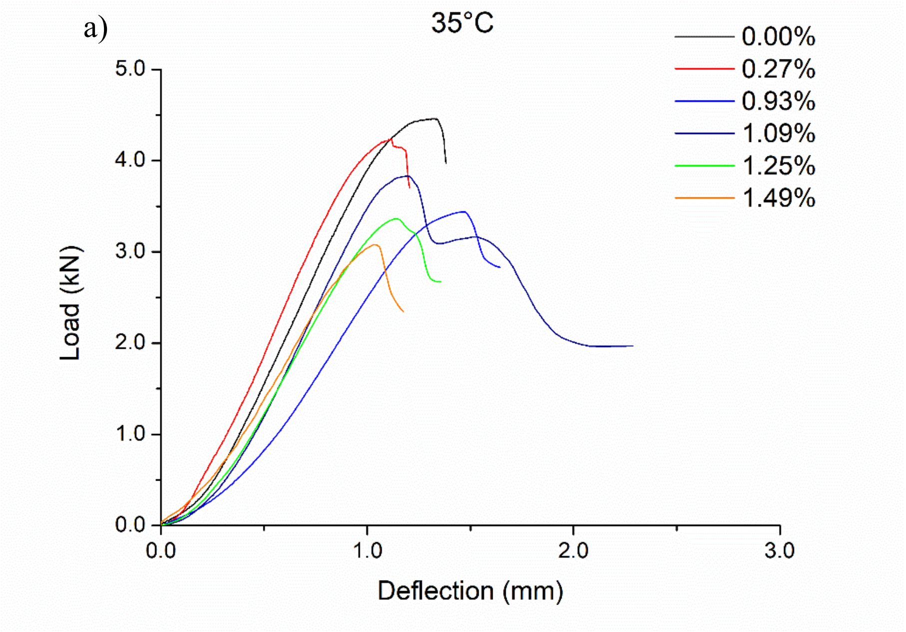
a)
35°C
0.00%
0.27%
0.93%
1.09%
1.25%
1.49%
Load (kN)
5.0
4.0
3.0
2.0
1.0
0.0
0.0
1.0
2.0
3.0
Deflection (mm)

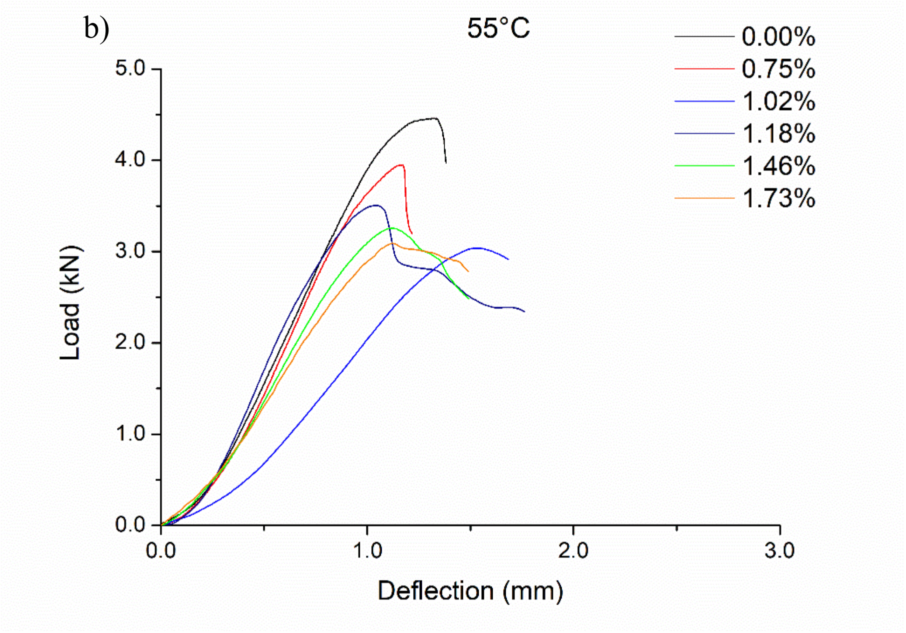
b)
55°C
0.00%
0.75%
1.02%
1.18%
1.46%
1.73%
Load (kN)
5.0
4.0
3.0
2.0
1.0
0.0
0.0
1.0
2.0
3.0
Deflection (mm)

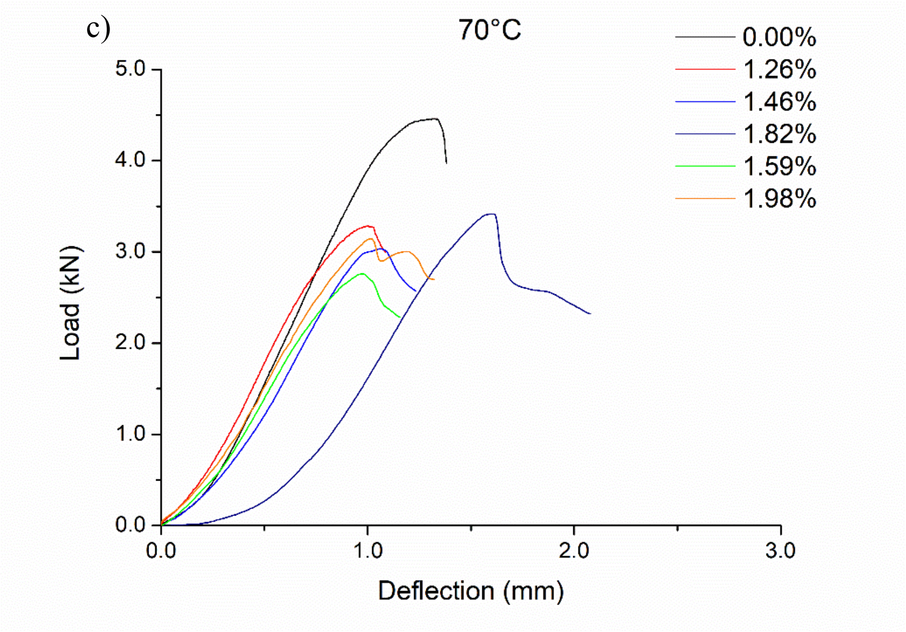

Figure 119. Interlaminar shear load *vs*. deflection curves with moisture absorbed for (a) 35°C, (b) 55°C and (c) 70°C.

Figure 120 shows the average and standard deviation values of the interlaminar shear strength of the composite as a function of aging time. Each value is an average of 15 (fifteen) specimens. Like the bending properties, the average interlaminar shear values presented a sharp initial drop followed by a stabilization for all temperatures. Like the bending tests, the shear strength plateau decreased with temperature. After 8500 hours of aging, there was no statistical difference between the strength values of all temperatures. Figure 121 shows the percentage retention curves for the temperatures tested as a function of aging time. These values are shown in Table 38.

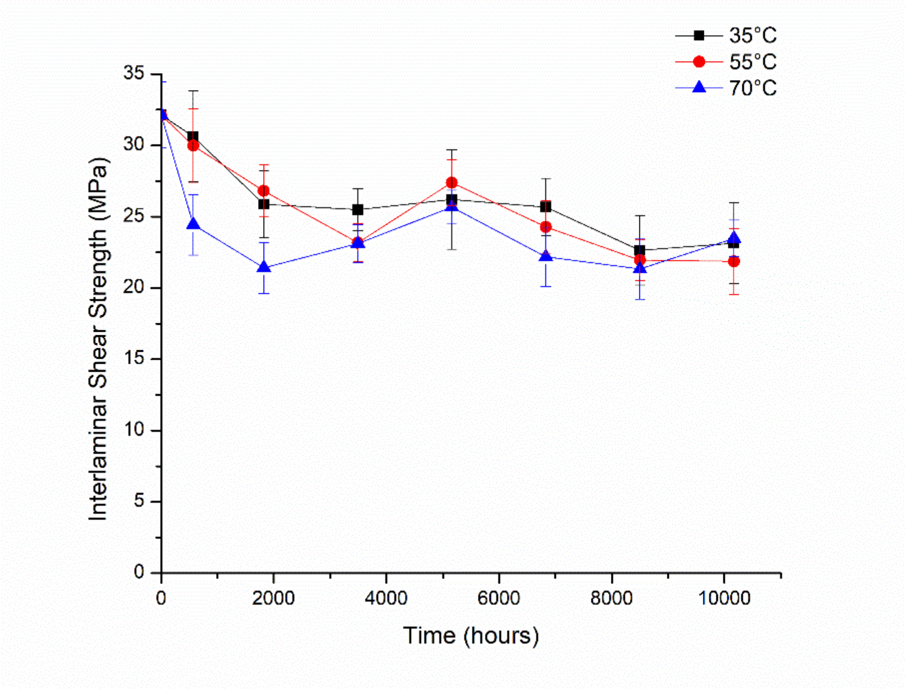

Figure 120. Interlaminar shear strength (ILSS) as a function of aging time.

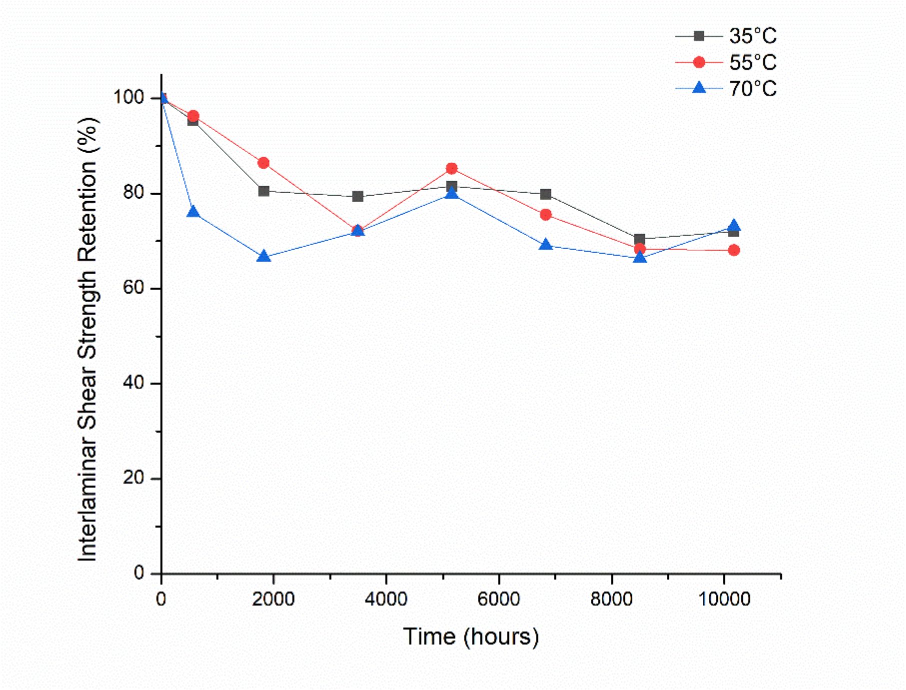

Figure 121. Interlaminar shear strength (ILSS) retention as a function of aging time.

Table 38. Average strength values and shear strength retentions for all aging temperatures with aging time.

Aging time	Temperature (°C)	Interlaminar Shear Strength (ILSS) (MPa)	Shear Strength Retention (%)
Unaged (R0)	**–**	32.13 ± 2.32	100.00
570h (R1)	**35**	30.63 ± 3.19	95.24

	55	29.98 ± 2.56	93.31
	70	24.44 ± 2.13	75.94
1820h (R2)	**35**	25.87 ± 2.35	80.52
	55	26.81 ± 1.82	83.44
	70	21.41 ± 1.79	66.64
3490h (R3)	**35**	25.61 ± 1.56	79.70
	55	27.00 ± 4.61	84.03
	70	23.12 ± 1.33	71.96
5160h (R4)	**35**	26.21 ± 3.48	81.57
	55	27.39 ± 1.59	85.25
	70	25.67 ± 1.19	79.89
6830h (R5)	**35**	25.67 ± 2.02	79.89
	55	24.28 ± 1.83	75.57
	70	22.19 ± 2.08	69.06
8500h (R6)	**35**	22.64 ± 2.43	70.46
	55	21.96 ± 1.46	68.35
	70	21.33 ± 2.11	66.39
10170h (R7)	**35**	23.15 ± 2.84	72.05
	55	21.87 ± 2.31	68.07
	70	23.48 ± 1.28	73.08

Figure 122 shows the relationship between the strength values and the moisture absorbed. Like the bending tests, the ILSS values presented a better fit for each individual temperature (Figure 122a) than for all temperatures together (Figure 122b). Once again, this leads to the assumption that the properties degradation is not only moisture-induced but also thermally affected. Therefore, both temperature and moisture ingress negatively affect the material’s structural integrity.

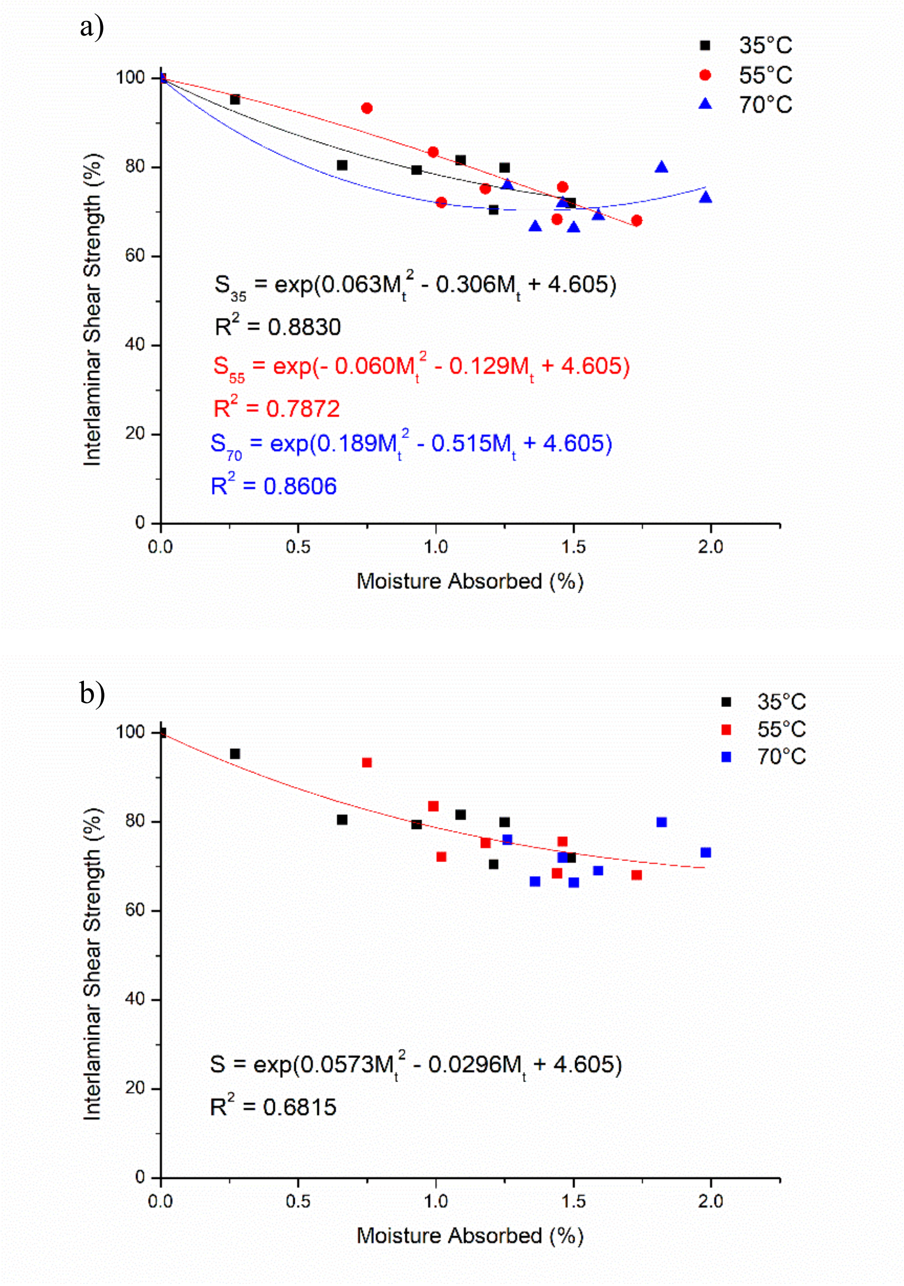

Figure 122. Interlaminar shear strength retention as a function of moisture absorbed with exponential fitting for (a) each temperature individually and (b) all temperature data assembled.

Figure 123 shows the schematic typical failure modes expected for ILSS test. The circles point to load *vs*. displacement curves representing the various failure modes. The composites in this work exhibited a combination of homogeneous shear, discrete shear and permanent deformation failure modes. It is noteworthy that the tensile and compressive failure modes represented by numbers 30, 31 and 40 in Figure 123 are not acceptable for short beam shear tests. These failure modes were not observed in the samples of this work. The occurrence of these failure modes might indicate incorrect span between the supports [225].

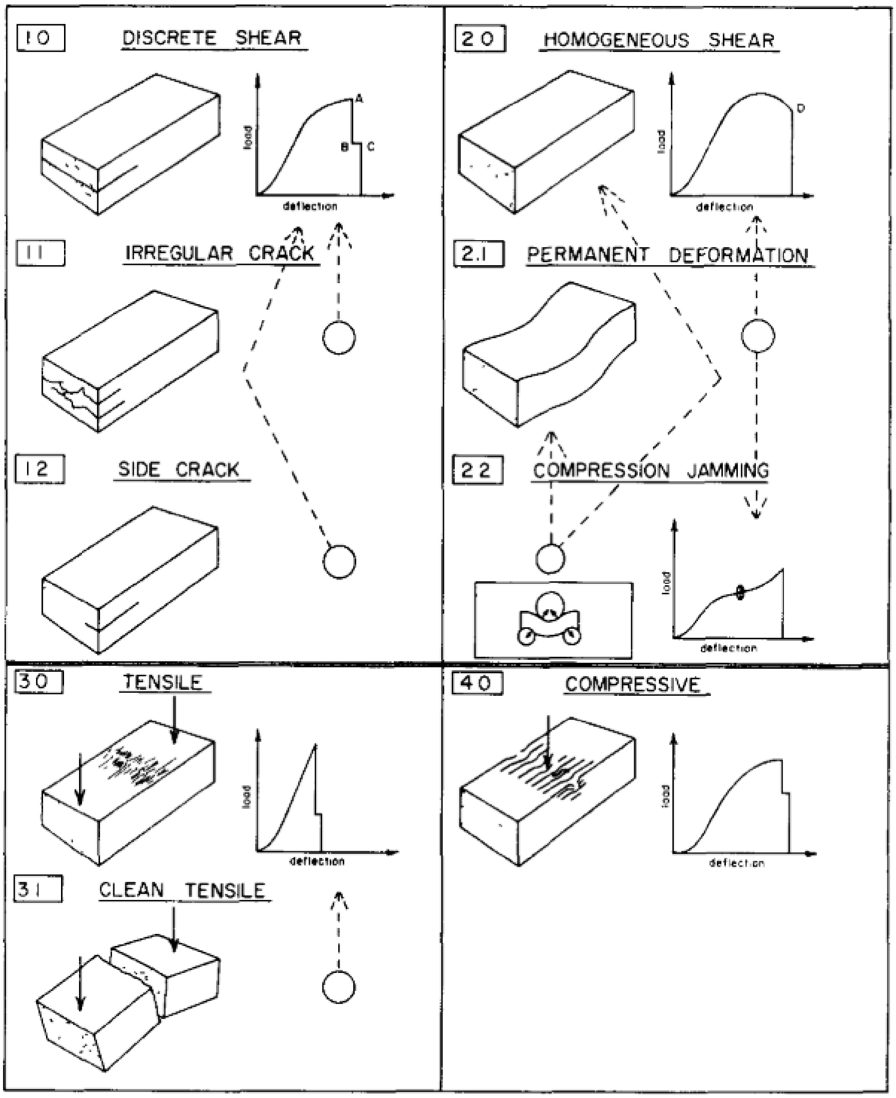

Figure 123. Failure modes that can be found in ILSS tests [224].

Figure 124 shows the failure modes found in the ILSS tests in this work. Basically, there was a combination of interlaminar crack and inelastic deformation. The inelastic deformation failure mode was more prominent at the early stages of aging, which leads to the assumption that the interlaminar strength of the laminates used were higher than the shear strength in the tested plane. Figure 124a shows an unaged specimen after failure, showing the inelastic deformation and few delamination on the compressed side of the specimen. Figures 124b and 124c show two specimens aged after 570 hours at 35°C, showing shear cracks indicated by the white arrow (Figure 124b) and white ellipse (Figure 124c); the latter one indicates the shear crack on the mid-plane of the composite, which is one of the failure modes recommended by ASTM D2344 standard [159,226]. In some samples, the tensile failure mode could be seen, as in Figure 124d, combined with interlaminar crack.

The interlaminar crack in the specimens' mid-point cannot be clearly seen in the pictures, therefore Figure 124e shows an example of shear displacement caused by a short beam shear test, where the motion of the planes is represented by the black arrows. Additionally, according to Daniels *et al*. [224], samples that do not show clear sign of failure after the load has reached its peak are assumed to have failed by a shearing mechanism. Finally, Figure 124f shows interlaminar failure at multiple layers of the composite. The representative pictures of the failure modes for each group of samples can be found in Appendix B. Table 39 summarizes the changes in failure modes observed for the ILSS specimens with aging.

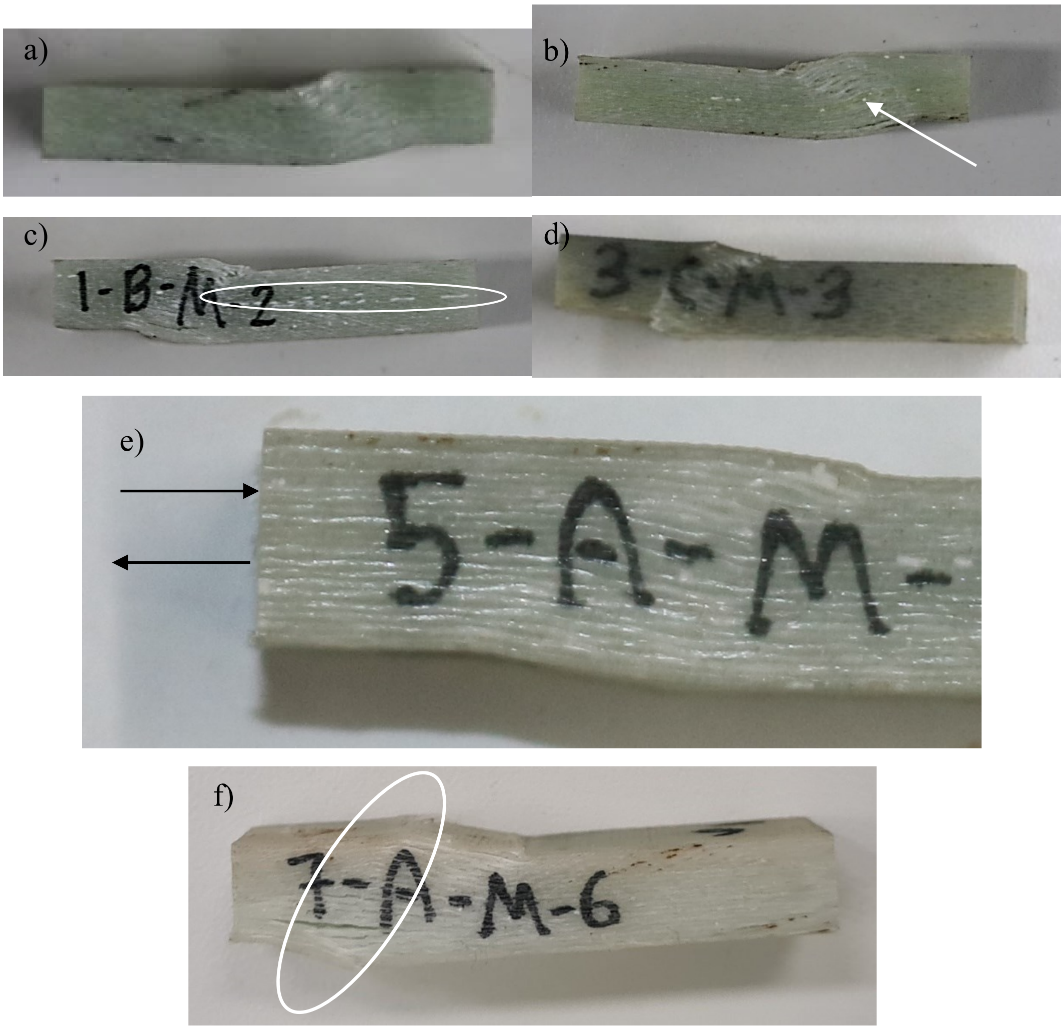

Figure 124. Typical failure modes obtained in ILSS tests. (a) unaged sample, (b) and (c) 570-hours aged samples at 35°C, (d) 3490-hours aged sample at 70°C, (e) 6830-hours aged sample at 35°C and (f) 10170-hours aged sample at 35°C.

Table 39. Typical ILSS failure modes for each aging period and temperature.

	Main failure modes

Aging period (hours)	**Temperature (°C)**	Shear failure	Inelastic deformation	Interlaminar shear
R0 (0 hours)	-	✓	✓	
R1 (570 hours)	35	✓	✓	✓
	55	✓	✓	✓
	70	✓	✓	✓
R2 (1820 hours)	35	✓	✓	✓
	55	✓	✓	✓
	70	✓	✓	✓
R3 (3490 hours)	35	✓	✓	✓
	55	✓	✓	✓
	70	✓	✓	✓
R4 (5160 hours)	35	✓	✓	
	55	✓	✓	✓
	70	✓	✓	✓
R5 (6830 hours)	35	✓	✓	✓
	55	✓	✓	✓
	70	✓	✓	✓
R6 (8500 hours)	35	✓	✓	✓
	55	✓	✓	✓
	70	✓	✓	✓
R7 (10170 hours)	35	✓	✓	✓
	55	✓	✓	✓
	70	✓	✓	✓

4.4.3. Mechanical Properties' Prediction

One of the main goals of performing accelerated aging tests, i.e., aging tests at temperatures higher than room temperature, is the possibility of reaching higher degradation levels at a shorter time scale. Therefore, these accelerated tests would allow the assessment of degradation rate for higher temperatures and, through mathematical manipulations, it would be possible to extrapolate these results to temperatures out of the test temperature range. This would allow the prediction of the service-life of the material in service conditions without the necessity to perform extremely time-consuming aging tests at the temperatures of interest.

Therefore, in this section a prediction model will be developed and the results found in the mechanical tests aforementioned will be used to predict the service-life of the composite repair at 25°C, which is the average room temperature in the offshore platforms, where these materials are generally employed to repair corroded oil and gas metallic pipes [25]. Numerous works were found in literature about Arrhenius and Phani and Bose models (discussed in Sections 2.4.2.1 and 2.4.2.2, respectively) [72,111,112,136,227,228], but none of the manuscripts found by the author predicted the long-term service-life after salt fog tests.

4.4.3.1. Arrhenius Model

Basically, the model to be applied consists of an combination of the Phani and Bose model [136] (Section 2.4.2.2) and Arrhenius model (Section 2.4.2.1). The Phani and Bose model is described by Equation 83, where σ_0 is the strength value of the unaged composite, σ_∞ the long-term strength value, t the aging time in hours and τ the fitted parameter for this model.

$$\sigma = (\sigma_0 - \sigma_\infty)e^{-\frac{t}{\tau}} + \sigma_\infty \tag{83}$$

However, a small modification was made to this equation to account for the property percentage retention instead of the absolute strength value, resulting in Equation 84, where S is the property retention, S_∞ is the long-term retention plateau and 100 is the retention of the unaged material.

$$S = (100 - S_\infty)e^{-\frac{t}{\tau}} + S_\infty \tag{84}$$

This model is only valid when the degradation mechanism is the same throughout the aging time and does not change with temperature. Therefore, if the material experiences hydrolysis after a period of time, the property loss will be greater and this model is no longer valid. As an example, Figure 125 shows a comparison of a property degradation without hydrolysis (I), for which the Phani and Bose model is valid, and with hydrolysis (II) [229].

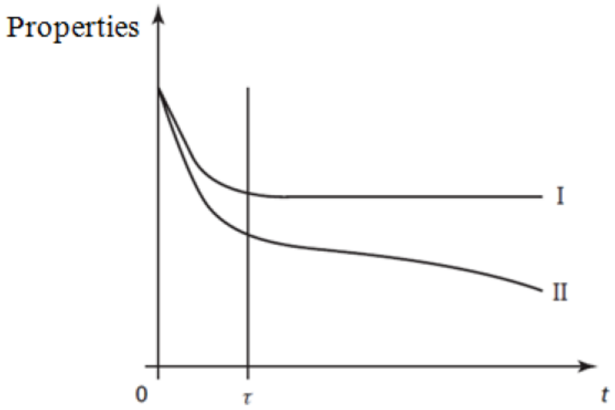

Figure 125. Property degradation as a function of aging time for I – a material without hydrolysis and II – a material suffering hydrolysis [229].

Thus, the first step is to fit equation 84 by non-linear regression to the experimental data from the destructive tests discussed in Sections 4.4.1 and 4.4.2. The optimization method chosen was the least square method. This fit was done to flexural strength and modulus and interlaminar shear strength. Little has been found in the literature about modulus prediction models, mostly for strength. The fitted graphs are shown in Figure 126. Both τ and S_∞ parameters were set as unknown output variables to be obtained from the regression.

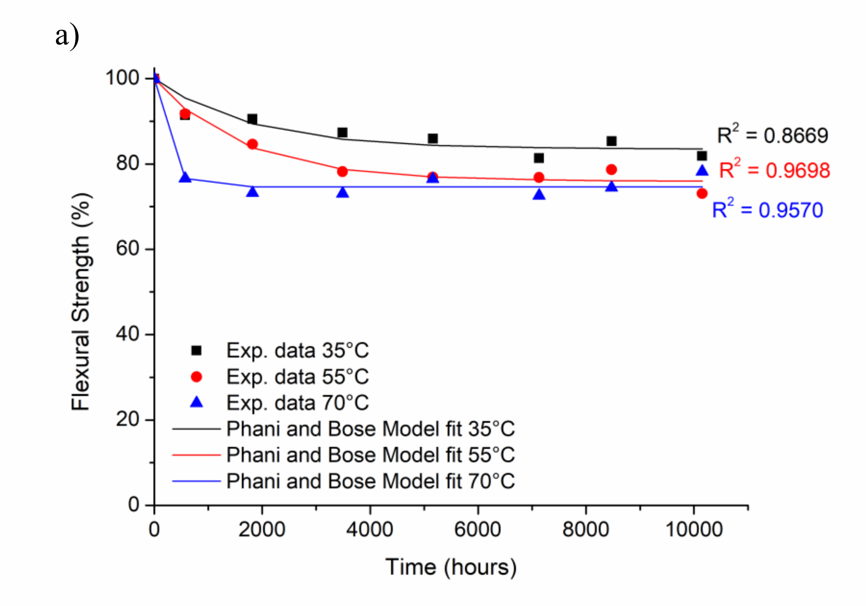

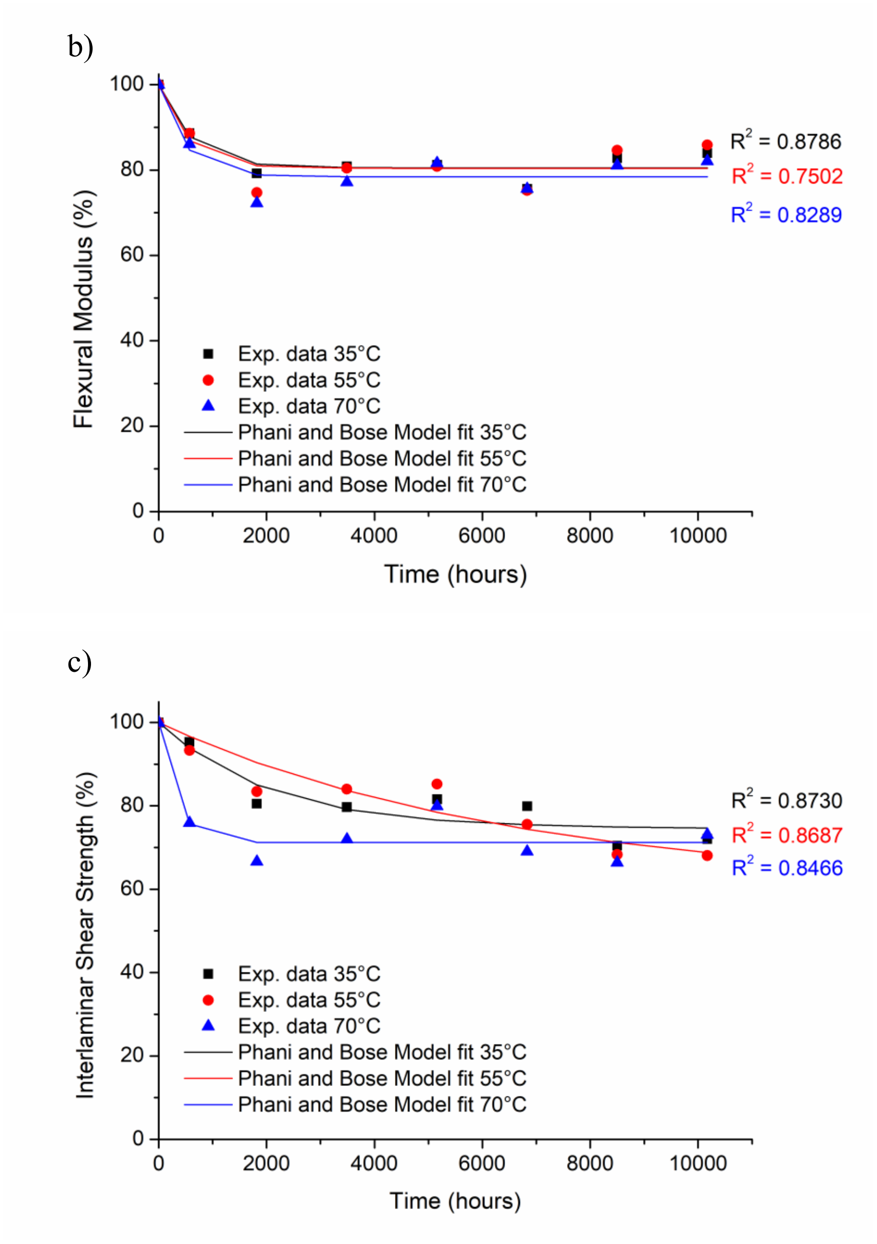

Figure 126. Phani and Bose model fit for (a) flexural strength, (b) flexural modulus and (c) interlaminar shear strength.

The resulting equations for each property are shown in Equations 85 – 93. *S* and *E* stand for strength and modulus, respectively.

Bending strength:

$$S_{35} = 16.50e^{-\frac{t}{1794.21}} + 83.50 \qquad (R^2 = 0.8639 \text{ for T} = 35°C) \quad (85)$$

$$S_{55} = 21.40e^{-\frac{t}{1207.04}} + 78.60 \qquad (R^2 = 0.9322 \text{ for T} = 55°C) \quad (86)$$

$$S_{70} = 25.42e^{-\frac{t}{223.94}} + 74.58 \qquad (R^2 = 0.9618 \text{ for T} = 70°C) \quad (87)$$

Bending modulus:

$$E_{35} = 18.80e^{-\frac{t}{596.45}} + 81.20 \qquad (R^2 = 0.8683 \text{ for T} = 35°C) \quad (88)$$

$$E_{55} = 18.96e^{-\frac{t}{524.60}} + 81.04 \qquad (\mathrm{R}^2 = 0.7369 \text{ for T} = 55°\mathrm{C}) \quad (89)$$

$$E_{70} = 21.08e^{-\frac{t}{477.02}} + 78.92 \qquad (\mathrm{R}^2 = 0.8295 \text{ for T} = 70°\mathrm{C}) \quad (90)$$

Interlaminar shear strength:

$$S_{35} = 25.47e^{-\frac{t}{2049.71}} + 74.53 \qquad (\mathrm{R}^2 = 0.8730 \text{ for T} = 35°\mathrm{C}) \quad (91)$$

$$S_{55} = 39.63e^{-\frac{t}{6565.46}} + 60.37 \qquad (\mathrm{R}^2 = 0.8687 \text{ for T} = 55°\mathrm{C}) \quad (92)$$

$$S_{70} = 28.81e^{-\frac{t}{310.92}} + 71.19 \qquad (\mathrm{R}^2 = 0.8466 \text{ for T} = 70°\mathrm{C}) \quad (93)$$

From these equations, the parameters τ and S_∞ were obtained. In addition, the property degradation rate (k) can be calculated from the τ term, according to Equation 94. The fitted parameters for each property and temperature are shown in Table 40, along with the degradation rates (k).

$$k\ (h^{-1}) = \frac{1}{\tau} \qquad (94)$$

Table 40. Fitted parameters and degradation rates for each property.

Property	**Temperature (°C)**	**S_∞ (%)**	**τ (hours)**	**k (hours^{-1})**
Flexural Strength	35	83.51	1761.20	5.68×10^{-4}
	55	75.95	1612.18	6.20×10^{-4}
	70	74.66	220.54	4.53×10^{-3}
Flexural Modulus	35	80.54	576.78	1.73×10^{-3}
	55	80.39	511.86	1.95×10^{-3}
	70	78.41	462.26	2.16×10^{-3}
Interlaminar Shear Strength	35	74.53	2049.71	4.88×10^{-4}
	55	60.37	6565.46	1.52×10^{-4}
	70	71.19	306.89	3.26×10^{-3}

For the flexural strength and flexural modulus, the degradation rate increased with temperature, as expected. It should be noticed that for the flexural modulus there was a marginal difference between temperatures. This is due to the fact that the moisture-induced effects on property degradation occur on the matrix and interfaces and modulus is a fiber-dominated property. On the other hand, for the ILSS there was an unexpected decrease in the degradation rate from 35 to 55°C, followed by a new increase at 70°C. Consequently, both S_∞ and τ did not follow the expected trend, which is a continuous decrease in these parameters with temperature, which would indicate stronger degradation levels and rates, like the ones for the flexural properties. This was caused by the lack of statistical difference between the interlaminar properties at 35 and 55°C. Figure 127 shows the fitted Phani and Bose model for the ILSS data along with the standard deviation. It can be seen that, considering the standard deviation, the strength level at low temperatures (35 and 55°C) was nearly the same within the experiment time. Since the interlaminar shear strength is a matrix-dominated property, it is more affected by the proximity to T_g than the bending properties.

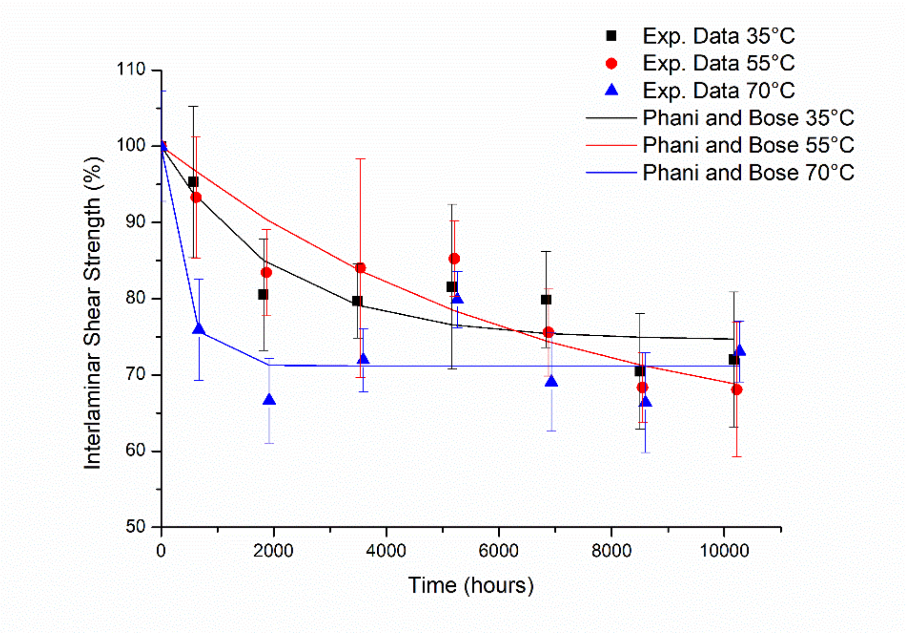

Figure 127. Phani and Bose model fit for ILSS data and their standard deviation.

For the Arrhenius plot, the time needed to reach certain retention levels was calculated by Equation 95, which is basically the manipulation of Equation 84. For each property and temperature, the fitted parameters displayed in Table 38 (τ and S_∞) were substituted into the respective equations 85 – 93 with the parameter S varying from 100% to the lowest retention plateau obtained. The most important characteristic of this model is that it only allows the Arrhenius plot of the retention levels within the experimental data. In other words, it is only possible to plot this graph for retention levels higher than the retention plateau (S_∞) obtained from the fitting, since a lower level will not be reached. That is, if in equation 95 the value substituted in parameter S is lower than S_∞, the equation results in the natural logarithm of a negative value. Therefore, based on the experimental retention range obtained for each mechanical property, different retention ranges were used for the Arrhenius plots. For example, for the flexural strength the minimum retention level in the Arrhenius curve was 83.51%, while for ILSS it was 71.19% (Table 38). After calculating the time needed for each retention level of each property from Equation 95, the Arrhenius curves for each property could be plotted in logarithmic scale (Figure 128). As expected from the Arrhenius plots, the lower the temperature, the longer the time required to reach a certain retention level due to its lower environmental harshness. From a practical point of view, with these charts it is possible to assess when the repair will need to undergo a repair and/or replacement, so these plots are extremely useful in real-life applications.

$$t = -\tau ln\left(\frac{S-S_{\infty}}{100-S_{\infty}}\right) \qquad (95)$$

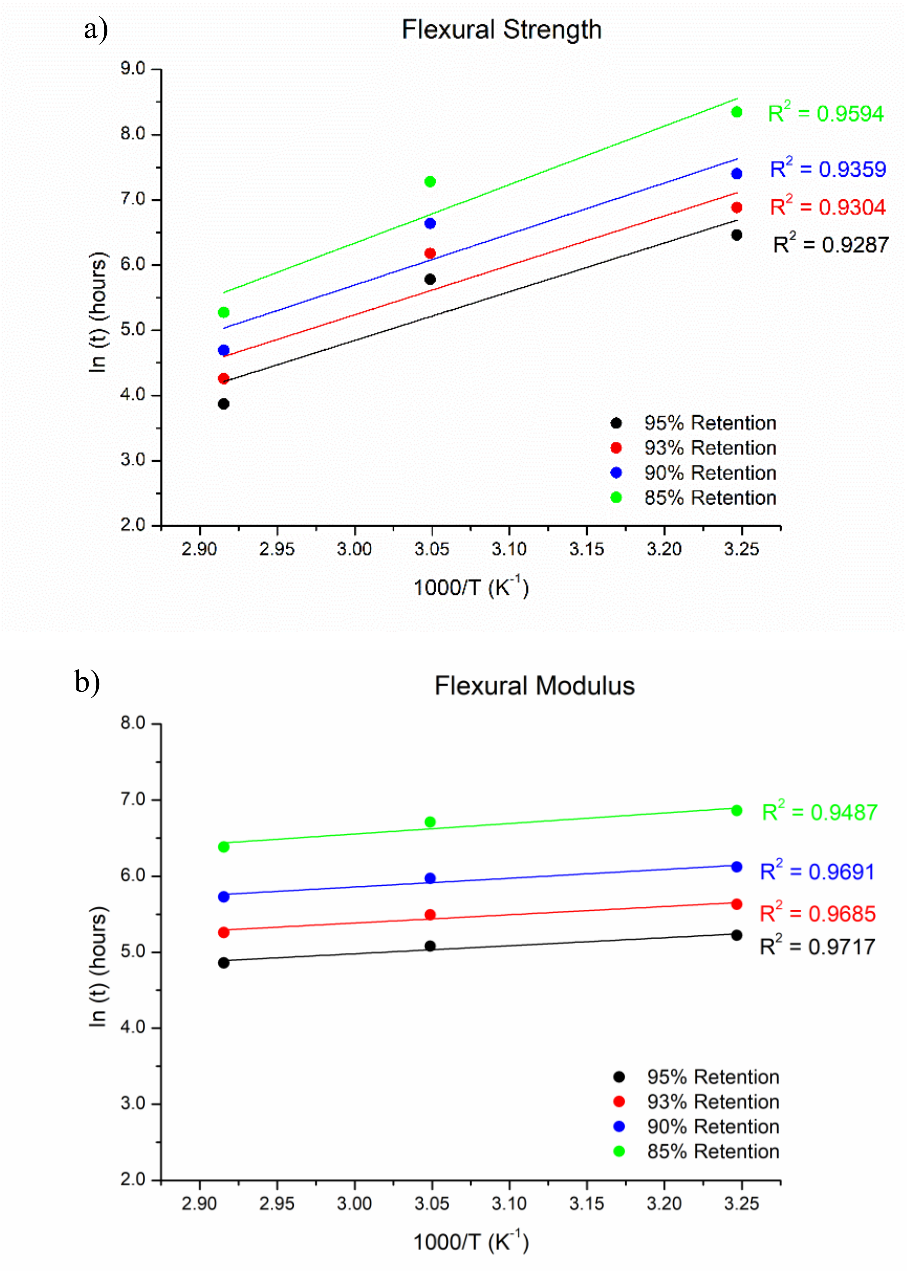

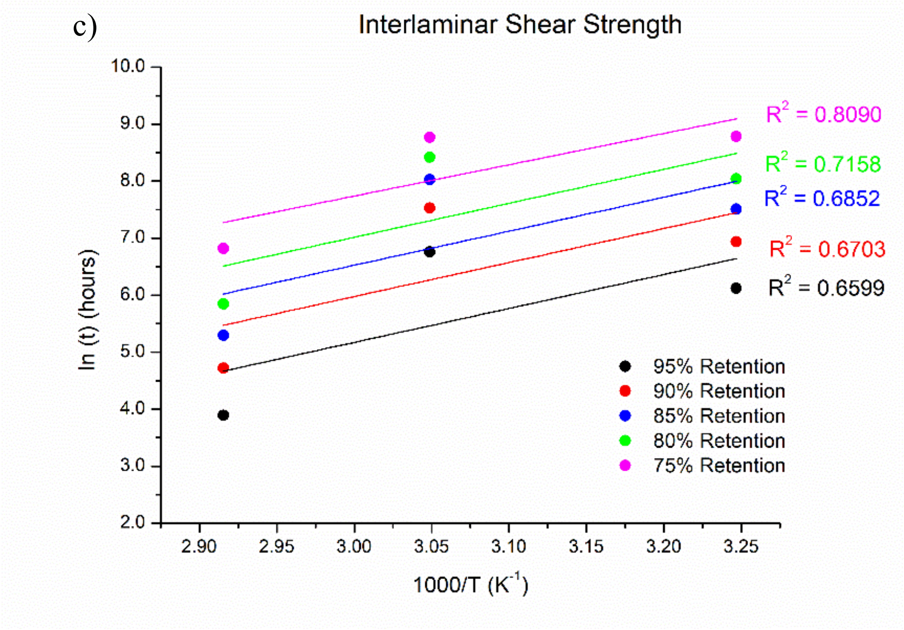

Figure 128. Arrhenius plots of the composite's service-life for (a) flexural strength, (b) flexural modulus and (c) interlaminar shear strength.

4.4.3.2. Properties prediction at room temperature

From literature, the most commonly used method for service-life prediction for temperatures other than the experimental temperature range is the application of the Time-Shift Factor (*TSF*), which is a parameter described by Equation 96, where T_0 is a reference temperature, which can be one of the experimental temperatures, T_1 the temperature of interest, t_0 and t_1 are the times taken to reach certain retention level at T_0 and T_1 respectively, k_0 and k_1 are the degradation rates at T_0 and T_1 respectively, E_a is the activation energy, A is an empirical constant and R is the universal gas constant [72,227,228].

$$TSF = \frac{t_0}{t_1} = \frac{k_0}{k_1} = \frac{A\,exp(-E_a/RT_1)}{A\,exp(-E_a/RT_0)} = exp\left[\frac{E_a}{R}\left(\frac{1}{T_0} - \frac{1}{T_1}\right)\right] \qquad (96)$$

From this equation, after taking a reference temperature, such as 35°C, it is possible to estimate the time taken to reach the retention levels at temperatures out of the experimental temperature range, such as 25°C, and substitute the values found into equation 84 to plot the material's service-life at any temperature. However, it only allows the extrapolation of the retention range attained experimentally. For example, at 35°C the lowest flexural strength retention level was 83.51%, therefore this would be the lowest level to be extrapolated to other temperature. As it is shown in Table 38, the long-term retention plateau (S_∞) varies with temperature, thus this extrapolation might be either underestimated or overestimated when done to other temperature, since the harshness of the degradation varies with temperature.

Therefore, the methodology proposed here is to plot the S_∞ and τ parameters found in Table 38 for each property as a function of temperature and adjust the graph to obtain a correlation equation. Then, by substituting the desired temperature into these equations, the parameters can be obtained and substituted into equation 84 to obtain the service-life prediction.

Taking the flexural strength as an example, Figure 129 shows the fitting results for the parameters S_∞ and τ. The temperature chosen to extrapolate these parameters and calculate the service-life of the repair was 25°C, which is the average room temperature that these pipeline repairs are exposed to in offshore platforms [25]. By substituting 25°C into the equations shown in Figure 129, the parameters S_∞ and τ obtained for this temperature are 86.53% (286 MPa) and 2729.39 hours, respectively, meaning that at this temperature the environmental effects are less aggressive than at the test temperatures. From the parameter τ the degradation rate calculated from equation 94 is found to be 3.84 x 10^{-4} hours^{-1}.

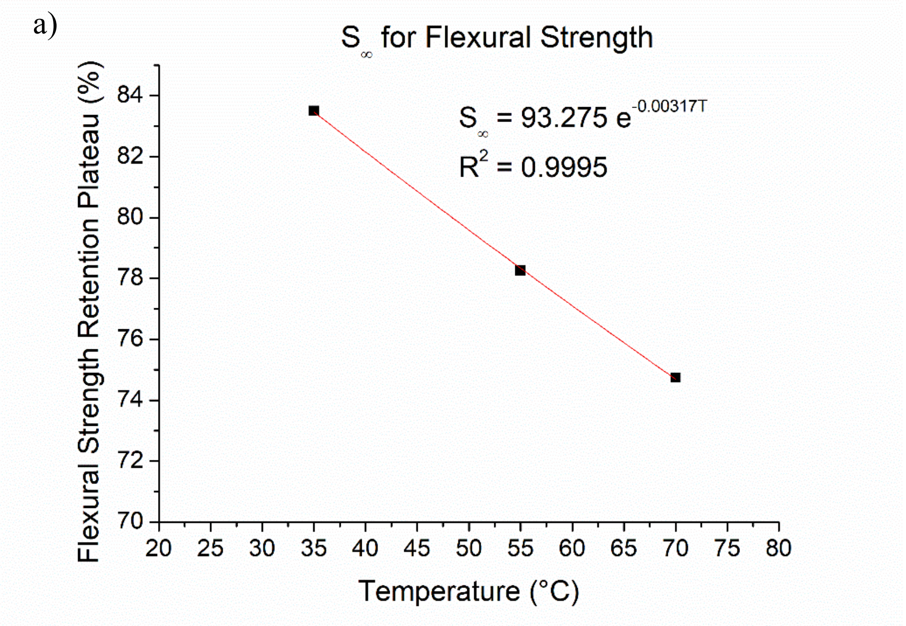

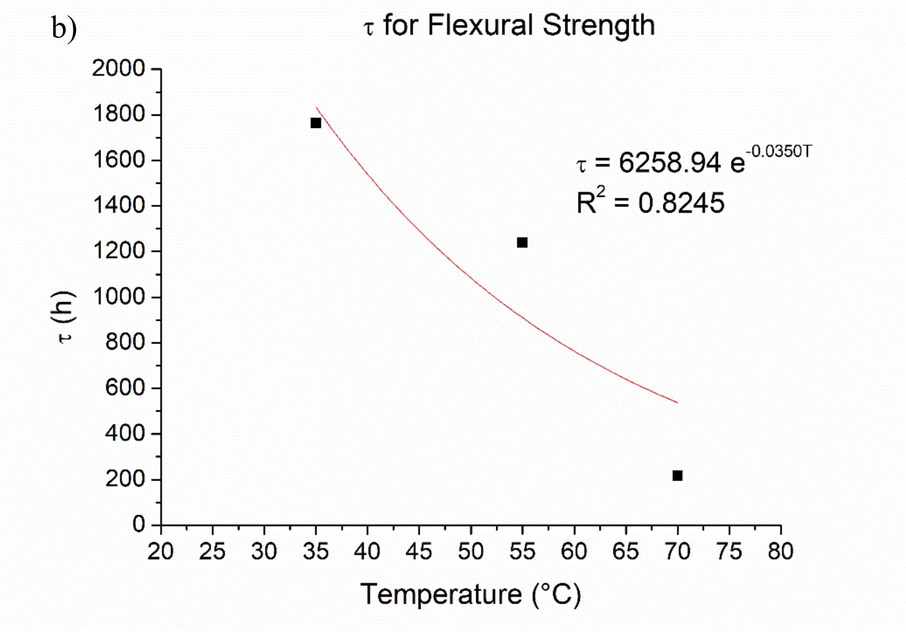

Figure 129. Fitting for (a) S_∞ and (b) τ for flexural strength.

The same methodology was attempted to be done to flexural modulus and interlaminar shear strength. However, for the case of interlaminar shear, it was shown in the previous section that there was an improper trend for the fitted parameters (Table 38), making the extrapolation unreliable. Also, Figure 127 showed that, statistically, there was no difference between the strength levels attained at 35 and 55°C. Therefore, both low temperatures data were merged into one series of data and it was adjusted to Phani and Bose model. Figure 130 shows the resulting curves for the adjust to the low temperatures assembled, namely 35 + 55°C, and 70°C. The values found for S_∞ were 70.22% and 71.19% for 35 + 55°C and 70°C, respectively, while the values for τ were 3527 and 306.89 hours for "35 + 55°C" and 70°C, respectively. Thus, the retention levels reached for all temperatures were nearly the same; the exposure to 70°C only made this retention be reached faster. Hence, it can be considered that the S_∞ value for 25°C would be the same as those found in the analysis of Figure 130. It is assumed then that it would be 70.70%, which is an average from the S_∞ values obtained for 35 + 55°C (70.22%) and 70°C (71.19%). As a conclusion, the ILSS service-life could not be extrapolated to 25°C, although the retention plateau is known. This similar behavior between low temperatures was also seen in the thickness swelling behavior (Section 4.3 – Figure 107) and in the similar saturation moisture content (Section 4.2.1 – Table 12).

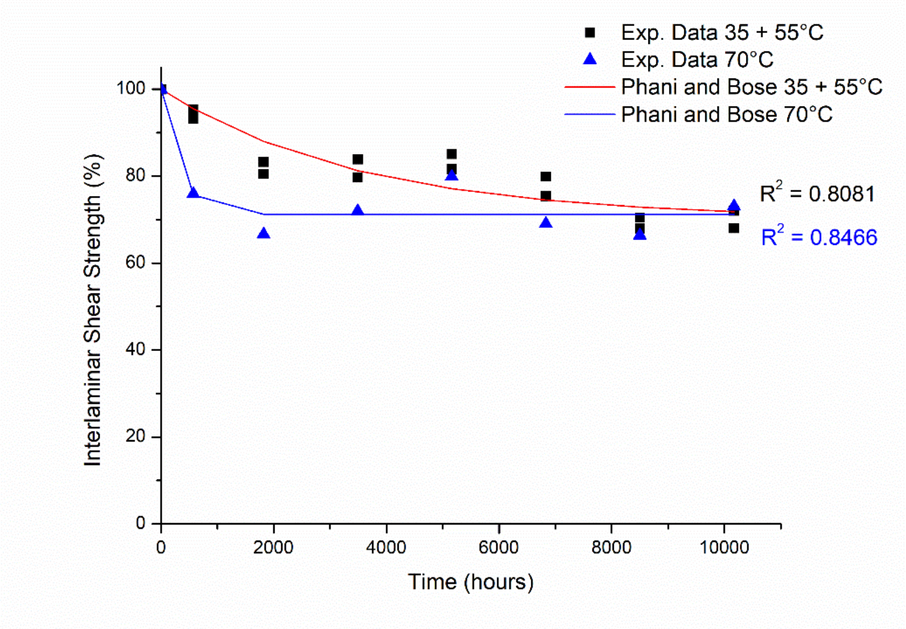

Figure 130. Phani and Bose fitted curves for the ILSS data of 35 and 55°C merged together and 70°C.

Figure 131 shows the fitted curves for E_∞ for flexural modulus.

a)

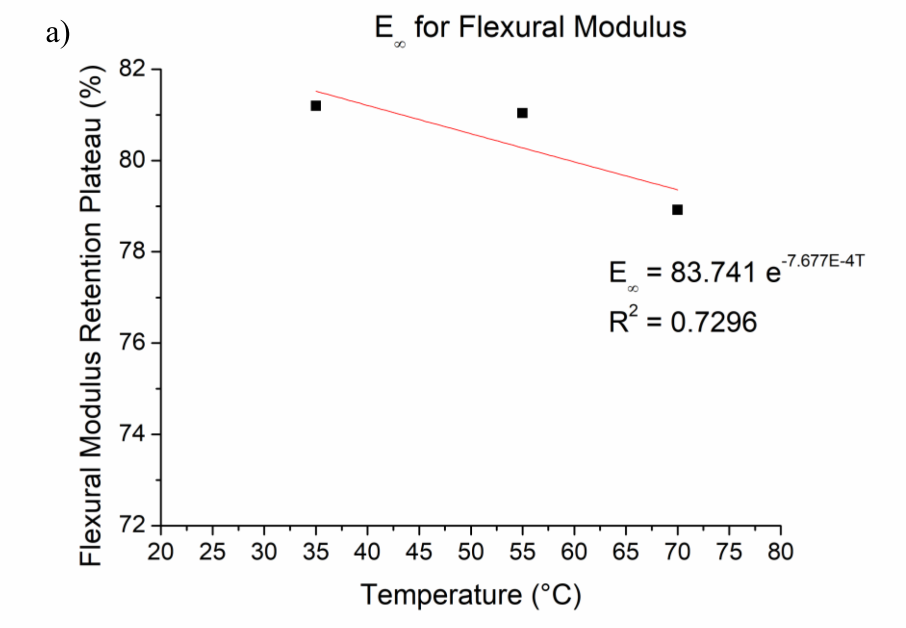

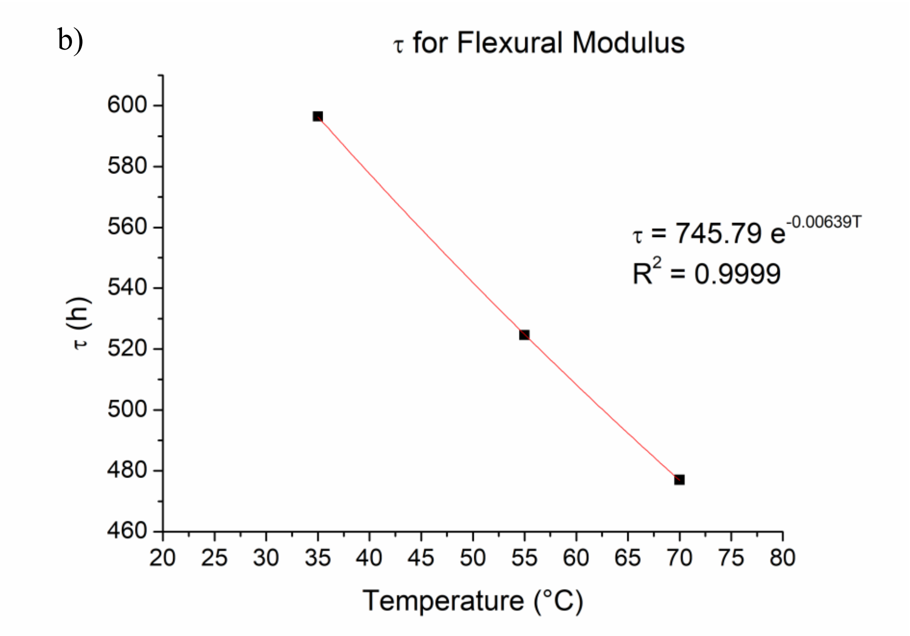

Figure 131. Fitted (a) and (b) for S_∞ and τ for Flexural Modulus, respectively.

Table 41 summarizes these parameters extrapolated to 25°C for the flexural properties, along with the degradation rate (*k*). Similar values were found in literature. Jesthi and Nayak [35] found 90% of retention for flexural strength of glass-fiber composites after immersion in seawater for three months, Murthy *et al.* [230] reported 86% retention level for flexural strength for GFRP immersed in seawater for 100 days, and Sinmazçelik and Arici [231] found a ILSS retention level of 74% for CFRP immersed in seawater at 20°C for 90 days, similar to those ones found in Figure 130.

Table 41. Fitted parameters for 25°C (S_∞ - saturation retention content, τ – fitted parameter, k – degradation rate), including the absolute values for the flexural properties.

	Temperature (°C)	S_∞ (%)	σ_R / E	τ (h)	k (h^{-1})
Flexural Strength	25	86.53	286.06 MPa	2729.39	3.66×10^{-4}
Flexural Modulus	25	82.18	19.97 GPa	635.59	1.57×10^{-3}

By applying the values listed in Table 38 in the Phani and Bose equation (Equation 84), the time taken to reach specific retention levels is calculated. As an example, for the flexural strength, the time taken to reach 90% retention at 35°C is 1643 hours, while for 25°C it would take 3702 hours to reach the same retention level. Figure 132 shows the experimental values for the temperatures tested together with their Phani and Bose model fit and the service-life prediction for 25°C from the above-mentioned methodology. In the chart legends, the term “P. B.” stands for

"Phani and Bose". As expected, at 25°C the retention level was higher than at other higher temperatures, especially for flexural strength, while for flexural modulus it was slightly higher, owing to the lower effect of moisture on the fiber-dominated modulus. Therefore, it can be considered that the flexural modulus plateau is virtually the same for all temperatures, with temperature accelerating the property loss.

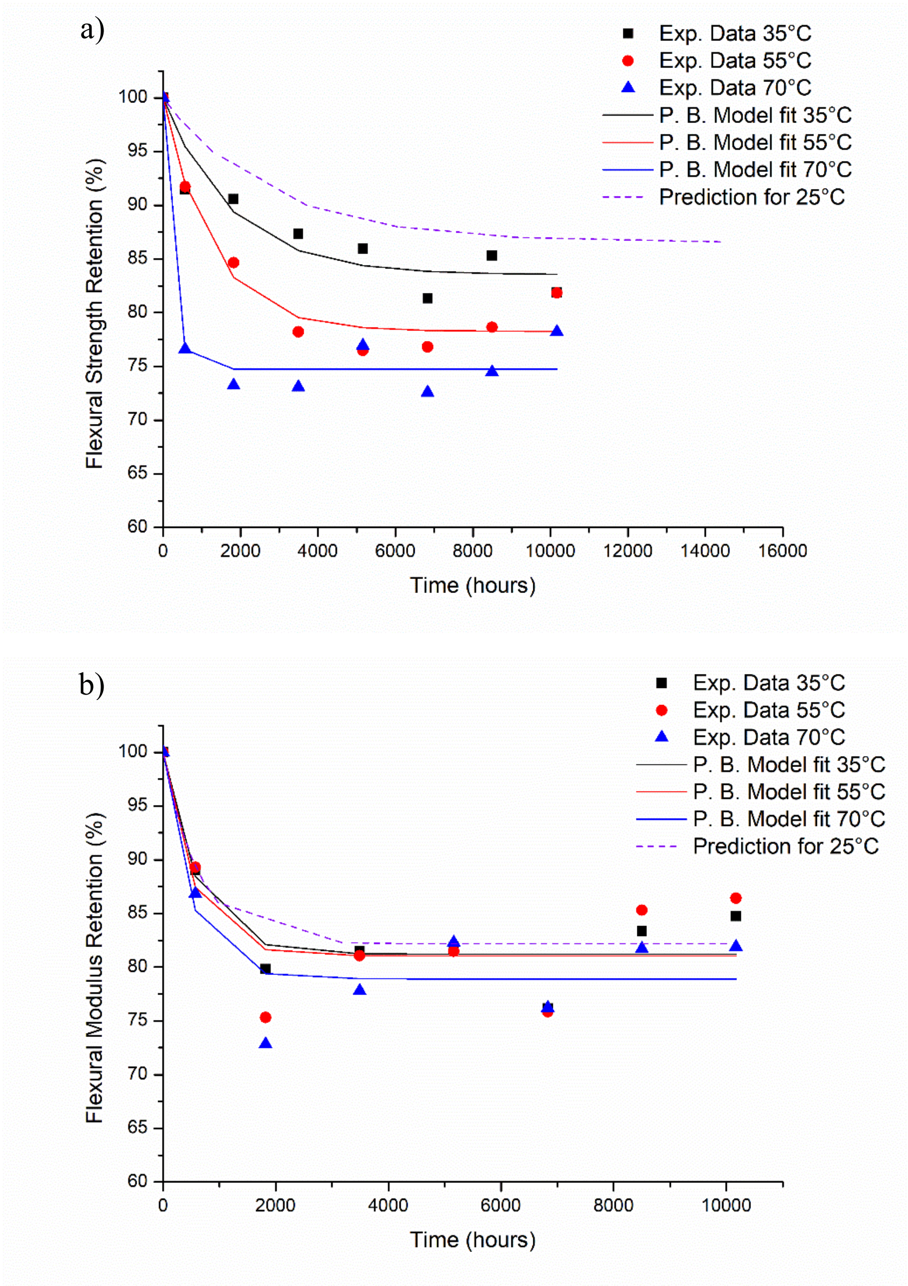

Figure 132. Prediction for 25°C for (a) flexural strength and (b) flexural modulus.

4.5. Non-Destructive Testing (NDT)

Non-Destructive Tests were developed in order to facilitate inspection in real-life applications in order to detect defects and monitor the material's integrity without the need to submit it to destructive tests. The first NDT to be discussed in this topic is the Impulse Excitation Technique (IET), also called as *Sonelastic*®, which enables the determination of elastic and viscous properties of the materials. Then, the Colorimetry results will be presented as visual evidence of the hygrothermal degradation suffered by the materials.

4.5.1. Impulse Excitation Technique (IET)

Figure 133 shows the Young modulus obtained for the bending FRP specimens (Figure 133a) and the absorption neat epoxy resin specimens (Figure 133b) at all testing temperatures as a function of aging time. Since the IET test on the FRP is performed in the flexural mode with bending specimens, the stiffness measured is comparable to the bending modulus. From Figure 133, it can be seen that there was a decrease trend for both materials at all temperatures, evidencing that the plasticization outweighed the post-cure, although there was no visible difference between the values for the three temperatures, if considering the standard deviation, especially for the FRP. Moreover, the modulus values found for the unaged neat epoxy system corroborates with literature, which states it can vary from 2.41 to 3.81 GPa, depending on the nature of the hardener and the curing degree of the material [182,232,233].

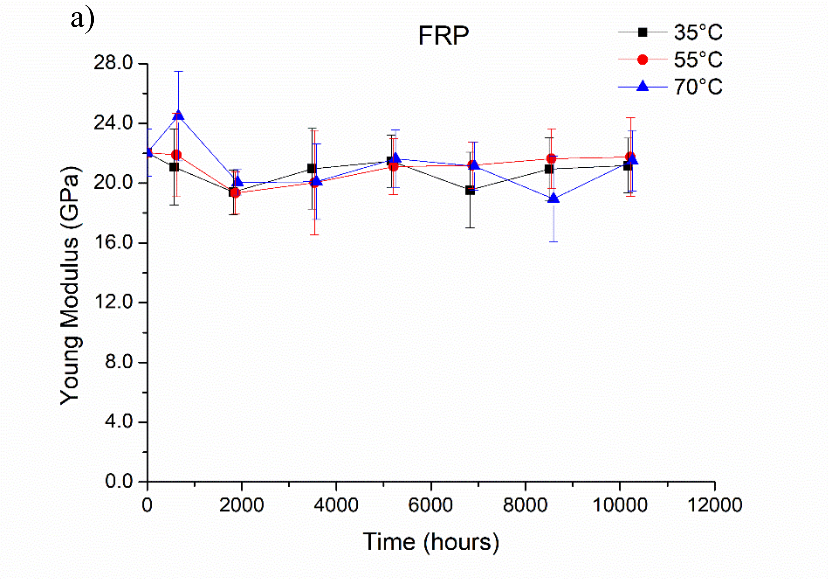

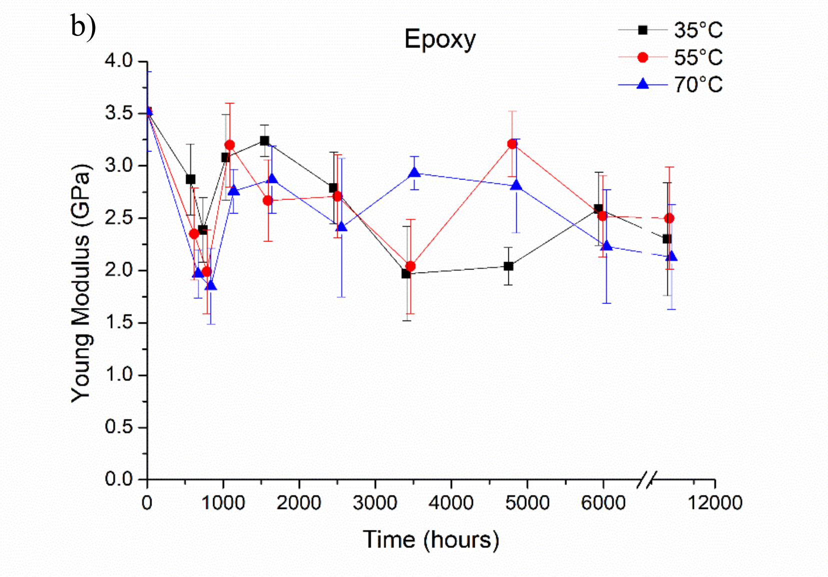

Figure 133. Young Modulus obtained for (a) FRP and (b) neat epoxy resin from IET technique for 35, 55 and 70°C.

Figure 134 shows the comparison between the modulus measured by the IET test and that from the destructive bending tests for the FRP for all temperatures.

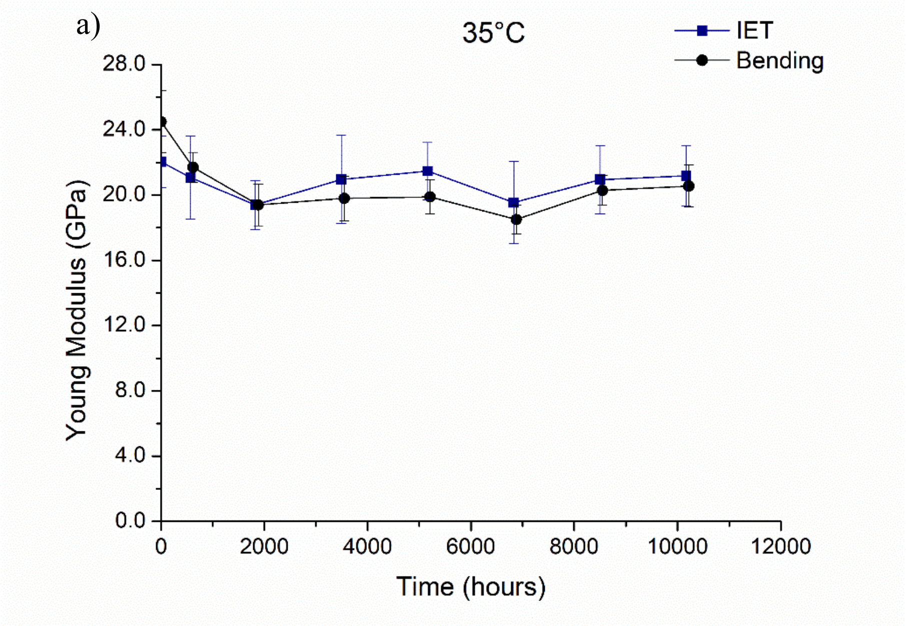

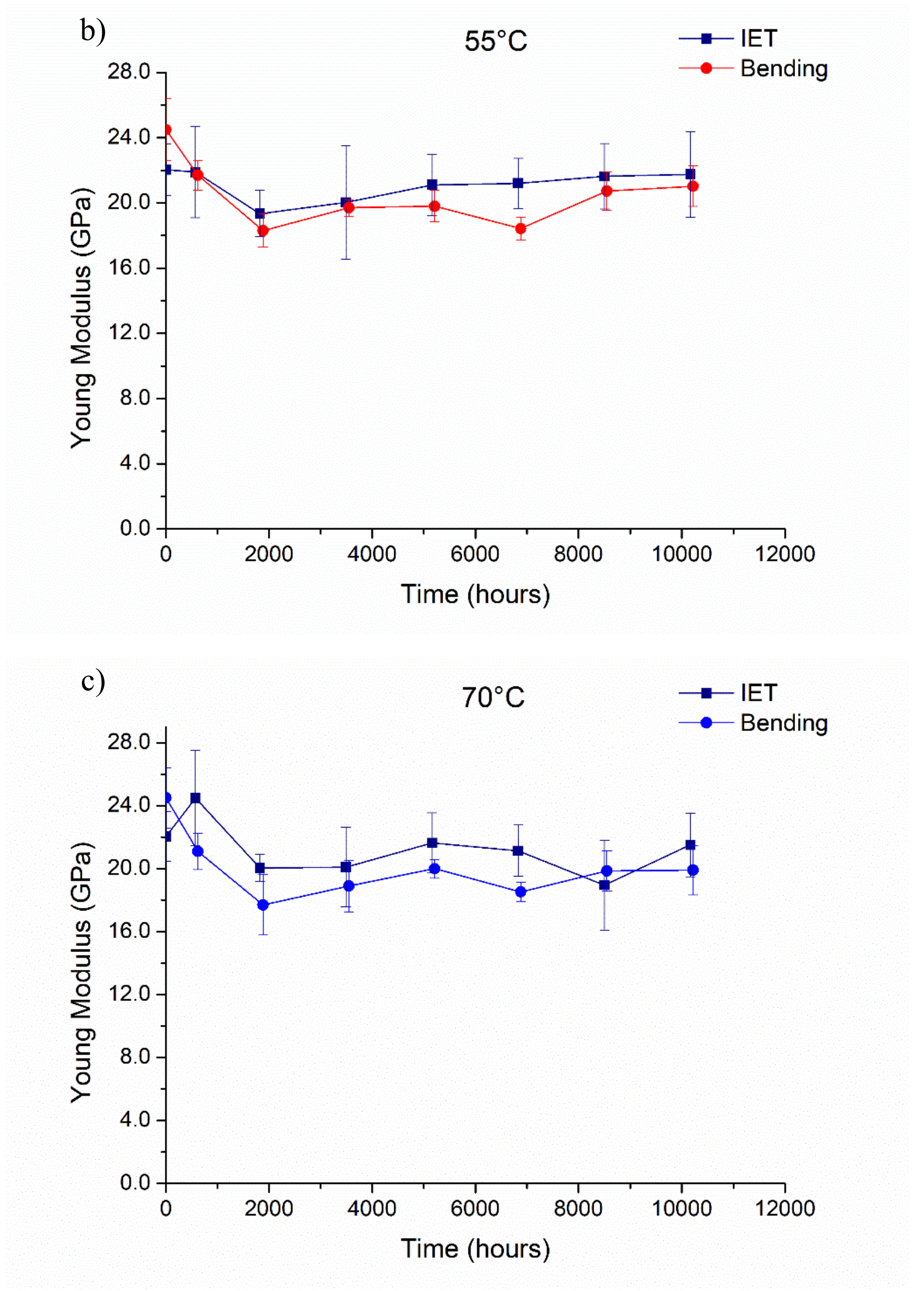

Figure 134. Comparison between the modulus obtained on IET and destructive bending tests for (a) 35°C, (b) 55°C and (c) 70°C.

It should be noted that the IET test showed a good correlation with the destructive test, which is a good indicator that this test provides reliable information about the elastic properties of the material, therefore, if a large size IET equipment is developed, it could be applied in the offshore field to accurately evaluate the progress of material degradation. Table 42 summarizes the average modulus obtained from both techniques along with the experimental error in relation to the IET test. It can be seen that the experimental errors between the techniques are reasonably low. Some works correlated Young modulus obtained from destructive tests and non-destructive techniques, including IET, and also showed small deviations [147,234,235]. For the aged specimens, the detected modulus depends on the magnitude of the damage. In other words, a located damage, such as a debonding in the specimen's neutral zone, it is not likely that it will be detected by the IET technique [147].

Table 42. Comparison between the bending modulus obtained by IET and destructive bending tests.

	35°C			55°C			70°C		
Aging time (hours)	IET Modulus (GPa)	Bending Modulus (GPa)	Error (%)	IET Modulus (GPa)	Bending Modulus (GPa)	Error (%)	IET Modulus (GPa)	Bending Modulus (GPa)	Error (%)
0	22.04	24.50	-10.04	22.04	24.50	-10.04	22.04	24.50	-10.04
570	21.07	21.70	-2.90	21.89	21.70	0.88	24.49	21.10	16.07
1820	19.39	19.40	-0.05	19.34	18.30	5.68	20.05	17.70	13.28
3490	20.96	19.80	5.86	20.03	19.70	1.68	20.10	18.90	6.35
5160	21.47	19.90	7.89	21.11	19.80	6.62	21.64	20.00	8.20
6830	19.55	18.51	5.62	21.20	18.43	15.03	21.14	18.52	14.15
8500	20.95	20.29	3.25	21.64	20.73	4.39	18.95	19.86	-4.58
10170	21.18	20.56	3.02	21.76	21.03	3.47	21.51	19.90	8.09

Figure 135 shows the tan δ graphs for the FRP and epoxy. A decrease in tan δ can be seen for the FRP, whereas a slight increase is observed for the neat epoxy resin. The former agrees with the DMA results, evidencing the post-cure suffered by the composite, even though the modulus decreased (Figure 133). For the tan δ, the IET test seems to be more sensitive to post-cure than to plasticization. On the other hand, for the neat epoxy, a mild plasticization was observed.

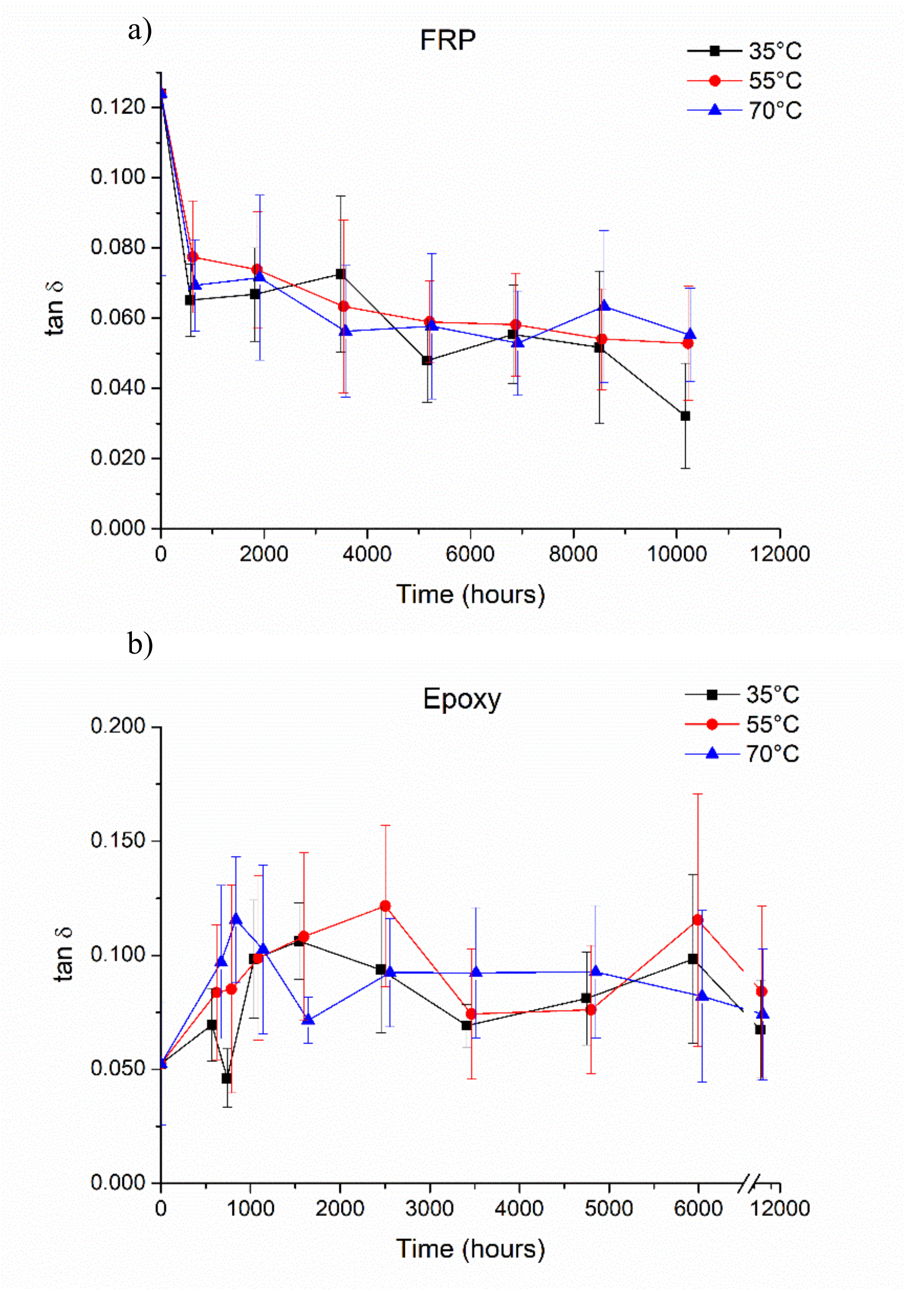

Figure 135. Tan δ curves obtained from IET tests for (a) FRP and (b) neat epoxy resin.

4.5.2. Colorimetry

Colorimetry tests were taken in order to evaluate the visual effects from the aging caused on the materials. Figure 136 shows the change in the parameter *L* (lightness) for all materials, including the coated FRP. Each value is an average from three absorption specimens. The higher its value the lighter the sample is, and the lower the *L* value, the darker the sample is. For the FRP, there was a decrease in lightness, meaning that the samples became darker in color, while the neat epoxy resin became lighter in color.

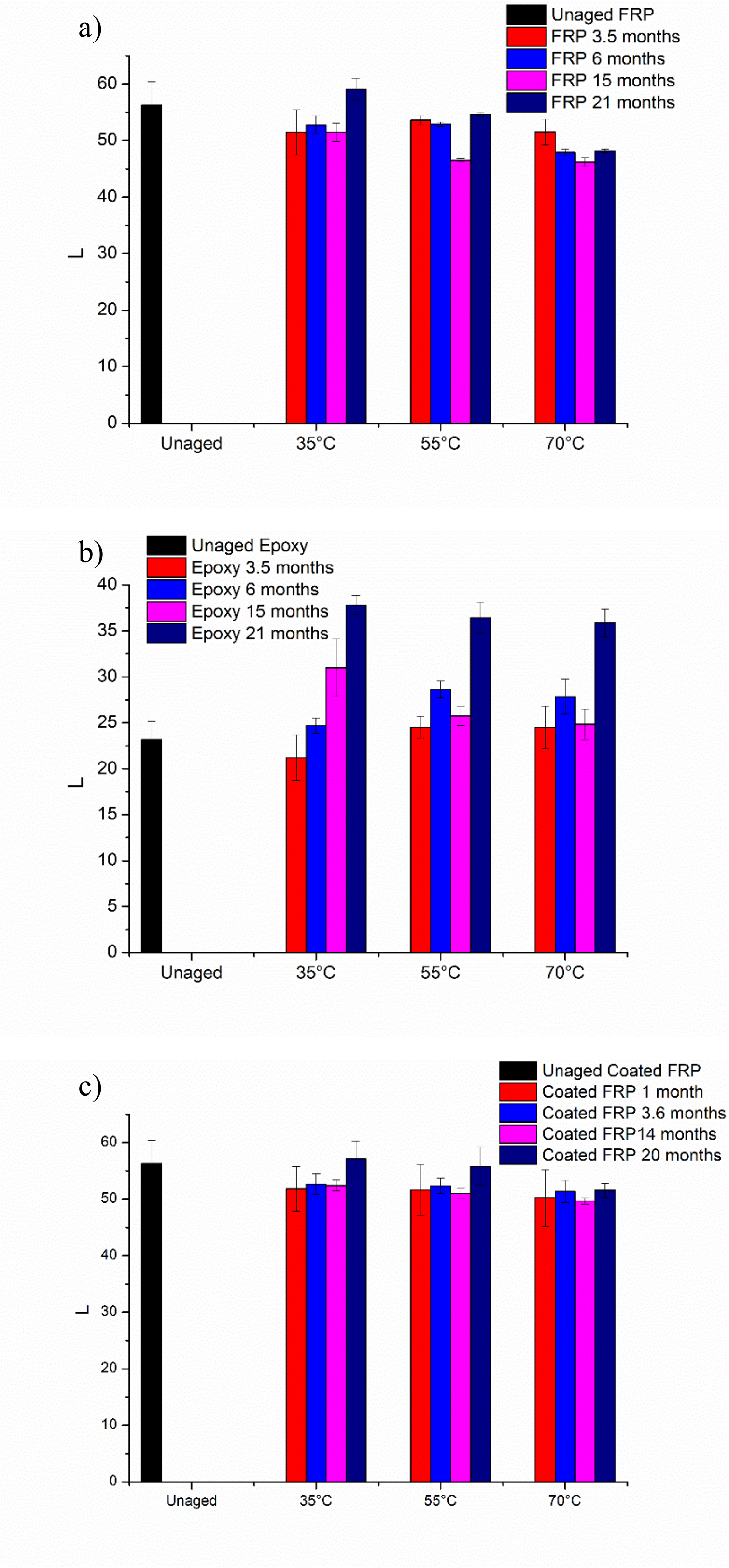

Figure 136. Variation of the lightness (*L*) parameter with temperature and aging time.

Table 43 displays the variation of the parameters *L*, *a*, *b* and *E* for the three materials. It is said that for ΔE^* values lower than 1, the color difference is imperceptible to the human eye, for values between 1 and 3.3, it is perceptible to the trained eye and for values over 3.30, it is perceptible to everyone [151,152]. It can be seen that the color shift (ΔE^*) became more significant with aging time and temperature, indicating chemical effects caused by exposure to temperature, such as post-cure [150], and moisture, such as hydrolysis [149]. The latter has already been discarded in Section 4.2.2. Moreover, after long-term exposure to hygrothermal conditions, all ΔE^* values were perceptible to everyone (> 3.3). For the parameter *a* ((a^-): green; (a^+): red), it can be noted that the general trend was that the specimens would acquire a reddish color. Regarding the parameter *b* ((b^-): blue; (b^+): yellow), it can be noted that the specimens acquired a yellow color, which could be associated with epoxy oxidation during curing under hygrothermal conditions and this resin yellowing is said to be irreversible [236]. The same results were found in literature [236,237]

Table 43. Change in the color parameters with aging time and temperature.

Time (hours)	**Temperature (°C)**	**ΔL**	**Δa**	**Δb**	**ΔE**
			FRP		
2454	35	-4.815	-0.057	1.303	4.989
	55	-2.678	-0.833	3.066	4.155
	70	-4.758	0.313	9.197	10.360
4386	35	-3.510	-0.209	1.947	4.019
	55	-3.373	0.552	5.416	6.404
	70	-8.347	-0.323	9.818	12.891
10875	35	-4.812	0.115	1.120	4.942
	55	-9.791	0.439	6.258	11.628
	70	-10.112	-0.174	12.703	16.237
15171	35	2.803	-0.305	1.384	3.141
	55	-1.682	0.078	8.567	8.731
	70	-8.092	1.35	13.071	15.432
			Epoxy		
2454	35	-1.944	0.758	1.735	2.714
	55	1.381	0.547	1.437	2.067
	70	1.345	0.894	1.739	2.373
4386	35	1.522	0.800	2.729	3.226
	55	5.452	0.536	3.138	6.313
	70	4.688	1.014	5.569	7.350
10875	35	7.831	0.694	5.653	9.683

	55	2.580	0.474	1.794	3.178
	70	1.661	0.723	2.027	2.719
15171	35	14.64	1.03	1.555	14.758
	55	13.297	-0.048	3.255	13.689
	70	12.69	1.393	2.942	13.101
		Coated FRP			
672	35	28.663	-1.706	4.630	29.085
	55	28.470	-1.811	6.078	29.168
	70	27.076	-1.520	7.861	28.235
2535	35	29.506	-1.534	4.885	29.947
	55	29.193	-1.515	6.749	30.001
	70	28.206	-2.230	10.321	30.118
10149	35	29.254	-0.180	9.087	30.633
	55	27.834	-2.715	8.628	29.267
	70	26.469	-2.421	15.917	30.981
14733	35	33.877	-0.82	5.461	34.324
	55	32.651	-2.666	12.007	34.891
	70	28.384	-0.857	16.361	32.773

By using the color converter software *Color Calculator* and inputting the parameters *L*, *a* and *b*, the colors could be simulated. Figure 137 shows the simulated colors of the unaged and aged specimens of neat epoxy, FRP and coated FRP. It should be noted that the neat epoxy's simulated color does not correspond to the actual color presented by the aged epoxy (Figure 138). This may be credited to the translucency of the epoxy resin. The stronger shift in color with temperature is evident in these figures. Figure 138 shows the pictures of the aged specimens at 70°C after the final aging times (15171 hours for FRP and neat epoxy and 14733 hours for the coated FRP). The temperature of 70°C was chosen for its higher environmental aggressiveness.

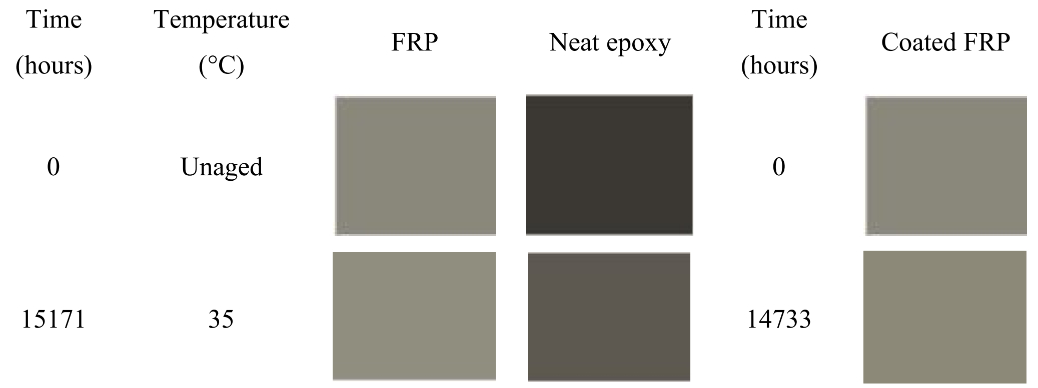

Figure 137. Evolution of color for the three materials with temperature and time.

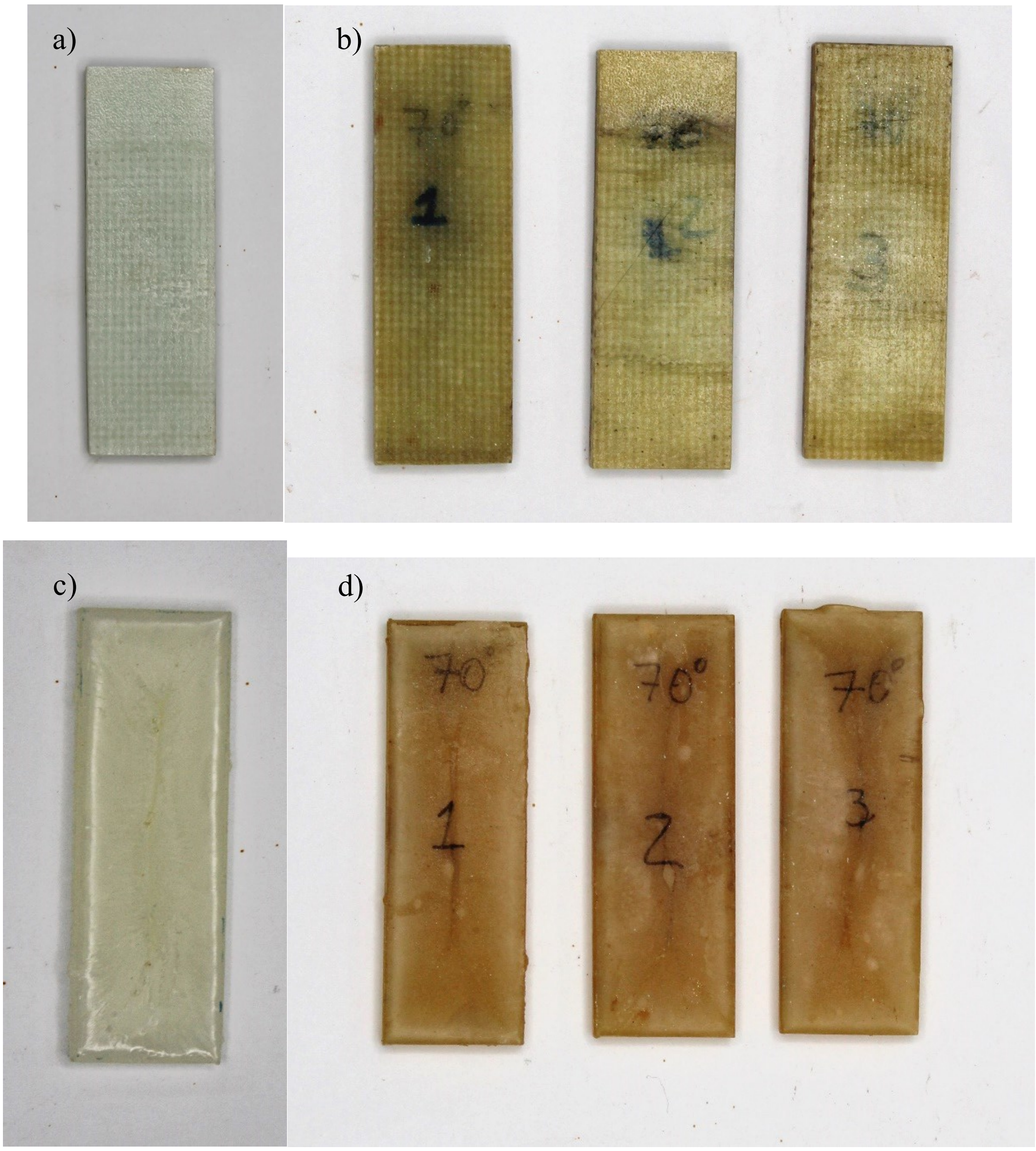

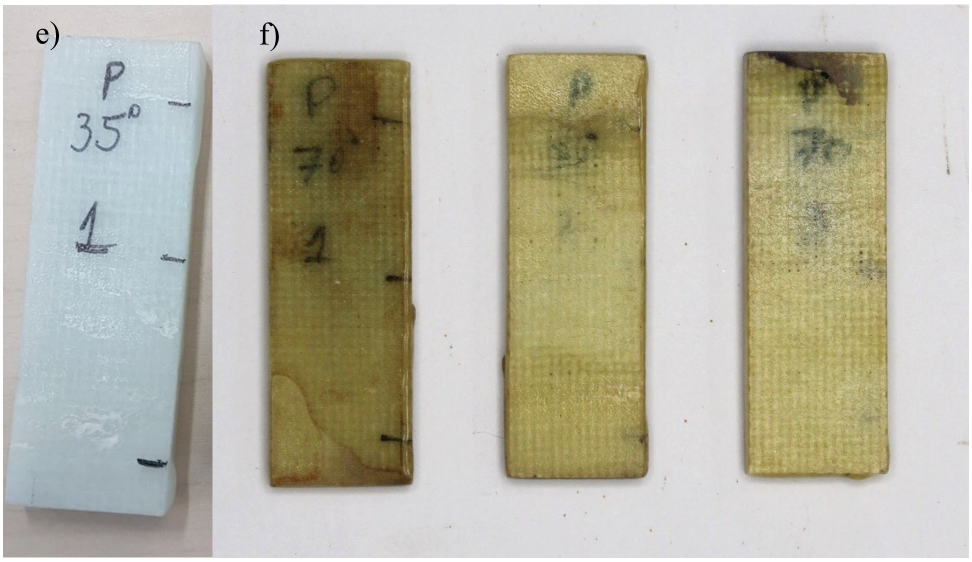

Figure 138. (a) Unaged FRP, (b) 15171-hours aged FRP, (c) unaged epoxy resin, (d) 15171-hours aged epoxy, (e) unaged coated FRP and (f) 14733-hours aged coated FRP at 70°C.

5. Conclusions

In this work, the hygrothermal degradation mechanisms of a glass fiber/epoxy matrix composite and its neat epoxy matrix were discussed. It was seen that temperature is an essential factor for accelerating composite degradation. The higher the temperature, the stronger the moisture diffusion into the material. For the FRP, low temperatures did not seem to significantly influence the saturation moisture content, whereas at 70°C it increased. On the other hand, the neat epoxy resin presented a decrease in absorption content with temperature, pointing to the hypothesis of post-curing, which would promote two mechanisms: (i) increase the polymer's crosslink density, making moisture penetration more difficult, and (ii) decrease of the hydrophilic sites, since the curing reaction breaks the -C-O bond. This post-curing hypothesis was supported by the FTIR, DSC and DMA analyses.

Deviations from the Fickian absorption pattern were observed, like pseudo-plateaus, especially for the FRP at 70°C. Therefore, non-Fickian models were implemented to the experimental data to account for all possible phenomena related to moisture absorption. The results found were in agreement with findings in literature. Both relaxation time and relaxation-related moisture absorption content decreased with temperature. The less crosslinked phase of the polymer was found to consist of a highly polar dense phase. Moreover, a strong bond between bound water molecules and the polymer's polar sites was found. A modification in the BH model was proposed to account for the effects of post-cure on moisture absorption mechanisms, and the post-cure rate was found to increase with temperature, showing that post-cure should be taken into account. The FRP also presented post-curing, however its moisture absorption capacity did not decrease with temperature, due to the presence of interfaces and possible voids arising from the composite manufacturing process.

The swelling behavior of all materials was assessed and it was seen that the free volume content did not significantly change with temperature. In addition, the orthotropy of the composite was made evident from the linear swelling strains, since the swelling in the thickness direction was much higher than in the other directions, while the isotropic neat epoxy resin did not show a difference between them. The relationship between the swelling strains in the FRP and the neat epoxy resin was evaluated, and an increase in the swelling capacity with temperature was observed.

Moreover, it was observed that the proportionality between the volumetric swelling strains of composite and neat epoxy increased with temperature, meaning that stronger interchain distancing occurred as moisture was absorbed. A Fickian-like model was proposed for the thickness swelling strain and good correlation was found for 70°C, while at lower temperatures the curve did not present a good fitting, due to both large data scattering and lack of short-term data. Furthermore, at 35 and 55°C the composites presented the same statistical thickness swelling strain saturation. Comparatively, the estimated swelling front penetration was higher than the moisture diffusivity through the samples' thickness, which might indicate that the swelling front penetrates the material at a faster rate than moisture.

The mechanical properties were found to be affected by both moisture and temperature, since at higher temperatures the composite absorbed more moisture and reached lower retention levels. The post-curing seen in the thermal analyses were not reflected in an improvement in mechanical properties, leading to the assumption that plasticization outweighed post-cure. The flexural modulus was seen to be little affected by moisture, provided that modulus is a fiber-dominated property and the moisture absorbed by glass fibers is negligible. It was observed that, for all temperatures, the mechanical properties presented an initial sharp decrease followed by a stabilization, presenting a plateau. This plateau decreased with temperature. A methodology for predicting mechanical property at temperatures other than the experimental temperature range based on a modification of the Phani and Bose model was presented. The service-life of the flexural properties could be estimated for 25°C, while for the interlaminar shear strength it could not be estimated due to the lack of statistical difference among the experimental results, preventing the trend of variation of parameters with temperature from being obtained.

The non-destructive Impulse Excitation Technique showed to be accurate when measuring the composite's flexural modulus, and values similar to those obtained in the destructive bending tests were obtained. Therefore, in real-life applications, a large-sized *Sonelastic* equipment to monitor the progress of stiffness with time in the field would be profitable. Additionally, the colorimetry tests showed that temperature and moisture affected the polymeric structure by changing the composite and epoxy's color.

6. Recommendations for Future Works

As a suggestion of improvements in the analyses performed in this work, short-term swelling measurements could be taken for a more reliable fitting of the Fickian thickness swelling proposed in this work, providing a finer assessment of the swelling front progression inwards the composite and time to reach swelling saturation. Moreover, an in-depth investigation should be carried out on the relationship between the stabilization of volumetric swelling strain and the stabilization of moisture-induced plasticization.

The methodology proposed in this work for service-life prediction should be also performed for other types of composites with other thermoset matrices and fibers and varying stacking configurations to investigate the universal applicability of this method.

A longer exposure time could also be performed to investigate the occurrence of other degradation mechanism, like hydrolysis. If any hydrolysis occurs, either in the matrix or in the fiber, this effect could be incorporated into both the non-Fickian and the property prediction models to estimate the time required to chemically degrade any of the composite's components.

In order to perform a more accurate simulation of real-life applications, the application of sustained load during hygrothermal aging in a salt spray environment could be done to take into account the loads that the repair should withstand, like vibrations and the fluid and pipe weights, for example. Moreover, for underwater repairs, a hydrostatic pressure should be also incorporated.

A correlation between the color change and the variation of the flexural mechanical properties could be analyzed as an attempt to use this non-destructive method as a cheaper tool to monitor the strength loss of the composite.

7. Bibliography

[1] M. Shamsuddoha, M.M. Islam, T. Aravinthan, A. Manalo, K. tak Lau, Effectiveness of using fibre-reinforced polymer composites for underwater steel pipeline repairs, Compos. Struct. 100 (2013) 40–54. https://doi.org/10.1016/j.compstruct.2012.12.019.

[2] K.S. Lim, S.N.A. Azraai, N.M. Noor, N. Yahaya, An Overview of Corroded Pipe Repair Techniques Using Composite Materials, Int. J. Mater. Metall. Eng. 10 (2016) 19–25.

[3] M. Abbas, M. Shafiee, An overview of maintenance management strategies for corroded steel structures in extreme marine environments, Mar. Struct. 71 (2020). https://doi.org/10.1016/j.marstruc.2020.102718.

[4] P. Jurišić, J. Parunov, Y. Garbatov, Aging effects on ship structural integrity, Brodogradnja. 68 (2017) 15–28. https://doi.org/10.21278/brod68202.

[5] C. Guedes Soares, Y. Garbatov, A. Zayed, Effect of environmental factors on steel plate corrosion under marine immersion conditions, Corros. Eng. Sci. Technol. 46 (2011) 524–541. https://doi.org/10.1179/147842209X12559428167841.

[6] F. Pomies, L.A. Carlsson, J.W. Gillespie, Marine environmental effects on polymer matrix composites, ASTM Spec. Tech. Publ. (1995) 283–303. https://doi.org/10.1520/stp14020s.

[7] T.C. Nguyen, Y. Bai, X.L. Zhao, R. Al-Mahaidi, Durability of steel/CFRP double strap joints exposed to sea water, cyclic temperature and humidity, Compos. Struct. 94 (2012) 1834–1845. https://doi.org/10.1016/j.compstruct.2012.01.004.

[8] Y. Bai, T.C. Nguyen, X.L. Zhao, R. Al-Mahaidi, Environment-assisted degradation of the bond between steel and carbon-fiber-reinforced polymer, J. Mater. Civ. Eng. 26 (2014) 1–8. https://doi.org/10.1061/(ASCE)MT.1943-5533.0000951.

[9] M. Heshmati, R. Haghani, M. Al-Emrani, Environmental durability of

adhesively bonded FRP/steel joints in civil engineering applications: State of the art, Compos. Part B Eng. 81 (2015) 259–275. https://doi.org/10.1016/j.compositesb.2015.07.014.

[10] M.W. Keller, B.D. Jellison, T. Ellison, Moisture effects on the thermal and creep performance of carbon fiber/epoxy composites for structural pipeline repair, Compos. Part B Eng. 45 (2013) 1173–1180. https://doi.org/10.1016/j.compositesb.2012.07.046.

[11] L.C. Hollaway, J. Cadei, Progress in the technique of upgrading metallic structures with advanced polymer composites, Prog. Struct. Eng. Mater. 4 (2002) 131–148. https://doi.org/10.1002/pse.112.

[12] M. Shamsuddoha, L.P. Djukic, M.M. Islam, T. Aravinthan, A. Manalo, Mechanical and thermal properties of glass fiber–vinyl ester resin composite for pipeline repair exposed to hot-wet conditioning, J. Compos. Mater. 51 (2017) 1605–1617. https://doi.org/10.1177/0021998316661869.

[13] G. Huang, H. Sun, Effect of water absorption on the mechanical properties of glass/polyester composites, Mater. Des. 28 (2007) 1647–1650. https://doi.org/10.1016/j.matdes.2006.03.014.

[14] T.-C. Nguyen, Y. Bai, X.-L. Zhao, R. Al-Mahaidi, Effects of ultraviolet radiation and associated elevated temperature on mechanical performance of steel/CFRP double strap joints, Compos. Struct. 94 (2012) 3563–3573. https://doi.org/10.1016/j.compstruct.2012.05.036.

[15] N. Coniglio, K. Nguyen, R. Kurji, E. Gamboa, Characterizing water sorption in 100% solids epoxy coatings, Prog. Org. Coatings. 76 (2013) 1168–1177. https://doi.org/10.1016/j.porgcoat.2013.03.011.

[16] J. Summerscales, Durability of composites in the marine environment, 2014. https://doi.org/10.1007/978-94-007-7417-9_1.

[17] M. Heshmati, R. Haghani, M. Al-Emrani, Effects of moisture on the long-term performance of adhesively bonded FRP/steel joints used in bridges, Compos. Part B Eng. 92 (2016) 447–462. https://doi.org/10.1016/j.compositesb.2016.02.021.

[18] N. Tual, N. Carrere, P. Davies, T. Bonnemains, E. Lolive, Characterization of sea water ageing effects on mechanical properties of carbon/epoxy composites for tidal turbine blades, Compos. Part A Appl. Sci. Manuf. 78 (2015) 380–389. https://doi.org/10.1016/j.compositesa.2015.08.035.

[19] F.C. Campbell, Manufacturing Processes For Advanced Composites, Elsevier, 2004.

[20] R.F. Gibson, Principles of Composite Materials, McGraw-Hill, 1994.

[21] I.L. Santana, E. Lodovici, J.R. Matos, I.S. Medeiros, C.L. Miyazaki, L.E. Rodrigues-Filho, Effect of experimental heat treatment on mechanical properties of resin composites, Braz. Dent. J. 20 (2009) 205–210. https://doi.org/10.1590/S0103-64402009000300006.

[22] Y.H. Bagis, F.A. Rueggeberg, The effect of post-cure heating on residual, unreacted monomer in a commercial resin composite, Dent. Mater. 16 (2000) 244–247. https://doi.org/10.1016/S0109-5641(00)00006-3.

[23] W.K. Goertzen, M.R. Kessler, Dynamic mechanical analysis of carbon/epoxy composites for structural pipeline repair, Compos. Part B Eng. 38 (2007) 1–9. https://doi.org/10.1016/j.compositesb.2006.06.002.

[24] S. Cabral-Fonseca, J.R. Correia, M.P. Rodrigues, F.A. Branco, Artificial Accelerated Ageing of GFRP Pultruded Profiles Made of Polyester and Vinylester Resins: Characterisation of Physical-Chemical and Mechanical Damage, Strain. 48 (2012) 162–173. https://doi.org/10.1111/j.1475-1305.2011.00810.x.

[25] I. Kafodya, G. Xian, H. Li, Durability study of pultruded CFRP plates immersed in water and seawater under sustained bending: Water uptake and effects on the mechanical properties, Compos. Part B Eng. 70 (2015) 138–148. https://doi.org/10.1016/j.compositesb.2014.10.034.

[26] M.L. Costa, S.F.M. De Almeida, M.C. Rezende, Hygrothermal effects on dynamic mechanical analysis and fracture behavior of polymeric composites, Mater. Res. 8 (2005) 335–340. https://doi.org/10.1590/S1516-14392005000300019.

[27] C. Yang, X. Xing, Z. Li, S. Zhang, A Comprehensive Review on Water Diffusion in Polymers Focusing on the Polymer–Metal Interface Combination, Polymers (Basel). 12 (2020) 138. https://doi.org/10.3390/polym12010138.

[28] F. Riebel, T. Keller, Long-Term Compression Performance of a Pultruded GFRP Element Exposed to Concrete Pore Water Solution, J. Compos. Constr. 11 (2007) 437–447. https://doi.org/10.1061/(asce)1090-0268(2007)11:4(437).

[29] T. Yilmaz, T. Sinmazcelik, Effects of hydrothermal aging on glass-fiber/polyetherimide (PEI) composites, J. Mater. Sci. 45 (2010) 399–404. https://doi.org/10.1007/s10853-009-3954-1.

[30] A. Zafar, F. Bertocco, J. Schjødt-Thomsen, J.C. Rauhe, Investigation of the long term effects of moisture on carbon fibre and epoxy matrix composites, Compos. Sci. Technol. 72 (2012) 656–666. https://doi.org/10.1016/j.compscitech.2012.01.010.

[31] ASME, ASME PCC-2 : Repair of Pressure Equipment and Piping, Asme. 2008 (2006) 240. https://www.asme.org/products/codes-standards/pcc2-2015-repair-pressure-equipment-piping-(1).

[32] N. Sateesh, P.S. Rao, D.V. Ravishanker, K. Satyanarayana, Effect of Moisture on GFRP Composite Materials, in: 4th Int. Conf. Mater. Process. Charact., 2015: pp. 2902–2908.

[33] H.S. Choi, K.J. Ahn, J.D. Nam, H.J. Chun, Hygroscopic aspects of epoxy/carbon fiber composite laminates in aircraft environments, Compos. Part A Appl. Sci. Manuf. 32 (2001) 709–720. https://doi.org/10.1016/S1359-835X(00)00145-7.

[34] N. Guermazi, A. Ben Tarjem, I. Ksouri, H.F. Ayedi, On the durability of FRP composites for aircraft structures in hygrothermal conditioning, Compos. Part B Eng. 85 (2016) 294–304. https://doi.org/10.1016/j.compositesb.2015.09.035.

[35] D.K. Jesthi, R.K. Nayak, Evaluation of mechanical properties and morphology of seawater aged carbon and glass fiber reinforced polymer

hybrid composites, Compos. Part B Eng. 174 (2019) 106980. https://doi.org/10.1016/j.compositesb.2019.106980.

[36] B.C. Ray, Temperature effect during humid ageing on interfaces of glass and carbon fibers reinforced epoxy composites, J. Colloid Interface Sci. 298 (2006) 111–117. https://doi.org/10.1016/j.jcis.2005.12.023.

[37] M. Heshmati, R. Haghani, M. Al-Emrani, Durability of bonded FRP-to-steel jointsEffects of moisture, de-icing salt solution, temperature and FRP type, Compos. Part B Eng. 119 (2017) 153–167. https://doi.org/10.1016/j.compositesb.2017.03.049.

[38] E. Barjasteh, S.R. Nutt, Moisture absorption of unidirectional hybrid composites, Compos. Part A Appl. Sci. Manuf. 43 (2012) 158–164. https://doi.org/10.1016/j.compositesa.2011.10.003.

[39] S.G. Prolongo, M.R. Gude, A. Ureña, Water uptake of epoxy composites reinforced with carbon nanofillers, Compos. Part A Appl. Sci. Manuf. 43 (2012) 2169–2175. https://doi.org/10.1016/j.compositesa.2012.07.014.

[40] M. Shettar, U.A. Kini, S. Sharma, P. Hiremath, M.C. Gowrishankar, Study on the mechanical properties of nanoclay-epoxy composites under different hygrothermal aging conditions, Mater. Res. Express. 6 (2019) 85333. https://doi.org/10.1088/2053-1591/ab2502.

[41] N. Merah, O. Mohamed, Nanoclay and water uptake effects on mechanical properties of unsaturated polyester, J. Nanomater. 2019 (2019). https://doi.org/10.1155/2019/8130419.

[42] P. Gilormini, J. Verdu, On the role of hydrogen bonding on water absorption in polymers, Polymer (Guildf). 142 (2018) 164–169. https://doi.org/10.1016/j.polymer.2018.03.033.

[43] M.J. Adamson, Thermal expansion and swelling of cured epoxy resin used in graphite/epoxy composite materials, J. Mater. Sci. 15 (1980) 1736–1745. https://doi.org/10.1007/BF00550593.

[44] Y. Diamant, G. Marom, L.J. Broutman, The effect of network structure on moisture absorption of epoxy resins, J. Appl. Polym. Sci. 26 (1981) 3015–

3025. https://doi.org/10.1002/app.1981.070260917.

[45] A.M. Visco, N. Campo, P. Cianciafara, Comparison of seawater absorption properties of thermoset resins based composites, Compos. Part A Appl. Sci. Manuf. 42 (2011) 123–130. https://doi.org/10.1016/j.compositesa.2010.10.009.

[46] M. Nodehi, Epoxy, polyester and vinyl ester based polymer concrete: a review, Innov. Infrastruct. Solut. 7 (2022). https://doi.org/10.1007/s41062-021-00661-3.

[47] F.A. Ramirez, L.A. Carlsson, B.A. Acha, Evaluation of water degradation of vinylester and epoxy matrix composites by single fiber and composite tests, J. Mater. Sci. 43 (2008) 5230–5242. https://doi.org/10.1007/s10853-008-2766-z.

[48] O.C. Trautschold, A Literature Review on the Study of Moisture in Polymers, 2016.

[49] S. Pandiyan, J. Krajniak, G. Samaey, D. Roose, E. Nies, A molecular dynamics study of water transport inside an epoxy polymer matrix, Comput. Mater. Sci. 106 (2015) 29–37. https://doi.org/10.1016/j.commatsci.2015.04.032.

[50] C. Wu, W. Xu, Atomistic simulation study of absorbed water influence on structure and properties of crosslinked epoxy resin, Polymer (Guildf). 48 (2007) 5440–5448. https://doi.org/10.1016/j.polymer.2007.06.038.

[51] P. Davies, F. Mazéas, P. Casari, Sea water aging of glass reinforced composites: Shear behaviour and damage modelling, J. Compos. Mater. 35 (2001) 1343–1372. https://doi.org/10.1106/MNBC-81UB-NF5H-P3ML.

[52] G. Apolinario, P. Ienny, S. Corn, R. Léger, A. Bergeret, J.-M. Haudin, Effects of Water Ageing on the Mechanical Properties of Flax and Glass Fibre Composites: Degradation and Reversibility, in: RILEM Bookseries, 2016: pp. 183–196. https://doi.org/10.1007/978-94-017-7515-1_14.

[53] C.H. Shen, G.S. Springer, Moisture Absorption and Desorption of Composite Materials, J. Compos. Mater. 10 (1976) 2–20.

https://doi.org/10.1177/002199837601000101.

[54] J. Crank, The Mathematics of Diffusion, 2nd ed., 1975.

[55] A.A.C. Pereira, J.R.M. D'Almeida, Effect of the hardener to epoxy monomer ratio on the water absorption behavior of the DGEBA/TETA epoxy system, Polimeros. 26 (2016) 30–37. https://doi.org/10.1590/0104-1428.2106.

[56] S.W. Tsai, H.T. Hahn, Introduction to Composite Materials, Technomic, 1980. https://doi.org/10.1145/2820400.

[57] K.J. Wong, Moisture absorption characteristics and effects on mechanical behaviour of carbon/epoxy composite: application to bonded patch repairs of composite structures, 2013. http://ieeexplore.ieee.org/lpdocs/epic03/wrapper.htm?arnumber=6611889.

[58] E.P. Gellert, D.M. Turley, Seawater immersion ageing of glass-fibre reinforced polymer laminates for marine applications, Compos. Part A Appl. Sci. Manuf. 30 (1999) 1259–1265. https://doi.org/10.1016/S1359-835X(99)00037-8.

[59] L. Bian, J. Xiao, J. Zeng, S. Xing, Effects of seawater immersion on water absorption and mechanical properties of GFRP composites, J. Compos. Mater. 46 (2012) 3151–3162. https://doi.org/10.1177/0021998312436992.

[60] A. Chateauminois, L. Vincent, B. Chabert, J.P. Soulier, Study of the interfacial degradation of a glass-epoxy composite during hygrothermal ageing using water diffusion measurements and dynamic mechanical thermal analysis, Polymer (Guildf). 35 (1994) 4766–4774. https://doi.org/10.1016/0032-3861(94)90730-7.

[61] M. Heshmati, R. Haghani, M. Al-Emrani, Durability of bonded FRP-to-steel joints: Effects of moisture, de-icing salt solution, temperature and FRP type, Compos. Part B Eng. 119 (2017) 153–167. https://doi.org/10.1016/j.compositesb.2017.03.049.

[62] Y. Fan, A. Gomez, S. Ferraro, B. Pinto, A. Muliana, V. La Saponara, Diffusion of water in glass fiber reinforced polymer composites at different temperatures, J. Compos. Mater. 53 (2019) 1097–1110.

https://doi.org/10.1177/0021998318796155.

[63] D.A. Porter, K.E. Easterling, Phase Transformations in Metals and Alloys, Springer-Science+Business Media, B. V., 1992.

[64] Y. Chen, J.F. Davalos, I. Ray, H.Y. Kim, Accelerated aging tests for evaluations of durability performance of FRP reinforcing bars for concrete structures, Compos. Struct. 78 (2007) 101–111. https://doi.org/10.1016/j.compstruct.2005.08.015.

[65] I. Panaitescu, T. Koch, V.M. Archodoulaki, Effects of temperature, humidity and automotive fluids exposure on glass fiber/polyurethane composites, Polym. Compos. 40 (2019) 2357–2367. https://doi.org/10.1002/pc.25094.

[66] W. Chu, L. Wu, V.M. Karbhari, Durability evaluation of moderate temperature cured E-glass/vinylester systems, Compos. Struct. 66 (2004) 367–376. https://doi.org/10.1016/j.compstruct.2004.04.058.

[67] B. De Parscau Du Plessix, F. Jacquemin, P. Lefébure, S. Le Corre, Characterization and modeling of the polymerization-dependent moisture absorption behavior of an epoxy-carbon fiber-reinforced composite material, J. Compos. Mater. 50 (2016) 2495–2505. https://doi.org/10.1177/0021998315606510.

[68] M. Robert, P. Wang, P. Cousin, B. Benmokrane, Temperature as an accelerating factor for long-term durability testing of FRPs: Should there be any limitations?, J. Compos. Constr. 14 (2010) 361–367. https://doi.org/10.1061/(ASCE)CC.1943-5614.0000102.

[69] H. Li, K. Zhang, X. Fan, H. Cheng, G. Xu, H. Suo, Effect of seawater ageing with different temperatures and concentrations on static/dynamic mechanical properties of carbon fiber reinforced polymer composites, Compos. Part B Eng. 173 (2019) 106910. https://doi.org/10.1016/j.compositesb.2019.106910.

[70] T.S. Grant, W.L. Bradley, In-Situ Observations in SEM of Degradation of Graphite/Epoxy Composite Materials due to Seawater Immersion, J. Compos. Mater. 29 (1995) 852–867. https://doi.org/10.1177/002199839502900701.

[71] Y. Fang, K. Wang, D. Hui, F. Xu, W. Liu, S. Yang, L. Wang, Monitoring of seawater immersion degradation in glass fibre reinforced polymer composites using quantum dots, Compos. Part B Eng. 112 (2017) 93–102. https://doi.org/10.1016/j.compositesb.2016.12.043.

[72] M.A.G. Silva, B.S. da Fonseca, H. Biscaia, On estimates of durability of FRP based on accelerated tests, Compos. Struct. 116 (2014) 377–387. https://doi.org/10.1016/j.compstruct.2014.05.022.

[73] ASTM D1141-98, Standard Practice for the Preparation of Substitute Ocean Water, ASTM Int. 98 (2013) 1–3. https://doi.org/10.1520/D1141-98R13.2.

[74] C. Humeau, P. Davies, F. Jacquemin, Moisture diffusion under hydrostatic pressure in composites, Mater. Des. 96 (2016) 90–98. https://doi.org/10.1016/j.matdes.2016.02.012.

[75] W.C. Tucker, R. Brown, Moisture Absorption of Graphite/Polymer Composites Under 2000 Feet of Seawater, J. Compos. Mater. 23 (1989) 787–797. https://doi.org/10.1177/002199838902300802.

[76] A. Avena, A.R. Bunsell, Effect of hydrostatic pressure on the water absorption of glass fibre-reinforced epoxy resin, Composites. 19 (1988) 355–357. https://doi.org/10.1016/0010-4361(88)90122-X.

[77] C. Helbling, V.M. Karbhari, Durability of composites in aqueous environments, Durab. Compos. Civ. Struct. Appl. (2007) 31–71. https://doi.org/10.1533/9781845693565.1.31.

[78] S. Teixeira de Freitas, M.D. Banea, S. Budhe, S. de Barros, Interface adhesion assessment of composite-to-metal bonded joints under salt spray conditions using peel tests, Compos. Struct. 164 (2017) 68–75. https://doi.org/10.1016/j.compstruct.2016.12.058.

[79] INTERNATIONAL STANDARD, ISO 24817 - Petroleum, petrochemical and natural gas industries — Composite repairs for pipework — Qualification and design, installation, testing and inspection, 2 (2017) 86.

[80] I. 61851, International Standard, 61010-1 © Iec2001. 2006 (2006) 13.

[81] V.M. Karbhari, J.W. Chin, D. Hunston, B. Benmokrane, T. Juska, R.

Morgan, J.J. Lesko, U. Sorathia, D. Reynaud, Durability gap analysis for fiber-reinforced polymer composites in civil infrastructure, J. Compos. Constr. 7 (2003) 238–247. https://doi.org/10.1061/(ASCE)1090-0268(2003)7:3(238).

[82] H. Levine, L. Slade, Water as a plasticizer: physico-chemical aspects of low-moisture polymeric systems, in: Water Sci. Rev. 3, Cambridge University Press, 1988: pp. 79–185. https://doi.org/10.1017/CBO9780511552083.002.

[83] H. Gu, Dynamic mechanical analysis of the seawater treated glass/polyester composites, Mater. Des. 30 (2009) 2774–2777. https://doi.org/10.1016/j.matdes.2008.09.029.

[84] K. Berketis, D. Tzetzis, P.J. Hogg, Impact damage detection and degradation monitoring of wet GFRP composites using noncontact ultrasonics, Polym. Compos. 30 (2009) 1043–1049. https://doi.org/10.1002/pc.20652.

[85] A. Kootsookos, A.P. Mouritz, Seawater durability of glass- and carbon-polymer composites, Compos. Sci. Technol. 64 (2004) 1503–1511. https://doi.org/10.1016/j.compscitech.2003.10.019.

[86] M. Heshmati, R. Haghani, M. Al-Emrani, Hygrothermal durability of adhesively bonded FRP/steel joints, 2015.

[87] A.P. Chakraverty, U.K. Mohanty, S.C. Mishra, A. Satapathy, Sea water ageing of GFRP composites and the dissolved salts, IOP Conf. Ser. Mater. Sci. Eng. 75 (2015). https://doi.org/10.1088/1757-899X/75/1/012029.

[88] T. Muthukumar, A. Aravinthan, K. Lakshmi, R. Venkatesan, L. Vedaprakash, M. Doble, Fouling and stability of polymers and composites in marine environment, Int. Biodeterior. Biodegrad. 65 (2011) 276–284. https://doi.org/10.1016/j.ibiod.2010.11.012.

[89] S. Alsayed, Y. Al-Salloum, T. Almusallam, S. El-Gamal, M. Aqel, Performance of glass fiber reinforced polymer bars under elevated temperatures, Compos. Part B Eng. 43 (2012) 2265–2271. https://doi.org/10.1016/j.compositesb.2012.01.034.

[90] J.M. Sousa, J.R. Correia, J. Gonilha, S. Cabral-Fonseca, J.P. Firmo, T.

Keller, Durability of adhesively bonded joints between pultruded GFRP adherends under hygrothermal and natural ageing, Compos. Part B Eng. 158 (2019) 475–488. https://doi.org/10.1016/j.compositesb.2018.09.060.

[91] Y. Wang, J. Meng, Q. Zhao, S. Qi, Accelerated Ageing Tests for Evaluations of a Durability Performance of Glass-fiber Reinforcement Polyester Composites, J. Mater. Sci. Technol. 26 (2010) 572–576. https://doi.org/10.1016/S1005-0302(10)60087-4.

[92] L.C. Hollaway, A review of the present and future utilisation of FRP composites in the civil infrastructure with reference to their important in-service properties, Constr. Build. Mater. 24 (2010) 2419–2445. https://doi.org/10.1016/j.conbuildmat.2010.04.062.

[93] Krauklis, Gagani, Echtermeyer, Long-Term Hydrolytic Degradation of the Sizing-Rich Composite Interphase, Coatings. 9 (2019) 263. https://doi.org/10.3390/coatings9040263.

[94] J. El Yagoubi, G. Lubineau, A. Traidia, J. Verdu, Monitoring and simulations of hydrolysis in epoxy matrix composites during hygrothermal aging, Compos. Part A Appl. Sci. Manuf. 68 (2015) 184–192. https://doi.org/10.1016/j.compositesa.2014.10.002.

[95] F. Ellyin, R. Maser, Environmental effects on the mechanical properties of glass-fiber epoxy composite tubular specimens, Compos. Sci. Technol. 64 (2004) 1863–1874. https://doi.org/10.1016/j.compscitech.2004.01.017.

[96] M.K. Antoon, J.L. Koenig, Irreversible effects of moisture on the epoxy matrix in glass-reinforced composites, Composites. 12 (1981) 298. https://doi.org/10.1016/0010-4361(81)90073-2.

[97] C.L. Schutte, Environmental durability of glass-fiber composites, Mater. Sci. Eng. R. 13 (1994) 265–323. https://doi.org/10.1016/0927-796X(94)90002-7.

[98] K. Aniskevich, A. Aniskevich, A. Arnautov, J. Jansons, Mechanical properties of pultruded glass fiber-reinforced plastic after moistening, Compos. Struct. 94 (2012) 2914–2919. https://doi.org/10.1016/j.compstruct.2012.04.030.

[99] O. Starkova, S. Chandrasekaran, T. Schnoor, J. Sevcenko, K. Schulte, Anomalous water diffusion in epoxy/carbon nanoparticle composites, Polym. Degrad. Stab. 164 (2019) 127–135. https://doi.org/10.1016/j.polymdegradstab.2019.04.010.

[100] W.K. Loh, A.D. Crocombe, M.M.A. Wahab, I.A. Ashcroft, Modelling anomalous moisture uptake, swelling and thermal characteristics of a rubber toughened epoxy adhesive, Int. J. Adhes. Adhes. 25 (2005) 1–12. https://doi.org/10.1016/j.ijadhadh.2004.02.002.

[101] D.G. dos Santos, Estudo Termo-hídrico e Caracterização Meânica de Compósitos de Matriz Polimérica Reforçados com Fibra Vegetal: Simulação 3D e Experimentação, Universidade Federal de Campina Grande, 2017.

[102] A. Al-Mosawe, R. Al-Mahaidi, X.-L. Zhao, Effect of CFRP properties, on the bond characteristics between steel and CFRP laminate under quasi-static loading, Constr. Build. Mater. 98 (2015) 489–501. https://doi.org/10.1016/j.conbuildmat.2015.08.130.

[103] Z. Huo, M. Mohamed, J.R. Nicholas, X. Wang, Experimentation and simulation of moisture diffusion in foam-cored polyurethane sandwich structure, J. Sandw. Struct. Mater. 18 (2016) 30–49. https://doi.org/10.1177/1099636215582218.

[104] J. Wang, R. Liu, D. Liu, S. Park, Advancement in simulating moisture diffusion in electronic packages under dynamic thermal loading conditions, Microelectron. Reliab. 73 (2017) 42–53. https://doi.org/10.1016/j.microrel.2017.04.018.

[105] K. Zhang, H. Li, H. Cheng, B. Luo, P. Liu, Combined effects of seawater ageing and fatigue loading on the bearing performance and failure mechanism of CFRP/CFRP single-lap bolted joints, Compos. Struct. 234 (2020) 111677. https://doi.org/10.1016/j.compstruct.2019.111677.

[106] L.F.M. da Silva, P.J.C. das Neves, R.D. Adams, J.K. Spelt, Analytical models of adhesively bonded joints-Part I: Literature survey, Int. J. Adhes. Adhes. 29 (2009) 319–330. https://doi.org/10.1016/j.ijadhadh.2008.06.005.

[107] Y. Zhang, A.P. Vassilopoulos, T. Keller, Effects of low and high

temperatures on tensile behavior of adhesively-bonded GFRP joints, Compos. Struct. 92 (2010) 1631–1639. https://doi.org/10.1016/j.compstruct.2009.11.028.

[108] A. Agarwal, S.J. Foster, E. Hamed, T.S. Ng, Influence of freeze-thaw cycling on the bond strength of steel-FRP lap joints, Compos. Part B Eng. 60 (2014) 178–185. https://doi.org/10.1016/j.compositesb.2013.12.024.

[109] A. Al-Shawaf, R. Al-Mahaidi, X.L. Zhao, Effect of elevated temperature on bond behaviour of high modulus CFRP/steel double-strap joints, Aust. J. Struct. Eng. 10 (2009) 63–74. https://doi.org/10.1080/13287982.2009.11465033.

[110] Y. Yu, S.P. Chiew, C.K. Lee, Bond failure of steel beams strengthened with FRP laminates - Part 2: Verification, Compos. Part B Eng. 42 (2011) 1122–1134. https://doi.org/10.1016/j.compositesb.2011.03.016.

[111] Y. Chen, J.F. Davalos, I. Ray, Durability Prediction for GFRP Reinforcing Bars Using Short-Term Data of Accelerated Aging Tests, J. Compos. Constr. 10 (2006) 279–286. https://doi.org/10.1061/(asce)1090-0268(2006)10:4(279).

[112] L.C. Bank, T.R. Gentry, B.P. Thompson, J.S. Russell, A model specification for FRP composites for civil engineering structures, Constr. Build. Mater. 17 (2003) 405–437. https://doi.org/10.1016/S0950-0618(03)00041-2.

[113] W. Feng, F. Xu, W. Xie, Y. Zang, X. Zhang, Hygrothermal aging effects on the mechanical behavior of scarf-repaired composite laminates, J. Adhes. 96 (2020) 1233–1257. https://doi.org/10.1080/00218464.2019.1589457.

[114] X. Jiang, J. Song, X. Qiang, H. Kolstein, F. Bijlaard, Moisture absorption/desorption effects on flexural property of Glass-fiber-reinforced polyester laminates: Three-point bending test and coupled hygro-mechanical finite element analysis, Polymers (Basel). 8 (2016). https://doi.org/10.3390/polym8080290.

[115] A. Regazzi, R. Léger, S. Corn, P. Ienny, Modeling of hydrothermal aging of short flax fiber reinforced composites, Compos. Part A Appl. Sci. Manuf. 90 (2016) 559–566. https://doi.org/10.1016/j.compositesa.2016.08.011.

[116] X. Jiang, C. Luo, X. Qiang, Q. Zhang, H. Kolstein, F. Bijlaard, Coupled hygro-mechanical finite element method on determination of the interlaminar shear modulus of glass fiber-reinforced polymer laminates in bridge decks under hygrothermal aging effects, Polymers (Basel). 10 (2018). https://doi.org/10.3390/polym10080845.

[117] S. Panthapulakkal, M. Sain, Studies on the water absorption properties of short hemp-glass fiber hybrid polypropylene composites, J. Compos. Mater. 41 (2007) 1871–1883. https://doi.org/10.1177/0021998307069900.

[118] D. De Kee, Q. Liu, J. Hinestroza, Viscoelastic (Non-Fickian) Diffusion, Can. J. Chem. Eng. 83 (2005) 913–929. https://doi.org/10.1002/cjce.5450830601.

[119] Y.J. Weitsman, M. Elahi, Effects of fluids on the deformation, strength and durability of polymeric composites - an overview, Mech. Time-Dependent Mater. 4 (2000) 107–126. https://doi.org/10.1023/A:1009838128526.

[120] H.G. Carter, K.G. Kibler, Langmuir-Type Model for Anomalous Moisture Diffusion In Composite Resins, J. Compos. Mater. 12 (1978) 118–131. https://doi.org/10.1177/002199837801200201.

[121] G.E. Guloglu, M.C. Altan, Non-fickian moisture absorption in polymers coated with a thin nanocomposite layer, Proc. Am. Soc. Compos. - 29th Tech. Conf. ASC 2014; 16th US-Japan Conf. Compos. Mater. ASTM-D30 Meet. (2014).

[122] G.E. Guloglu, Y.K. Hamidi, M.C. Altan, Fast recovery of non-fickian moisture absorption parameters for polymers and polymer composites, Polym. Eng. Sci. 57 (2017) 921–931. https://doi.org/10.1002/pen.24469.

[123] F.B. Boukhoulda, L. Guillaumat, J.L. Lataillade, E. Adda-Bedia, A. Lousdad, Aging-impact coupling based analysis upon glass/polyester composite material in hygrothermal environment, Mater. Des. 32 (2011) 4080–4087. https://doi.org/10.1016/j.matdes.2011.03.009.

[124] P. Surathi, V.M. Karbhari, Hygrothermal effects on durability and moisture kinetics of fiber-reinforced polymer composites, 2006.

[125] L.R. Grace, M.C. Altan, Characterization of anisotropic moisture absorption

in polymeric composites using hindered diffusion model, Compos. Part A Appl. Sci. Manuf. 43 (2012) 1187–1196. https://doi.org/10.1016/j.compositesa.2012.03.016.

[126] G.E. Guloglu, A Comprehensive Study on Moisture Absorption of Thermosetting Polymers, Micro- and Nanocomposites, and Foams, University of Oklahoma, 2018.

[127] P.M. Jacobs, E.R. Jones, Diffusion of moisture into two-phase polymers - Part 1 The development of an analytical model and its application to styrene-ethylene/butylene-styrene block copolymer, J. Mater. Sci. 24 (1989) 2343–2347. https://doi.org/10.1007/BF01174494.

[128] P.M. Jacobs, E.R. Jones, Diffusion of moisture into two-phase polymers Part 2: Styrenated polyester resins, J. Mater. Sci. 24 (1989) 2343–2347. https://doi.org/10.1007/BF01174494.

[129] C. Maggana, P. Pissis, Water sorption and diffusion studies in an epoxy resin system, J. Polym. Sci. Part B Polym. Phys. 37 (1999) 1165–1182. https://doi.org/10.1002/(SICI)1099-0488(19990601)37:11<1165::AID-POLB11>3.0.CO;2-E.

[130] M.D. Placette, X. Fan, J.H. Zhao, D. Edwards, Dual stage modeling of moisture absorption and desorption in epoxy mold compounds, Microelectron. Reliab. 52 (2012) 1401–1408. https://doi.org/10.1016/j.microrel.2012.03.008.

[131] L.R. Bao, A.F. Yee, C.Y.C. Lee, Moisture absorption and hygrothermal aging in a bismaleimide resin, Polymer (Guildf). 42 (2001) 7327–7333. https://doi.org/10.1016/S0032-3861(01)00238-5.

[132] A.R. Berens, H.B. Hopfenberg, Diffusion and relaxation in glassy polymer powders: 2. Separation of diffusion and relaxation parameters, Polymer (Guildf). 19 (1978) 489–496. https://doi.org/10.1016/0032-3861(78)90269-0.

[133] D.A. Bond, P.A. Smith, Modeling the Transport of Low-Molecular-Weight Penetrants Within Polymer Matrix Composites, Appl. Mech. Rev. 59 (2006) 249–268. https://doi.org/10.1115/1.2202873.

[134] K.K. Phani, N.R. Bose, Hydrothermal ageing of CSM-laminate during water immersion — an acousto-ultrasonic study, J. Mater. Sci. 21 (1986) 3633–3637. https://doi.org/10.1007/BF02403012.

[135] J. Wang, H. GangaRao, R. Liang, D. Zhou, W. Liu, Y. Fang, Durability of glass fiber-reinforced polymer composites under the combined effects of moisture and sustained loads, J. Reinf. Plast. Compos. 34 (2015) 1739–1754. https://doi.org/10.1177/0731684415596846.

[136] K.K. Phani, N.R. Bose, Temperature dependence of hydrothermal ageing of CSM-laminate during water immersion, Compos. Sci. Technol. 29 (1987) 79–87. https://doi.org/10.1016/0266-3538(87)90050-9.

[137] A. Kuraishi, Durability analysis of composite structures using the accelerated testing methodology, Stanford University, 2001. http://adsabs.harvard.edu/abs/2001PhDT.......154K.

[138] A.E. Krauklis, A.G. Akulichev, A.I. Gagani, A.T. Echtermeyer, Time-temperature-plasticization superposition principle: Predicting creep of a plasticized epoxy, Polymers (Basel). 11 (2019). https://doi.org/10.3390/polym11111848.

[139] G. Pritchard, S.D. Speake, The use of water absorption kinetic data to predict laminate property changes, Composites. 18 (1987) 227–232. https://doi.org/10.1016/0010-4361(87)90412-5.

[140] R. Halmshaw, Non-destructive Testing Techniques, in: Nondestruct. Test., Butterworth-Heinemann, London, 1991. https://doi.org/10.1016/B978-0-340-67648-6.50005-0.

[141] ASTM E1876, Standard Test Method for Dynamic Young's Modulus , Shear Modulus , and Poisson's Ratio by Impulse Excitation of Vibration, Astm. i (2015) 1–17. https://doi.org/10.1520/E1876-15.responsibility.

[142] L.B. Otani, A.H.A. Alves, J.D.D. Melo, S.C. Amico, Caracterização dos módulos elásticos de compósitos utilizando a Técnica de Excitação por Impulso, (2014) 36. https://doi.org/10.13140/RG.2.1.2599.8248.

[143] A. Yan, Durability of Glass Fiber/Vinyl Ester Composites as Bridge Deck

Subject to Weathering Conditions, Wayne State University, 2005. http://www.ncbi.nlm.nih.gov/pubmed/810049%0Ahttp://doi.wiley.com/10.1002/anie.197505391%0Ahttp://www.sciencedirect.com/science/article/pii/B9780857090409500205%0Ahttp://www.ncbi.nlm.nih.gov/pubmed/21918515%0Ahttp://www.cabi.org/cabebooks/ebook/20083217094.

[144] ATCP, Manual de Instalação e Operação - Software Sonelastic 3.0, 55 (n.d.).

[145] N.L. Batista, K. Iha, E.C. Botelho, Evaluation of weather influence on mechanical and viscoelastic properties of polyetherimide/carbon fiber composites, J. Reinf. Plast. Compos. 32 (2013) 863–874. https://doi.org/10.1177/0731684413482994.

[146] K. Cheour, M. Assarar, D. Scida, R. Ayad, X.L. Gong, Effect of water ageing on the mechanical and damping properties of flax-fibre reinforced composite materials, Compos. Struct. 152 (2016) 259–266. https://doi.org/10.1016/j.compstruct.2016.05.045.

[147] D.S. Paolino, H. Geng, A. Scattina, A. Tridello, M.P. Cavatorta, G. Belingardi, Damaged composite laminates: Assessment of residual Young’s modulus through the Impulse Excitation Technique, Compos. Part B Eng. 128 (2017) 76–82. https://doi.org/10.1016/j.compositesb.2017.07.008.

[148] M. Zhang, B. Sun, B. Gu, Accelerated thermal ageing of epoxy resin and 3-D carbon fiber/epoxy braided composites, Compos. Part A Appl. Sci. Manuf. 85 (2016) 163–171. https://doi.org/10.1016/j.compositesa.2016.03.028.

[149] A. Simar, M. Gigliotti, J.C. Grandidier, I. Ammar-Khodja, Evidence of thermo-oxidation phenomena occurring during hygrothermal aging of thermosetting resins for RTM composite applications, Compos. Part A Appl. Sci. Manuf. 66 (2014) 175–182. https://doi.org/10.1016/j.compositesa.2014.07.007.

[150] J. Pospíšil, Z. Horák, J. Pilař, N.. Billingham, H. Zweifel, S. Nešpůrek, Influence of testing conditions on the performance and durability of polymer stabilisers in thermal oxidation, Polym. Degrad. Stab. 82 (2003) 145–162. https://doi.org/10.1016/S0141-3910(03)00210-6.

[151] R. Siakeng, M. Jawaid, M. Asim, S. Siengchin, Accelerated weathering and

soil burial effect on biodegradability, colour and textureof coir/pineapple leaf fibres/PLA biocomposites, Polymers (Basel). 12 (2020). https://doi.org/10.3390/polym12020458.

[152] Z. Ergücü, L.S. Türkün, A. Aladag, Color Stability of Nanocomposites Polished with One-Step Systems, Oper. Dent. 33 (2008) 413–420. https://doi.org/10.2341/07-107.

[153] MacSeal, Relatório Técnico - Ensaios mecânicos de tração do laminado de reparo PIPEFIX 50 e PIPEFIX 90 em conformidade com a Norma ASTM D3039, 2019.

[154] O. Corning, SE1200 - Product Information, (n.d.).

[155] MacSeal, PIPEFIX - Relatório Técnico: Confecção de corpos de prova, 2020.

[156] ASTM B117-18, Standard Practice for Operating Salt Spray (Fog) Apparatus., Water. 03 (2003) 1–15. https://doi.org/10.1520/C0192.

[157] ASTM D570, Standard Test Method for Water Absorption of Plastics, ASTM Stand. 98 (2014) 25–28. https://doi.org/10.1520/D0570-98R10E01.2.

[158] ASTM D790-17, Flexural Properties of Unreinforced and Reinforced Plastics and Electrical Insulating Materials, ASTM Stand. (2017) 12. https://doi.org/10.1520/D0790-17.2.

[159] A. D2344-16, Standard Test Method for Short-Beam Strength of Polymer Matrix Composite Materials, Annu. B. ASTM Stand. 00 (2011) 1–8. https://doi.org/10.1520/D2344.

[160] ASTM D4065-12, Standard Practice for Plastics : Dynamic Mechanical Properties : Determination and Report of Procedures, Annu. B. ASTM Stand. i (2012) 1–7. https://doi.org/10.1520/D4065-12.1.8.

[161] ASTM D3171-15, Standard Test Methods for Constituent Content of Composite Prepreg, Am. Stand. Test. Methods. (2016) 1–6. https://doi.org/10.1520/D3171-22.Copyright.

[162] J. Schindelin, I. Arganda-Carreras, E. Frise, V. Kaynig, M. Longair, T. Pietzsch, S. Preibisch, C. Rueden, S. Saalfeld, B. Schmid, J.-Y. Tinevez, D.J. White, V. Hartenstein, K. Eliceiri, P. Tomancak, A. Cardona, Fiji: an open-source platform for biological-image analysis, Nat. Methods. 9 (2012) 676–682. https://doi.org/10.1038/nmeth.2019.

[163] S. Ahn, J.C. Lee, K.Y. Kim, Preparation and characterization of glass-fiber-reinforced modified polyphenylene oxide by a direct fiber feeding extrusion process, Appl. Sci. 11 (2021). https://doi.org/10.3390/app112110266.

[164] D. Romanzini, A. Lavoratti, H.L. Ornaghi, S.C. Amico, A.J. Zattera, Influence of fiber content on the mechanical and dynamic mechanical properties of glass/ramie polymer composites, Mater. Des. 47 (2013) 9–15. https://doi.org/10.1016/j.matdes.2012.12.029.

[165] Y. Wang, Z. Meng, W. Zhu, B. Wan, B. Han, G. Cai, X. Yin, Y. Bai, Hygrothermal aging behavior and aging mechanism of carbon nanofibers/epoxy composites, Constr. Build. Mater. 294 (2021) 123538. https://doi.org/10.1016/j.conbuildmat.2021.123538.

[166] B. Sharma, R. Chhibber, R. Mehta, Seawater ageing of glass fiber reinforced epoxy nanocomposites based on silylated clays, Polym. Degrad. Stab. 147 (2018) 103–114. https://doi.org/10.1016/j.polymdegradstab.2017.11.017.

[167] V. Cecen, Y. Seki, M. Sarikanat, I.H. Tavman, FTIR and SEM analysis of polyester- and epoxy-based composites manufactured by VARTM process, J. Appl. Polym. Sci. 108 (2008) 2163–2170. https://doi.org/10.1002/app.27857.

[168] Z. Wu, S. Li, M. Liu, Z. Wang, X. Liu, Liquid oxygen compatible epoxy resin: modification and characterization, RSC Adv. 5 (2015) 11325–11333. https://doi.org/10.1039/C4RA14100H.

[169] M. Torres-Carrasco, J.G. Palomo, F. Puertas, Sodium silicate solutions from dissolution of glasswastes. Statistical analysis, Mater. Construcción. 64 (2014) e014. https://doi.org/10.3989/mc.2014.05213.

[170] G.Z. Xiao, M. Delamar, M.E.R. Shanahan, Irreversible interactions between water and DGEBA/DDA epoxy resin during hygrothermal aging, J. Appl.

Polym. Sci. 65 (1997) 449–458. https://doi.org/10.1002/(sici)1097-4628(19970718)65:3<449::aid-app4>3.0.co;2-h.

[171] F. Ferdosian, Z. Yuan, M. Anderson, C. (Charles) Xu, Synthesis and characterization of hydrolysis lignin-based epoxy resins, Ind. Crops Prod. 91 (2016) 295–301. https://doi.org/10.1016/j.indcrop.2016.07.020.

[172] R. Krishna, A. Revathi, S. Srihari, R. Rao, Post-curing Effects on Hygrothermal Behavior of RT-cured Glass/Epoxy Composites, J. Reinf. Plast. Compos. 29 (2010) 325–330. https://doi.org/10.1177/0731684408097767.

[173] S. Beura, D.D. Pradhan, A.P. Chakraverty, D.N. Thatoi, U.K. Mohanty, Moisture effects leading to Tg depression in GFRP composites: An analysis, Mater. Today Proc. 62 (2022) 5987–5991. https://doi.org/10.1016/j.matpr.2022.04.965.

[174] H. Zhao, R.K.Y. Li, Effect of water absorption on the mechanical and dielectric properties of nano-alumina filled epoxy nanocomposites, Compos. Part A Appl. Sci. Manuf. 39 (2008) 602–611. https://doi.org/10.1016/j.compositesa.2007.07.006.

[175] T. Peret, A. Clement, S. Freour, F. Jacquemin, Effect of mechanical states on water diffusion based on the free volume theory: Numerical study of polymers and laminates used in marine application, Compos. Part B Eng. 118 (2017) 54–66. https://doi.org/10.1016/j.compositesb.2017.02.046.

[176] K. Utaloff, M.H. Kothmann, M. Ciesielski, M. Döring, T. Neumeyer, V. Altstädt, I. Gorman, M. Henningsen, Improvement of fracture toughness and glass transition temperature of DGEBA-based epoxy systems using toughening and crosslinking modifiers, Polym. Eng. Sci. 59 (2019) 86–95. https://doi.org/10.1002/pen.24870.

[177] M. Boutin, A. Rogeon, M. Aufray, R. Piquet, A. Rouilly, Influence of flax fibers on network formation of DGEBA/DETA matrix, Compos. Interfaces. 28 (2021) 17–34. https://doi.org/10.1080/09276440.2020.1736454.

[178] E. Ernault, E. Richaud, B. Fayolle, Thermal-oxidation of epoxy/amine followed by glass transition temperature changes, Polym. Degrad. Stab. 138

(2017) 82–90. https://doi.org/10.1016/j.polymdegradstab.2017.02.013.

[179] T.M. Le, B. Fatahi, H. Khabbaz, W. Sun, Numerical optimization applying trust-region reflective least squares algorithm with constraints to optimize the non-linear creep parameters of soft soil, Appl. Math. Model. 41 (2017) 236–256. https://doi.org/10.1016/j.apm.2016.08.034.

[180] P. Nogueira, C. Ramírez, A. Torres, M.J. Abad, J. Cano, J. López, I. López-Bueno, L. Barral, Effect of water sorption on the structure and mechanical properties of an epoxy resin system, J. Appl. Polym. Sci. 80 (2001) 71–80. https://doi.org/10.1002/1097-4628(20010404)80:1<71::AID-APP1077>3.0.CO;2-H.

[181] C. Chen, W. Zhang, Y. Li, L. Gu, Y. Luo, M. Qin, J. Zhang, Z. He, H. Wang, Y. Zheng, D. Yao, The Influence of Moisture Absorption-Drying of Composite Materials on the Bonding Performance of the Joints, Macromol. Mater. Eng. 2200463 (2022) 1–10. https://doi.org/10.1002/mame.202200463.

[182] F.G. Garcia, B.G. Soares, V.J.R.R. Pita, R. Sánchez, J. Rieumont, Mechanical properties of epoxy networks based on DGEBA and aliphatic amines, J. Appl. Polym. Sci. 106 (2007) 2047–2055. https://doi.org/10.1002/app.24895.

[183] T. Bond, Amine curing agents for epoxy resins, 1989.

[184] N.C.W. Judd, Absorption of water into carbon fibre composites, Br. Polym. J. 9 (1977) 36–40. https://doi.org/10.1002/pi.4980090106.

[185] A.N. Rajaram, C. Gin Boay, N. Srikanth, Effect of curing on the hygrothermal behaviour of epoxy and its carbon composite material, Compos. Commun. 22 (2020). https://doi.org/10.1016/j.coco.2020.100507.

[186] R.O. Ebewele, Polymer Science and Technology, CRC Press, Nova York, 2000.

[187] L. Calabrese, V. Fiore, T. Scalici, A. Valenza, Experimental assessment of the improved properties during aging of flax/glass hybrid composite laminates for marine applications, J. Appl. Polym. Sci. 136 (2019) 1–12.

https://doi.org/10.1002/app.47203.

[188] Z.A. Oguz, A. Erklig, Ö.Y. Bozkurt, Degradation of hybrid aramid/glass/epoxy composites hydrothermally aged in distilled water, J. Compos. Mater. 55 (2021) 2043–2060. https://doi.org/10.1177/0021998320984237.

[189] J.D. Tanks, Y. Arao, M. Kubouchi, Diffusion kinetics, swelling, and degradation of corrosion-resistant C-glass/epoxy woven composites in harsh environments, Compos. Struct. 202 (2018) 686–694. https://doi.org/10.1016/j.compstruct.2018.03.078.

[190] J.C. Radha, C. Ranganathaiah, Effect of the fiber orientation on the sorption kinetics of seawater in an epoxy/glass composite: A free-volume microprobe study, J. Appl. Polym. Sci. 109 (2008) 1302–1309. https://doi.org/10.1002/app.28100.

[191] X. Jiang, H. Kolstein, F. Bijlaard, X. Qiang, Effects of hygrothermal aging on glass-fibre reinforced polymer laminates and adhesive of FRP composite bridge: Moisture diffusion characteristics, Compos. Part A Appl. Sci. Manuf. 57 (2014) 49–58. https://doi.org/10.1016/j.compositesa.2013.11.002.

[192] A.D. Crocombe, Y.X. Hua, W.K. Loh, M.A. Wahab, I.A. Ashcroft, Predicting the residual strength for environmentally degraded adhesive lap joints, Int. J. Adhes. Adhes. 26 (2006) 325–336. https://doi.org/10.1016/j.ijadhadh.2005.04.003.

[193] M. Bordes, P. Davies, J.-Y. Cognard, L. Sohier, V. Sauvant-Moynot, J. Galy, Prediction of long term strength of adhesively bonded steel/epoxy joints in sea water, Int. J. Adhes. Adhes. 29 (2009) 595–608. https://doi.org/10.1016/j.ijadhadh.2009.02.013.

[194] J. Zhou, J.P. Lucas, Hygrothermal effects of epoxy resin. Part I: the nature of water in epoxy, Polymer (Guildf). 40 (1999) 5505–5512. https://doi.org/10.1016/S0032-3861(98)00790-3.

[195] A. Zafar, F. Bertocco, J. Schjødt-Thomsen, J.C. Rauhe, Investigation of the long term effects of moisture on carbon fibre and epoxy matrix composites, Compos. Sci. Technol. 72 (2012) 656–666.

https://doi.org/10.1016/j.compscitech.2012.01.010.

[196] Y.Z. Wan, Y.L. Wang, Y. Huang, B.M. He, K.Y. Han, Hygrothermal aging behaviour of VARTMed three-dimensional braided carbon-epoxy composites under external stresses, Compos. Part A Appl. Sci. Manuf. 36 (2005) 1102–1109. https://doi.org/10.1016/j.compositesa.2005.01.003.

[197] C. Arribas, M.G. Prolongo, M. Sánchez-Cabezudo, R. Moriche, S.G. Prolongo, Hydrothermal ageing of graphene/carbon nanotubes/epoxy hybrid nanocomposites, Polym. Degrad. Stab. 170 (2019) 109003. https://doi.org/10.1016/j.polymdegradstab.2019.109003.

[198] S. Roy, W.X. Xu, S.J. Park, K.M. Liechti, Anomalous Moisture Diffusion in Viscoelastic Polymers: Modeling and Testing, J. Appl. Mech. 67 (2000) 391–396. https://doi.org/10.1115/1.1304912.

[199] G. Serpe, N. Chaupart, J. Verdu, Ageing of polyamide 11 in acid solutions, Polymer (Guildf). 38 (1997) 1911–1917. https://doi.org/10.1016/S0032-3861(96)00705-7.

[200] O. Starkova, S.T. Buschhorn, E. Mannov, K. Schulte, A. Aniskevich, Water transport in epoxy/MWCNT composites, Eur. Polym. J. 49 (2013) 2138–2148. https://doi.org/10.1016/j.eurpolymj.2013.05.010.

[201] N. Guermazi, K. Elleuch, H.F. Ayedi, The effect of time and aging temperature on structural and mechanical properties of pipeline coating, Mater. Des. 30 (2009) 2006–2010. https://doi.org/10.1016/j.matdes.2008.09.003.

[202] L.-R. Bao, A.F. Yee, Effect of temperature on moisture absorption in a bismaleimide resin and its carbon fiber composites, Polymer (Guildf). 43 (2002) 3987–3997. https://doi.org/10.1016/S0032-3861(02)00189-1.

[203] L.T. Drzal, The role of the fiber-matrix interphase on composite properties, Vacuum. 41 (1990) 1615–1618. https://doi.org/10.1016/0042-207X(90)94034-N.

[204] X. Yin, Y. Liu, Y. Miao, G. Xian, Water absorption, hydrothermal expansion, and thermomechanical properties of a vinylester resin for fiber-

reinforced polymer composites subjected to water or alkaline solution immersion, Polymers (Basel). 11 (2019). https://doi.org/10.3390/polym11030505.

[205] E. Ernault, E. Richaud, B. Fayolle, Thermal oxidation of epoxies: Influence of diamine hardener, Polym. Degrad. Stab. 134 (2016) 76–86. https://doi.org/10.1016/j.polymdegradstab.2016.09.030.

[206] J.L. Thomason, Investigation of composite interphase using dynamic mechanical analysis: Artifacts and reality, Polym. Compos. 11 (1990) 105–113. https://doi.org/10.1002/pc.750110206.

[207] S. Mallarino, J.F. Chailan, J.L. Vernet, Interphase investigation in glass fibre composites by micro-thermal analysis, Compos. Part A Appl. Sci. Manuf. 36 (2005) 1300–1306. https://doi.org/10.1016/j.compositesa.2005.01.017.

[208] E.K. Drown, Characterization of the interphase and its influence on the behavior of glass-reinforced epoxy composites, Michigan State University, 2001.

[209] X. Jiang, H. Kolstein, F.S.K. Bijlaard, Moisture diffusion and hygrothermal aging in pultruded fibre reinforced polymer composites of bridge decks, Mater. Des. 37 (2012) 304–312. https://doi.org/10.1016/j.matdes.2012.01.017.

[210] U. Saeed, H. Al-Turaif, M.E. Siddiqui, Stress relaxation performance of glass fiber-reinforced high-density polyethylene composite, Polym. Polym. Compos. 29 (2021) 705–713. https://doi.org/10.1177/0967391120932062.

[211] N. Obaid, M. Kortschot, M. Sain, Understanding the Stress Relaxation Behavior of Polymers Reinforced with Short Elastic Fibers, Materials (Basel). 10 (2017) 472. https://doi.org/10.3390/ma10050472.

[212] A.V. Oskouei, S.M. Taleie, Experimental investigation of relaxation of fiber-reinforced polymer composites, J. Reinf. Plast. Compos. 29 (2010) 2705–2718. https://doi.org/10.1177/0731684409357256.

[213] L. Yin, C. Zhang, W. Yang, Y. Tian, B. Yan, Y. Liu, Y. Wang, Research on water absorption characteristic of cycloaliphatic epoxy resin insulator, in:

2020 IEEE 1st China Int. Youth Conf. Electr. Eng., IEEE, 2020: pp. 1–5. https://doi.org/10.1109/CIYCEE49808.2020.9332754.

[214] E.C. Botelho, M.L. Costa, L.C. Pardini, M.C. Rezende, Processing and hygrothermal effects on viscoelastic behavior of glass fiber/epoxy composites, J. Mater. Sci. 40 (2005) 3615–3623. https://doi.org/10.1007/s10853-005-0760-2.

[215] F.X. Perrin, M.H. Nguyen, J.L. Vernet, Water transport in epoxy–aliphatic amine networks – Influence of curing cycles, Eur. Polym. J. 45 (2009) 1524–1534. https://doi.org/10.1016/j.eurpolymj.2009.01.023.

[216] A. Roy, E. Gontcharova-Bénard, J.-L. Gacougnolle, P. Davies, Hygrothermal Effects on Failure Mechanisms of Composite/Steel Bonded Joints, in: Time Depend. Nonlinear Eff. Polym. Compos., ASTM International, 100 Barr Harbor Drive, PO Box C700, West Conshohocken, PA 19428-2959, 2000: pp. 353-353–19. https://doi.org/10.1520/STP15843S.

[217] P. Sun, Y. Zhao, Y. Luo, L. Sun, Effect of temperature and cyclic hygrothermal aging on the interlaminar shear strength of carbon fiber/bismaleimide (BMI) composite, Mater. Des. 32 (2011) 4341–4347. https://doi.org/10.1016/j.matdes.2011.04.007.

[218] Y. Yu, P. Li, G. Sui, X. Yang, H. Liu, Effects of hygrothermal aging on the thermal-mechanical properties of vinylester resin and its pultruded carbon fiber composites, Polym. Compos. 30 (2009) 1458–1464. https://doi.org/10.1002/pc.20712.

[219] P. Alam, C. Robert, C.M. Ó Brádaigh, Tidal turbine blade composites - A review on the effects of hygrothermal aging on the properties of CFRP, Compos. Part B Eng. 149 (2018) 248–259. https://doi.org/10.1016/j.compositesb.2018.05.003.

[220] R. Attukur Nandagopal, C. Gin Boay, S. Narasimalu, An empirical model to predict the strength degradation of the hygrothermal aged CFRP material, Compos. Struct. 236 (2020) 111876. https://doi.org/10.1016/j.compstruct.2020.111876.

[221] A. Jumahat, C. Soutis, F.R. Jones, A. Hodzic, Fracture mechanisms and

failure analysis of carbon fibre/toughened epoxy composites subjected to compressive loading, Compos. Struct. 92 (2010) 295–305. https://doi.org/10.1016/j.compstruct.2009.08.010.

[222] I.R. Chowdhury, N.P. O'Dowd, A.J. Comer, Experimental study of hygrothermal ageing effects on failure modes of non-crimp basalt fibre-reinforced epoxy composite, Compos. Struct. 275 (2021) 114415. https://doi.org/10.1016/j.compstruct.2021.114415.

[223] A.M. Amaro, P.N.B. Reis, M.F.S.F. de Moura, Delamination Effect on Bending Behaviour in Carbon-Epoxy Composites, Strain. 47 (2011) 203–208. https://doi.org/10.1111/j.1475-1305.2008.00520.x.

[224] B.K. Daniels, N.K. Harakas, R.C. Jackson, Short beam shear tests of graphite fiber composites, Fibre Sci. Technol. 3 (1971) 187–208. https://doi.org/10.1016/0015-0568(71)90002-9.

[225] R.P. Reed, M. Madhukar, B. Thaicharoenporn, N.N. Martovetsky, Low-temperature mechanical properties of glass/epoxy laminates, in: AIP Conf. Proc., 2014: pp. 109–116. https://doi.org/10.1063/1.4860612.

[226] X. Wang, X. Zhao, Z. Wu, Z. Zhu, Z. Wang, Interlaminar shear behavior of basalt FRP and hybrid FRP laminates, J. Compos. Mater. 50 (2016) 1073–1084. https://doi.org/10.1177/0021998315587132.

[227] L. Sang, C. Wang, Y. Wang, W. Hou, Effects of hydrothermal aging on moisture absorption and property prediction of short carbon fiber reinforced polyamide 6 composites, Compos. Part B Eng. 153 (2018) 306–314. https://doi.org/10.1016/j.compositesb.2018.08.138.

[228] R. Guo, G. Xian, F. Li, C. Li, B. Hong, Hygrothermal resistance of pultruded carbon, glass and carbon/glass hybrid fiber reinforced epoxy composites, Constr. Build. Mater. 315 (2022) 125710. https://doi.org/10.1016/j.conbuildmat.2021.125710.

[229] C. HUMEAU, Contribution to the study of coupling between moisture diffusion and mechanical stress, in high performance marine materials, Université Bretagne Loire, 2017.

[230] H.N. Narasimha Murthy, M. Sreejith, M. Krishna, S.C. Sharma, T.S. Sheshadri, Seawater Durability of Epoxy/Vinyl Ester Reinforced with Glass/Carbon Composites, J. Reinf. Plast. Compos. 29 (2010) 1491–1499. https://doi.org/10.1177/0731684409335451.

[231] T. Sinmazçelik, A.A. Arici, Influence of various fluids on the interlaminar shear strength (ILSS) and impact behaviour of carbon/pei composites, J. Mater. Sci. 41 (2006) 3255–3262. https://doi.org/10.1007/s10853-005-5475-x.

[232] D. Tzetzis, K. Tsongas, G. Mansour, Determination of the Mechanical Properties of Epoxy Silica Nanocomposites through FEA-Supported Evaluation of Ball Indentation Test Results, Mater. Res. 20 (2017) 1571–1578. https://doi.org/10.1590/1980-5373-mr-2017-0454.

[233] F. Jeyranpour, G. Alahyarizadeh, B. Arab, Comparative investigation of thermal and mechanical properties of cross-linked epoxy polymers with different curing agents by molecular dynamics simulation, J. Mol. Graph. Model. 62 (2015) 157–164. https://doi.org/10.1016/j.jmgm.2015.09.012.

[234] A. Djabali, L. Toubal, R. Zitoune, S. Rechak, An experimental investigation of the mechanical behavior and damage of thick laminated carbon/epoxy composite, Compos. Struct. 184 (2018) 178–190. https://doi.org/10.1016/j.compstruct.2017.09.069.

[235] K. Lasn, A.T. Echtermeyer, A. Klauson, F. Chati, D. Décultot, Comparison of laminate stiffness as measured by three experimental methods, Polym. Test. 44 (2015) 143–152. https://doi.org/10.1016/j.polymertesting.2015.04.006.

[236] C. Wu, B.C. Meng, L. Tam, L. He, Yellowing mechanisms of epoxy and vinyl ester resins under thermal, UV and natural aging conditions and protection methods, Polym. Test. 114 (2022) 107708. https://doi.org/10.1016/j.polymertesting.2022.107708.

[237] Y. Fang, P. Chen, R. Huo, Y. Liang, L. Wang, W. Liu, Hygrothermal ageing of polymeric sandwich structures used in structural engineering, Constr. Build. Mater. 165 (2018) 812–824.

https://doi.org/10.1016/j.conbuildmat.2018.01.072.

Appendix A - Composites' manufacturing process

The manufacturing process of the composite materials adopted by the manufacturer is described as follows:

i. A demolding layer was applied to a MDF plate and the laboratory's temperature and moisture were registered for the better control of the resin mixture;
ii. Mixing of resin's lamination components A and B following the mass relation of 5,7A:1B specified by the manufacturer;
iii. Application of a resin layer with the aid of a wool roll;
iv. Application of a glass-fiber layer (Figure A.1);
v. Pressing with a metallic roll (Figure A.2);
vi. Processes iii to v were repeated until the twentieth layer;
vii. Application of a final resin layer (Figure A.3);
viii. Application of a Peel-Ply layer, a nonstick fabric designed to finish the surface and leave a surface suitable to the painting process, if needed (Figure A.4);
ix. After cured, each plate was demolded from the MDF plate and properly identified with the plate's number. Overall, fifteen plates were fabricated to be cut to produce the samples. The nominal thickness of the plates 6 mm. Following on the measurements of the samples after the cutting process the average thickness is 6.70 ± 0.05 mm.

A. 1. Application of a glass-fiber layer [155].

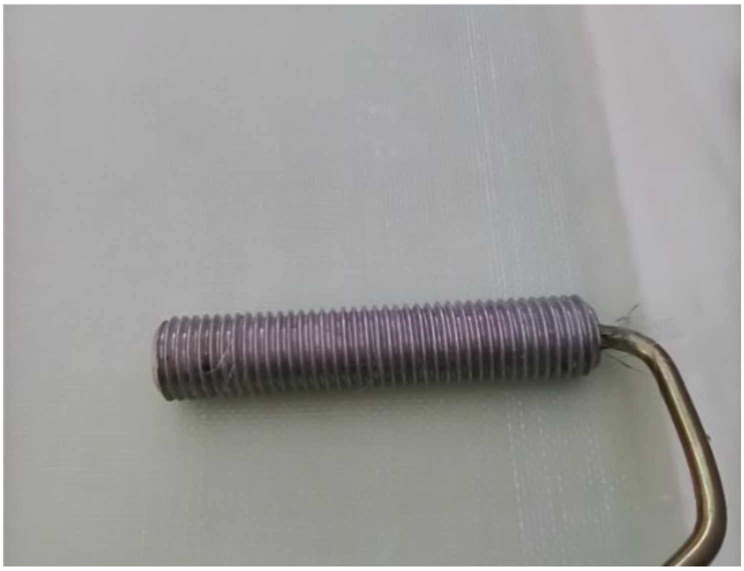

A. 2. Pressing with a metallic roll [155].

A. 3. Application of a resin layer [155].

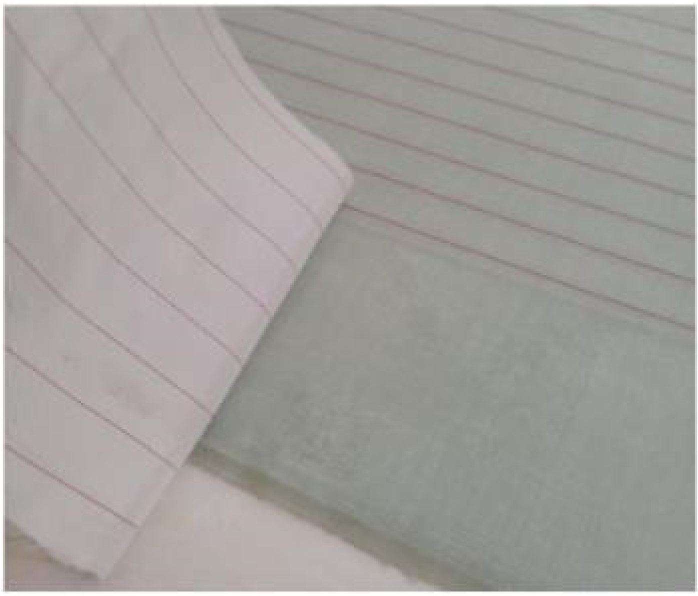

A. 4. Application of a peel-ply fabric layer [155].

Appendix B – Failure modes for the destructive tests

B.1 – Bending tests

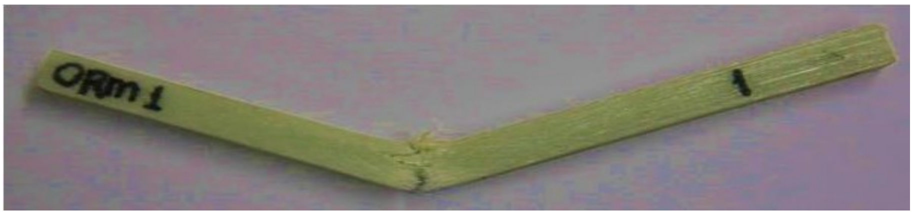

B. 1. Failure mode for the unaged bending specimens.

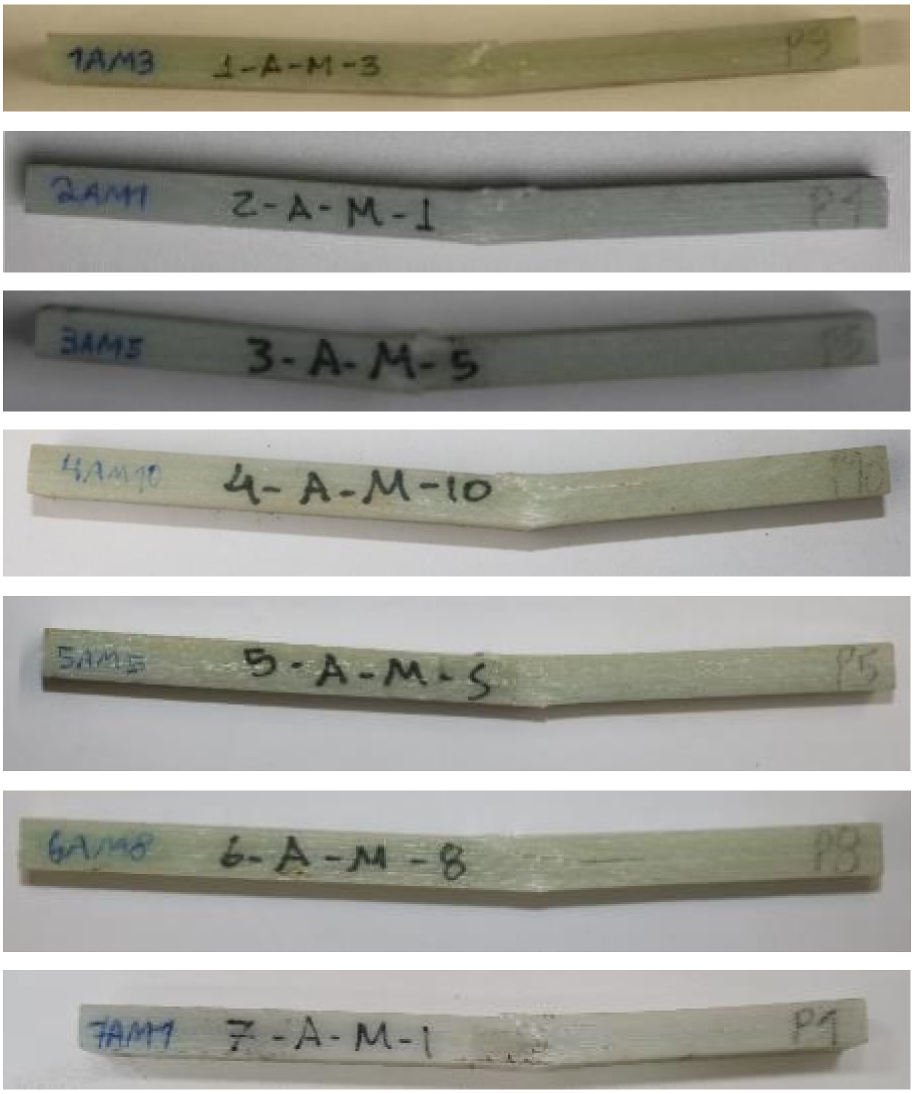

B. 2. Failure modes for the aged bending specimens (R1 – R7) at 35°C.

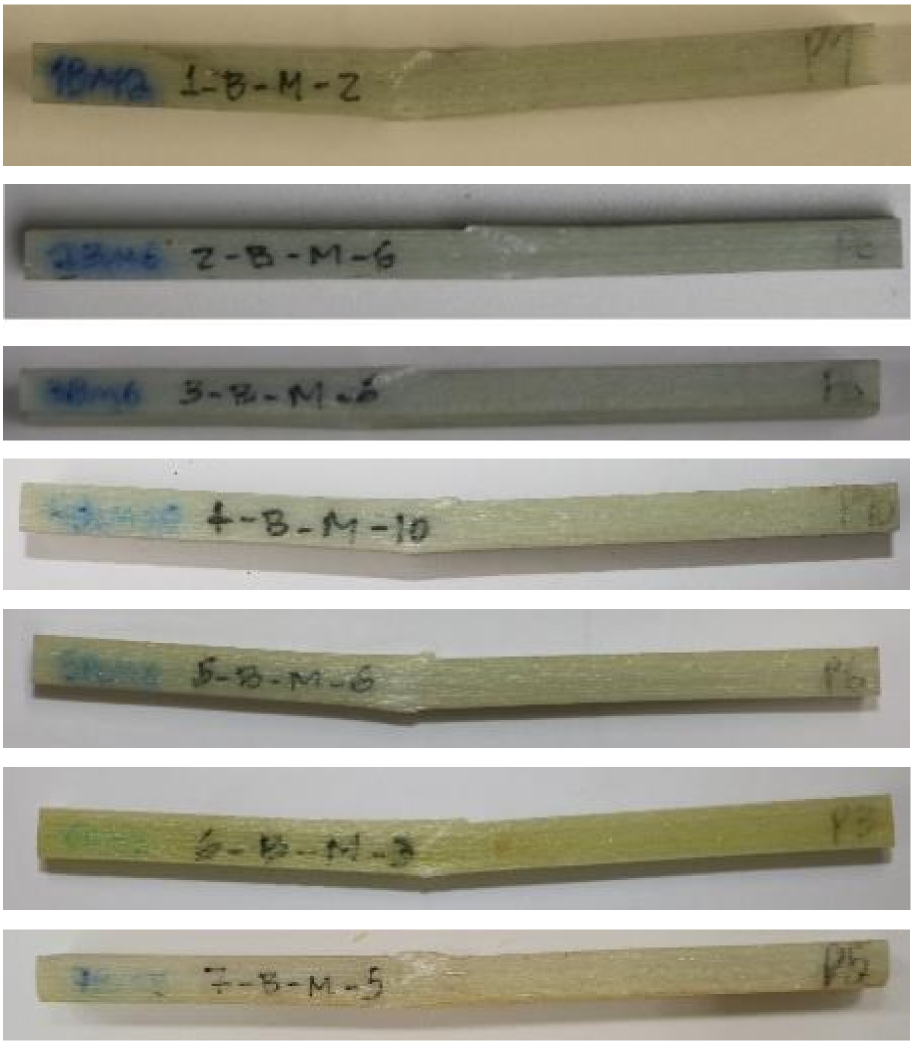

B. 3. Failure modes for the aged bending specimens (R1 – R7) at 55°C.

B. 4. Failure modes for the aged bending specimens (R1 – R7) at 70°C.

B.2 – Interlaminar Shear Tests

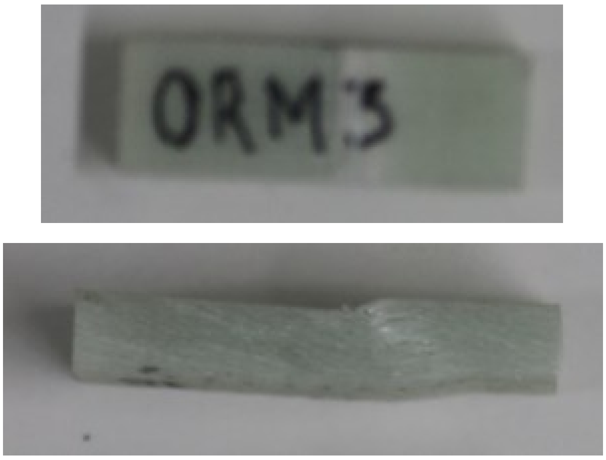

B. 5. Failure mode for the unaged ILSS specimens.

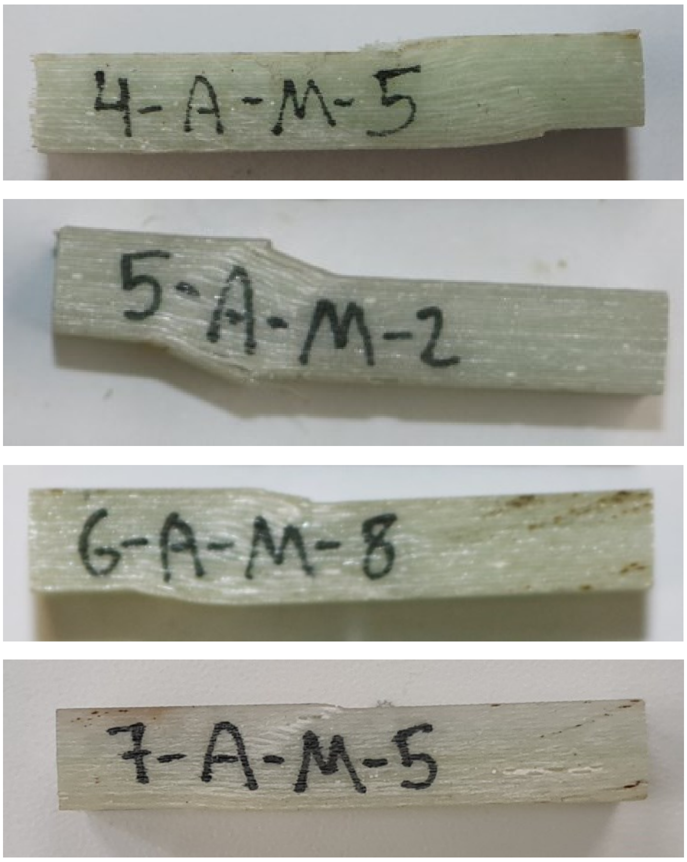

B. 6. Failure modes for the aged ILSS specimens (R1 – R7) at 35°C.

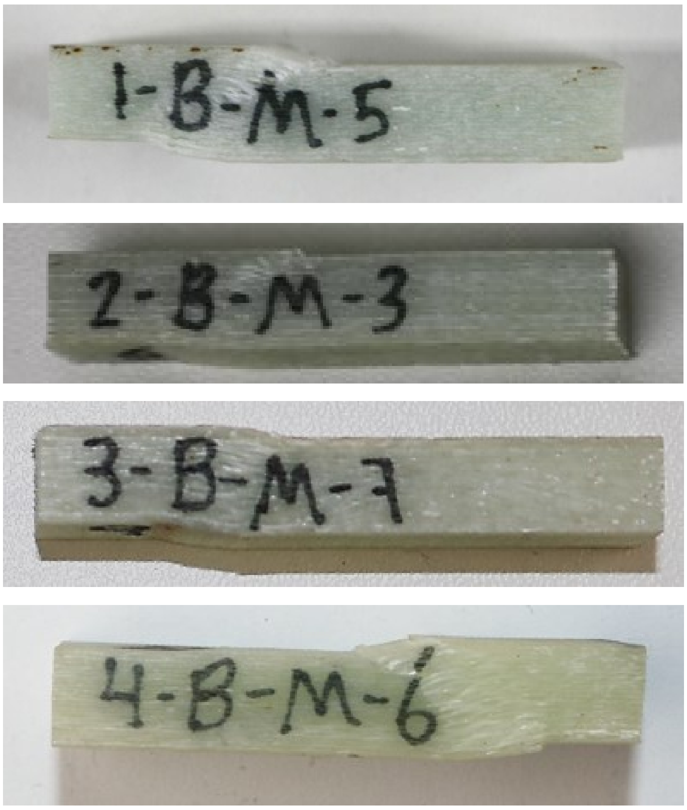

B. 7. Failure modes for the aged ILSS specimens (R1 – R7) at 55°C.

B. 8. Failure modes for the aged ILSS specimens (R1 – R7) at 70°C.